

THE DETECTION OF ADHESIVE WEAR ON CYLINDER LINERS  
FOR SLOW SPEED DIESEL ENGINE THROUGH TRIBOLOGY,  
TEMPERATURE, EDDY CURRENT AND ACOUSTIC EMISSION  
MEASUREMENT AND ANALYSIS

**AKM KHORSHED ALAM**

The Thesis is submitted for the  
DEGREE OF DOCTOR OF PHILOSOPHY  
Faculty of Science, Agriculture and Engineering  
UNIVERSITY OF NEWCASTLE UPON TYNE  
December, 2013

## **ABSTRACT**

The research concerns the condition monitoring of cylinder liner of large bore diesel engines using various methodologies to identify the onset of scuffing. The reasons of scuffing, improved designs and operational processes to prevent its occurrence were discussed.

The research focused on modeling the normal condition of the cylinder liner with sufficient lubrication and detecting the precursor of scuffing by reducing the lubrication. The four detection systems used on the test facilities and field tests of the cylinder liners used tribology, temperature sensor, eddy current sensor and acoustic emission sensor.

Experimental assessment of eddy current sensor was conducted for insufficient lubricating oil conditions for different cylinder liner wall pressures using a specially designed test facility. Field tests of temperature sensor and eddy current sensor were carried out on a 800mm bore worn cylinder liner of a container ship in service. Field test of acoustic emission sensor was carried out on a high speed automobile engine.

Scuffing detection by temperature sensing should be considered as the last safety barrier, as it registers the after effect of scuffing and solely depends on the localized condition and the material's thermal status.

Mounting eddy current sensors are considered intrusive. Four sensors per cylinder are needed, which are prone to damage by the rings when the liner wears out. Additionally, the sensors measure only small section of the rings and their lubrication condition.

Acoustic emission analysis effectively detects onset of scuffing on the cylinder liners and the rings. Initial findings from the lab and the field test on a four stroke engine confirmed this. However, more field tests under various loading condition on a slow speed engine is needed to understand the various event alignment and the non-routine detection, such as scuffing. They can be coupled with thermocouples to serve as a secondary protection.

## **ACKNOWLEDGEMENTS**

First of all, I am sincerely grateful to my supervisor, Professor A P Roskilly for his important and valuable support throughout this work, and for giving me the opportunity to work in this stimulating research. His wide knowledge, personal guidance and encouragement have provided a strong basis for this thesis.

I would also like to thank Dr Jorge Antunes, Professor Krishnan Balasubramaniam and Dr Vis for their kind support and assistance.

During the entire study, I have collaborated with many colleagues for whom I have great regard. I want to extend my warmest thanks to all of them for all their help, guidance, encouragement, and friendship during my graduate study.

On a personal level, I wish to express my deepest gratitude to my family members for their love, encouragement, help and support. Whilst writing this acknowledgement, my thoughts go to my late father M A Malik, who lived his whole life searching for truth and knowledge. It is only for the knowledge of his children he would always be proud of and always reserved his worthy praise for it. I would also like to express my indebtedness to my mother Rabeya Khatoon and two sisters (Shirin Sahana and Laila Rihana) for their continuous support and care.

## TABLE OF CONTENTS

<b>TITLE</b>	i
<b>ABSTRACT</b>	ii
<b>ACKNOWLEDGEMENTS</b>	iii
<b>TABLE OF CONTENTS</b>	iv-x
<b>LIST OF TABLES</b>	xi
<b>LIST OF FIGURES</b>	xii-xvii
<b>NOMENCLATURES</b>	xviii-xxiii
<b>Chapter 1. Inroduction:</b>	
1.0 Introduction	1-5
1.1 Aims and objectives	5
1.2 Methodology	5
1.3 Structure of the thesis	6
<b>Chapter 2. Literature Review:</b>	
2.1 Causes of scuffing	
2.1.1 Starved lubrication	7-8
2.1.2 Initiation of scuffing on piston rings and cylinder liner	8
2.1.3 Coefficient of friction	8
2.1.4 Volatility of cylinder lubricating oil	8
2.1.5 Carbon deposit	9
2.1.6 Water in scavenge air	9
2.1.7 Slow burning fuel	9
2.1.8 Catfines in fuel	9
2.1.9 High temperature of cylinder liner wall	9
2.1.10 Modern engine design and operation	10
2.1.10.1 Piston ring pack designs	11
2.1.10.2 Piston ring operation condition	11-12
2.1.10.3 Piston ring running-in	12-14
2.1.10.4 Piston ring manufacturing model	14-26
2.1.10.5 Piston ring leakage areas	26-27
2.1.10.6 Piston ring thermal deformation	27-30
2.1.10.7 Piston ring flutter	30-31



2.1.10.8 Loss of ring tension	31
2.1.10.9 Fitting of new rings	31
2.1.10.10 Pressure distribution along the ring set	31-35
2.1.10.11 Consequences of ring behavior	35
2.2 Counter-measures for Scuffing	35-36
2.2.1 Thermal correction	36
2.2.2 Correction by pressure	37-40
2.2.3 Correction by wear	40
2.2.4 Shape correction:	41
2.2.4.1 Chamfered ring ends	42
2.2.4.2 Running in	42-43
2.2.4.3 Cylinder liner surface	44
2.2.5 Correction by material	
2.2.5.1 Cast iron	44
2.2.5.2 Chromed ring grooves	44
2.2.5.3 Other coatings	45
2.2.6 Correction by revolving piston ring	45
2.2.7 Carbon control by flame ring	46
2.2.8 Slide valves	46
2.2.9 Effective purification and filtration of fuel oil	46
2.2.10 Correction by lubrication	46-47
2.2.10.1 Lubricants delivery	47
2.2.10.2 Lubricants formulation	47-48
2.3 Detection methods of scuffing	48-50
2.3.1 Tribological method	51-53
2.3.2 Thermoelectric Method	53
2.3.2.1 Thermocouples	53-56
2.3.2.2 Resistance Temperature Devices	56-57
2.3.2.3 Thermistors	57-60
2.3.3 Eddy Current Method	60-62
2.3.4 Acoustic emission method	62-67
2.4 Summary of literature review and the need of the research	68-69

### Chapter 3. Theory and Modeling:

3.1 Theory and modeling of tribology method	
3.1.1 Theory of piston ring tribology	70
3.1.1.1 Entraining velocity	70-71
3.1.1.2 Surface roughness	72
3.1.1.3 Characterisation by statistical parameters	72-74
3.1.1.4 Spatial characteristics of real surface	74-76
3.1.1.5 Optimum surface roughness	77
3.1.1.6 Composite roughness	78-79
3.1.1.7 Specific film thickness	79
3.1.1.8 $\frac{\eta N}{P}$ diagram	79-83
3.1.1.9 Dynamic viscosity	83-84
3.1.1.10 Viscosity-Shear stress	85
3.1.1.11 Viscosity-Shear rate relationship	86
3.1.1.12 Reynold's hydrodynamic lubrication equation	87
3.1.1.12.1 Equilibrium of an element	87
3.1.1.12.2 Shear stress	87
3.1.1.12.3 Velocity in 'X' direction	88
3.1.1.12.4 Continuity of flow in a column	89-92
3.1.1.12.5 Reynold's equation for squeeze film	93-97
3.1.1.12.6 Squeeze time	97
3.1.1.12.7 Cavitation and squeeze effect	97
3.1.1.13 Gas pressure and hydrodynamic pressure	98
3.1.2 Mathematical modeling of tribology method	98
3.1.2.1 Piston ring hydrodynamic and Squeeze film combined lubrication mathematical model	98
3.1.2.1.1 Piston ring bearing geometry	99-104
3.1.2.1.2 Radial force balance	105-106
3.1.2.2 Piston ring boundary lubrication model	106-109
3.1.2.3 Piston ring mixed lubrication model	109-111
3.1.2.4 Piston ring 'No Lubrication Model'	111-114

3.2 Theory and modeling of thermoelectric method	
3.2.1 Theory of thermoelectric method	114-115
3.2.2 Mathematical modeling of thermoelectric method	115-119
3.3 Theory and modeling of eddy current method	
3.3.1 Theory of eddy current method	119-120
3.3.1.1 Effective depth	120-121
3.3.1.2 Eddy current sensors	121-122
3.3.1.2.1 Sensor construction	122
3.3.1.2.2 Spot size, Target size and range	122-123
3.3.1.2.3 Target materials and rotating targets	123-124
3.3.1.2.4 Environmental parameters: temperature	124
3.3.1.2.5 Probe mounting	124-125
3.3.1.2.6 Error sources	125
3.3.1.2.7 Linearity	125-126
3.3.1.2.8 Effective sensor range	126
3.3.1.2.9 Cable length	126
3.3.1.2.10 Frequency range and power consumption	127
3.3.2 Mathematical model of eddy current scuffing detection	127-128
3.4 Theory and modeling of acoustic emission method	
3.4.1 Theory of acoustic emission method	128-130
3.4.1.1 Fundamentals of AE measurement	130-132
3.4.1.2 Factors affecting AE response	132
3.4.1.3 Detection of AE	133-134
3.4.1.4 Acoustic wave properties	134-135
3.4.1.5 AE sensors	135-136
3.4.2 Mathematical modeling of acoustic emission method	136-140
3.4.2.1 Mathematical model	140-142
3.4.2.2 Signal Processing:	142-146
3.4.2.3 Source localization	146-147
3.4.2.3.1 1-dimensional localization	147-149
3.4.2.3.2 2-dimensional localization	149-150
3.4.2.3.3 Optimization	150-151

3.5 Summary of modeling of scuffing detection methods	152
<b>Chapter 4. Experimental tests:</b>	
4.1 Analytical simulation of tribology model	153
4.2 Field test of thermoelectric sensor	153-155
4.3 Field test of eddy current sensor	
4.3.1 Jig test	
4.3.1.1 Materials	156
4.3.1.2 Scope of analysis work	156-157
4.3.1.2.1 Surface metallographic examination	157
4.3.1.2.2 Sectional metallographic examination	157
4.3.1.2.3 Hardness test	158
4.3.1.2.4 Energy dispersive X-ray (EDX)	158
4.3.1.2.5 Chemical analysis	159
4.3.1.3 Fabrication of test jig	160-161
4.3.1.3.1 Load cell calibration	161-162
4.3.1.3.2 Jig test Analysis	163-164
4.3.1.3.3 Potential issues with test jig	164-165
4.3.2 Engine test	
4.3.2.1 Engine detail	165-167
4.3.2.2 System concept	167
4.3.2.3 System architecture	168-171
4.3.2.4 Engine load and cylinder pressure	171-173
4.3.2.5 Software development and system variables	173-175
4.4 Field test of AE sensors	
4.4.1 Lab test	
4.4.1.1 Development and Characterization of sensor	175
4.4.1.2 Development of electronics and data acquisition hardware	175
4.4.1.3 Fabrication of test rig	176
4.4.1.4 Integration of hardware and sensors	176
4.4.1.5 Test rig preliminary data analysis	176-182

4.4.2 Engine test	
4.4.2.1 Sensor mounting locations	182-186
4.4.2.2 Data collected on single cylinder engine	184-187
4.4.2.3 Methodology followed	188
4.4.2.4 Development of DSP algorithms	189
<b>Chapter 5. Results and Discussion:</b>	
5.1 Tribology model –results and discussion	190
5.1.1 Hydrodynamic lubrication	190
5.1.1.1 To find constants $C_1$ and $C_2$	190-191
5.1.1.2 $P_z$ profile	191-192
5.1.1.3 Hydrodynamic pressure distribution	192-193
5.1.1.4 Oil film thickness profile	193
5.1.1.5 Load, Friction force and Coefficient of friction	194-196
5.1.1.6 Lubricant volume	196
5.1.1.7 Multiple compression ring	196-197
5.1.1.8 Limitation of the model	197-198
5.1.2 Boundary lubrication	198
5.1.3 Mixed lubrication	198
5.2 Thermoelectric analysis - results and discussion	199-203
5.3 Eddy current analysis – results and discussions	
5.3.1 Baseline tests	203
5.3.2 Wear tests	204-205
5.3.3 Sensor output from engine cylinder 4	206-211
5.3.4 Notes on data analysis	211-212
5.4 Acoustic emission analysis- results and discussions	
5.4.1 Time domain analysis	
5.4.1.1 Comparison between reference condition and worn out rings	212-213
5.4.1.2 Comparison between reference condition and worn out piston	214
5.4.1.3 Comparison between reference condition and Oil starve condition	215

5.4.2 Frequency domain analysis	216-219
5.4.2.1 Segmentation of the data	220
5.4.2.2 Feature extraction	221-232
<b>Chapter 6. Conclusion and Future work:</b>	233-236
 <b>Appendices</b>	
Liner Material Analysis	237-245
Manual for Tribological model of scuffing detection	246-254
 <b>References</b>	255-268

## LIST OF TABLES

<b>Tables</b>	<b>Page</b>
Table 2.1. Piston rings geometry characteristics	19
Table 2.2 Comparative analyses of three sensors	50
Table 2.3 Thermocouple Types	54
Table 2.4 Comparison of thermocouple, RTD and Thermistor	60
Table 3.1: Typical Surface finish of cylinder liner	76
Table 3.2 Characteristics of liner surfaces & Greenwood-Tripp Parameters	107
Table 3.3 Factors affect relative amplitude of acoustic emission response	131
Table 4.1 Detail specification of the engine and experiment condition	152
Table 4.2 Hardness values of the specimen	157
Table 4.3 Chemical composition of specimen	157
Table 4.4 Elemental composition of specimen	158
Table 4.5 Close end gaps of rings	183
Table 5.1 Load cell readings with no load	203
Table 5.2 Load cell readings after ring was loaded	203
Table 5.3 Details of the segments extracted	219
Table 5.4 Features extracted for different domains of the signal	221
Table 5.5 Different fault and features that indicate their presence	226
Table 5.6 Consolidated results of frequency domain analysis	231

## LIST OF FIGURES

<b>Figures</b>	<b>Page</b>
Figure 1.1 Contributing factors to piston ring and cylinder liner wear	2
Figure 1.2 Abrasive Wear	3
Figure 1.3 Corrosive wear	4
Figure 1.4 Scuffing on piston ring surface	5
Figure 2.1 Piston ring operations condition	12
Figure 2.2 Engine load and Ring shape	14
Figure 2.3 Ideal pressure distribution around a piston ring cross section	15
Figure 2.4 Variation of wall pressure with $D/a$ for different values of 'f'	17
Figure 2.5 $D/a$ , commonly used; from the above graph	17
Figure 2.6 Piston ring stress during working and fitting	18
Figure 2.7 Relationship of Cylinder diameter and Ring height	20
Figure 2.8 Ring Height and Width Vs Cylinder Diameter of 2-S engines	20
Figure 2.9 Variation of stresses $K_{B1}$ and $K_{B2}$ with $D/a$ against values of 'f'	21
Figure 2.10 Stress – deformation diagram	23
Figure 2.11 Piston ring set acting as a labyrinth	24
Figure 2.12 Temperature profile and distribution of piston rings	28
Figure 2.13 Pressure distribution in a ring set with a gastight top ring	32
Figure 2.14 Measured/calculated inter-ring gas pressure of a 2-S cylinder	34
Figure 2.15 Ring running under good conditions	38
Figure 2.16 Gas pressure distribution around irregular ring profiles	39
Figure 2.17 Curvature Distribution of top ring	43
Figure 2.18 Typical Thermocouple setup with cold junction compensation	55
Figure 2.19 Four wire RTD connection	57
Figure 2.20 Acoustic emission principle	62
Figure 3.1 Crank mechanism	69
Figure 3.2 Roughness average (centre line average)	71
Figure 3.3 Root mean square roughness (RMS or $R_q$ )	72
Figure 3.4 Effect of averaging on $R_a$ value	72
Figure 3.5 Auto-covariance function	73-74



Figure 3.6 Auto-correlation function	74
Figure 3.7 Structure function	75
Figure 3.8 Optimum surface roughness diagram	76
Figure 3.9 Composite roughness	77
Figure 3.10 Lubrication regime	78
Figure 3.11 Effect of viscosity, speed, and load on bearing friction	79
Figure 3.12 Effect of viscosity, speed, and load on film thickness	80
Figure 3.13 Oil film thickness against crank angle	81
Figure 3.14 Oil film thickness on top ring at 2 <sup>nd</sup> ring TDC position against engine load%	82
Figure 3.15 Relationship of force, area and velocity gradient	84
Figure 3.16 Shear stress- shear rate characteristic of a Newtonian fluid	85
Figure 3.17 An element of fluid of hydrodynamic film in equilibrium position 'p' is the pressure, $\tau_x$ is the shear stress acting in the 'x' direction	86
Figure 3.18 Velocity profiles at the entry of the hydrodynamic film	87
Figure 3.19 Continuity of flow in a column	88
Figure 3.20 Maximum pressure and the pressure gradient	90
Figure 3.21 Squeeze film lubrication	92
Figure 3.22 Squeeze film between two parallel plates	93
Figure 3.23 Geometry of the parabolic wedge bearing	98
Figure 3.24 Application of geometry of parabolic wedge bearing in piston ring	98
Figure 3.25 Hydrodynamic pressure distribution in a starved piston ring/liner conjunction	102
Figure 3.26 Forces acting on a piston ring at steady state condition	104
Figure 3.27 Asperity contact pressure against oil film thickness	108
Figure 3.28 Different lubrication regimes encountered during an expansion stroke at 120r/min and 3 Kgf.	109
Figure 3.29 Friction results exhibiting 3 lubrication regimes	110
Figure 3.30 Fourier profile of temperature readings	117
Figure 3.31 Fourier profile of temperature reading	118
Figure 3.32 Eddy current sensor (ring/liner)	119

Figure 3.33 Eddy current sensor	120
Figure 3.34 Eddy-Current Probe Construction	121
Figure 3.35 Eddy-Current probe spot size	121
Figure 3.36 Magnetic field induces eddy current in conductive target	122
Figure 3.37 Interference of eddy-current probes mounted near each other	123
Figure 3.38 Mounting hardware interfere with eddy probe magnetic field	124
Figure 3.39 Linearity Error - Measured data deviates from the straight line	125
Figure 3.40 Comparison of NDT principles - active/ passive techniques	128
Figure 3.41 AE Detection System	130
Figure 3.42 Detection of AE wave	132
Figure 3.43 Linear System	139
Figure 3.44 Overall process	141
Figure 3.45 Signal Processing	143
Figure 3.46 Overview of BSS	144
Figure 3.47 Sample output from array of (8) sensors.	147
Figure 3.48 Principle of a 1-dimensional localization	147
Figure 3.49 Two-Dimensional localization using hyperbola method	149
Figure 3.50 System structure for proposed approach	150
Figure 4.1 Physical hardware system of liner temperature monitoring	154
Figure 4.2 Test Jig for eddy emission analysis	159
Figure 4.3 zeroed load cell output Vs pressure	161
Figure 4.4 Marked 3 features for testing accuracy of measurement	163
Figure 4.5 Liner details of the specimen	164
Figure 4.6 Liner details of the specimen	165
Figure 4.7 System concept	166
Figure 4.8 Block diagram for the whole system for 4 cylinders	167
Figure 4.9 Cylinder Liner	168
Figure 4.10 Cylinder liner sensor holes	168
Figure 4.11 Four encapsulated sensors fitted to the four liner holes	169
Figure 4.12 Pictorial view of the eddy sensor	169
Figure 4.13 Sensor sectional drawing with cable	170

Figure 4.14 Crank angle/Cylinder pressure from Performance analyzer @ 85% MCR	171
Figure 4.15 Pressure angle diagram from Liner guardian software	172
Figure 4.16 Aligning Angle against roughness	172
Figure 4.17 data capturing software configuration	174
Figure 4.18 Schematic of test rig	175
Figure 4.19 Pencil load break test data of Kistler and in-house PZT crystal sensor against (a) time (b) frequency	177
Figure 4.20 Preliminary test data of Aluminum pin on stainless steel disc (a) time (b) frequency	178
Figure 4.21 Preliminary test data of mild steel pin on stainless steel disc (a) time (b) frequency	178
Figure 4.22 Preliminary test data of mild steel pin on stainless steel disc with/without lubrication (a) time (b) frequency	179
Figure 4.23 Comparison of AE amplitudes of aluminum and mild steel pins	179
Figure 4.24 Preliminary statistical data analysis of aluminum and mild steel pin on stainless steel disc (a) SD-Aluminum (b) SD Mild steel (c) Comparison of SD (d) AE count rate-Aluminum (e) AE count rate-Mild steel	181
Figure 4.25 Sensor locations	182
Figure 4.26 Schematic of sensors location	183
Figure 4.27 Sample data of one engine cycle acquired using sensor-1	183
Figure 4.28 Data from in-house PZT sensors (a) Sensor output from Spark plug side, (b) Zoomed in view (c) Sensor output from opposite side of Spark plug (d) Zoomed in view	186
Figure 4.29 Data from Kistler sensors (a) Sensor output from opposite side of Spark plug (b) Zoomed in view	187
Figure 4.30 Methodology followed for the study	188
Figure 5.1 Hydrodynamic pressure distribution in ring/liner conjunction	192
Figure 5.2 Film thickness against crank angle	192
Figure 5.3 Load against crank angle	193
Figure 5.4 Coefficient of friction against crank angle (Viscous shear )	195
Figure 5.5 Multiple ring pack	196

Figure 5.6 Fluctuating temperature of the cylinder liner	198
Figure 5.7 Sinusoidal wave (Liner Temperature fluctuates frequently)	199
Figure 5.8 Fourier profile of temperature reading	199
Figure 5.9 Cylinder liner high temperature alarm	201
Figure 5.10 Cylinder liner temperature deviation alarm	201
Figure 5.11 Baseline test of test jig of eddy current analysis	202
Figure 5.12 Roughness profile at stepped number of strokes	204
Figure 5.13 Sensor output from engine cylinder unit 4	205
Figure 5.14 Gap between crown/skirt and cylinder liner	206-207
Figure 5.15 Different surface morphologies of rings and liner with same $R_a$ values (a) acceptable morphology with valleys but no peaks and (c) not acceptable morphologies	208
Figure 5.16 Variation of standard deviation of roughness	209
Figure 5.17 Comparison between reference condition and worn out rings	212
Figure 5.18 Schematic showing the difference in contact area between fresh and worn-out piston rings: a) Fresh piston ring b) Worn out piston ring c) 40X Magnified view of piston ring contact area between fresh and worn-out piston rings. $t_2 > t_1$	212
Figure 5.19 Comparison between reference condition and worn out piston	213
Figure 5.20 Comparison between reference and oil starved conditions	214
Figure 5.21 Samples of Signal, FFT and STFT	216
Figure 5.22 STFT of the data reference condition	217
Figure 5.23 STFT of the data for worn out rings	218
Figure 5.24 STFT of the for worn out piston	218
Figure 5.25 STFT of the data for oil starved condition	218
Figure 5.26 One engine cycle showing different segments	219
Figure 5.27 Three domains of signal	220
Figure 5.28 comparison of features between reference condition and worn out piston rings for segments 3 and 3*. a) Positive peak, b) Standard deviation, c) Skewness, d) Kurtosis.	223
Figure 5.29 comparison of features between reference condition and worn out piston for segments 3 and 3*	224

Figure 5.30 comparison of features between reference and oil starved condition for segments 1 and 1*	225
Figure 5.31 One engine cycle showing different segments	226
Figure 5.32 STFT of data showing different frequency bands and filters applied	227
Figure 5.33 Comparison of standard deviation in the frequency band of 0-50 kHz in the segments near TDC.	228
Figure 5.34 Comparison of standard deviation in frequency band of 50-175 kHz	229
Figure 5.35 Comparison of standard deviation in frequency band of 175-275 kHz	230
Figure A1-1 Cutout Sample Of a used (damaged) Cylinder Liner	236
Figure A1-2 Surface Metallography – Original Surface (As-Received and After Light Polishing & Etching)	237
Figure A1-3 Surface Metallography – 0.1mm Below Surface	238
Figure A1-4 Sectional Metallography – Below Surface	239
Figure A1-5 Sectional Metallography – 1mm Below Surface	240
Figure A1-6 Sectional Metallography – 10mm Below Surface	241
Figure A1-7 EDX Spectrum – Below Surface	242
Figure A1-8 EDX Spectrum – 1mm Below Surface	243
Figure A1-9 EDX Spectrum – 10mm Below Surface	244

## NOMENCLATURE

Symbol	Description	unit
A	wetted surface area	(m <sup>2</sup> )
ACVF	[R <sub>r</sub> ] autocovariance function	
ACF	[ρ <sub>r</sub> ] autocorrelation function	
A <sub>d</sub>	flaw detector data for a defect	
A <sub>f</sub>	flaw detector data for group of defects	
A <sub>r</sub>	real area of contact with tangential force present	(m <sup>2</sup> )
A <sub>r0</sub>	real area of contact in the absence of tangential force	(m <sup>2</sup> )
a	radial ring thickness	(mm)
a(t)	acoustic emission signal	
a <sub>1</sub> , b <sub>1</sub> , c <sub>1</sub>	curve fitting constants determined through a calibration process	
a*b*c*	zone	
a <sub>asp</sub>	friction coefficient governed by the surface properties	
B, b	axial ring height	(mm)
B <sub>a</sub>	adiabatic bulk modulus for fluid	(Pa)
C	arbitrary constant assumed to have a value close to 10	
CLA	centre line average	
C <sub>m</sub>	sliding speed (mean piston speed)	(m/s)
c	constant	
c <sub>s</sub>	speed of sound	(m/s)
c <sub>sp</sub>	specific heat	(J/kg. °C)
D	nominal ring diameter	(mm)
D'	total distance between the sensor and the ring surface	(m)
d'	distance of the sensor head from liner surface	(m)
dM	time step (length of filter)	
E, E'	Young's modulus	(Pa)
E, E <sub>1</sub> , E <sub>2</sub>	Young's modulus of two contacting surfaces	(N/mm <sup>2</sup> )
F	force	(N)
F <sub>B</sub>	frequency bins (Total order of filter)	
F <sub>e</sub>	excitation frequency of the circuit	(Hz)
F <sub>h</sub>	hydrodynamic shear force/unit circumferential length (radial)	(N/m)

$F_p$	ring pivot friction force/unit circumferential length (radial)	(N/m)
$F(f), G(f), W(f)$	Fourier transforms of $f(t), g(t)$ and $w(t)$	
$f$	piston acceleration	(m/s <sup>2</sup> )
$f_1, g_1$	twice differential function	
$f(t)$	input function	
$G_{ij,k}$	Green's tensor	
$g(t)$	output function	
$H$	ring....	
$H_{init.}$	magnetic field coming from the source	(T)
$H_{max.}$	magnetic field maximum above the flaw	(T)
$H_{mean.}$	mean value	(T)
$h$	oil film thickness	(m)
$h_d$	depth of the defect	(m)
$h(\Theta)$	hydrodynamic oil film thickness at angle $\Theta$	(m)
$I$	current	(amps)
$i$	order of filters, 1 <sup>st</sup> , 2 <sup>nd</sup> , 3 <sup>rd</sup> etc	
$j$	spatial distance	(m)
$[j - mdM]$	delay	
$K'$		
$K_d$	dissipation constant	(mW/ <sup>0</sup> C)
$K_u$	Kurtosis	
$K_w$	wave number	
$k$	exposed length of starved piston ring at top end of the ring face	(m)
$L$	sampling length	(m)
$L_s$	piston stroke as a function of crank angle	(m)
$L_w$	window length	
$l_r$	length of liner and ring thickness	(m)
$l$	connecting rod length	(m)
$l$	exposed length of starved piston ring at bottom end of the ring face	(m)
$M$	mass of piston ring/unit circumferential length	(kg/m)
$m$	time	(s)
$N$	speed	(RPM)

n	frequency	(Hz)
n <sub>g</sub>	amount of substance of gas	(moles)
P	pressure	(Pa)
P <sub>C</sub>	cylinder wall pressure	(N/mm <sup>2</sup> )
P <sub>D</sub>	diametral tension	(N)
P <sub>d</sub>	acoustic pressure (p-p <sub>0</sub> )	(Pa)
P <sub>g</sub>	power generated	(watt)
P <sub>n</sub>	normal contact stress (pressure)	(Pa)
P <sub>0</sub>	material plastic flow stress in absence of tangential (frictional) force	(Pa)
P <sub>s</sub>	spring(sealing) force/unit circumferential length (radial)	(N/m)
P <sub>T</sub>	tangential tension	(N)
P <sub>y</sub>	plastic flow stress of the material	(Pa)
P <sub>z</sub>	hydrodynamic normal force/unit circumferential length (radial)	(N/m)
p <sub>1</sub>	pressure above piston ring	(Pa)
p <sub>2</sub>	pressure below piston ring	(Pa)
$\frac{\Delta p}{\Delta t}$	scuffing index	(Pa.s)
Q	stored energy	(J)
R	crank radius	(m)
R <sub>a</sub>	average roughness	(m)
R <sub>a</sub> ( $\Theta$ )	ring roughness at angle $\Theta$	(m)
R <sub>d</sub>	average distance over a stripe	(m)
R <sub>g</sub>	ideal gas constant	(J·K <sup>-1</sup> ·mol <sup>-1</sup> )
R <sub>k</sub>	main roughness	( $\mu$ m)
R <sub>p</sub>	piston/groove reaction force/unit length (axial)	(N/m)
R <sub>pk</sub>	peak roughness	( $\mu$ m)
R <sub>q</sub>	root mean square roughness	(m)
R <sub>t</sub>	thermistor resistance	( $\Omega$ )
R <sub>s</sub>	average roughness integrated over a stripe and the piston stroke	(m)
R <sub>vk</sub>	valley roughness	( $\mu$ m)
r	position of the source	
r <sub>d</sub>	distance monitored per stroke over a stripe and piston stroke	(m)
r <sub>h</sub>	radius of the hydraulic ram	(m)



$r_s$	average roughness monitored/stroke over a stripe and piston stroke(m)	
$S_d$	condensation, the change density for a given ambient fluid density	
$S_e$	ratio of temperature and power	( $^{\circ}\text{C}/\text{mW}$ )
$S_f$	fitted gap clearance of ring	(mm)
$S_k$	Skewness	
$S_{op}$	free opening of ring	(mm)
$S(\tau)$	structure function	
$S_T$	transducer area	( $\text{m}^2$ )
STFT	short time fourier transform	
$s$	distance between the two sensors	(m)
$T$	temperature of the gas	(K)
$T, T_1, T_2$	temperature	( $^{\circ}\text{C}$ )
$T_k$	temperature	(K)
$T_0$	temperature of the surroundings	( $^{\circ}\text{C}$ )
$T_r$	transducer response	
$T(R)$	temperature of the thermistor as a function of its resistance R	( $^{\circ}\text{C}$ )
$t_0$	source time	(s)
$t_1, t_2$	onset time	(s)
$t_1, t_2, t_3$	arrival times of the compressional wave	(s)
$U$	piston velocity	(m/s)
$\frac{u}{h}$	shear rate	( $\text{s}^{-1}$ )
$V$	volume of the gas	( $\text{m}^3$ )
$V_1$	voltage	(volt)
$V(t)$	AE sensor voltage	(v)
$V_t$	voltage drop across the thermistor	(volt)
$v$	sound velocity of the material	(m/s)
$\nu_1, \nu_2$	Poisson's ratio of contacting surfaces	
$W$	normal force (load)	(N)
$W_a(t)$	transfer function of amplifier	
$W_f(t)$	transfer functions of filter	
$w(f)$	function of frequency response	
$w(t)$	transfer function	

$X_{c1}, X_{c2}$	boundaries of ring-liner surfaces that in asperity contact for $h/\sigma < 4$ (m)	
$X_{C.P.}$	axial location of hydrodynamic normal force from mid plane of ring	(m)
$x, z$	axial and radial co-ordinates	
$\bar{x}, \bar{z}$	location of piston ring centre of mass	(m)
$x_1, x_2$	distance from the source to the sensors	(m)
$x_d$	distance between probe position and defect position on the surface	(m)
$x_j$	signal	
$x_0, y_0$	source location	(m)
$Z$	height of the profile along 'x'	(m)
$Z_d$	gap between probe and surface of an object	(m)
$Z_0, S_0$	constants, characteristics for oil, independent of temperature/ pressure	
$z_s$	offset between asperity height mean and surface height mean	(m)
$\alpha$	pressure-viscosity coefficient	(m <sup>2</sup> /N)
$\alpha^*$	Roelands pressure-viscosity coefficient, function of both 'p' and 'θ'	(m <sup>2</sup> /N)
$\beta$	related constant of $S_0$	
$\beta^*$	decay constant of exponential ACF	(m)
$\beta_a$	asperity peak radius of curvature	(μm)
$\gamma^*$	window function	
$\delta$	Dirac's delta function	
$\sigma$	composite surface roughness	(m)
$\sigma_1 [R_{q1}]$	root mean square (rms) roughness value of surface 1	(m)
$\sigma_2 [R_{q2}]$	root mean square (rms) roughness value of surface 2	(m)
$\sigma_c$	conductivity of the target material	
$\Delta\sigma_{jk}$	internal stress	(Pa)
$\mu$	coefficient of friction	(-)
$\mu_m$	magnetic permeability of the target material	
$\lambda$	specific oil film thickness	
$\omega$	angular velocity of crank	(rad/s)
$\theta$	crank angle from TDC	(°)
$\theta_0$	reference or ambient temperature	(K)
$\eta$	dynamic viscosity	(Pa.s)
$\eta_a$	asperity density per unit area	(no. of asp/m <sup>2</sup> )

$\eta_0$	atmospheric viscosity	(Pa.s)
$\eta_r$	viscosity at pressure 'p' and temperature 'θ'	(Pa.s)
$\omega$	angular frequency of wave	(rad/s)
$\Delta$	error	(m)
$\Delta_d$	effective depth of eddy current sensor	(m)
$\rho$	density	(kg/m <sup>3</sup> )
$\epsilon$	coefficient of thermal expansion	(m/m.°C)
$\tau$	shear stress	(Pa)
$\tau_x$	shear stress acting in the 'x' direction	(Pa)
$\Phi(z)$	probability distribution of asperity heights	
*	source location	(m)

## Chapter 1. Introduction

---

For large bore diesel engine, various components are subjected to wear in service. Among the main components, the wear can be categorized as either bearing or piston ring-liner wear.

Piston ring-liner wear can further be classified as controllable progressive or uncontrollable sudden wear.

Controllable progressive wear of piston rings and cylinder liners can be detected using condition monitoring tools so that their life span can be optimised against other cost related variables.

Uncontrollable sudden wear, on the other hand, leads to catastrophic failures in the absence of proper and timely detection.

Adhesive wear or scuffing of the cylinder liner uncontrollable wear, which leads to a catastrophic failure and the major challenge is to detect its symptoms and undertake appropriate action at the right time to avoid considerable downtime and repair cost.

Figure 1.1 shows a flowchart of various types of piston ring and cylinder liner wear which results from a large number of material and service variables, their relationship and interaction.

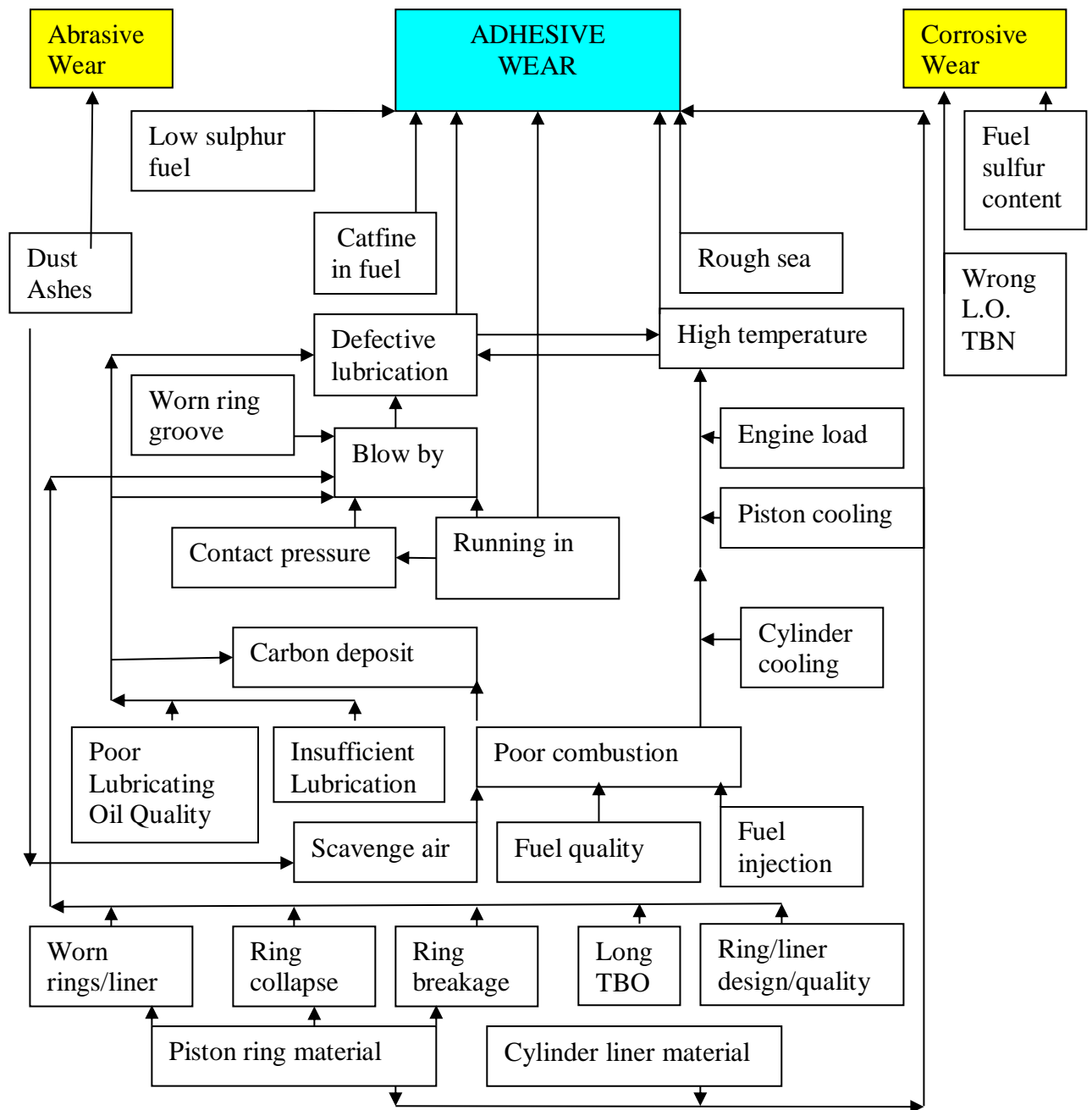


Figure 1.1 Contributing factors to piston ring and cylinder liner wear

There are predominantly three types of wear,

- Abrasive wear,
- Corrosive wear, and
- Adhesive wear (scuffing)

All three types of wear occur simultaneously, but their predominance or share of the total wear may differ.

Abrasive wear of cylinder liner and piston rings may be caused by hard particles suspended in the cylinder lubricating oil such as carbon deposits from fuel combustion or metallic particles, either from already started wear or from catalytic fines which are present in the fuel oil. These particles wear the surface of the

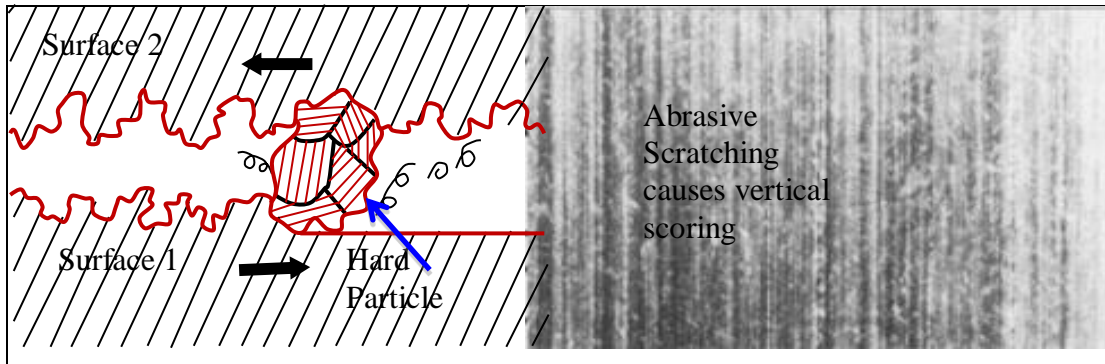


Figure 1.2 Abrasive Wear

cylinder liner and the piston rings by continuous ploughing and scratching as shown in Figure 1.2.

Under normal operating conditions there will be low levels of abrasive wear and acceptable time between overhauls are achieved. The running surface of piston rings and cylinder liner shows a smooth polished appearance and the rings remain free to move in their grooves and there is still tension left in all rings.

However, with high levels of abrasive wear the surface shows vertical scratches, the size of which depends on the grade of the particles causing the wear. The particles can also affect the sides of the piston rings as they jam into the ring grooves, causing "pitting" of the surface.

Corrosive wear of piston rings and cylinder liners, otherwise known as low temperature corrosion, is caused by the chemical reaction of the piston rings and cylinder liner metal surface with sulphuric acid formed from the sulphur and water vapour in the combustion gases. Sulphuric acid is formed provided the ambient

temperature is lower than the dew point of the water vapour. At high pressure of compression and combustion in the cylinder, the dew point for acid formation can

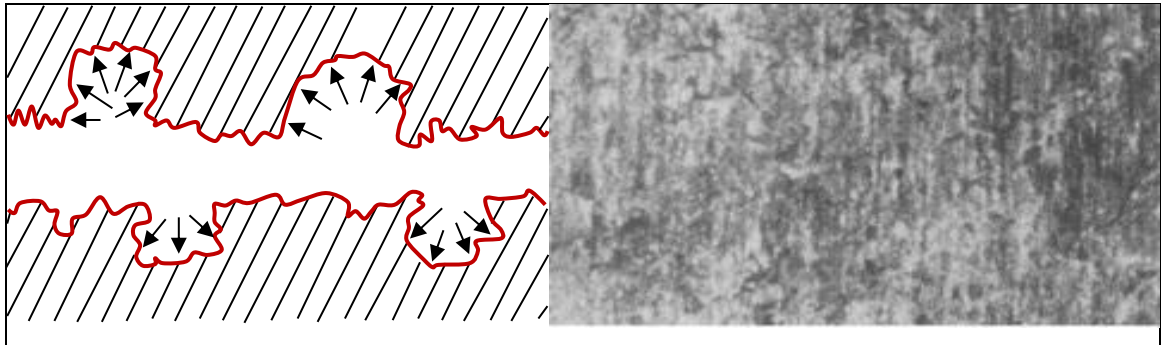


Figure 1.3 Corrosive wear

be as high as 180 deg C. Corrosive wear deposits fill up the pores of the cylinder liner surface as shown by the arrows in Figure 1.3. With alkaline cylinder lubricating oils, it is possible to keep the corrosive wear within tolerable limits, despite operating on heavy fuel oil with high sulphur content.

It is difficult to observe corrosive wear on piston ring running surfaces as the continuous abrasive wear polishes off the corrosion deposit. However, on cylinder liner walls and piston ring sides corrosion can be visible.

Adhesive wear (scuffing) starts when the surfaces are insufficiently lubricated and direct metal contact between the piston ring and cylinder liner takes place. This contact increases friction and consequently increases the surface temperature locally which in turn reduces the fatigue resistance of the material. The loss of strength causes cracks below the heated zone and surface breaks into the form of flakes. Piston ring scuffing is a randomly occurring phenomenon, which consists of local micro welding, or material adhesion, between a piston ring and a cylinder liner.

This phenomenon is a type of macrodelamination during which a large amount of material is removed from the surface. The friction is so intense that the surface is

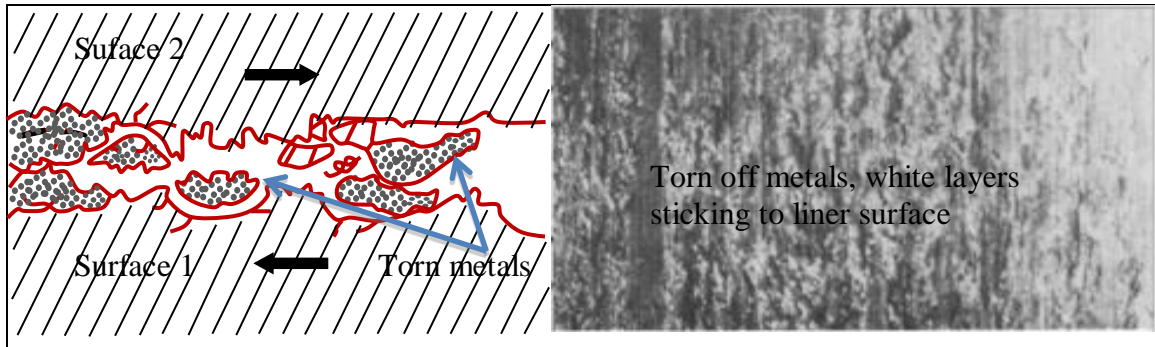


Figure 1.4 Scuffing on piston ring surface

melted and forms so called "white layers" which are very hard and brittle. When they crack, small hard particles flake off and plough the surface, giving the typical scuffing appearance as shown in the Figure 1.4.

On the piston rings and cylinder liner surfaces evidence of scuffing may be found in the shape of wear scars indicating plastic deformation, abrasive ploughing and the adhesive transfer of work hardened cast iron to the chromium plated piston ring, and a "white layer" that indicates that the temperature has locally exceeded  $750^{\circ}\text{C}$ [1].

### 1.1 Aims and objectives:

Scuffing, also referred to as microseizure, was defined as "gross damage characterized by the formation of local welds between sliding surfaces. This thesis looks at the various reasons of scuffing. It also looks at the design and operational solutions advocated to prevent scuffing at the first place. Through modeling, lab experiments and applying on real large bore engine, it aims to compare and find the most suitable precursor and detection method of scuffing.

### 1.2 Methodology:

The methodology followed in comparing and finding suitable precursor and detection is based on forming mathematical models of the different detection method followed by experiments. The experiment results were checked and validated against the mathematical models.



### **1.3 Structure of the thesis:**

In the subsequent chapters of literature review, the causes and solutions of scuffing along with four detection methods, namely tribology analysis, temperature, eddy current and acoustic emission analysis are described. Next under the chapters of theory and modeling, experimental tests and results and discussions, all four above stated detection methods are separately described prior to drawing the conclusion.

## Chapter 2. Literature Review

---

### 2.1 Causes of scuffing:

There are many causes of microseizure or scuffing of piston rings and cylinder liners. A few major reasons of scuffing are described below:

#### 2.1.1 *Starved Lubrication:*

The adhesive wear or scuffing phenomenon is normally preceded by conditions of locally starved lubrication, and the occurrence of flash temperatures, or hot spots, where piston ring and cylinder metal to metal contact occurs. The local temperature increase can, in turn, cause the formation of local thermal expansion of the cylinder wall material towards the bore (thermal bump), which instantly leads to an increase in the ring and liner contact pressure. [2]

##### 2.1.1.1 *Oil film thickness and surface composite roughness:*

The lubrication conditions may be poor either owing to high surface roughness that contributes to lower specific oil film thickness,  $\lambda$  which is the ratio of oil film thickness over composite roughness of the surfaces or to cylinder bore polishing with lowered  $R_{vk}$ , known as valley depth and lubricant retention region, that has erased the honing marks and consequently, the oil reservoirs from the surface. The cylinder liner bore polishing can be a consequence of two- and three-body abrasive wear, which are between the asperities of two rubbing surfaces and hard particle trapped between the rubbing surfaces respectively and plastic material flow at the ring and liner surfaces [2].

If the wear rate is sufficient to remove the thermal bump as soon as it develops then the condition remains stationary, otherwise, the contact severity will continue to increase [3]. At high temperatures this is aggravated through lubricant degradation in the surrounding areas, in terms of reduced viscosity, oil vaporisation, carbon deposition and additive stripping [4]. Ultimately, if lubrication is not reestablished the condition escalates until the point where local flash temperatures exceeding 400 °C can occur, resulting in the local welding of asperities [5]. The problem is then spread by the movement of the piston through

tearing or dragging of the surfaces. Poor running-in properties of piston rings, owing to surface layers that are too wear resistant, may increase the risk of scuffing.

#### ***2.1.2 Initiation of scuffing on piston rings and cylinder liner:***

It is presumed that scuffing is initiated on ring surfaces rather than liners. This is because ring surface conditions are more severe since friction is experienced continuously as opposed to an area on a liner, which experiences friction only intermittently. Scuffing occurs initially at the top ring as it tends to carry the highest gas loading and experience the highest temperatures.

#### ***2.1.3 Coefficient of friction:***

It was reported from earlier resistance tests that scuffing occurred at a coefficient of friction of  $\mu > 0.11$ , while at a coefficient of friction of  $\mu < 0.1$  scuffing did not occur [6].

#### ***2.1.4 Volatility of cylinder lubricating oil:***

Protection against scuffing is achieved by engine lubricating oil additives, which promote the formation of an effective boundary lubrication film and thus suppress the scuffing phenomenon. The effect of this reaction layers at the ring/liner contact was found with different oil formulations, where large differences in time-to-scuff under otherwise identical sliding conditions have been shown [2].

However, for each reaction layer system formed from surface-reactive additives there is a maximum temperature, above which the reaction layer breaks down and the probability of scuffing increases significantly. The volatility of the oil at the cylinder wall determines the evaporation rate of the oil or part of its' constituents at high temperature, and thus relates to the availability of the oil at the piston ring and cylinder liner metallic contact [1].

### ***2.1.5 Carbon deposit:***

Excessive deposits of carbon on the top land of the piston, i.e. above the top piston ring, may displace or scrape away the oil film from the liner. Carbon deposits in ring grooves can initiate scuffing through restriction of ring movement leading to greater contact pressure [6].

### ***2.1.6 Water in scavenge air:***

Although the occurrence of scuffing is generally associated with extreme conditions of temperature or pressure, there are a number of other possible causes [3]. Others have identified specific causes from operational experience, for instance, the presence of water in the scavenge air [7]

### ***2.1.7 Slow burning fuel:***

Fuel injection patterns and combustion characteristics are a further possible source as a slow burning fuel may burn away the oil film [7].

### ***2.1.8 Catfines in fuel:***

Catfines are used in the refinery process and some of those catfines find their way into the residual fuel. If inadequately treated by purifiers and filters, these catfines may find their way to the engine and damage the engine through abrasion and scuffing.

### ***2.1.9 High temperature of cylinder liner wall:***

High engine load, long flame length, direct impingement of fuel injection on the liner wall, high piston coolant and cylinder jacket coolant temperatures and blow by of the combustion gases owing to worn piston rings and cylinder liner etc. causes cylinder wall temperature to rise. These results into total evaporation of lubricating oil from the liner surface or at least reduces the viscosity of the lubricating oil, which in turn affects the hydrodynamic lubrication between the rings and the liner.

### ***2.1.10 Modern engine design and operation:***

Modern engines with high liner temperatures, keeping operation above the dew point of exhaust gas water vapour, reduce the corrosive wear, but increase the chance of high adhesive wear.

One of several locations, where the risk of scuffing is large is between piston top dead centre (TDC) and its mid-stroke where the product  $F \times v$  (force and velocity) reaches a maximum.

Previous experimental investigations have shown that an increase in operating temperature, an increase in load and an increase in the oscillating frequency of the test samples shorten the time before scuffing occurs, while a good availability of lubricating oil increases the time before scuffing occurs [2].

Incidents of scuffing have increased over the last few decades due to the continued development of large-bore, two-stroke engines. During this time, the indicated mean effective pressure for engines from one manufacturer has increased from 13 to 19.5 bar with peak firing pressures similarly rising from 90 to 150 bar [7].

Engine operating parameters for 1980 and 1990 were compared and found that in this period the likelihood of scuffing had increased by a factor of 2.2 when taking into account maximum cylinder pressure, mean piston speed and oil film temperature [8].

The research provided a number of examples, collated from users of large two stroke diesel engines, where scuffing has led to cylinder overhaul suggested that newly designed engines operate on a knife edge with little or no apparent reserve for out-of-the-normal operation [3].

#### ***2.1.10.1 Piston ring pack designs:***

Effective ring pack design is crucial for sealing the combustion chamber from the underpiston scavenge space of slow speed engines. Therefore piston sealing has been researched extensively and recent improvements have been introduced in design, material and coating technology.

Modern engines usually have 4 to 5 rings. The top or the top two rings could have a barrel shape or special taper face. The top rings outward face are often plasma coated or laser treated, which provides a harder wearing surface. The lower grooves have the normal profiled cast iron rings.

All these ring pack designs significantly affect the cylinder liner wear, especially adhesive wear.

Both power loss and oil consumption have recently been reduced markedly through improved understanding of piston ring tribology. An excellent review of tribological aspects of piston assembly design has been presented by Ruddy, and Hillyard. [9].

#### ***2.1.10.2 Piston ring operation conditions:***

Piston rings, as well as piston and the cylinder liners are subjected to cyclical extreme pressure and temperature, which deforms these components on instantaneous basis within their elastic limits. These components are designed to operate satisfactorily under such dynamically deformed expected conditions. However, with longer operating periods the operating conditions for the piston rings will change and be affected by engine combustion, cooling and lubrication. All these are also related to the continuous wear of piston rings, ring grooves and cylinder liner owing to friction, impact and chemical corrosion, which can result in a significant change in the pressure distribution within the ring pack and consequently completely change thermal and mechanical loads on the rings. The effect of cyclical pressure and temperature on piston rings, piston and cylinder liner is shown in figure 2.1 below.

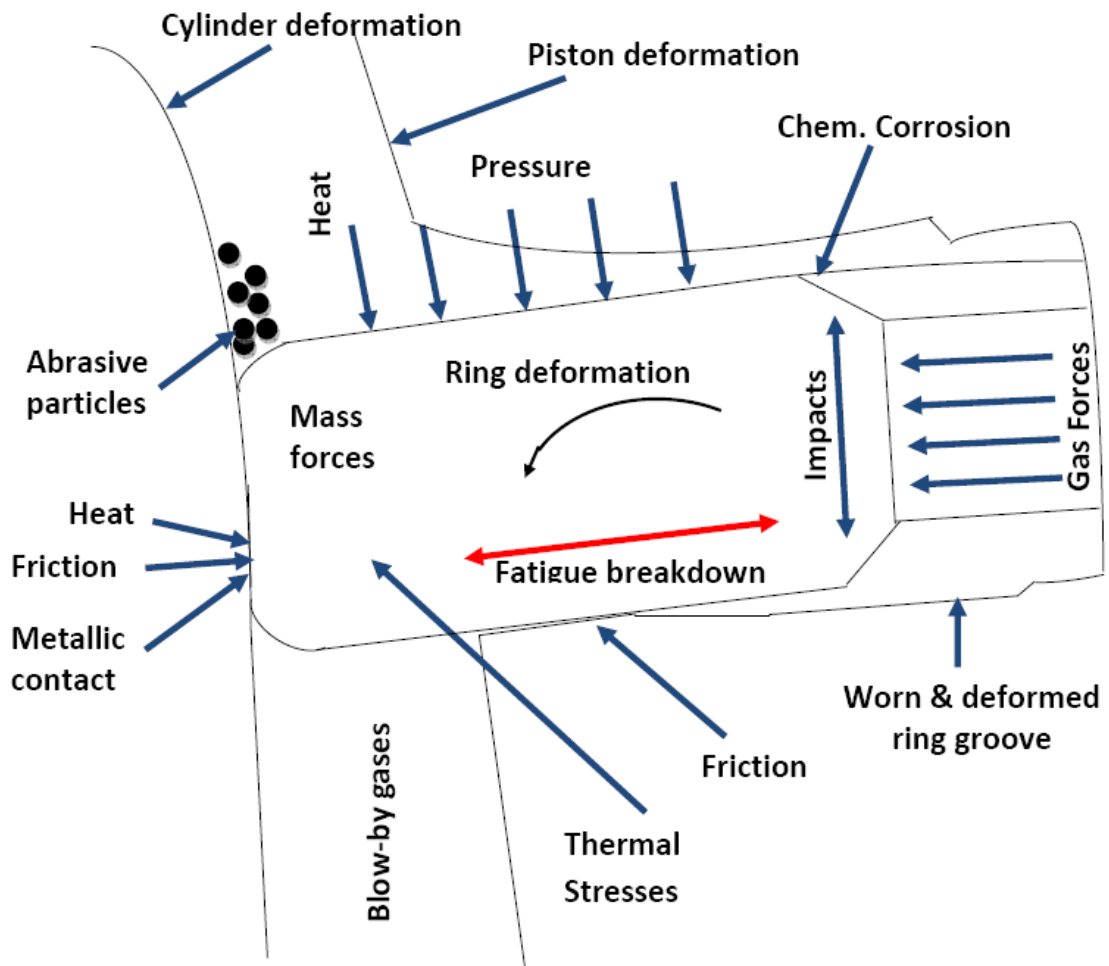


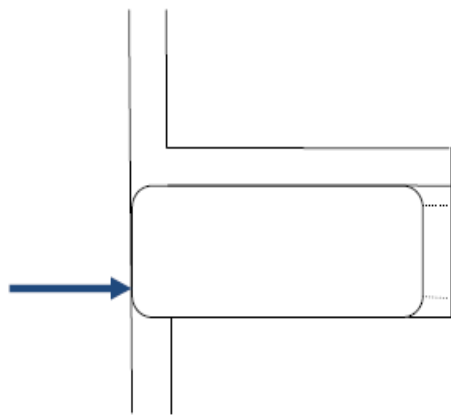
Figure 2.1 Piston ring operations condition [11]

#### **2.1.10.3 Piston ring running-in:**

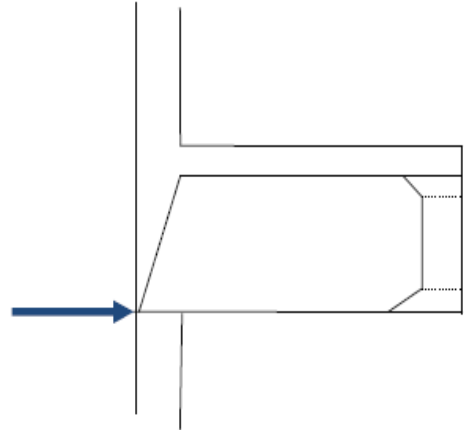
Upon installation, piston rings have to "run in" properly. Running-in involves gradual increment of the contacting surfaces (by blunting the sharp edges of the asperities and reducing their heights) of both piston rings and cylinder liner (if it is new) through a stepped increase of engine load along with ample lubrication. Piston ring contact position is load dependent as shown in figure 2.2 (a). Hence, each level of engine load requires its "running-in" procedure. Improper or inadequate running-in causes sharp asperity contacts, which ultimately results in micro welding seizure and scuffing.

When plain cast iron rings are used, a certain amount of wear is necessary to match the rings and liner to each other. In order to allow this "running-in" wear to take place with as little risk as possible for scuffing to occur, the surfaces on new rings are machined with a specified roughness.

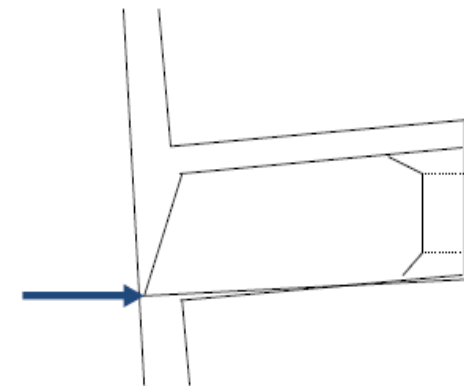
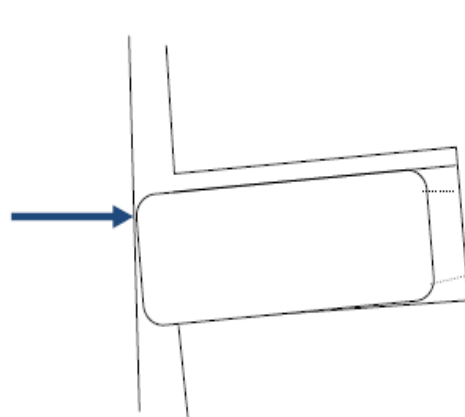
On rings with wear resistant coatings or treatments the formation of the natural ring shape through controlled wear would take too long a time and involve a great risk of severe damages to rings and liner. These types of rings are thus provided with a profiled running surface like tapered shape of figure 2.2 (b) allowing the same position of contact independent of load. Barrel shaped rings with same position of contact are also independent of engine load as shown in figure 2.2 (c).



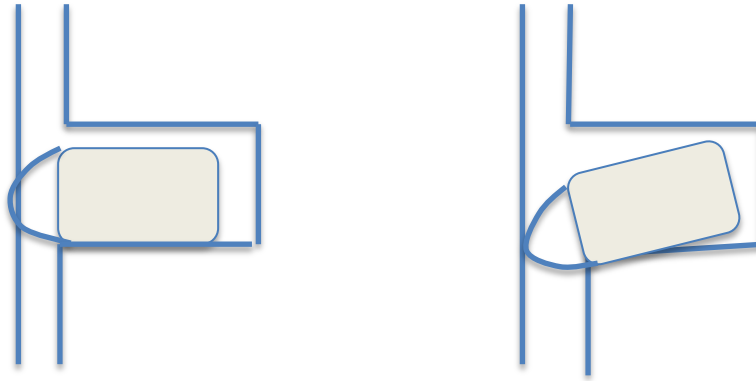
(a)



(b)







(c)

Figure 2.2 Ring shape (a) Load dependent position of contact with rectangular ring section (b) Taper shaped ring with same position of contact independent of engine load (c) Barrel shaped ring with same position of contact independent of engine load

#### **2.1.10.4 Piston rings manufacturing model:**

Over a number of years, engine makers have been striving to increase the mean effective pressure and mean piston speed of their engines. An enormous increase in peak pressure has been developed in order to decrease the specific fuel consumption. Hence, the necessity of the piston rings to seal the combustion chamber between the piston and the cylinder liner has become more demanding. Sealing can be optimal only if the rings make light-tight contact with the liner and the flank of its groove. Two basic effects must be distinguished: the primary sealing effect achieved by the inherent tension of the ring, which makes it lie up against the cylinder wall around the whole of its circumference, the secondary sealing effect caused by the gas pressure itself, which presses the ring additionally against the wall and the flank of the groove.

In its ideal condition, the piston ring of a slow speed two stroke diesel engine with unidirectional load rests on the piston ring groove against the force differential arising from the pressure difference of  $P_1$  and  $P_2$  over their exposed areas as

shown in figure 2.3.  $P_1$  represents the pressure of combustion or compression and  $P_2$  is the residual pressure of  $P_1$ , which leaked pass the piston ring.

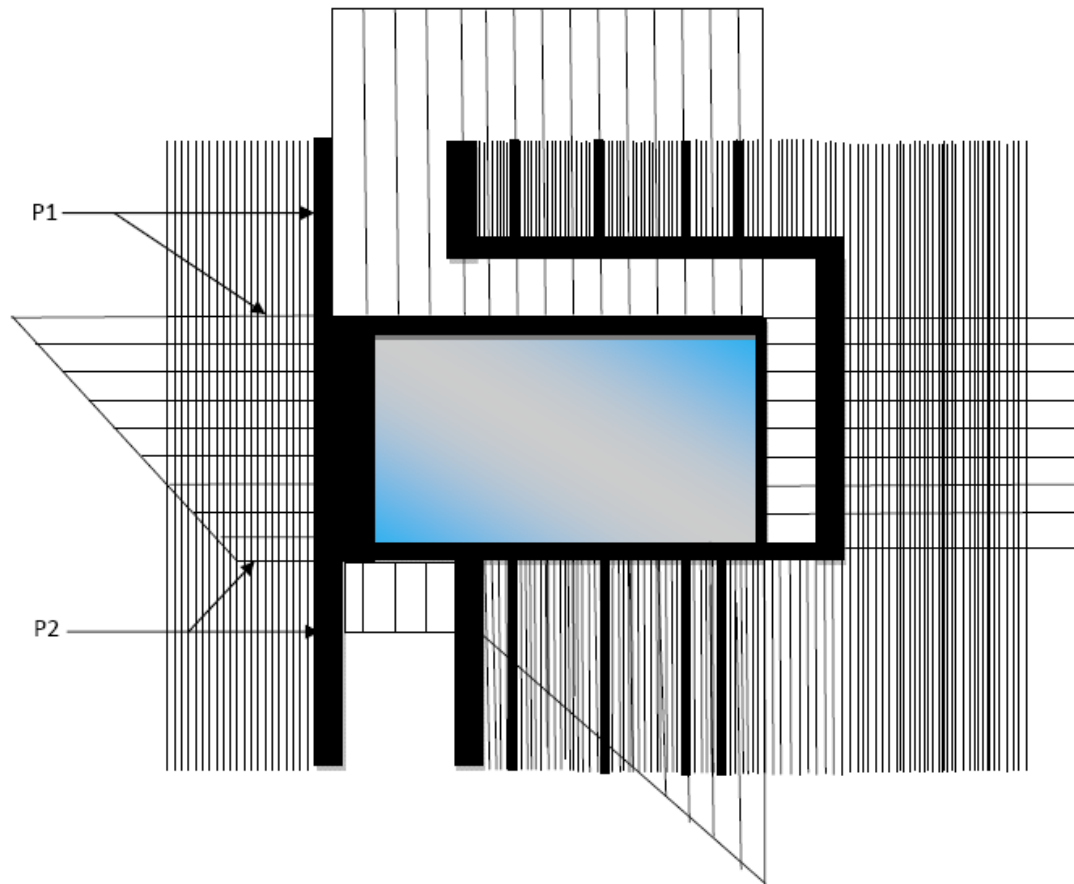


Figure 2.3 Ideal pressure distribution around a piston ring cross section

In the fitted position, the piston ring may be considered as a spring, whose tension keeps it in contact with the adjacent cylinder liner wall. The tension in the ring may be measured by applying a force tangentially, diametrically or circumferentially to the open ring in order to close it to the nominal working diameter.

The value of this tension may also be calculated theoretically from equation 2.1, which is derived from the complex mathematics of piston ring mechanics. The tangential tension " $P_T$ " is the most commonly calculated parameter in modern piston ring design and  $P_C$  is related to  $P_T$  .[10]

$$P_T = \frac{EBfD}{14.14 \left( \frac{D}{a} - 1 \right)^3} = \frac{P_D}{2.63} \quad (2.1)$$

$$P_c = \frac{200 * P_T}{B * D} \text{ and } f = \frac{S_{op} - S_f}{D} \quad (2.2)$$

It can be seen that the tension in the ring depends principally upon the ring geometry, but also upon its modulus of elasticity and gaps in the open and closed position. Of very great influence is the radial thickness. If 'a' in Equation 2.1 is high, the  $P_T$  value will also be high and vice versa. Low ring tension causes blow by of gases and high tension creates excessive load on the liner wall, which is one of the contributing factor to cylinder liner scuffing.

Figures 2.4 and 2.5 show the importance of the relationship between the diameter (D) and the radial thickness (a) of the piston ring and the impact of their ratio onto the cylinder wall pressure.

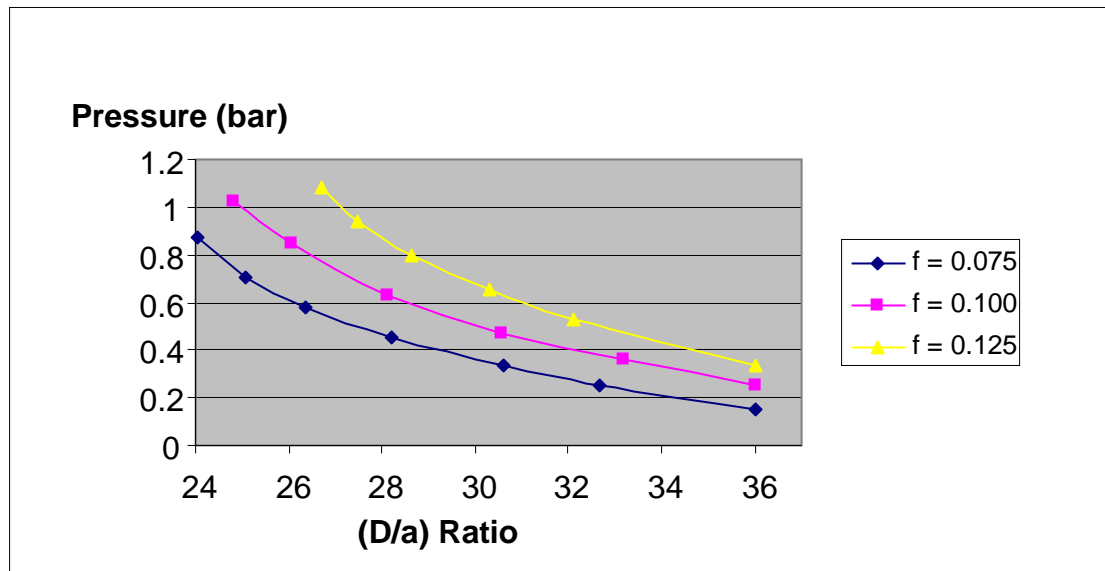


Figure 2.4 Variation of wall pressure with D/a for different values of f  
for  $E_r = 100,000 \text{ N/mm}^2$  (Data from reference) [10]

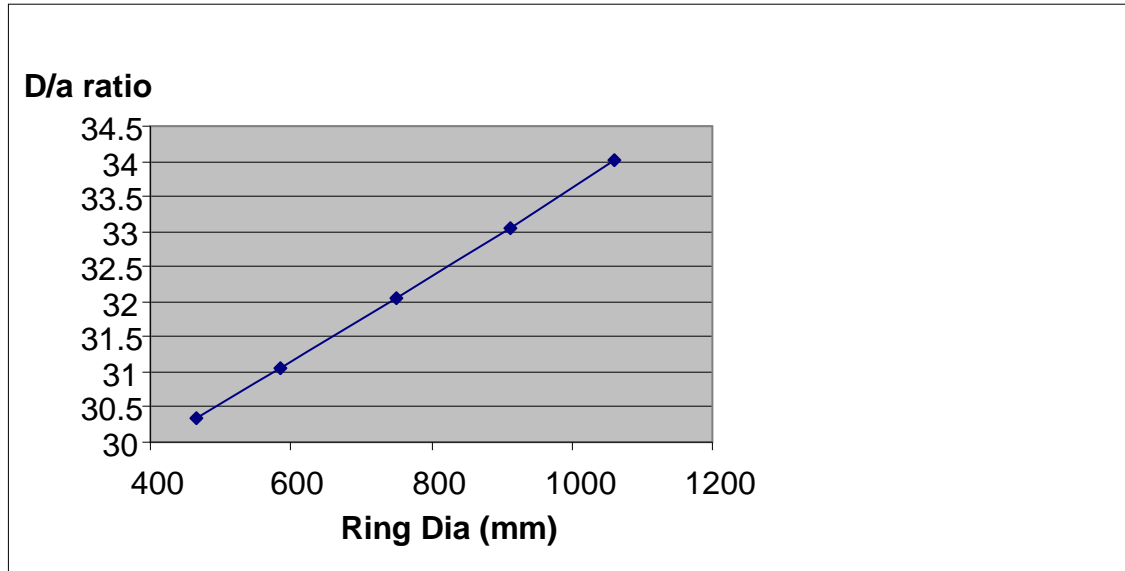


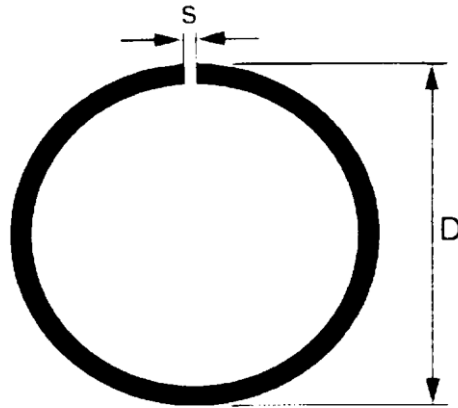
Figure 2.5 D/a ratio and the ring diameter (Data from reference) [10]

D/a ratio is commonly derived from its relationship with the ring diameter as shown in Figure 2.5. The wall thickness (a) and the ratio (f), defined in equation 2.2, must be calculated so that the ring is not overstressed during installation and operation. The position of maximum stress when the ring is closed to the cylinder diameter is opposite the gap and its value ( $K_{B1}$ ) can be calculated using equation 2.3.[10]

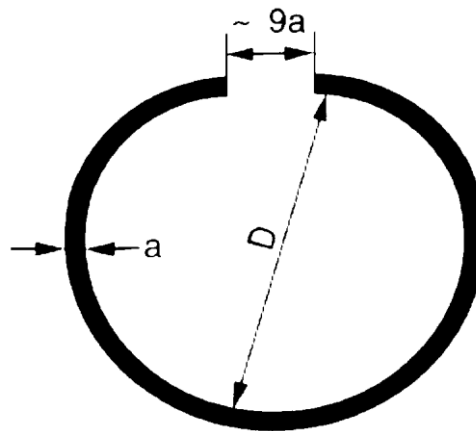
$$K_{B1} = \frac{0.424E * f}{\left(\frac{D}{a} - 1\right)} \quad (2.3)$$

To pass the piston for installation, the ring ends have to be separated by approximately  $9xa$  as shown in the figure 2.6. The maximum stress during the installation ( $K_{B2}$ ) may be calculated from the following equation 2.4.

$$K_{B2} = 0.64 \frac{4E - K_{B1}}{\left(\frac{D}{a} - 1\right)^2} \quad (2.4)$$



$K_{B1}$  = Maximum stress in working position



$K_{B2}$  = Maximum stress and gap during fitting

Figure 2.6 Piston ring stress during working and fitting

In diesel engines, the piston ring geometry is developed from experience and engine characteristics. The possibility of geometric variation is rather wide but limited as described above, only by the relationship  $D/a$ . Table 2.1 shows some important characteristics of piston ring geometries. From practice it also appears that the principal geometrical dimensions vary a lot from one engine type to another.

<b>Advantages</b>	<b>Disadvantages</b>
<b>LARGE AXIAL RING HEIGHT</b>	
Good heat transfer as large contact area with cylinder	Tendency to scuffing due to long contact surface
High stiffness	Large inertial mass
<b>SMALL AXIAL RING HEIGHT</b>	
Small frictional losses as small contact area	Less breakage resistance and increased ring wear
Small inertia as small mass	
Less scuffing problems	
Good conformability to lower flank of piston groove	
Tendency to twist	
<b>LARGE RADIAL WALL THICKNESS</b>	
High unit wall pressures possible	Little conformability in deformed cylinders
High radial stiffness	High fitting and working stresses as mass is large
<b>LOW RADIAL WALL THICKNESS</b>	
Good conformability in deformed cylinder	Tendency to radial ring fluttering, material fatigue and fracture
Light mass, low inertia	Sensitive to thermal deformation, blow-by and scuffing

Table 2.1. Piston rings geometry characteristics [11]

Even for the same engine type and model, piston rings may come with different height and width to suit its operational demand as shown in Table 2.1. Currently available range of axial ring heights and radial thicknesses in relation to the cylinder diameter of the engine were collected as shown in Figures 2.7 and 2.8.

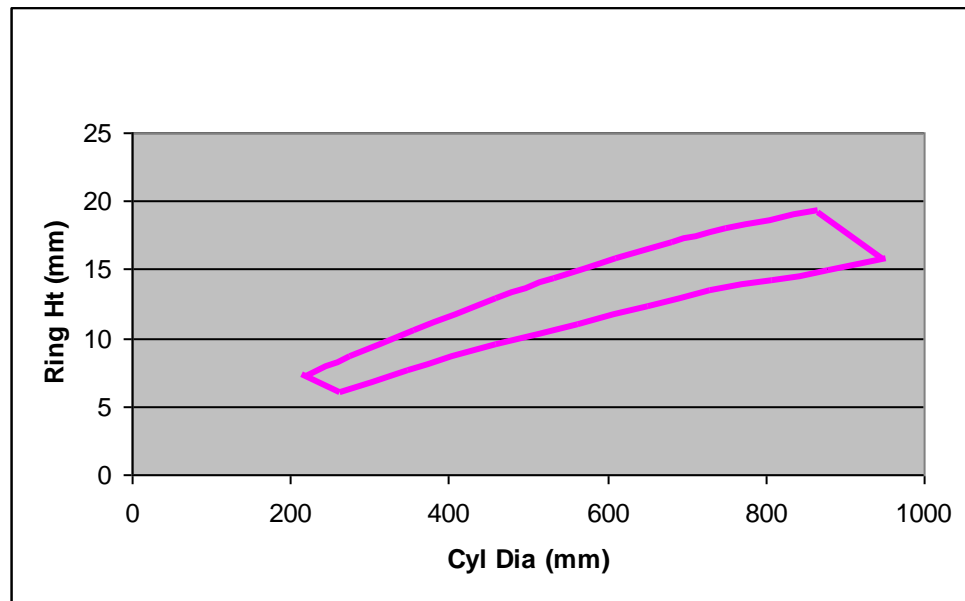


Figure 2.7 Relationship between Cylinder diameter and Ring height  
(Data from reference) [10]

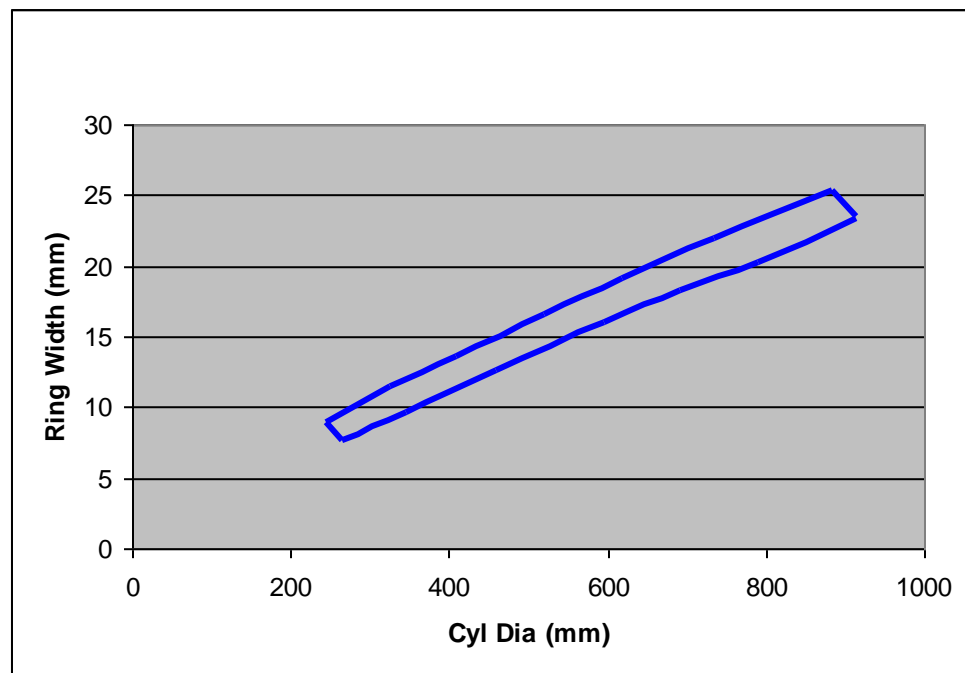


Figure 2.8 Ring Height and Width against Cylinder Diameter of 2-stroke engines(Data from reference) [10]

For the constant modulus of elasticity of  $E=100\text{KN/mm}^2$ ,  $D/a$  and pressure graphs, Figure 2.9 are drawn with Equation 2.3 and 2.4 for different values of 'f'. With higher  $D/a$  ratio, both  $K_{B1}$  and  $K_{B2}$  stresses are reduced. The reduction rate of  $K_{B1}$  is more or less linear and that of  $K_{B2}$  is exponential. For a very high  $D/a$  ratio, both  $K_{B1}$  and  $K_{B2}$  graphs approaches to the same level of stress as shown in figure 2.9.

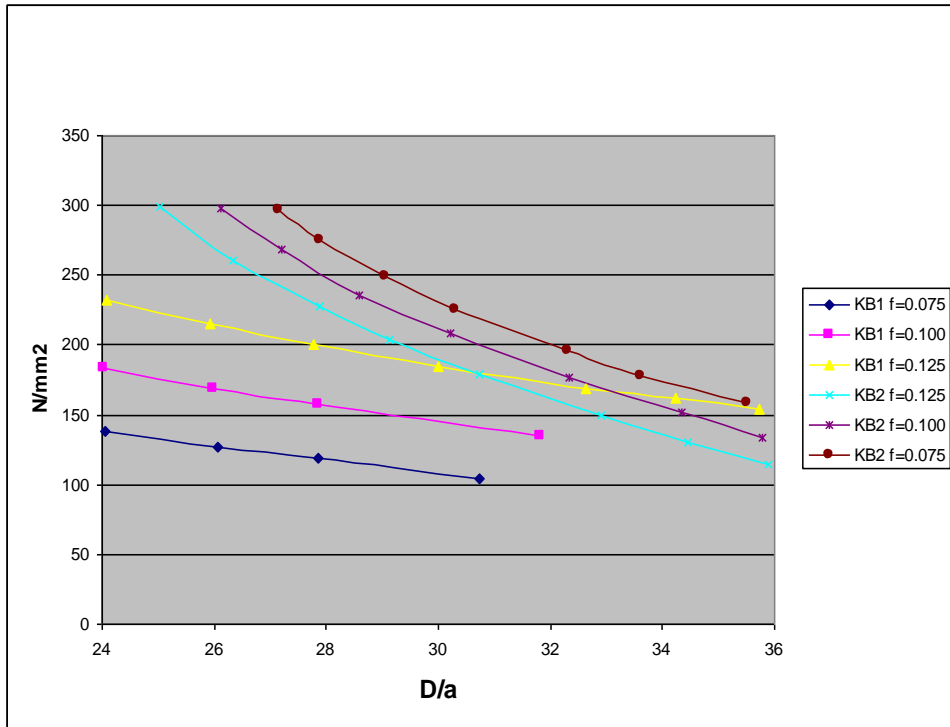


Figure 2.9 Variation of stresses  $K_{B1}$  and  $K_{B2}$  with  $D/a$  for different values of 'f'.

(Data from reference) [10]

From Equation 2.1, it can be seen that the value of  $P_T$ , the tangential force required to close the ring to its working diameter, depends upon the modulus of elasticity "E" of the ring material. Piston rings for slow speed engines are usually made of cast iron, an inhomogeneous material whose modulus of elasticity varies from point to point in the material. In order to obtain the desired pressure distribution around the ring, it is necessary to obtain as constant a value of "E" as possible for all points around the ring. This condition may only be approached by controlled ring metallurgy and is dependent upon the casting method of the ring and the details of foundry practice.



A regular and known modulus of elasticity is also required during the making of the ring so that the ring may indeed have the mechanical properties which the designer requires, and also so that the ring will not be overstressed or deformed during assembly. However because of the inhomogeneity of cast iron, the exact value of "E" ( $d_o/d_\delta$  in Figure 2.10) at all points of the ring cannot be known.

Two alternatives may therefore be used, either the original modulus " $E_0$ ", or the integrated value E, the latter is commonly used in piston ring practice and is usually denoted simply by "E". While mounting the piston ring on the piston crown, which is still outside the cylinder liner, the ring is subjected to stress and strain. Upon mounting the ring, the ring should go back to its free state,  $S_0$  i.e. where it originally was prior to stretching.

In reality, some permanent deformation may take place and instead of going back to the state  $S_0$ , it goes back to  $S_{01}$ . The ring is then enters the cylinder liner along with the piston crown and compressed inside the ring groove and is subjected to the closing stress as shown in the Figure 2.10. If the rings were withdrawn from the cylinder liner, instead of going back to  $S_{01}$ , it will go back to a different resting state, i.e.  $S_{02}$ .

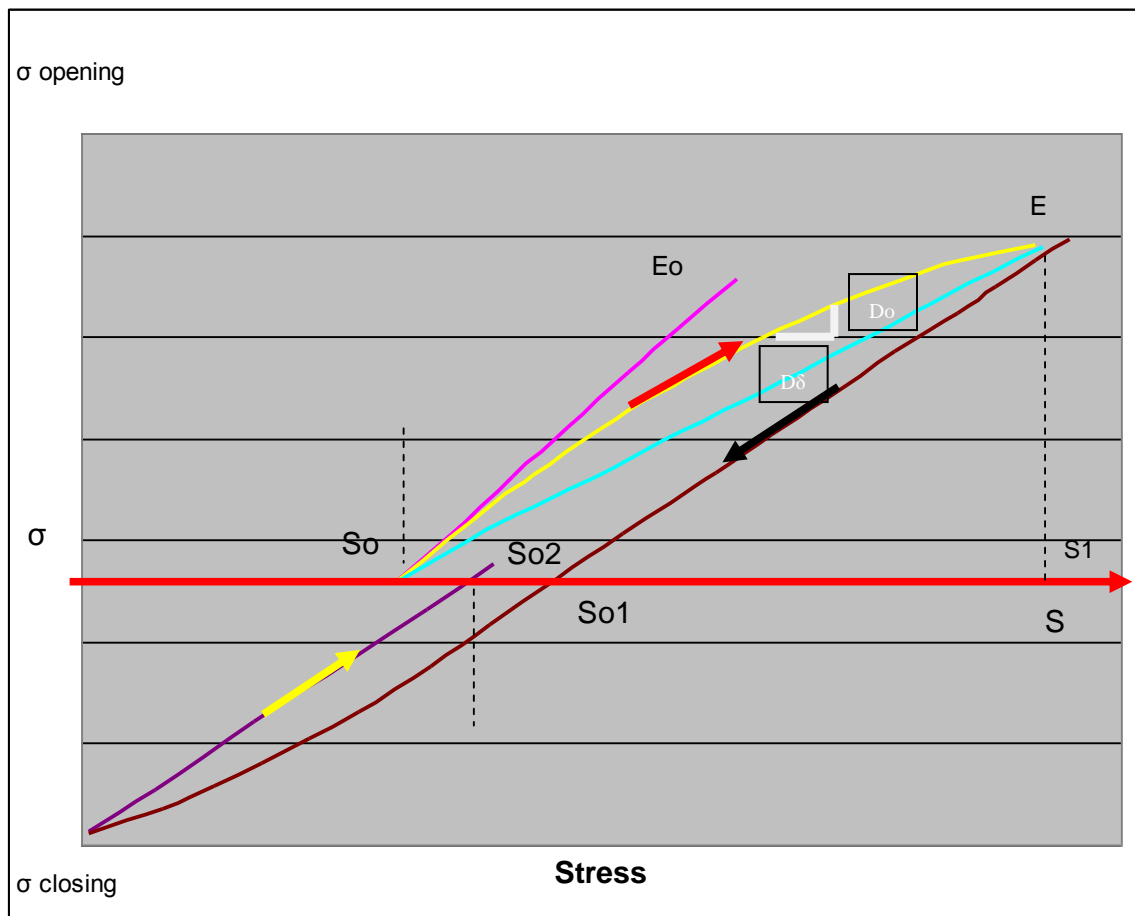


Figure 2.10 Stress – deformation diagram (graph plotted from literature data) [10]

High contact pressures and sliding speeds demand sufficient lubrication between piston ring and cylinder liner. Lubrication of rings is only effective, when the sealing is perfect. Blow-by gases may destroy any lubricating film present, particularly in large engines and promote scuffing. Thus satisfactory sealing is most important for stable operation.

The sealing action of a piston ring set may be simulated by a labyrinth. The leakage past a piston ring may occur at the joint, flank or circumference and the most significant leakage result from thermal deformations. Some deformations may be remedied automatically by a thermal mechanism, others behave in an unstable manner.

Minor faults in mutual contact may be also corrected by gas pressures forcing the ring against its contact surface. This corrective gas force depends mainly on the magnitude of the pressure drop taken up by an individual ring within the set. Since this in turn depends on the combination of the momentary leakage areas, many stable and unstable variations in pressure distribution may result.

The circumferential sealing of a ring under service conditions may be improved by a prophylactic correction of its shape. Wear will correct minor imperfections. Thus, a good running in process is important, and a little wear in service will stabilize operation.

#### **2.1.10.4.1 Labyrinth sealing theory:**

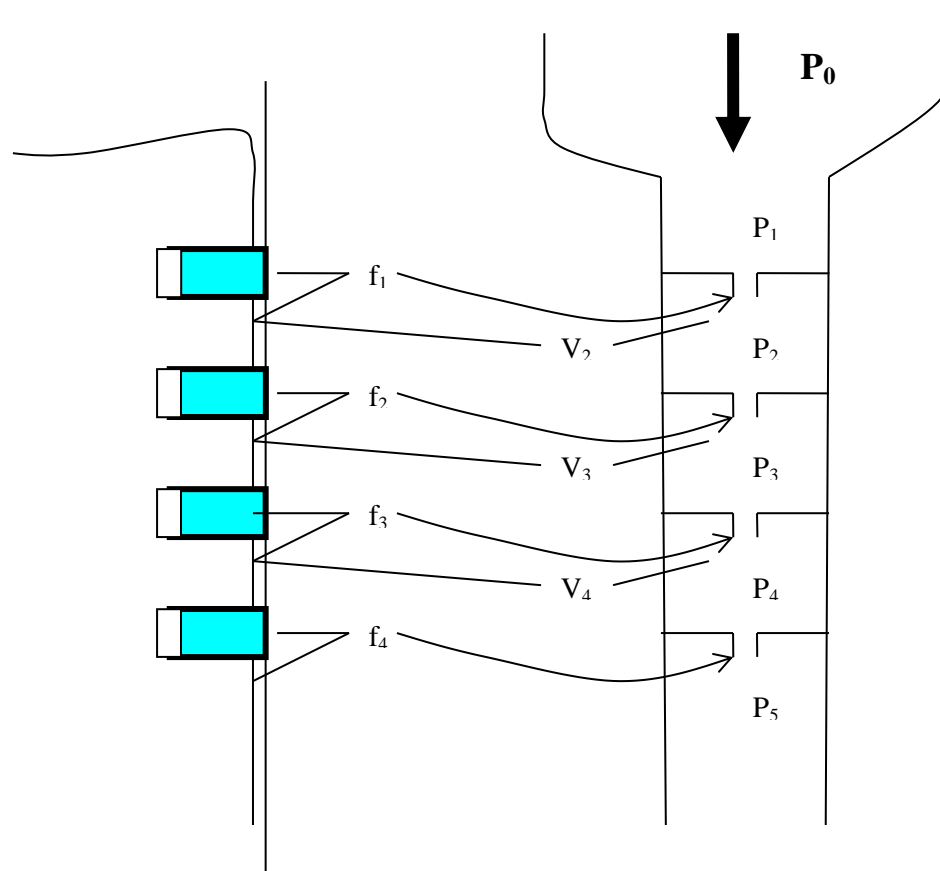


Figure 2.11 Piston ring set acting as a labyrinth

The action of a set of piston rings may be represented by a labyrinth consisting of a series of chambers with orifices between them, Figure 2.11, and the leakage flow

follows the same laws as for a labyrinth. Under static conditions, the volumes of the chambers have no influence, and the pressure distribution along a set of orifices of equal area may be easily calculated. For compressible gases the pressure drop follows the well-known Fanno curve in an entropy chart, the last orifice having the greatest pressure drop. [11]

If the labyrinth is to seal a pulsating pressure, as that found in the combustion chamber of an engine, conditions get more complicated. They are calculated for labyrinths of equal sections. The decisive factor for pressure distribution in such cases is the relation between the duration of a pressure cycle and the time necessary to fill a chamber of the labyrinth. This is determined by the relationship between the volume and area of the preceding orifice and the gas velocity. [11]

The 'relative filling time  $t_r$ ' in the equation 2.5 is the ratio of the absolute time necessary to fill up the first labyrinth chamber ' $t_f$ ' and the time available for this process during the pressure peak of the engine cycle, ' $t_0$ ':

$$t_r = \frac{t_f}{t_0} \quad (2.5)$$

The absolute filling time  $t_f$  may be determined in a much simplified way as shown in the equation 2.6.

$$t_f = K \frac{V_r}{f_r C_0} \quad (2.6)$$

where

$f_r$	Equivalent leakage area of a piston ring	(m <sup>2</sup> )
$C_0$	Gas velocity through leakage area	(m/s)
$V_r$	Volume of a labyrinth chamber	(m <sup>3</sup> )

For low 'relative filling time  $t_r$ ' (less than 1), corresponding to a large leakage area of an individual piston ring, the pressure will fill up the first chamber very quickly and penetrate deeper into the labyrinth. The steady state will be approached, with the last ring taking a major portion of the total pressure drop.

For high ' $t_r$ ' values (3 and more), the duration of the pressure cycle is not sufficient to fill even the first chamber, and the top ring will take most of the pressure drop. This is the case for very tight rings with good lubricating conditions.

#### ***2.1.10.5 Piston ring leakage areas:***

The total leakage area of a piston ring is the sum of the area at the joint, between the flanks of ring and groove, and between the ring face and the cylinder liner. These three areas may greatly vary in extent and any of them can outweigh the others. In addition to this static leakage, dynamic vibrations (ring flutter) may increase the leakage.

##### ***2.1.10.5.1 Joint leakage***

The leakage area at the joint is determined geometrically, and is independent of the pressure drop across the ring.

For a perfectly manufactured gastight joint, the leakage is negligible. For a normal straight or angle joint, the area is relatively small if the edges are sharp. The leakage area is also dependent on the clearance between piston and liner.

Chamfering the ring corners, frequently done to protect the ring from getting caught in the liner ports, will increase the leakage area many times.

##### ***2.1.10.5.2 Flank leakage***

For the seal between ring and groove, it is important to have smooth machining and perfect flatness of the ring flank and the original accuracy of the groove and its maintenance during service. Grooves are often chrome-plated. Imperfections due to a poor mutual fit of the two surfaces may be corrected by the gas pressure acting on the ring.

### ***2.1.10.5.3 Face leakage***

The leakage at the ring circumference is by far the most significant and may be many times that at all the other areas. It is not the scratches and scars that cause the greatest problem but the imperfection of the ring hugging the liner, chiefly in the region near the joint. In this case also certain imperfections may be corrected by the gas pressure forcing a faulty ring against the liner.

The ring may not have been manufactured to the correct shape, it may be deformed or worn to an incorrect form, or the liner is oval or uneven. However, the most serious deformations affecting the circumferential ring shape are caused by temperature differences under service conditions. [11]

### ***2.1.10.6 Piston ring thermal deformation:***

#### ***2.1.10.6.1 Salzmann type***

The ring of a diesel engine is usually hotter than the liner and its outer layers are cooled by the liner (unless friction heats it up) and the ring opens up even more. Its ends press hard against the liner and, at a certain distance from the ends, the leverage is sufficient to bend the ring together to a radius of curvature equal to that of the cylinder. Thus the ring is able to tightly hug the liner. Closer to the ring ends, however, this bending moment is not sufficient, and the ring is not in contact with the liner stays from the liner as shown in Figure 2.12 (zone B). This type of deformation was described by F. SALZMANN over eighty years ago [12] and may be counteracted by a preventative correction (bent inwards) of the ring form producing reduced or even negative pressure near the ends.

#### ***2.1.10.6.2 Stable type***

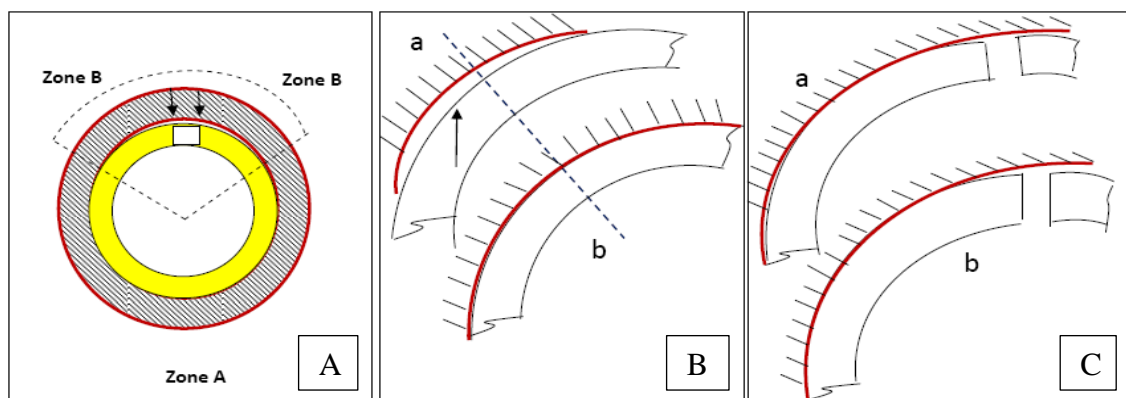
A less known form of heat deformation may correct the gaps if they occur in a continuous length of the ring, e.g. in zone B of Figure 2.12 A. If hot gases pass through a gap, they heat the outer layers of the ring as shown in Figure 1.16B-a

and causes the ring to expand and thus the ring touches the liner again as in Figure 2.12B-b. This self-sealing mechanism is very important for piston rings.

In practice there are however limits to the efficiency of this sealing action. If the gap is small in absolute dimensions, the temperature rise necessary to close it is only slight, and as long as the lubricating conditions in such a thermally sealed gap are adequate, operation may continue in a stable way with the gap just on the verge of opening and this portion of the ring running at a slightly higher temperature. This will usually be the case for small rings, e.g. those used in automotive engines.

Here the short time of every blow-by period, the relationship between the mass of blow-by gases to the heat absorbing surfaces around the gaps and the relationship between the absolute width of the gap to the absolute thickness of the oil film, also help to stabilise the conditions. Moreover, if the gap is wide, as in large engines, the blow-by gases have enough energy and time to burn the oil film and, when the ring touches the liner on a dry surface, friction will heat its outer layers and curve the ring inward. This would produce gaps on both sides of this spot, if they are not sealed by the same process.

#### 2.1.10.6.3 Unstable type



Temperature profile      Temperature      distribution

a. When leak  
b. when reseat

a. at beginning of blow-by  
b. at full blow by

A) HOT RING IN A LINER   B) SELF SEALING OF RINGS   C) INSTABILITY AT RING ENDS

Figure 2.12 Temperature profile and distribution of piston rings

Near the end of the ring, however, this action results in moving the ring end away from the liner. Through this gap, the blow-by gases will heat the ring-end on the outside even more, curving it inward and producing very wide gaps as in Figure 2.12C.

Cyclic gas pressures acting on rings lifted off the liner surface may be strong enough to break the ring by fatigue. Preliminary tests made on a special rig have shown that a ring end of a length corresponding to the width of a liner port may move several millimeters radially by thermal deformation. The fact that deformations of this magnitude occur in practice is confirmed by wear marks on rings that have performed very poorly. It is probably the effect of such deformations that causes most ring breakages.

Since a hot spot on the cylinder tends to protrude into the true cylindrical shape of the liner making it oval, the inward-bent ring ends would have to 'climb over this protrusion' if the ring rotated. This deformation thus prevents the ring effectively from turning around its groove, which would otherwise correct the situation.

If the second ring passes during its normal rotation with its joint underneath such a severely blowing top ring gap, the outer layers of this ring too will be heated by friction on this hot and dry spot, and the ends may be lifted off the liner with the same disastrous effect.

In the same manner, the third and even the lower rings may also lose their seals at the joint, and a wide path will be opened for blow-by. It is stopped only by the last ring, which will be forced by the whole pressure of the combustion chamber against the groove and liner. It is extremely hard to visualise friction under such conditions. Its effects will wear and damage this last ring and the liner.

The heat produced by such severe blow-by may be high enough to cause overstressing of the liner, which would eventually result in fatigue cracks.



#### **2.1.10.6.4 Axial thermal deformations:**

A similar type of heat deformation mechanism also acts in the axial direction if the ring lifts off the groove flank for some reason. At any part of its periphery except the ends, hot blow-by will correct this deformation. However, at the ring ends, conditions are just as unstable as those described for the radial direction. Here too marks on the rings confirm that such deformations actually occur in service. If they are large enough, they will make the ring end jam in its groove.

#### **2.1.10.7 Ring flutter:**

A further possibility of ring leakage is dynamic flutter. In the axial direction this is caused by reversal in the direction of the pressure drop, by friction, and, particularly in high-speed engines, by inertia.

During the jump from one groove flank to the other, the momentary leakage area is many times larger than that of a well-sealing ring, and it is often sufficient to equalize the pressures in the adjoining labyrinth chambers. In this case, the knock on the other groove flank will not be severe enough to do any damage. In other cases however, inertia, friction and sharp pressure reversal will drive the ring hard against the other flank, and damage and wear will result, which may be further worsened by a lack of lubrication at this spot.

With poorly sealing rings (low relative filling times  $t_f$ ), the pressure penetrates deep into the ring set. The top ring may be thrown upward when the pressure in the combustion chamber drops more quickly than that between the rings. Cases of high wear have occurred on the top groove flank, which always indicate unfavorable lubricating and sealing. The basic correction is to eliminate the cause by improving running conditions, and thus reduce the leakage. Passive correction is obtained by protecting not only the bottom, but also the top flank by chrome-plating.

Flutter in radial direction may be caused by very sharp pressure rises during combustion (combustion knock) when the pressure cannot penetrate fast enough through the clearance above the ring into the space behind the ring, or if friction and inertia lift the ring against an existing positive pressure difference, and the pressure in the groove becomes lower than that above the ring. This momentary radial collapse is rendered more severe by ring profiles that are balanced, by intention or wear, in the radial direction.

#### ***2.1.10.8 Loss of Ring Tension:***

Loss of tension takes place during operation, due to wear and the effect of operating temperature. Beside the modulus of elasticity and free gap, the tension of a new ring depends upon the third power of the radial width, which means that a wear of 15% of the original width will reduce the ring tension by more than 50%. The effect of operating temperatures, which tend to progressively reduce the natural tension, depends on material choice and manufacturing method. High temperatures are also caused by blow-by of hot gases and can cause a complete loss of tension and collapse of the ring. [11]

#### ***2.1.10.9 Fitting of New Rings:***

During the fitting of a ring over the piston, the ring suffers a high degree of overstressing as mentioned earlier. The fitting of a ring, if done incorrectly, deforms the ring and causes it to become unserviceable.

#### ***2.1.10.10 Pressure distribution along the ring set:***

The analysis of the various causes of leakage described above has shown that a great many variables are involved. For a ring set to perform its basic duty best, i.e. to seal pressures by the cooperative action of the individual rings, the efficiency of this cooperation is determined by the local and momentary distribution of the total pressure drop among the individual rings. This distribution is influenced by the momentary relationship between individual leakage areas to their corresponding chambers and, for imperfect rings, this is in turn dependent on the correction by the pressure drops across by each individual ring, and vice versa.

For low 'relative filling time'  $t_r$  (less than 1), corresponding to a large leakage area of an individual piston ring, the pressure will fill up the first chamber very quickly and penetrate deeper into the labyrinth. The steady state will be approached, with the last ring taking a major portion of the total pressure drop.

For high  $t_r$  values (3 and more) the duration of the pressure cycle is not sufficient to fill even the first chamber, and the top ring will take most of the pressure drop, which is reflected as  $P_1$  in Figure 2.13. This is the case for very tight rings with good lubricating conditions. In this case, the pressure drop at the successive rings namely  $P_2$  and  $P_3$  will be very small.

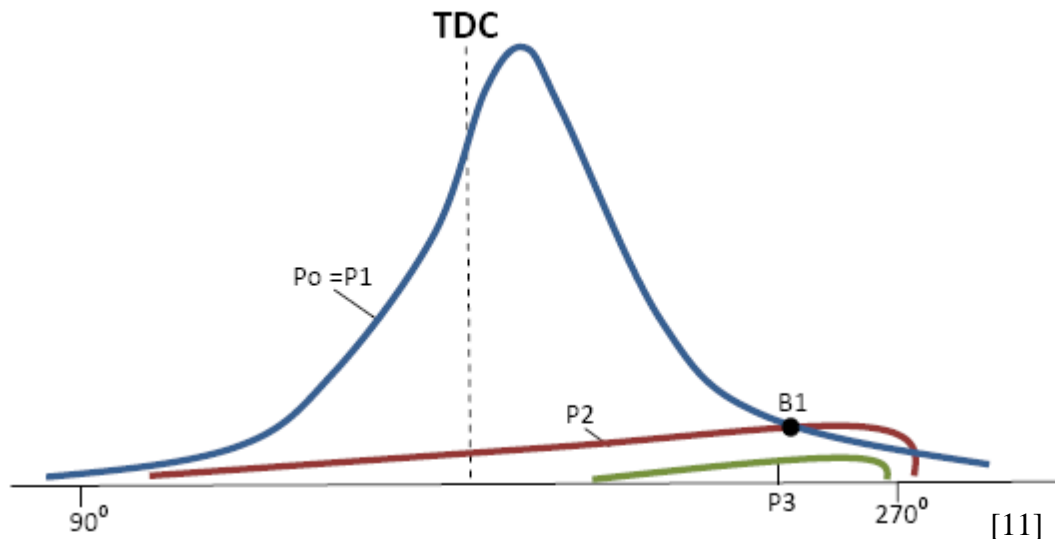


Figure 2.13 Pressure distribution in a ring set with a gastight top ring

With perfect rings and good lubrication, operation is stable. However, with rings that are not quite so perfect and under poorer general conditions, many stable and unstable combinations are possible.

#### **2.1.10.10.1 Principle of pressure concentration:**

This principle is simple if the ring set consists of one ring only. This ring alone is responsible for sealing the whole pressure drop, which will in turn assist it in correcting a faulty shape and keep the ring in good contact with the cool liner

surface and groove flank, thus lowering its temperature and preventing destruction of the lubricating film by blow-by. On the other hand, it has to carry the whole load alone and will consequently wear more if the lubrication conditions are not quite right.

Concentration of the seal onto one top ring may also be achieved by a combination of a perfectly sealing top ring with normal, less tight, rings following it. In this case, the top ring will be initially so tight as not to leave to the following ones any pressure to assist them in sealing. This renders the top ring tighter, unloads the others still more, and finally it bears the load alone.

In practice this means that, if the general conditions have been good enough to be improved almost to perfection by a good seal of the top ring, such a combination will run well and with little wear. However, if they have been so poor that the benefit brought about by good sealing of the top ring is not always sufficient to ensure very good lubrication, severe wear will result. Under still worse conditions (worn or distorted liners, poor maintenance of the injection equipment, poor lubrication, overloaded engines, etc.), a gastight top ring will break very quickly.

#### 2.1.10.10.2 Principle of pressure distribution:

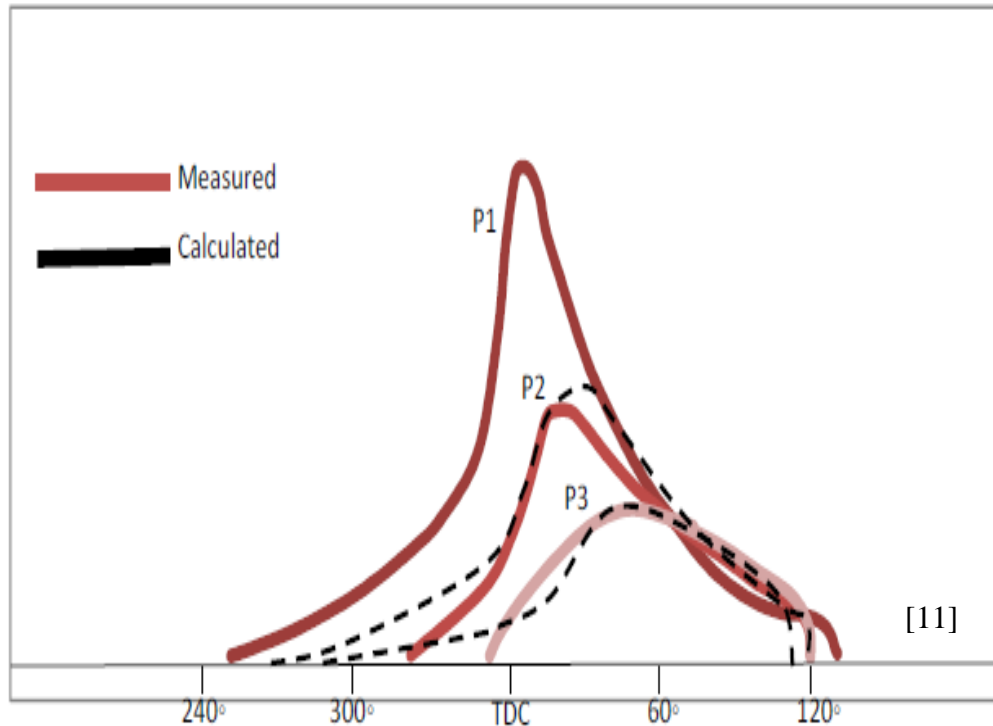


Figure 2.14 Measured/calculated inter-ring gas pressure of a 2-stroke cylinder

The obvious remedy appears to be the distribution of the pressure drop so as to allow each ring to take its own fair share of the load; this is, however, not so easy. With a labyrinth of constant sections having an adequate 'relative filling time  $t_r$ ' of about  $\frac{1}{4}$ , this effect may be readily achieved. In this case, each ring temporarily takes over some pressure and, having good contact with the liner during this time, it can cool off and maintain lubrication. Under unfavorable conditions however, the top ring may be so leaky that it will take no pressure drop whatsoever at any time. Consequently, there is nothing to force it against the other sealing surface but its own elasticity, which is some 10 to 100 times smaller than the gas pressure. It loses the cooling contact with the liner in most places, gets hot as a result of blow-by and friction, and will distort even more.

This is true of very leaky top rings that are found 'dry' upon dismantling. The same applies of course if a ring is broken. Such a hot ring moves over most of the

running surface of the liner and burns the little lubrication still left there, thus ruining the running conditions for the other rings and the piston skirt.

Figure 2.14 shows the pressure distribution of a ring set of three as  $P_1$ ,  $P_2$  and  $P_3$ , which have been calculated and the various pressure distributions along the ring set have been measured on moving rigs. [14,15]

#### **2.1.10.11 Consequences of ring behaviour:**

A piston ring needs to be mechanically perfect when running as it can. It has to adapt itself to its narrow confinement under the influence of changing temperatures and pressures.

In general, the various stages of services are; first, the ideal condition with the rings sealing properly all around and lubricated well. The next stage is characterised by slight deformations that might be corrected by blow-by heat and gas pressure, still allowing stable operation. Finally, the deformations become so large as to produce instability with destructive results leading to scuffing and possibly also affecting the running of the piston skirt.

### **2.2 Countermeasures for Scuffing:**

Onset of scuffing could take place for numerous reasons as shown on the flowchart under section 1. Once the rise in potential for any of those variables is discovered, appropriate measures can be undertaken accordingly in order to mitigate or diminish the possibility of scuffing.

When scuffing is observed it is important to establish if it is actively occurring or if it is recovering from the condition. If recovering, the lubrication will have been re-established and a new running-in process occurs to the cost of higher wear than normal. In the severe and active stage all measurements possible should be initiated to avoid further damage and replacement of piston rings, increased cylinder oil feed rate and control of operating parameters.

The extent and severity of scuffing determines the consequences. For minor instances, normal stable operation can usually be recovered. Wilson [3] comments that increasing the lubricating oil supply may not necessarily accomplish this and instead suggested that the oil film may be re-established by lowering the liner cooling water temperature so to permit greater heat transfer away from the surface. No action can help for major scuffing over a broad area. In this case, the liner and the rings certainly need to change.

In principle, anything that helps the ring to maintain its correct sealing conditions should be facilitated and the operating conditions must be eased. It is necessary to preclude distortions, excessive pressures and temperatures, maintain satisfactory lubricating conditions, eliminate blow-by, and apply correct cooling.

There are several mechanisms automatically helping the ring to correct faults and stabilize operation. Care should be taken to let them work freely and not disturb their action. For this, a careful analysis of operating details has to be made.

In practice this means:

- Correct mechanical design
- Careful manufacture, assembly and maintenance
- Good quality of rings
- Sufficient lubrication, both quantitatively and qualitatively

To maintain stable operation, ring deformations have to be corrected right from the start in order to re-establish sealing. For this, several mechanisms may be utilized.

### **2.2.1 Thermal correction:**

The stabilizing second type of thermal deformation has been described earlier.

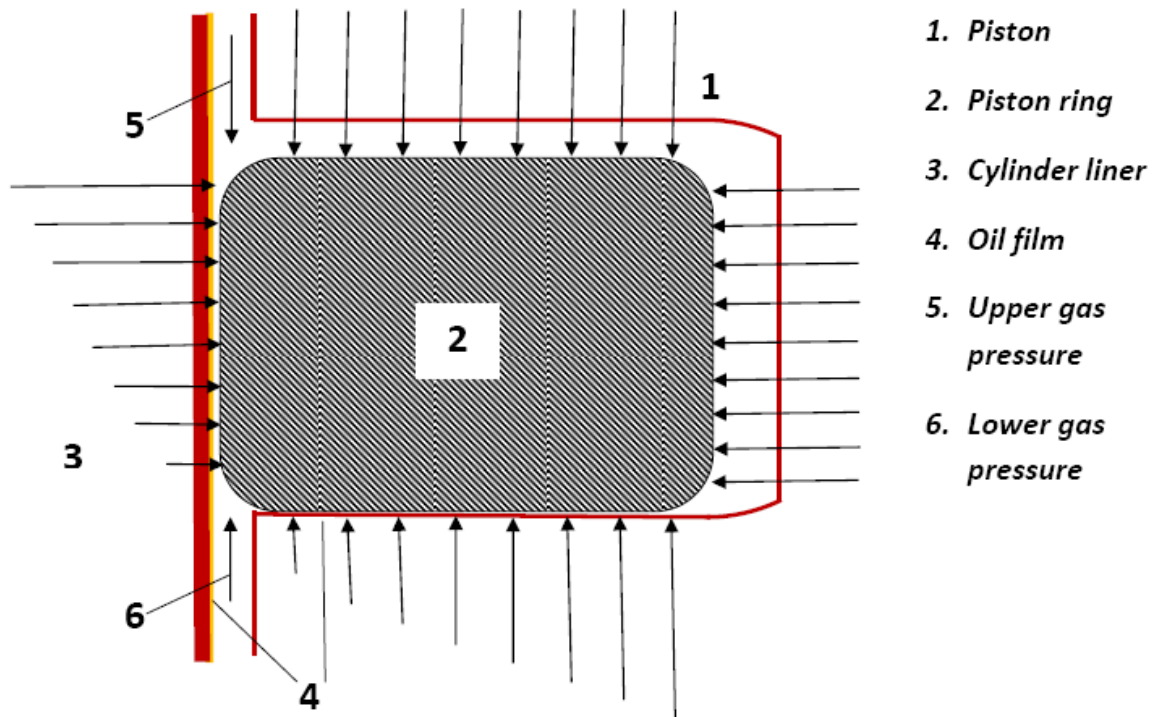
### **2.2.2 Correction by pressure:**

Gas pressure corrects the deformed rings. The correction by gas pressure forcing a deformed ring against the liner or the groove flank is due to the momentary pressure difference across a ring and the distribution of this pressure around the ring profile.

Under ideal conditions the ring runs as shown in Figure 2.15. In practical service however, conditions are quite different. Irregular wear of ring, liner and piston ring groove, mechanical and thermal deformations of liner, piston and ring, and transversal motion of the piston in the cylinder will alter the ideal configuration, thus resulting in many different cases of pressure distribution. Some basic cases are shown in Figure 2.16.

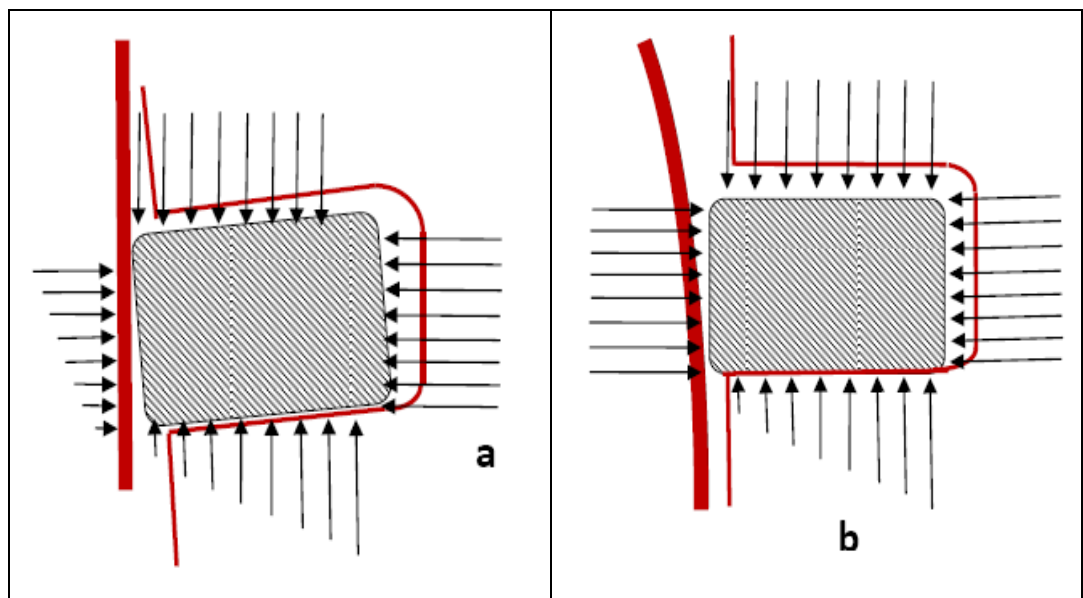
At that, the ring profile usually wears to a curve, resulting in a compromise between the rectilinear shape shown in Figure 2.16, and numerous variations of partly loaded and partly balanced profiles in both radial and axial directions takes place. The deviations may be very small, i.e. in thousandths. The deviations vary in different places of the ring circumference or even during the different phases of the cycle, but they greatly influence the radial and axial forces acting on the rings.





**Ring:** fully loaded radially, balanced radially, fully loaded axially, balanced axially,

Figure 2.15 Ring running under good conditions



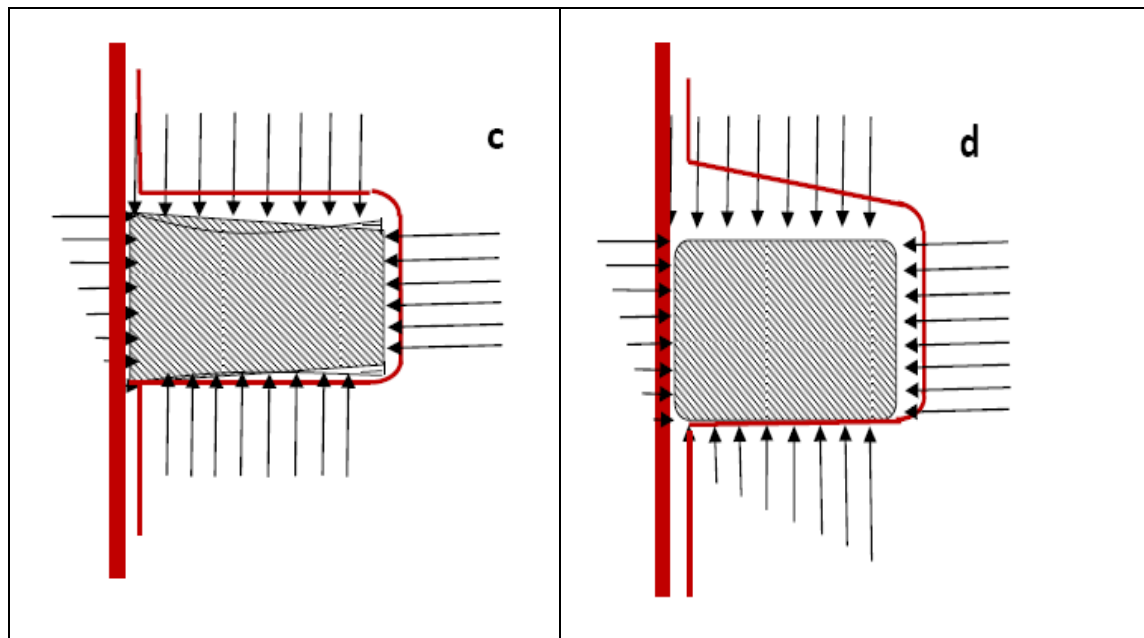


Figure 2.16 Gas pressure distribution around irregular ring profiles

The profile of the ring are often shaped and designed to balance the radial pressure on the profile in order to protect the ring from excessive wear and scuffing or to improve oil consumption. These types of rings may run well in the service with adequate lubrication and sealing. They may not experience high temperatures or large deformations. Nevertheless, in reality the rings are subjected to cyclical deformations within the elastic limits, which are interrelated with their lubrication behaviour. By pre-profiling a ring, its way of finding its self-adjusted profile is interrupted and the gas force may not be adequate to correct the deformations. Hence, such rings may fail in service under difficult conditions.

Slant rings (top edge cut off) reduce the radial gas force and the resulting friction. Nevertheless, the pressure on the bottom part (the ring face touching the liner) increases. It will however prevent the concentration of the radial gas force on the top edge (e.g. in the case of ring 'a' shown in Figure 2.16, 'top edge bearing'), which frequently results in scuffing. In a similar way, rings machined to a barrel shape, thus imitating in advance the favorable profile otherwise produced by wear, also prevent force concentrations on the top edge, but they press with their 'bulge' against the liner with very high specific pressures. This speeds up their running-in

and sealing. The formation of a lubricating film on these rings is facilitated by their gradual lead-in for the oil. Under extreme conditions, the elasticity of the materials will also assist in maintaining a satisfactory load-carrying film. The specific pressures are already so high that the barrel-shaped ring face and the liner material will yield elastically, and the surface peaks that would otherwise pierce the oil film are reduced as a result. Consequently, full lubrication may be established by an elasto-hydrodynamic film [11].

With the barrel shape ring, very little oil supply is adequate for sealing and forming the load carrying film. Even a boundary layer of oil will allow the ring to operate quite stably. Nevertheless, even the barrel shape rings will be subjected to scuffing if the trace of oil is blown off or burnt.

Furthermore, effective correction by pressure demands from the very beginning a sufficiently high pressure difference sealed by the piston ring. A poorly sealing top ring may not be capable of keeping a sufficiently large portion of the total pressure drop for itself if the sealing is taken over by other tighter rings. Consequently, the top ring will never seal.

### **2.2.3 Correction by wear:**

Wear assists in correcting high spots. Under service conditions that are not too unfavorable, wear will automatically produce a ring shape that is best adapted to those specific conditions. Under too severe conditions however, although the high spots might be still corrected by wear, the rings become badly distorted during this process by friction, blow-by and temperature differences. The shapes then produced by wear will consequently not be able to perform satisfactorily. The rings thus obtained are excessively worn in some places of their periphery, e.g. near the ends, so that they will never seal properly again. These rings may lose their tension or even break.

#### **2.2.4 Shape correction:**

This fault may be compensated by designed machining of the ring 'smaller' than the cylinder compressing the gap completely, and turning the ring undersize to a radius  $R_K$ . When released, the ring will spring open to the shape with reduced pressure at the ends, giving a safety margin for hugging the liner when the ring is hot under service conditions.

If the correction is large enough, the rings will show a light near their ends. The usual specification of this light gap by width and length is very coarse and may be even misleading. It should be supplemented by the measurement of the radius of curvature.

By comparing ring shapes with temperatures measured in service it has been found that a ring usually wears to the shape corresponding to its temperature and that, on the other hand, it reaches at its ends the temperature corresponding to its correction.

Under good conditions, a cool top ring (usually running at 150°C in a liner of 80 to 150°C) needs little correction. A correction of 1% is usually sufficient, as shown by the fact that this correction is maintained even after wear in long service.

Still cooler (e.g. lower) rings will wear less at their ends. Rings running hotter, like most top rings in severe service, wear more at their ends and will correct themselves to a shape with about 2%.

Rings that have suffered high temperatures in service will attain an excessive correction with too much 'toe-in' at their ends. This is harmful, for the ring ends may be heated on the outside and bend inwards, losing their sealing ability.

#### ***2.2.4.1 Chamfered ring ends:***

Chamfering the rings at their ends will increase the leakage of an individual ring and lead to deeper penetration of the pressure into the ring set. While it may protect the ring against getting caught in insufficiently chamfered liner port, it will certainly tend to reduce the pressure load carried by this ring (a reduction beneficial to wear, but detrimental to stability) and lead to greater fouling. The chamfering of otherwise identical rings will raise the temperature of the ends by about 80°C and thus require greater correction.

#### ***2.2.4.2 Running-in:***

New piston rings should be really manufactured to shape adapted as closely as possible to the actual conditions required during service. But in practice a compromise must be drawn to simplify the spare parts inventory, and thus the transition from a ring shape not suitable for the operation conditions to the correct one is often left to the wear during running-in.

In order to facilitate this very important process and to obtain rapid sealing, a sufficiently high wear rate has to be maintained. All means designed to reduce wear (beneficial to later operation) have to be avoided, which is easily understandable in the light of the theory of the scuffing mechanism. Thus very smooth surfaces, or the use of fuels with a very low sulfur content, or wear-reducing oils like most HD (Heavy Duty) and alkaline oils will often lead to trouble, particularly to scuffing. During later service, some stable wear is beneficial too, for it helps the ring to adapt itself to changing operating conditions.

A very effective way of facilitating running-in is the application of a thin galvanic copper layer, which brings about rapid sealing and thus prevents distortion by blow-by. This beneficial effect is indicated by the absence of lacquer on the liner surface. Breaking up the ring surface by circumferential grooves and filling them with copper, produces a very effective anti-scuff surface that will last for quite a while until the grooves are worn off. Running-in additives to the fuel or lubricating

oil, which produce abrasive compounds, also increase the initial wear and may be beneficial to rapid and clean running-in.

An appropriate roughness ('as smooth as possible but as rough as necessary') also facilitates running-in. In practice, manufacturers manufacture the liners of large engines with a roughness of some CLA of  $5.3\text{ }\mu\text{m}$  by boring only, and the ring face has a fine thread resembling the grooves of a gramophone record. During the first few hours of running-in, a new engine will consequently sound like a twittering flock of birds. But the rings are afterwards polished by abrasion to such a smoothness that they reveal their microstructure when viewed through the metalloscope. This can be achieved only if running-in is effected by pure abrasion without excessive temperatures and assisted by sufficient lubricating oil present in the pockets of the rough surface.

The increase in the engine load has to be rapid enough to avoid excessive polishing of the surface at low loads when the thermal distortions due to normal operating temperatures are not attained yet.

The curvature distribution of a top new ring and a ring run for 5000 hours is shown in Figure 2.17.

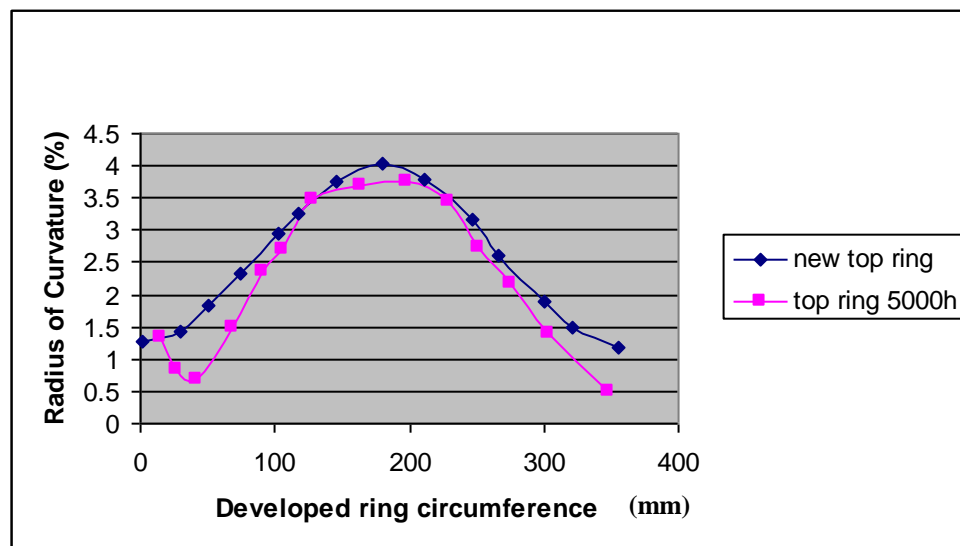


Figure 2.17 Curvature Distribution of top ring

#### **2.2.4.3 Cylinder liner surface:**

Improvement has been made on the cylinder liner surface for spreadability of the lubricants and its retention. Compared to honing, the spreadability of the cylinder oil is better with the wave cut; in particular, the spreadability in the circumferential direction is more effective.[16]

#### **2.2.5 Correction by Materials:**

##### **2.2.5.1 Cast iron:**

With perfect lubrication, the materials of the rings and liners should have no influence at all, but as lubrication is not always perfect, the quality of both materials plays a decisive role. The rings and liners are usually made of cast iron. Here good perlitic structures with flake graphite (ASTM type A3-A5) are necessary. Hard constituents in the form of phosphide crystals arranged in a grid are beneficial to wear and scuff resistance. On the other hand, too much phosphide may render the iron brittle. Thus a compromise of about 0.4% phosphorus is considered to be the best for liners.

Rings made of spheroidal graphite cast iron having higher strength and toughness are less subject to breakage, but on account of their poorer running qualities they often suffer from scuffing and higher wear. The running-in process is particularly difficult and may be improved by copper-plating and grooving the ring face. Under extremely bad running conditions, SG iron rings may be the only answer, but sometimes higher wear will result. The same is true of high-alloy and heat-treated ring materials, so that these and SG iron rings are mostly used with chrome and other special running layers.

##### **2.2.5.2 Chromed ring grooves:**

Ring groove chroming helps to reduce the accelerated groove wear and maintain the axial clearance between the grooves and the rings. Premature groove wear, especially at the edges, causes the ring to slant and break in service.

### **2.2.5.3 Other coatings:**

Surface coatings of rings with plasma and coatings of liner surfaces were shown to give improved sliding wear performances [4, 17, 18].

More resistant layers on the rings, e.g. combinations of metal carbides applied by plasma-spaying should reduce wear even further and thus prolong ring life. At the same time they should provide emergency lubrication by the oil contained in their pores. On the other hand, these highly wear-resistant rings will maintain their original shape and, owing to their inherent nature, resist correction by wear, which might be necessary at times. Consequently, under difficult conditions, it may result in either leaking or scuffing.

### **2.2.6 Correction by revolving piston rings:**

In principle, the best way of improving the running properties of piston rings and their lubrication is to superpose a second direction of motion over the normal alternating piston movement. This will always shift any critical spots on the ring to fresh, cool and well-lubricated portions of the cylinder liner and consequently interrupt the mechanism of scuffing described at the beginning of this article.

The formation of scratches and wear grooves will be precluded, and both the liner and the ring will become polished to a high mirror finish. As a result of rotation, oil will be evenly distributed over the entire circumference and both the formation of dry spots and heavy oil stresses – which otherwise result in high oil consumption – will be consequently prevented.

The normal slow rotation of piston rings around the groove circumference is beneficial in this regard, but it is too slow and, in particular, unreliable. The drive must be consequently positive and powerful enough to enforce rotation even under adverse conditions, for it is then that rotation is most needed.



### **2.2.7 Carbon control by flame ring:**

Excessive carbon problem at the top land of the piston may be addressed by using a steel ring often called a piston cleaning ring or a flame ring. The diameter of the piston cleaning ring is made slightly smaller than that of the top end of the cylinder liner. This assists in scraping off the excessive carbon deposits from the piston top land before the deposits can form a hard layer [13].

### **2.2.8 Slide valves (sacless injectors):**

Introduction of slide valves or sacless injector resulted in complete combustion and hence, eliminated the oil dripping and after burning of the fuel responsible for heavy carbon deposit on the piston top land and the ring landings between the grooves, which caused cylinder liner polishing and also high liner temperature.

### **2.2.9 Effective purification and filtration of fuel oil:**

Purifiers can remove 65~70% of catfines from the fuel and the remaining catfines can be arrested by installing 10micron intermediate backwash filter in the engine fuel system. Statistically, more than 70% of the catfines in bunker fuel were found to be bigger than 10 micron size. Hence bulk of the residual catfines and other bigger contaminants in the fuel can be removed by 10micron backwash filters. The remaining small amount of catfines then can be arrested by 5 micron disposable catfine filters prior to the injection pumps of the engine. This way, the catfine filters are not burdened by other contaminants and this results into higher longevity of these expensive 5 micron disposable catfine filters.

### **2.2.10 Correction by Lubrication:**

Lubricating film is indispensable to separate the rubbing surfaces and to maintain low friction coefficients. This film also assists in sealing small gaps. It has to be spread all over the rubbing surfaces and maintained there in spite of all influences tending to rub it off or destroy it by burning. Consequently, the oil has to be supplied in a sufficient quantity and distributed evenly.

The usual assumption of the film thickness used for test jigs and calculations, viz. that there is plenty of oil, is in practice probably valid in exceptional cases only. It is especially near the TDC position of the top ring that many indications point to a great scarcity of oil, which reduces the thickness of an oil film at this spot to minimum values. Extreme economy in oil consumption may reduce the film thickness at the critical spots below the admissible limits, and trouble will result.

#### ***2.2.10.1 Lubricants delivery:***

The lubricant delivery system has also been improved through development of high speed [19] electronically controlled with adjustable feed rate against sulphur content of the fuel, which is used in M.A.N. engines known as Alpha lubricator [20].

Another development was swirl spray [21] optimized timing injection systems. Recent development of Pulse lubricator from Wartsila and Electronic controlled Lubricator (ECL) from Mitsubishi heavy industries are also based on electronically controlled high pressure lubrication, which certainly improved and optimised the lubricant delivery to the rings/liner. This has been aided by investigations to enhance understanding of oil distribution and retention on different liner surfaces [16].

#### ***2.2.10.2 Lubricants formulation:***

A lot of efforts have been made to improve lubricant formulation to offer greater scuffing resistance [16]. Oil quality is also of great importance. The oil has to resist thermal, chemical and mechanical influences.

Viscosity of the lubricants at high temperature is a very important characteristic of the cylinder lubricants. There are different temperature-friction characteristics for lubricants with different bases and the same additive package and there are also different temperature-friction characteristics during heating up and cooling down for each blend. Single-base lubricants have more promising temperature-friction characteristics than those of a blend of a high-viscosity base and a low-viscosity base at high temperature.[22]

Despite the adoptions of countermeasures in material and component design and machinery operation including the lubricating oil delivery, as discussed above, scuffing problem still persists. Hence, the detection of scuffing at very natal stage or as a precursor plays a vital role in the prevention of scuffing.

### **2.3 Detection methods of scuffing:**

Various methods can be used to detect scuffing.

Onset of scuffing can be detected through analysis of the tribological model of the whole two stroke cycle of the engine. By appropriate modeling, the transition of hydrodynamic to boundary or even the mixed lubrication scenerios can be projected for different loading condition of the engine.

There are also several intrusive monitoring techniques, which utilise transducers mounted flush with the cylinder liner wall. These include proximity, inductive, capacitance and flash temperature monitoring.

Proximity sensors measure the distance between each ring and liner surface. This can be used to determine whether a ring is working satisfactorily, if it is sticking in its groove or has collapsed, or if it is broken or is missing. The use of proximity sensors requires a magnetic material; therefore rings coated with an antimagnetic material such as plasma sprayed will not produce a signal until the coating is worn.

Commercial ring monitoring systems, described by Fog [29], have been developed which are based upon inductive monitoring of the top ring. These require installation of a special top ring whose construction contains either a non-magnetic band or a separate wear groove. These systems can be used to monitor ring wear, ring rotation and the occurrence of sticking or collapsed rings. However, these techniques are limited in that only the top ring operation is monitored and measurements are taken at only one point on the piston stroke. A derivative of this method a transducer based upon wear-down resistive elements, which is fitted flush with the liner. A measure of the element resistance generates a signal proportional to the amount of wear [30].

Capacitive transducers have been widely used to measure oil film thickness. This technique is considered to provide the most quantifiable results [31]. They work by measuring the capacitance formed between the piston ring and a probe mounted in the cylinder liner, or vice-versa, with oil serving as the dielectric material. One of the main problems with this technique is that it relies upon the assumption that the region between the ring, or liner, and the probe is flooded with oil. If however, there are gaseous inclusions, such as may be introduced through cavitation, then the oil dielectric is changed causing errors in the film thickness measurement [32].

Compared to the eddy current sensors, though the capacitive sensors have some advantage with regard to the resolution and not sensitive to the material changes, they are not suitable for the dirty or wet environment and they need a large gap between the sensor and the target and their temperature range is very low.

Among other noncontact sensing technologies are the optical and laser, which in addition to having operational drawbacks, are quite expensive.

Traditional method of detection of scuffing is through the cylinder liner temperature monitoring devices. Since scuffing is accompanied by very high flash temperatures, the monitoring of these flashes can be a sensitive indicator. To achieve this thermocouples with an extremely fast response time are mounted flush with the liner surface in the upper part of the cylinder. Martens [33] described the use of the rate of measured flashes as a parameter to indicate scuffing. However, since scuffing develops quickly, continuous monitoring and immediate reaction is required. A simpler but less sensitive indication of thermal overload can be obtained from the use of thermocouples embedded within the liner but away from the inner surface [33].

Recently acoustic emission detectors have been used for the detection of piston, whereby the scuffing damage is subdivided into scuffing origin, irreversible scuffing and severe scuffing [34].

Ultrasonic sensors, radar, and video cameras are active. A strain gauge (whose resistance changes with pressure applied) is passive. Some types of microphones

are active while others (like piezoelectric microphones) are passive. They generate an output with only the input energy they are sensing. They do not need a power source to generate an output (though the output will usually be very low and need to be amplified with an active device). Thermocouples and thermopiles are passive. They generate a voltage output using the temperature energy they are sensing. They do not require a battery to make their output. But similar to piezoelectric microphone, the output is very weak and probably needs to be amplified with an active device like an op-amp. Table 2.2 shows the comparative analysis of three types of sensors.

<b>Characteristics</b>	<b>Temperature Sensor</b>	<b>Eddy current Sensor</b>	<b>Acoustic Sensor</b>
Sensitivity	Low	Medium	High
Sensors number	1	1	More than 1
Precision	Medium	Medium	High
Signal Processing	Low level difficulty	Low level difficulty	High level difficulty
Accuracy	Medium	Medium	Higher than both
Couplant	Required	Not required	Required
SNR(Signal to Noise Ratio)	High	Low (If distance is reduced lowest)	Medium
Implementation	Easy	Difficult compared to temperature	Difficult than both
Cost	If thermocouple, lower. If RTD with Platinum wire, costly.	Lower than both(temperature and acoustic sensors)	Costlier than temperature(RTD, thermocouple) and eddy sensors
Efficiency	Medium	Medium	High

Table 2.2 Comparative analyses of three sensors [35]

### **2.3.1 Tribological Method:**

The model comprises the engine load, oil film thickness and coefficient of friction. By ensuring that these elements are within the threshold limit, scuffing can be avoided and any deviation from their recommended value serves as a precursor of scuffing.

Early analyses of ring lubrication were based upon a balance of radial forces, viscous shear considerations and application of Reynolds equation to a single ring, Dowson et al [23]. Reynolds equation takes into account parameters of geometry, viscosity, pressure and surface velocities, and can be solved for pressure distribution, load capacity, friction force and oil flow. Subsequent analyses offered a more realistic calculation of ring friction through the inclusion of asperity interaction and mixed lubrication models [24]. A significant improvement was made through consideration of the effects of the ring pack as a whole and the interaction of oil flow among the piston rings, i.e. the leading ring will lay down an oil film which supplies the following rings. Obviously, the existence of the front ring will reduce the oil supply amount for the following ring, which will result in insufficient supply problems and operate under 'starved lubrication' conditions, where the inlet region of the ring profile is starved of a full supply of lubricants [25, 26], as opposed to the unrealistic assumption of an unlimited supply of lubricant available at each ring throughout the engine cycle, termed 'fully flooded lubrication'.

S.M. Rhode [31] theoretically demonstrated that, both the mixed lubrication state (near the top and bottom dead centres) and the hydrodynamic lubrication state (at the middle point) existed during the whole stroke of a piston, and the friction forces were maximum at the dead points. The contacting load acting at the contacting asperities under the mixed lubricant state could also be calculated.[24]

C.L. Gui proposed that for a moderately or highly reinforced engine, it is necessary to consider the temperature field in lubrication analysis of piston assembly, and it is also important to determine the viscosity-temperature property of the lubricant base on the in-wall temperature of the cylinder liner. [27]

Greenwood and Tripp made an asperity contact model to describe the contact behaviour on rough surfaces of the piston assembly. The friction force resulting from the asperity contact can be obtained, which establishes the base for wear prediction [28]

Wear mechanism of piston assembly is very complicated. The influencing factors include lubrication state, heat, external or self-produced abrasive and erosion etc. So, it is nearly impossible to establish a precise model including all the mentioned factors to describe wear properties of a piston assembly. Therefore, it is more practical to adopt a simple model to include the common and main influencing factors.

To involve the comprehensive factors including film squeeze effect, insufficient oil supply, surface roughness, non-uniform distribution of circumferential ring spring forces into lubrication analysis of piston assembly, it is required to solve simultaneous equations including the 2-dimensional average Reynolds equation, film thickness equation, load equation, flow equation of insufficient oil supply and asperity contact equation. The axial and circumferential oil film thickness for piston ring-cylinder liner pair as well as the variations of friction power loss in a working period of an engine can be calculated.

The above studies suggest that tribological method can be used as a basis for prediction of oil film thickness. In some cases, the oil film thickness were actually measured through sensors. It does not consider many other dynamic factors the marine engines usually go through, especially in rough sea conditions, bad fuel and poor combustion etc. It is still considered very theoretical approach for prevention of scuffing through the prediction of maintaining adequate oil film thickness. So far, tribological model was not used as a basis for any secondary detection method and hence, this could be a useful study.

### **2.3.2 Thermoelectric Method (Temperature Sensor):**

Temperature is the most commonly used parameter in engineering. Accurate temperature measurement is needed in various types of applications like materials science, labs and in electrical/electronic and electrical products.

In our case, temperature indicates the cylinder liner surface temperature and the condition of lube oil. If temperature is very high, viscosity of oil reduces, which lead to higher friction and scuffing. Otherwise, the sensor detects the liner surface temperature which may experience scuffing owing to many variables as mentioned earlier.

Various types of sensors are used to measure temperature, out of which the most common are Thermocouples (TC), Resistance temperature detectors (RTD) and Thermistors and depending on the application, one may be more suitable than others.

When selecting a temperature sensor, several considerations need to be made, among which the common ones are the application type, the device to be measured, mounting area, distance from sensor to instrument, ambient temperature, temperature range and accuracy, time of response, linearity, safety factors and cost etc.

#### **2.3.2.1 Thermocouples**

Thermocouple is the most commonly used temperature sensor. TCs are not expensive. They are robust, can be used for long distance measurement and self powered. With various types of alloys, they cover a wide range of temperatures and sensitivity of measurement. The types of TCs such as J, K, T, E, R, S, B, and N, are distinguished by their material composition. 'K' type TC is the most commonly used thermocouple. Specification of different type of thermocouples is shown in Table 2.3.



Thermocouple Type	Materials	Range
J	Iron (+) Constantan (-)	-40 <sup>0</sup> to 760 <sup>0</sup> C
K	Chromel (+) Alumel (-)	-200 <sup>0</sup> to 1200 <sup>0</sup> C
T	Copper (+) Constantan (-)	-270 <sup>0</sup> to 400 <sup>0</sup> C
B	Platinum 30% Rhodium (+) Platinum 6% Rhodium (-)	20 <sup>0</sup> to 1820 <sup>0</sup> C
E	Chromel (+) Constantan (-)	-270 <sup>0</sup> to 910 <sup>0</sup> C
N	Nicrosil (+) Nisil (-)	-270 <sup>0</sup> to 1300 <sup>0</sup> C
S	Platinum 13% Rhodium (+) Platinum (-)	-50 <sup>0</sup> to 1760 <sup>0</sup> C

Table 2.3 Types, materials and temperature ranges of thermocouples [36]

The relationship between the temperature and the TC output voltage is non-linear. Hence, mathematical linearization is needed for the conversion of TC output voltage to temperature.

Thermocouples are made of two different types of metals. They are joined together at one end and open at the other. A thermal gradient takes place. TCs work on the basis of thermoelectric principle or the 'Seebeck effect'. The voltage is not generated at the junction of the two metals of the thermocouple but rather along that portion of the length of the two dissimilar metals that is subjected to a temperature gradient. Both lengths of dissimilar metals experience the same temperature gradient. At the end, the result is a measurement of the difference in temperature between the thermocouple junction and the reference or open junction.

The voltage signal at the open-end is a function of both closed-end and open-end temperature. Changes in the measured signal can only be considered as a function of  $T_1$ , provided  $T_2$  is held at a standard temperature as shown in figure 2.18.

The standard temperature for  $T_2$  is usually taken at  $0^\circ\text{C}$ . In practice, the difference between the actual temperature  $T_2$  and  $0^\circ\text{C}$  is corrected within the instrument. The term such as 'cold junction compensation' or 'ice-point' reference is used for such adjustment.

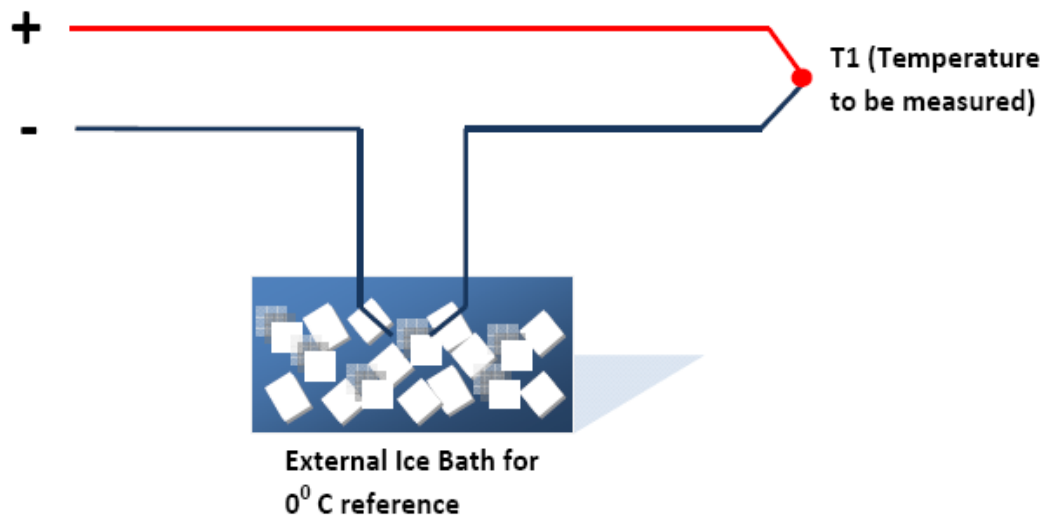


Figure 2.18 Typical Thermocouple setup with cold junction compensation

Compared to other types of temperature sensors, thermocouples have many advantages. Various types of TCs are available for a wide range of temperature. (Refer to Table 2.3 for thermocouple range). On the other hand, thermocouples need cold-junction compensation (CJC) for linearization, as they are non-linear.. Voltage signals of TCs are as low as tens to hundreds of micro-volts. Hence, TCs need proper methods and techniques so that the to noise and drift in low-voltage environments can be avoided. Accuracies of TCs are usually between 1%-3%. The accuracy mostly depends on the material consistency of the wire alloy and how accurate the cold junction is.

As the measurement devices (voltmeters, DMMs, etc.) have copper input terminals, only copper wire is to be used from the thermocouple connection to the

measurement device. Normally. If another alloy (tin, aluminum, etc.) are used, they introduce another thermocouple into the measurement.

To avoid problem, the voltmeter in a TC should be sensitive and accurate enough for the low-voltage signals. Shielding of TC is also necessary to prevent external noise.

### **2.3.2.2 Resistance Temperature (Thermal) Detector (Device):**

Resistance temperature detector (RTD) sensor is very accurate in the detection of temperature. The principle behind RTD is that the resistance and the temperature are proportionally related. Platinum is typically used in the construction of RTD. RTDs can measure quite a wide range of temperature between  $-270^{\circ}\text{C}$  to  $+850^{\circ}\text{C}$ .

As an RTD needs a current source to function, it also produces heat in the resistive element. This results into measurement error in the temperature measurements, which can be calculated by the equation 2.7:

$$\Delta T = P_g * S_e \quad (2.7)$$

where,

T is the temperature ( $^{\circ}\text{C}$ )

$P_g$  is the power generated (milliwatt)

$S_e$  is a constant, the ratio of temperature and power ( $^{\circ}\text{C}/\text{milliwatt}$ )

In a two-wire RTD, current is forced through it and the resulting voltage is measured. The main problem of this simple RTD is its measurement error as the lead resistance is part of the measurement.

In a three-wire RTD of the Figure 2.19, a third wire compensates for the lead resistance. This needs a three-wire compensating measurement unit. Alternatively, the contribution of the third wire is measured and subtracted from the overall measurement.

In a four-wire RTD, the current is forced on one set of wires and the voltage is measured on the other set. Four-wire RTD fully compensates for the lead resistance. The voltage is not measured at the same point as the source current. It

is measured at the resistive element. This means that the lead resistance is not part of the actual voltage measurement and hence the error is eliminated.

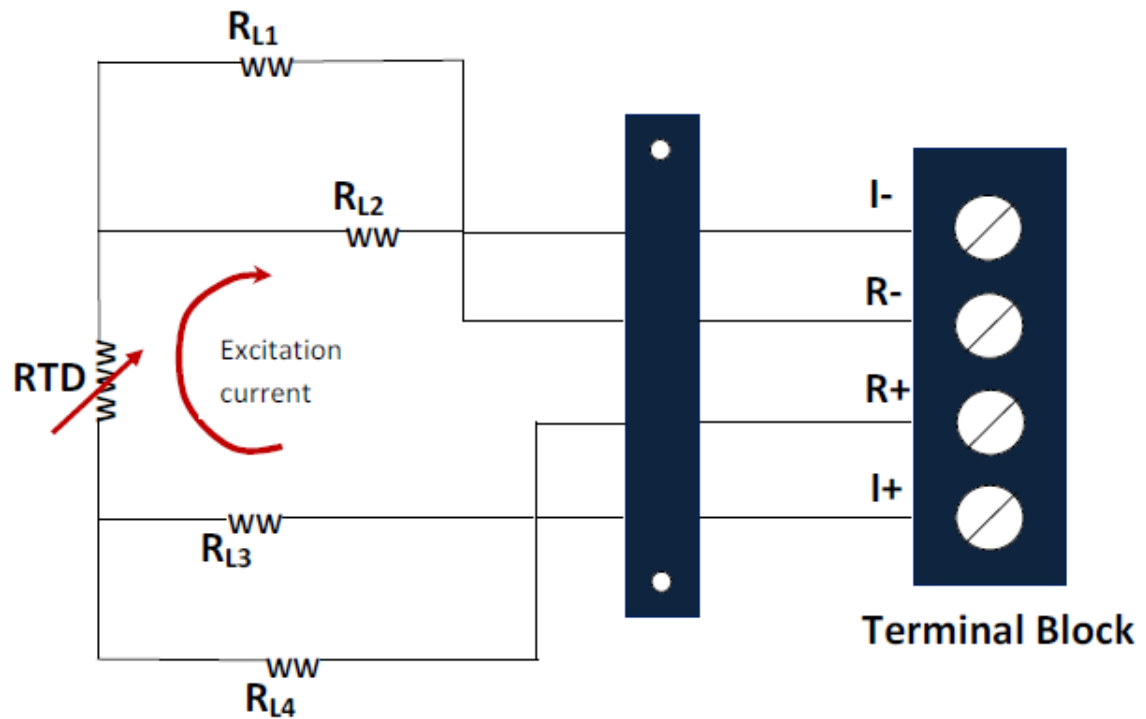


Figure 2.19 Four wire RTD connection [37]

RTDs are quite stable and very accurate compared to other temperature measurement devices.

Compared to thermocouples and thermistors, RTDs are quite expensive. RTDs also need a current source. RTDs have a small  $\Delta R$  against the temperature range; e.g. for the change of one degree Celsius, RTD change would be around  $0.1\Omega$ . Self-heating of the RTD could cause measurement inaccuracy, which is eliminated by using the four-wire RTD.

### 2.3.2.3 Thermistor:

Thermistor is another temperature sensor, which is also widely used in the industry. Similar to RTD, a thermistor changes resistance as temperature changes.

The resistance in thermistor can be directly or inversely proportional to the temperature; i.e. the resistance increases or decreases when the temperature increases or decreases. Thermistors are more non-linear than RTDs and hence also need a correction factor. The Stein-Hart equation is used to find the approximate values from individual thermistor curves, equation 2.8:

$$\frac{1}{T_k} = a_1 + b_1 \ln(R_t) + c_1 [ \ln(R_t) ]^3 \quad (2.8)$$

where,

$T_k$  is degrees (K)

$R_t$  is the thermistor resistance (ohms)

$a_1$ ,  $b_1$ , and  $c_1$  are curve fitting constants found from a calibration process.

#### **2.3.2.3.1 Self heating effect:**

Flowing current in a thermistor produces heat. This generated heat raises the temperature of the thermistor higher than its environment. If proper correction is not made, this electrical heating would cause very high error in the measurement of the temperature of the environment. On the other hand, this electrical heating effect itself can be exploited:

Thermistor power input is based on standard Ohm's law, equation 2.9:

$$P_E = V_t I \quad (2.9)$$

where

$P_E$  is the electrical input power (W)

$I$  is the current (A)

$V_t$  is the voltage drop across the thermistor (V)

This input power after being converted to heat energy is transferred to the surrounding environment, which can be expressed by Newton's law of cooling as in Equation 2.10:

$$P_T = K_d \{T(R) - T_0\} \quad (2.10)$$

where,

$P_T$  is the power converted to heat (mW)

$T(R)$  is the temperature of the thermistor as a function of its resistance  $R$  ( $^{\circ}\text{C}$ )

$T_0$  is the surrounding temperature ( $^{\circ}\text{C}$ )

$K_d$  is the dissipation constant in milliwatts/Celsius. It is a measure of the thermal connection of the thermistor to its surroundings.

In equilibrium condition, equation 2.11:

$$P_E = P_T \quad (2.11)$$

If the voltage is kept constant and with  $I = V_t / R$ , the equilibrium equation can now be solved for the ambient temperature as a function of the measured resistance of the thermistor, equation 2.12:

$$T(R) = T_0 + \frac{V_t^2}{K_d R} \quad (2.12)$$

Thermistors use just a standard two-wire measurement method and hence is very simple. As they are made very small, their response to temperature changes is very fast. They have higher sensitivity compared to that of RTDs.

Thermistors need linearization owing to their non-linear properties. Thermistors cover only a limited temperature range. They are not as strong as TCs and RTDs. Thermistors are semiconductors and hence they have de-calibration problems, especially at elevated temperatures. Thermistors also need a current source. Similar to RTDs, they have self-heating characteristics. Though constant DC is typically used as the test current, a pulsed DC current has the reduced self-heating effects as because the current is applied for only a short period of the measurement cycle.

Thermocouple, RTD, and thermistor are commonly used as temperature sensors. Comparisons of these three sensors are shown in Table 2.4. Thermocouples have the widest temperature measurement range and they are used for flue gas temperatures, coolant temperatures and other heating systems. Thermistors are commonly used in the low temperature range like in human environment (from  $0^{\circ}\text{C}$  to  $30^{\circ}\text{C}$ ), e.g. freezers. They are often used for measuring the temperature of the motor windings. On the other hand, as RTD's are very accurate, they are very

useful in the application of calibration and standards. Each sensor has its own merits and demerits. Hence, it is important to select the right sensor for the application so that the accuracy and the reliability of the temperature measurement can be obtained.

	<b>Thermocouple</b>	<b>RTD</b>	<b>Thermistor</b>
Range	-200 <sup>0</sup> to 2000 <sup>0</sup> C	-250 <sup>0</sup> to 850 <sup>0</sup> C	-100 <sup>0</sup> to 300 <sup>0</sup> C
Accuracy	>1 <sup>0</sup> C	0.03 <sup>0</sup> C	0.1 <sup>0</sup> C
Thermal response	Fast	Slow	Medium
Cost	Low	High	Low to moderate
Stability	Low	High	Medium

Table 2.4 Comparison of thermocouple, RTD and Thermistor [38]

Thermocouples are widely used to measure the temperature of the cylinder liner. But the temperature rise of the cylinder liner takes place after the scuffing already started and might have already damaged the cylinder liner and piston ring materials. Without close scrutinizing and analyzing the temperature profile, onset of scuffing detection cannot be determined. No such study was so far done.

### 2.3.3 Eddy current method:

Eddy current sensors measure distances, displacements, or positions of any electrically-conductive target. Eddy current sensors are ideally suited for applications in harsh industrial environments (pressure, dust, temperature). They are of high precision and resolution, non-contact and wear-free, insensitive to dirt, suitable for fast applications and very good price/performance ratio. Their measuring range of displacement is between 0.5 to 15mm. In special cases, the range could be as high as 0.5 to 80mm. [39]

The excellent immunity to severe environmental conditions of the eddy current measuring technique makes it possible to use this type of displacement sensors in running combustion engines. Lubricating oil, fuel or combustion gas in the measuring gap or next to the sensor have a negligible effect on the measuring

results even under the most difficult conditions. A noncontact sensor system allows to measure very fast changes in displacement (100,000 Hz) without affecting the target and no wear. Eddy current displacement sensors are installed at various positions in the internal combustion engine.

As the eddy current sensors are small, they can be used in the field condition. Examples of measurements already being carried out are valve lift, needle lift, breathing of the cylinder head, lubrication gap on the cylinder and piston secondary movement. The oil film thickness for combustion engines describes the gap and thus the quantity of oil between piston and cylinder wall – sometimes a determining factor for smooth operation and durability. As the oil film can only be integrated and measured in the firing condition, it is extremely difficult to manufacture sensors for these environmental conditions and also find space for them. The smallest, with a 2.4mm external diameter, is integrated into the cylinder wall and ground to its shape. It measures the distance from sensor to piston (the space available for the engine oil). [39]

A device for diagnosing wear on the sliding surface of a piston ring on a piston which is reciprocating inside a cylinder was applied in diesel engines and compressors, etc. A through-hole was bored in the cylinder wall to extend from the exterior to the interior, and an electric displacement sensor such as, for example, an eddy current type displacement sensor, was inserted into the through-hole inwardly toward the cylinder. The displacement sensor was utilised to measure a difference in an amount of wear between one piston ring coated with a wear resistant material and another piston ring without wear resistant material coated thereon, and its initial data and data were collected after use and were computed, which potentially permits an operator to diagnose the wear on the piston rings based on the change in thickness of the wear resistant material in use. [40]

The studies above suggest that eddy current sensors can detect the oil film thickness, roughness or the wear of the piston ring surface and can be a source of early detection of scuffing. However, no such study was done on large slow speed marine engines. Without proper trend analysis and monitoring the rate of increased



roughness, it is difficult to detect the onset of scuffing through eddy sensors. Nevertheless, monitoring the trend of the surface texture through eddy sensor has some advantage over the temperature sensors.

#### 2.3.4 Acoustic emission method:

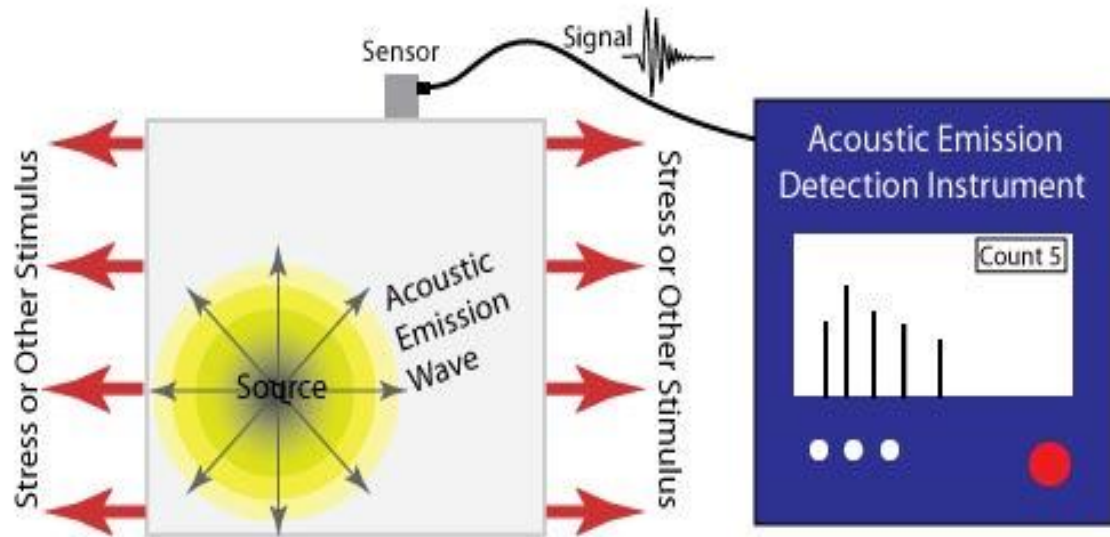


Figure 2.20 Acoustic emission principle [148]

The waves travel as compression, shear or surface waves. The stress waves generated are generally high frequency waves. Measurement of these high frequency waves avoids low frequency background noise (Vibration of structure).

Acoustic emission (AE) is referred to as the transient, high frequency elastic waves in the range of 0.1 to 1 MHz, which occur as the result of a rapid release of strain energy within or on the surface of a material [41]. These waves are also referred to as stress waves and run through the body at acoustic speeds.

Any form of atomic level material dislocations can generate AE and it has been claimed that displacement as small as one thousandth of an atomic radius can produce well-distinguished AE signals [42]

Typical sources of AEs include plastic deformation, micro-fracture, fluid flows, wear, sliding contact (friction) and mechanical impact. These generated waves can

be measured on the surface of interest by using AE sensors (typically piezoelectric sensors) and data acquisition system. AET (acoustic emission technology) offers the advantage of earlier failure detection due to its inherent higher sensitivity as compared to the low frequency vibration signals and other similar techniques. Hence this technique provides an opportunity to gain a deep understanding of the behavior of interacting materials in areas that are not easily accessible, as in the case of a piston ring and cylinder wall/ liner.

Since AE sensors can be located externally, the technique is inherently non-intrusive. Furthermore, the AE signals are associated with the actual operating and degradative processes, whereas other monitoring techniques typically measure the symptoms of degradation and are often intrusive [43]. Such are the benefits of AE monitoring that research into various applications has accelerated in recent years and commercial AE based monitoring systems have become established in a number of engineering disciplines [42].

AE has been used to assess engine condition. Gu and co-workers have performed a thorough investigation [44, 45, 46, 47], particularly of injector operation and combustion. They found that better quality diagnostic information was contained in the higher frequency band, 10 to 50 kHz, than at frequencies below 10 kHz. In the uppermost band they identified the combustion and power related signal source.

Various signal sources of AE in a running engine overlap, which makes it difficult to study. Recent works have tried to decompose the signal into individual source [44, 47].

Kimura et al [48] analysed sound generated in the range of 0.1 to 20 kHz from a medium speed, six-cylinder diesel engine. Frequency spectra were used in conjunction with a neural network in order to classify signals. Leaking exhaust gas and misfire of cylinders were successfully detected. Autar [49] detected valve leakage through the analysis of inlet manifold sound levels. Kawai et al [50] proposed a method whereby valve clearance could be estimated to an accuracy of 0.1mm from wavelet analysis of engine acoustic.

Koike et al [51] described the use of an ultrasonic microphone for non-contact detection of abnormal engine bearing wear due to oil-film deterioration. For this work, a microphone with a centre frequency of 80 kHz was used. The ultrasonic activity increased as the oil supply to the bearing was stopped and the progressive increment of ultrasonic activity was related to the scuffing.

The AE was found to be proportional to the wear rate of parts under study. The AE was found to be helpful in detecting different failure modes and fault conditions of the systems involved. The frequency contents of the AE data was correlated to different failure modes and surface conditions in some of the available literature.

The prior work in the field of monitoring IC engines using AE indicates its effectiveness and higher sensitivity as compared to methods like vibration based condition monitoring. EL-Ghamry et al. [52] explored the use of AET as an indirect method for measuring cylinder pressure in a diesel engine. The RMS AE signal was found to be well correlated with the pressure signal in the time and frequency domain.

Nivesrangsan et.al.[53] in their study of the mapping of AE signals and wave propagation in a diesel engine, showed the importance of locating the sensors close to the source. They also discussed the interaction in detail between the different cylinders of an engine and analysis of the same using the source location technique. The frequency contents of the signals were observed to range from 100 kHz to 400 kHz. The lower band of frequency ranging from 100 – 250 kHz was attributed to the mechanical activity of moving parts and the higher band ranging from 250 – 400 kHz was observed to be related to the fluid flow activity like fuel flow from injectors and gas flow.

Haq and Tamizharasan [54] studied application of AET to monitor piston ring wear in internal combustion engines. The study showed that the ring down count and RMS voltage were the effective indicators of the wear of piston ring.

Douglas et al. [55] used AET in their tribological studies of the interaction between piston ring and cylinder liner in diesel engines. Their work discusses the potential

AE source mechanisms of asperity contact, lubricant flow and gas blow-by etc. Various tests on motored and in-service small diesel engines and large, 2-stroke, marine diesel engines were done, where the effects of engine speed, load and lubrication on AE source emission was studied. It was found that the AE activity to be proportional to the speed of the engine. The possible AE sources are quoted as boundary lubrication and elasto-hydrodynamic lubrication of piston rings. The compression ring asperity contact during piston reversal was also found to be present in the collected data. Their study highlights the importance of AE as a non-intrusive technique for condition monitoring of engines.

AE analysis has proven to be well suited for monitoring crack initiation and propagation [56]. This has been ascertained through applications as varied as the monitoring of cables in suspension bridges [57] and of the structural integrity of historical statue [58].

The first published work concerning AE acquisition from engine was reported by West et al [59, 60]. However, these works made no attempt to understand the AE generated during engine operation. Nevertheless, it was recognized that certain aspects of engine operation could result in AE generation [59].

Gill et al [61] first reported on the possibility of engine diagnostic via AE measurements. They showed that events were generated from combustion, or combustion-related processes as well as valve activity of the cylinders of a four stroke engine.

Gill et al [62] further studied to investigate more detailed raw AE signals acquired from a fuel injector body of a diesel engine.

Many other researchers investigated AE relating to injection and combustion processes [63-70]. Berjger [64] confirmed that operation of a fuel injector without combustion was indeed a source of AE. Method of time-domain analysis of windowed injection/combustion event was used to identify operating conditions over varying load by Frances et al [67].

Chandroth et al [68] researched on data acquisition system with AE measurements and in-cylinder pressure data for the detection of combustion related faults in a small four stroke engine, which was further enhanced with neural network by Sharkey et al [69].

El-Ghamry et al [70] described a technique whereby the in-cylinder pressure trace could be reconstructed from the AE signal over the compression/expansion period.

Fog et al [71, 72] managed to detect exhaust valve leakage in a large, two stroke diesel engine using AE measurements and found it more effective than acceleration, in-cylinder pressure and temperature measurements.

El-Ghamry et al [73] investigated the usage of AE measurement for the detection of cylinder head gasket leak of a small four stroke engine.

Nivesrangsan et al [74-77] mapped AE events within the cylinder head of a small HSDI diesel engine. They introduced spatial reconstitution technique and source location technique [77] of the events using multi-sensor arrays.

Pontoppidan and co-workers [78-83] have investigated AE monitoring of the piston ring-pack and cylinder liner interface. Techniques such as 'event alignment' were also developed to account for variations in the timing of injection events due to load changes [86-88]. Statistical techniques such as ICA (independent component analysis) and PCA (principal component analysis) were used to investigate the data and it was found that changes in lubricating oil condition could readily be identified [82, 83].

Sigurdson et al [79] showed that AE generation was greater during operation with no lubricant supply than for normal conditions.

The possibility of using AE to study tribological behavior has been investigated and developed in a numerous published works covering various applications.

Precursors to more detailed studies was the initial understanding that AE arises from frictional processes that occur during manufacturing operations such as turning, grinding and forming [84-88]. Fundamental friction and wear characteristics

have been investigated on standard wear testing laboratory equipment [89-102]. These have identified systematic relationships between AE activity and the various parameters which govern friction and wear.

McBride et al [90] investigated AE generation during rotation of a steel cylinder loaded against a stationary steel ball with both lubricated and unlubricated contact considered. Boness et al [91] used the similar set up and found that AE generation was greater from unlubricated contact than the lubricated contact.

Other researchers [93-94] have verified the capability of using AE measurements to detect changes in wear regimes during unlubricated sliding. Jiaa and Dornfeld [93] studied long-distance unlubricated sliding using a pin-on-disk set-up.

Hamchi and Klamecki [94, 95] investigated the use of AE monitoring to discriminate between different wear mechanisms acting at an unlubricated pin-on-disc interface with various load and speeds.

Lingard and Ng [97] investigated AE generation during unlubricated sliding of a rotating disc loaded against a stationary disk. A range of disk materials, loads and speeds were investigated with torque friction measurements and wear scar dimensions recorded to aid interpretation of the AE data.

AE monitoring was applied for the problematic interfacial conditions, such as monitoring of hard disc drive magnetic storage devices [103-121] and also industrial applications such as gear box, mechanical seals and bearings [122-135].

The source of AE at ring/ liner interface may be due to many processes like asperity contact, blow by and hydrodynamic lubrication. Asperity contact due to boundary lubrication and hydrodynamic lubrication of compression rings are the source of AE for ring-liner interaction. The piston rings operate in a range of hydrodynamic to mixed lubrication as the piston speed varies considerably in a cycle. The compression rings have elasto-hydrodynamic lubrication away from dead centers, with maximum effect at the mid stroke of the piston. The above literature studies on AE emission have mostly focused on its relationship with the events in the combustion and not linked the AE emission and scuffing.

#### **2.4. Summary of literature review and the need of the research:**

In recent years, various studies were made to discover the causes and effects of scuffing and numerous steps were taken in design, operation and delivery of lubricants to prevent scuffing, as discussed under section 2.1 and 2.2. Yet, scuffing problem persists. Once scuffing is initiated, it becomes extremely difficult to contain. Scuffed debris from an affected unit is carried over to the other units through the common underpiston scavenge space. In that sense, it is very contagious. All cylinder liners and piston rings then experience this severe irreversible wear within a short time and, for this reason, often it is known as sudden wear syndrome. Hence, the detection of scuffing at very natal stage or as a precursor plays a vital role in the prevention of scuffing.

While the improved design and operation have not been fully successful to combat the scuffing incidents, early detection of scuffing became very important. Early detection of scuffing or determining scuffing precursor, till today, remains as a major challenge. Many of the online condition monitoring techniques used for piston and cylinder wall interaction, for example oil-film electrical capacitance, optical/ laser oil film thickness and floating bore friction measurements are intrusive in nature and require considerable modifications to the engine. These methods are more suitable for laboratory based experiments and do not have wide spread application in industry.

Lubrication modeling, cylinder liner temperature, eddy current and acoustic emission techniques, measurement and analysis on the contrary are comparatively non-intrusive methods for condition monitoring, without affecting the performance or reliability of the engine and also incorporating little or no engine modifications. Nevertheless, none of these methods is fully understood in terms of their sensitivities, accuracies, costs and reliabilities. Each of them has its merits and demerits as discussed under section 2.3. Moreover, tribological studies were very much limited to high and medium speed power-plant and automobile engines and ,other than a very few articles, no major study of scuffing was done on slow speed marine engines. So far, no research was based on the comparison of the

detection methods of scuffing of slow speed marine engines encompassing the reasons and solutions of such potential hazard.

Hence, it is necessary to understand scuffing from its fundamental, its causes and solutions. It is then necessary to model and experiment various methods of detection prior to recommending the best possible detection method, which would serve as a precursor of scuffing.



## Chapter 3. Theory and Modeling

---

In this chapter, theory and modeling of four detection methods, namely (1) tribology analysis, (2) temperature, (3) eddy current and (4) acoustic emission analysis are described.

### **3.1 Theory and modeling of tribology method:**

Onset of scuffing can be detected through understanding and simulating the tribological condition of piston ring and cylinder liner. To form the appropriate tribological model for determining the onset of scuffing requires understanding of surface roughness, oil film thickness, viscosity-shear stress relationship of lubricating oil. Reynold's equation of hydrodynamic lubrication serves as the base for tribology modeling. The modeling consists of the balance between the hydrodynamic lubricating oil pressure and the gas pressure on piston ring from the combustion chamber, which is described under section 3.1.13. The full modeling and the simulation and its usage can be found in the attached Excel file named, 'Tribology model' and in Appendix 2.

#### ***3.1.1 Theory of piston ring tribology:***

As long as the criteria of hydrodynamic lubrication are satisfied, scuffing cannot occur. When the hydrodynamic criteria remain unsatisfied and the oil film between the rubbing surfaces is insufficient to maintain separation of the asperities of the surfaces, boundary lubrication takes place. When the lubricants are absent, asperity contacts take place and plastic deformation or full blown scuffing takes place. Contributing factors to hydrodynamic and boundary lubrication conditions are discussed below.

##### ***3.1.1.1 Entraining velocity:***

The piston ring and a cylinder liner of an engine is a good example of a dynamically loaded bearing. In each cycle, the load varies rapidly and substantially. The entraining velocity varies in a roughly sinusoidal manner as shown in the Equation 3.1 of the Figure 3.1.

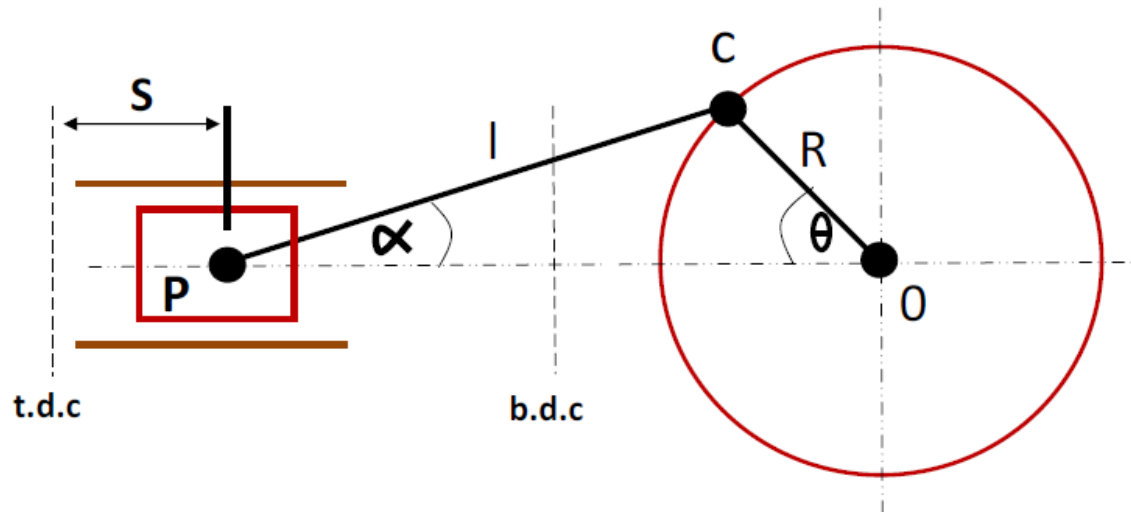


Figure 3.1 Crank mechanism

$$U = R\omega \left[ \sin\theta + \frac{1}{2} \frac{R}{l_c} \sin 2\theta + \dots \right] \quad (3.1)$$

where,

U is the piston velocity (m/s)

R is the crank radius (m)

$\omega$  is the angular velocity of crank (rad/s)

$\theta$  is the crank angle from TDC ( $^\circ$ )

$l_c$  is the connecting rod length (m)

The entraining velocity reduces to zero at the top and bottom dead centre position as the value of  $\sin(0)$  and  $\sin(180)$  is equal to zero.

The acceleration of the ring of Equation 3.2 has the impact on the phenomenon of ring lift:

$$f = R\omega^2 \left[ \cos\theta + \left( \frac{R}{l} \right) \cos\theta + \dots \right] \quad (3.2)$$

where,

f is the piston acceleration ( $\text{m/s}^2$ )

### 3.1.1.2 Surface roughness:

The typical roughness, i.e. the amplitude between peaks and valleys of all engineering surfaces are about 1µm. The profile of rough surface is most of the time random and a number of techniques and parameters have been developed to characterise surface topography, among which the statistical surface parameters is commonly used.

### 3.1.1.3 Characterisation by statistical parameters:

Real surfaces are difficult to define and in order to describe them at least two parameters are needed, one describing the variation in height (height parameters) and the other describing how height varies in the plane of the surface (spatial parameter). Height characteristics are described by parameters such as the centre-line average or roughness average (CLA or  $R_a$ ), Figure 3.2, Equation 3.3; root mean square roughness (RMS or  $R_q$ ), Figure 3.3, Equation 3.4 and many others.

Roughness average (CLA or  $R_a$ ):

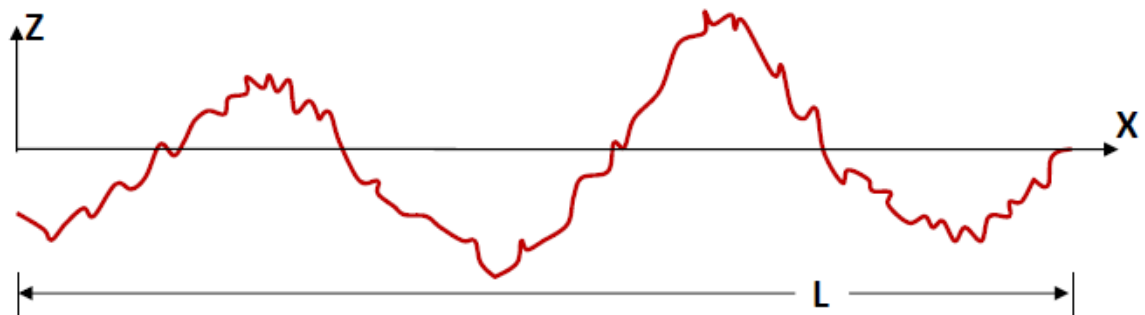


Figure 3.2 Roughness average (centre line average)

$$R_a = \frac{1}{L} \int_0^L |z| dx \quad (3.3)$$

where,

L is the sampling length (m)

Z is the height of the profile along 'x' (m)

Root mean square roughness (RMS or  $R_q$ ):

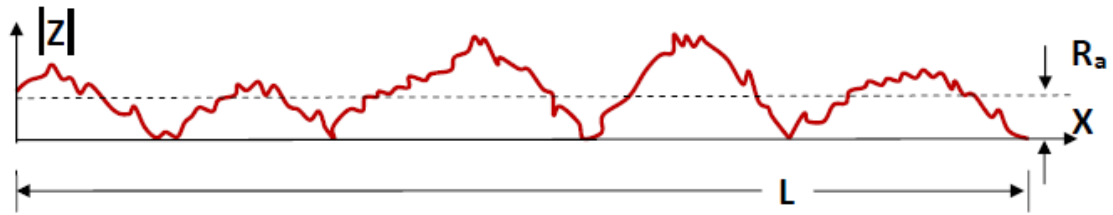


Figure 3.3 Root mean square roughness (RMS or  $R_q$ )

$$R_q = \sqrt{\frac{1}{L} \int_0^L z^2 dx} \quad (3.4)$$

$R_a$  represents the average roughness over the sampling length and one of the main disadvantages of this parameter is that it can give identical values for surfaces with totally different characteristics. Since the  $R_a$  value is directly related to the area enclosed by the surface profile about the mean line, any redistribution of material has no effect on its value.

This problem is illustrated in the Figure 3.4, where the material from the peaks of a 'bad' bearing surface are redistributed to form a 'good' bearing surface without any change in the  $R_a$  value.

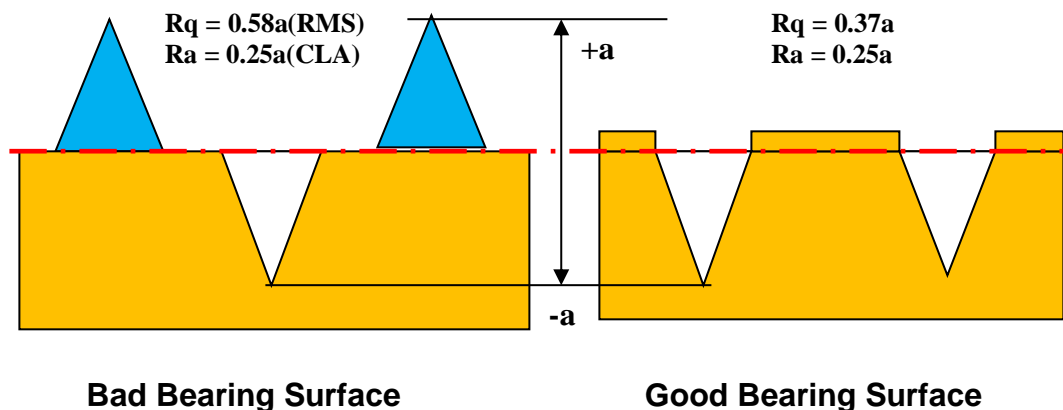


Figure 3.4 Effect of averaging on  $R_a$  value

The said problem of averaging of  $R_a$  method can be addressed by applying the RMS parameter as it is weighted by the square of the heights. This makes it more sensitive than ' $R_a$ ' with regard to the deviations from the mean line.

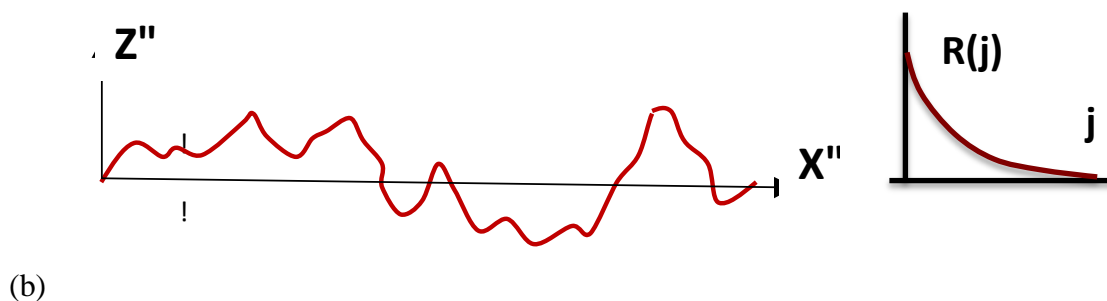
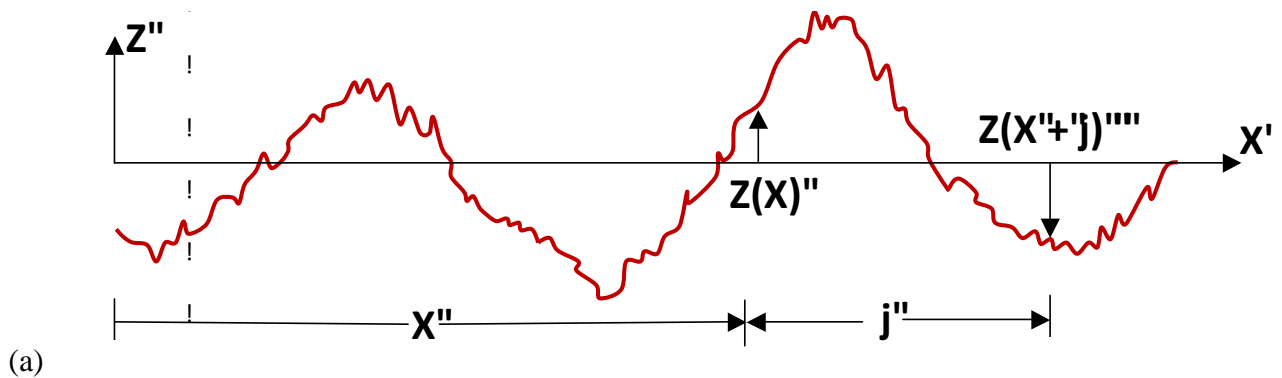
The relationship between rms and CLA (centre line average) values is given by the following Equation 3.5,

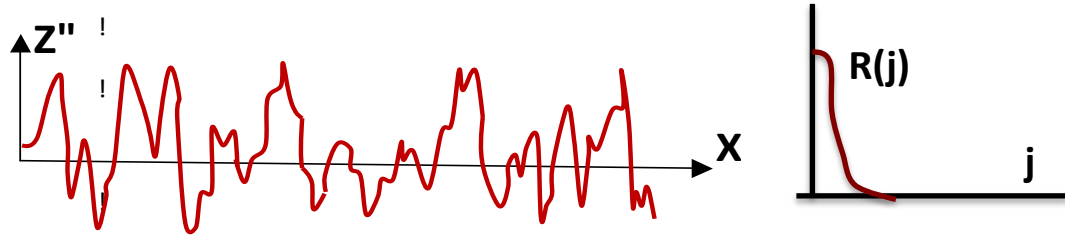
$$\sigma_{RMS} = 1.3\sigma_{CLA} \quad (3.5)$$

#### 3.1.1.4 Spatial characteristic of real surface:

Spatial characteristics of real surface can be explained by a few statistical functions. For two surfaces of same height parameters, their spatial arrangement can be different. Because of different spatial arrangements, their wear and frictional behaviour can also be different. The autocovariance function (ACVF), Figure 3.5 and Equation 3.6 or its normalized form the autocorrelation function (ACF), Figure 3.6 and Equation 3.7 are mostly used to describe spatial arrangement of a surface. By observing their decaying properties, these functions are used to differentiate between spatial surface characteristics of one from the other.

Autocovariance function (ACVF) or  $R(\tau)$ :





(c)

Figure 3.5 Auto-covariance function

$$R(\tau) = \lim_{L \rightarrow \infty} \frac{1}{L} \int_0^L z(x) z(x + \tau) dx \quad (3.6)$$

Autocorrelation function (ACF) or  $\rho(\tau)$  :

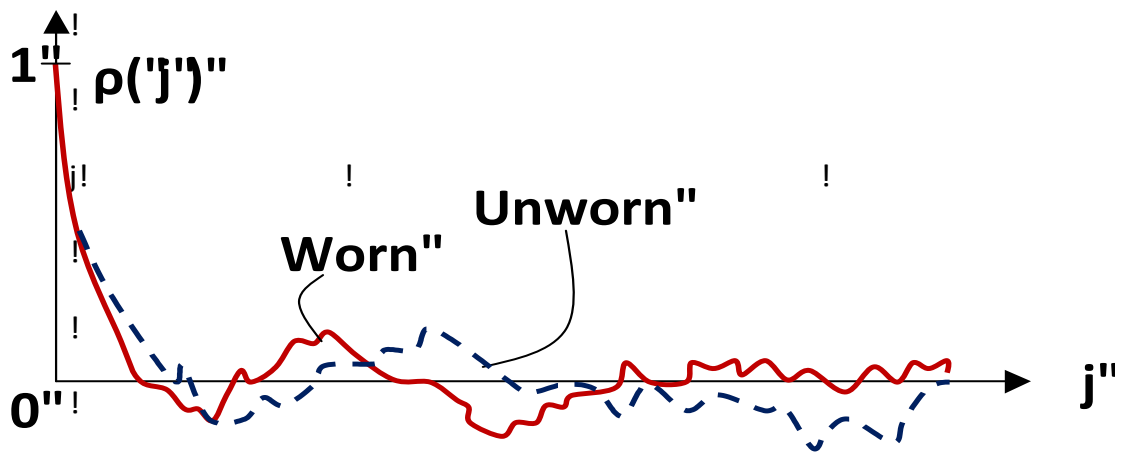
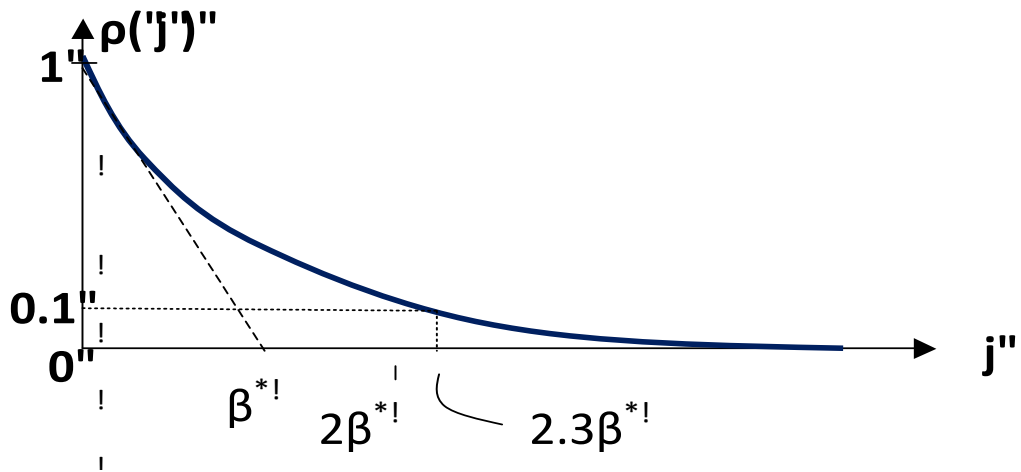


Figure 3.6 Auto-correlation function

$$\rho(\tau) = \frac{R_\tau}{R_q^2} \quad (3.7)$$

or, often used as  $\rho(\tau) = e^{-\tau/\beta^*}$  (3.7a)

where,

$\tau$  is the spatial distance (m)

$\beta^*$  is the decay constant of the exponential autocorrelation function (m)

The problem of autocorrelation function is its inadequate sensitivity, because of which they are not used to find changes in the topography of the surface during wear. Wear takes place almost at all wavelengths. Hence, the surface topography changes are hidden by ensemble averaging. Owing to this, the autocorrelation functions for worn and unworn surfaces can look almost similar as shown in the Figure 3.6 above.

The above stated problem can be addressed by applying a structure function, Figure 3.7 and Equation 3.8:

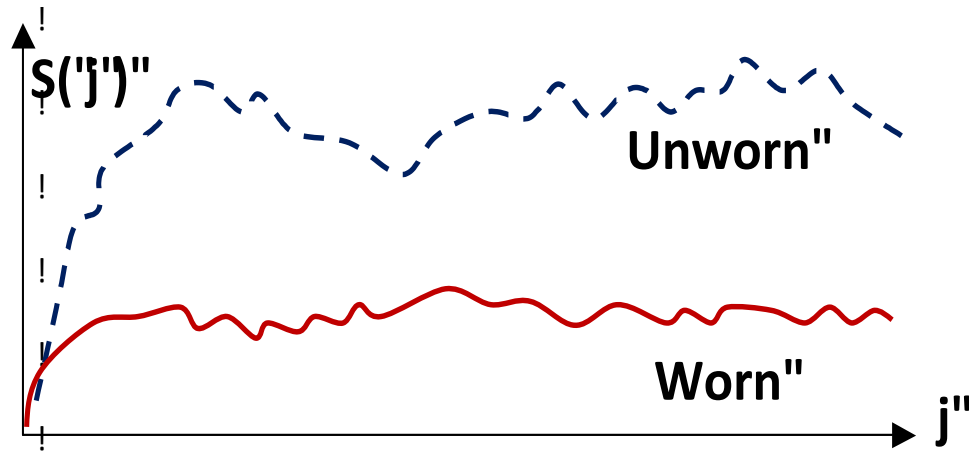


Figure 3.7 Structure function

$$S(\tau) = \lim_{L \rightarrow \infty} \frac{1}{L} \int_0^L [z(x) - z(x + \tau)]^2 dx \quad (3.8)$$

Structure function and autocorrelation function contain almost the same amount of information. However, the surface characteristics are more accurately described by the structure function.

### 3.1.1.5 Optimum surface roughness:

Surface roughness of engineering components determines the ability of the surfaces to support load. High or very low values of  $R_q$  can support only light loads, whereas, intermediate  $R_q$  values can support much higher loads. This is shown in the Figure 3.8 below. The optimum operating region under 'boundary lubrication' is based against the height and spatial surface characteristics. If surfaces are too rough then excessive wear takes place and in extreme case is followed by seizure. On the other contrary, surface failure may take place quite fast at very light load if the surfaces are too smooth, i.e., when  $\beta^* < 2 \mu\text{m}$ , as the area of contact is large.

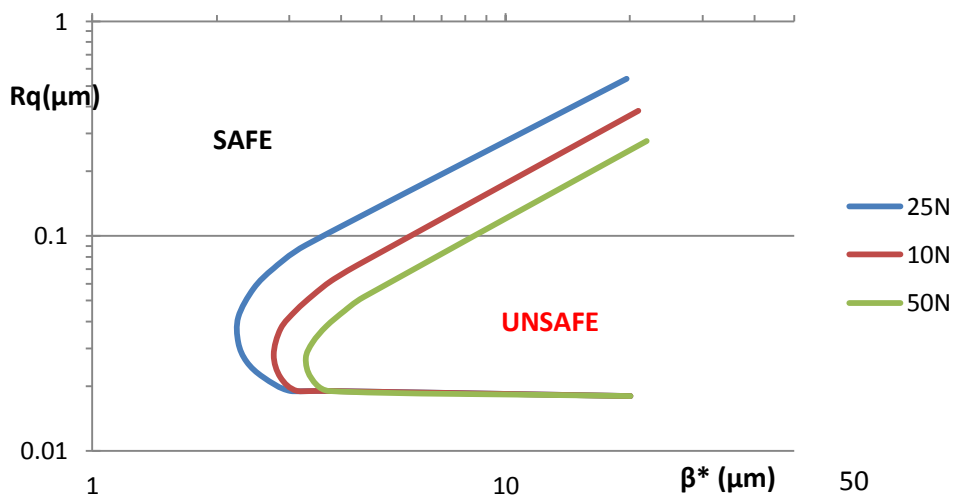


Figure 3.8 Optimum surface roughness diagram [153]

Typical roughness of piston rings and liners are listed in the table 3.1 below:

FINISH	Ra ( $\mu$ )
Engine cylinder liner (new)	10.0
Engine cylinder liner (in service)	0.50
Piston ring (new)	2.0
Piston ring (4000 hrs in service)	0.27

Table 3.1: Typical Surface finish of cylinder liner[153]



### 3.1.1.6 Composite roughness:

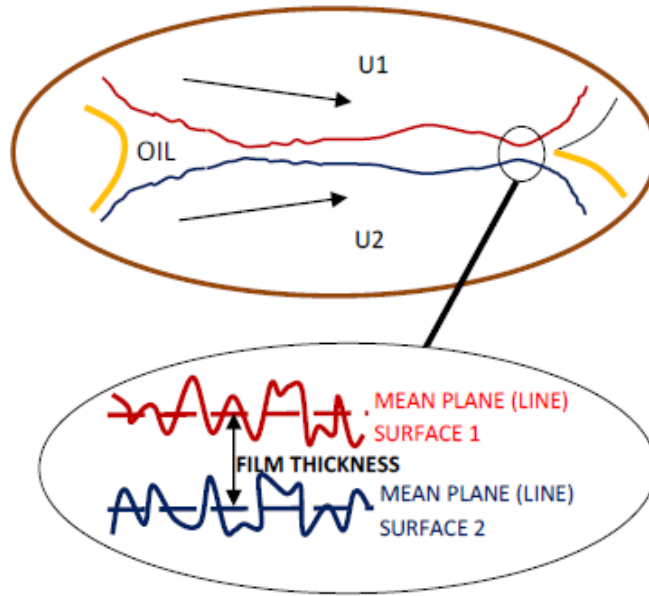


Figure 3.9 Composite roughness

The composite roughness of the two surfaces, Figure 3.9, can be calculated as the square root of the sum of the squares of the individual surface roughness, Equation 3.9 below.

$$\sigma = \sqrt{\sigma_1^2 + \sigma_2^2} \quad (3.9)$$

where  $\sigma_1$  [ $R_{q1}$ ] and  $\sigma_2$  [ $R_{q2}$ ] are the root mean square (rms) roughness values of the two surfaces.

Surface roughness is important in the consideration of hydrodynamic and elasto-hydrodynamic lubrication. One procedure adopted to determine the mode of lubrication is to assume that the bearing surfaces are perfectly smooth, to calculate the cyclic variation of film thickness and to relate the findings to the composite surface roughness of the ring face and cylinder liner. The ratio of calculated fluid film thickness to composite roughness is known as the specific film thickness, Lamda ( $\lambda$ ) ratio, Equation 3.10.

$$\lambda = \frac{h}{\sigma} \quad (3.10)$$

where 'h' is the calculated film thickness and ' $\sigma$ ' is the composite surface roughness.

If the  $\lambda$  ratio is greater than about 3, effective fluid film lubrication can be expected, whereas if it is less than unity conditions are akin to boundary lubrication. In the intermediate zone ( $1 < \lambda < 3$ ) a mixed lubrication regime will apply.

### 3.1.1.7 Specific film thickness:

Piston ring is subjected to hydrodynamic, mixed and boundary lubrication at different stages of the stroke owing to the film thickness between the cylinder liner and the ring, Figure 3.10.

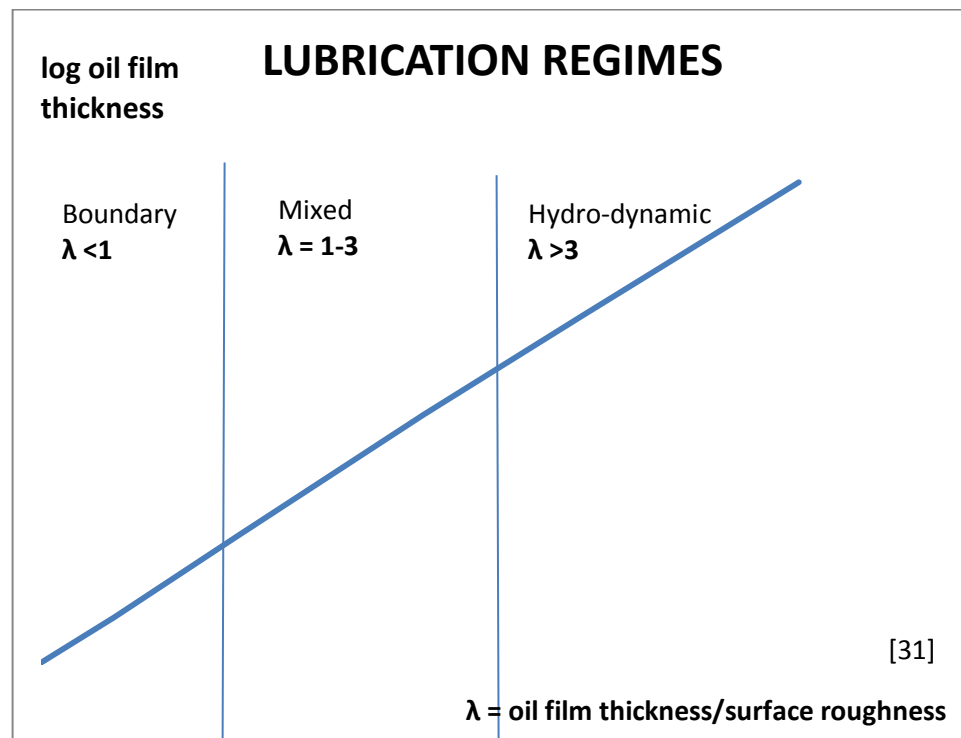


Figure 3.10 Lubrication regime

### 3.1.1.8 $\frac{\eta N}{P}$ diagram and oil film thickness:

The prerequisite of hydrodynamic lubrication is that oil of correct viscosity and in sufficient quantity is present at all times to fill up the clearance spaces of the bearings.

In hydrodynamic bearing lubrication, the formed oil wedge is a function of speed, load and oil viscosity. Under fluid film conditions, the oil film thickness increases if

the viscosity or speed increases. On the other hand, the oil film thickness decreases, if the load increases. The effects of viscosity  $\eta$ , speed  $N$ , and unit load  $P$  are combined and expressed in a single dimensionless factor called  $\frac{\eta N}{P}$  factor. The coefficient of friction in terms of  $\frac{\eta N}{P}$  can be shown by a curve as in Figure 3.11.

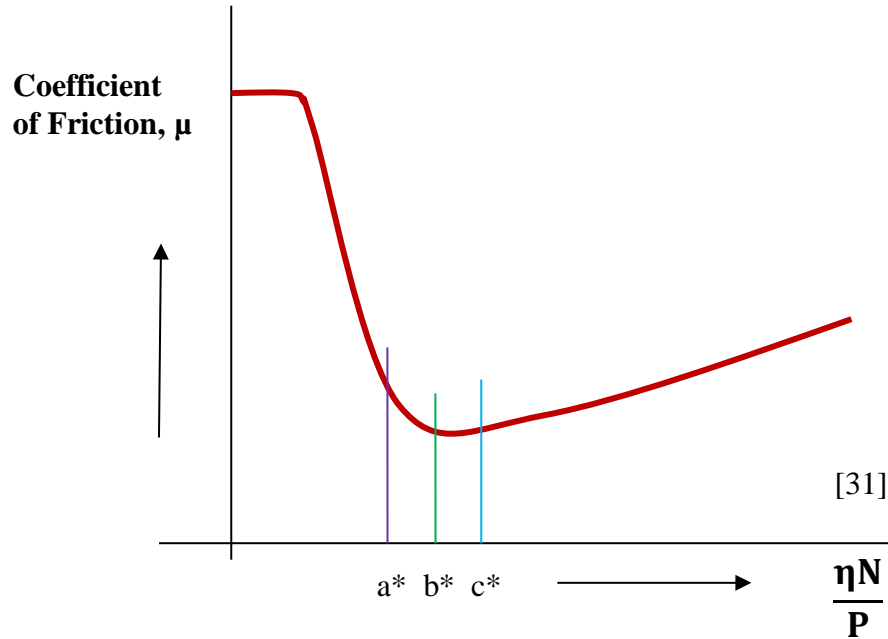


Figure 3.11 Effect of viscosity, speed, and load on bearing friction

For each hydrodynamic film bearing, there is a characteristic relationship between the coefficient of friction and the  $\frac{\eta N}{P}$ .

In the Figure 3.11, fluid film is present on the right hand side of the zone 'c\*'. On the other hand, boundary lubrication dominates to the left of zone 'a\*'. In this left side of zone 'a\*', the conditions do not allow the formation of fluid film and hence the coefficients of friction may reach very high and some degree of metallic friction and wear takes place.

In between the points 'a\*' and 'c\*', exists a zone, where the lubrication is considered as the mixed film lubrication. In this zone resides 'b\*', which is the minimum value of 'μ' corresponding to the  $\frac{\eta N}{P}$  value. When  $\frac{\eta N}{P}$  lies between 'b\*' and

'c\*', the friction is very low and it may be desirable to operate in this zone. However, the oil film in this zone may rupture for momentary change of load or reduction in speed. Hence, an adequate safety factor needs to be factored in the design so that the  $\frac{\eta N}{P}$  value resides on the right side of 'c\*'. The bearing safety factor is based on the ratio of the (operating  $\frac{\eta N}{P}$ ) and ( $\frac{\eta N}{P}$  at 'b\*'). A bearing safety factor in the order of 5 is commonly used.

In any operation, if the speed is increased, it will result in the increased  $\frac{\eta N}{P}$  and hence, the viscosity of oil may need to be decreased in order to maintain  $\frac{\eta N}{P}$  and  $\mu$  in the range of the design. On the other hand, if the load is increased, it will reduce the value of  $\frac{\eta N}{P}$ , and in this case, the viscosity of the oil will need to be increased in order to keep  $\frac{\eta N}{P}$  and  $\mu$  in the design range. The oil film thickness can also be directly related against  $\frac{\eta N}{P}$  as shown in the Figure 3.12.

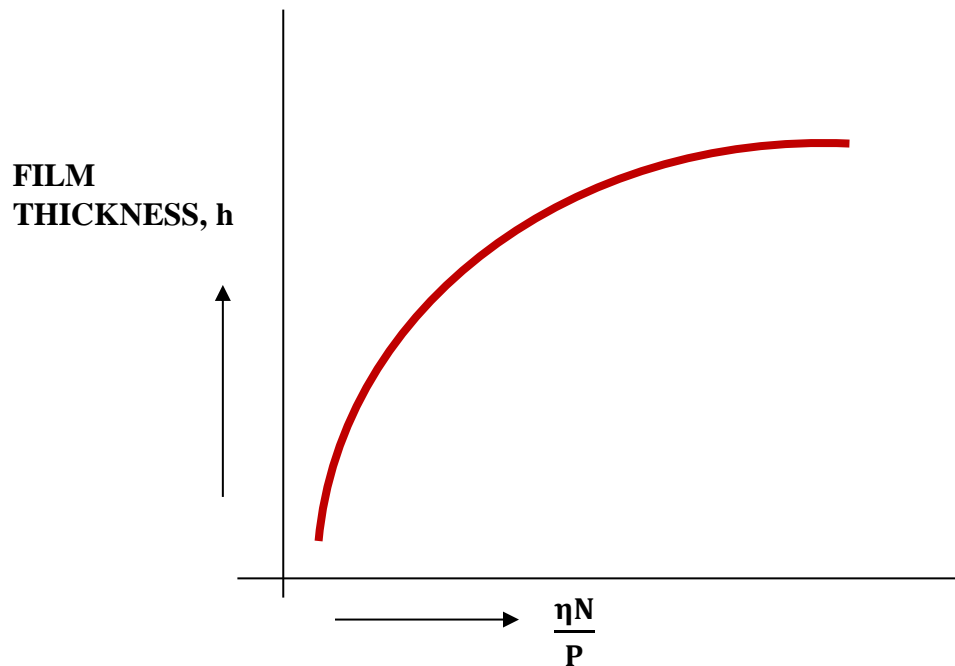


Figure 3.12 Effect of viscosity, speed, and load on film thickness [136]

The curve is typical of large, uniformly loaded, medium speed bearings. Adequate bearing safety factor will ensure the film thickness and will prevent the boundary lubrication i.e. metal to metal contact during normal variation in speed, load, and oil viscosity.

Although, the thickness of an oil film generated between two moving surfaces is a function of the oil viscosity, the relative speed and the load, in the case of the lubrication of cylinder liners and piston rings, the factors that most influence oil film thickness are viscosity and relative speed. Load has little effect in the reduction of oil film thickness once hydrodynamic lubrication is established. Hence, increased oil film thickness from increased load after tdc (where hydrodynamic lubrication begins) is observed in Figure 3.13. The relative effects of load on viscosity being such that a load increase of x100 is only equivalent to a viscosity decrease of 50%.

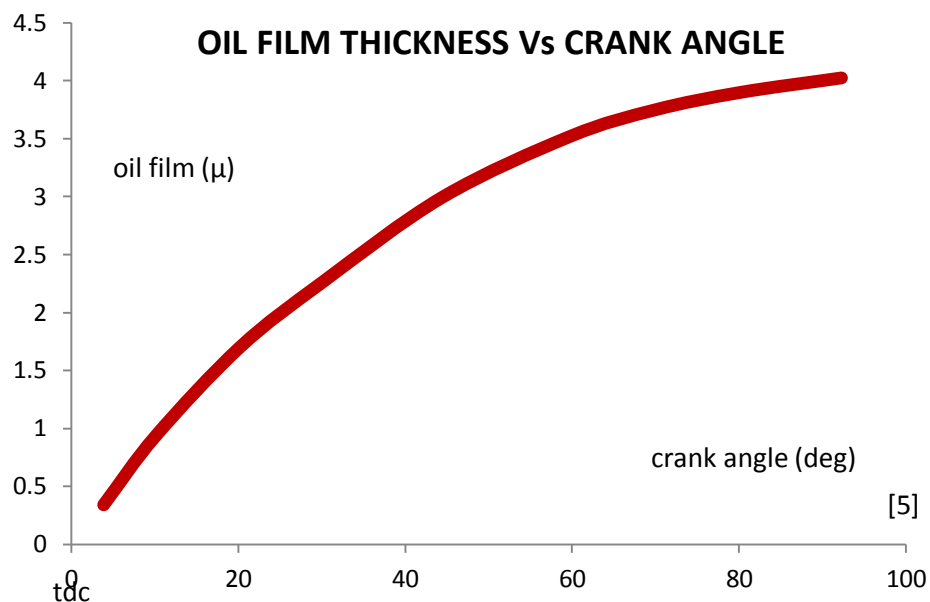


Figure 3.13 Oil film thickness against crank angle (source R W Allen, Castrol)

On the other hand, the typical result of oil film thickness from a series of measurements on the B&W test bed engine is shown in the Figure 3.14. Results are shown for the top ring at loads of 100% and 50%. Films are thicker on the compression stroke than on the expansion stroke and there is a clear load effect

with an almost doubling of minimum film thickness on the expansion stroke when the load is reduced. This can be explained as follows.

Around TDC, the piston speed is low which together with low oil viscosity (higher oil temperature) means that full hydrodynamic lubrication is not developed. These are the conditions for boundary lubrication where the load is shared between the lubricant film and the surface asperities. Under these conditions, small changes in viscosity result in large changes in load carrying ability and adhesive wear will take place once the conditions for boundary lubrication are established.

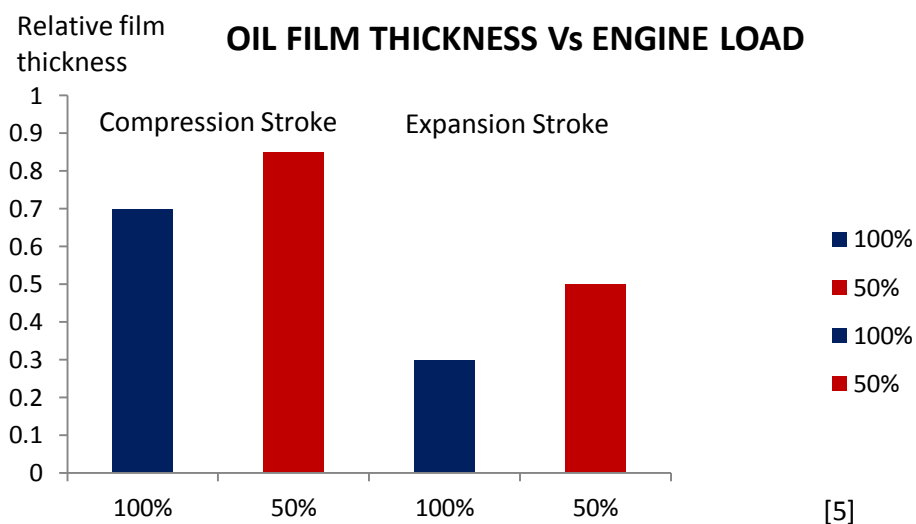


Figure 3.14 Oil film thickness on top ring at 2<sup>nd</sup> ring TDC position against engine load%

#### **3.1.1.9 Dynamic viscosity:**

In the separation of two surfaces by the lubricant film thickness, the viscosity of the oil at operating temperature plays a critical role. The viscosity of lubricating oil varies extensively with the operating temperature. Oil viscosity drop as the temperature increases. On the other hand, lubricant viscosity is directly proportional to the pressure. Oil viscosity increases as the pressure increases. The effect of pressure on most of the lubricants is quite substantial compared to those of temperature or shear, especially at high pressure.

Roelands [136, 137, 138] proposed a type of Barus equation in order to calculate the viscosity of the lubricant at a certain pressure and temperature.as in Equation 3.11:

$$\eta_R = \eta_0 e^{\alpha * p} \quad (3.11)$$

where,

$\eta_r$  viscosity at pressure 'p' and temperature 'θ' (Pas), Pascal .Sec

$\eta_0$  atmospheric viscosity (Pas)

$\alpha^*$  Roelands pressure-viscosity coefficient, a function of both 'p' and 'θ' (m<sup>2</sup>/N)

$p$  Pressure of interest (Pa)

The Roelands pressure-viscosity coefficient 'α\*' can be calculated from the Equation 3.11 (a):

$$\alpha * p = [\ln \eta_0 + 9.67] \left\{ \left( \frac{\theta - 138}{\theta_0 - 138} \right)^{-S_0} (1 + 5.1 * 10^{-9} p)^{Z_0} - 1 \right\} \quad (3.11a)$$

where,

$\theta_0$  reference or ambient temperature (K)

$\eta_0$  atmospheric viscosity (Pas)

$Z_0, S_0$  constants, characteristics for a specific oil, and independent of temperature and pressure. These constants can be calculated from the following Equation 3.11 (b) and 3.11(c):

$$Z_0 = \frac{\alpha}{5.1 * 10^{-9} [\ln \eta_0 + 9.67]} \quad (3.11 b)$$

$$S_0 = \frac{\beta(\theta_0 - 138)}{\ln \eta_0 + 9.67} \quad (3.11 c)$$

Where,

$\alpha$  is the pressure-viscosity coefficient (m<sup>2</sup> /N)

$\beta$  is given by the following Equation 3.11 (d) :

$$\beta = [\ln \eta_0 + 9.67] [1 + 5.1 * 10^{-9} p]^Z \left[ \frac{S_0}{(\theta_0 - 138)} \right] \quad (3.11 d)$$

The temperature and the viscosity of the lubricant change along the length of the stroke.

### 3.1.1.10 Viscosity-Shear stress:

A fluid film thickness of 'h' separates two flat surfaces as shown in the Figure 3.15. The force, 'F' is applied to move the upper surface, which is proportional to the wetted area, 'A' and the velocity gradient, 'u/h', as the individual fluid layer will be subjected to shear according to the thickness of the fluid film. In a thicker film, the shear is less than that of in a thin film, i.e.

$$F \propto A \cdot \frac{u}{h} \quad (3.12)$$

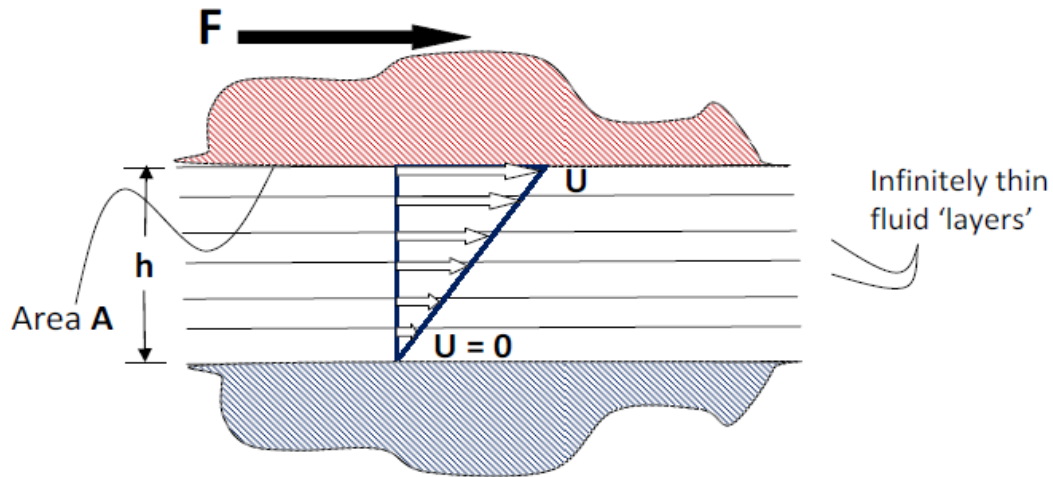


Figure 3.15 Relationship of force, area and velocity gradient

This relationship is true for most of the fluids. From the relationship of Equation 3.12, a new proportionality constant 'η' is derived. This constant is called the dynamic viscosity. Different fluids show a different proportionality constant 'η'. The Equation 3.12 can be written as Equation 3.13:

$$F = \eta A \cdot \frac{u}{h} \quad (3.13)$$

Rearranging gives:

$$\eta = \frac{F/A}{u/h} = \frac{\tau}{u/h} \quad (3.14)$$

where,

η      dynamic viscosity (Pa.s)

τ      shear stress acting on the fluid (Pa)

u/h    shear rate i.e., velocity gradient normal to the shear stress (s<sup>-1</sup>)



### 3.1.1.11 Viscosity-Shear rate relationship:

If we assume that the fluids are Newtonian, i.e., their shear stress is proportional to the shear rate and the slope represents the viscosity, we can show the relationship in a graph as in Figure 3.16.

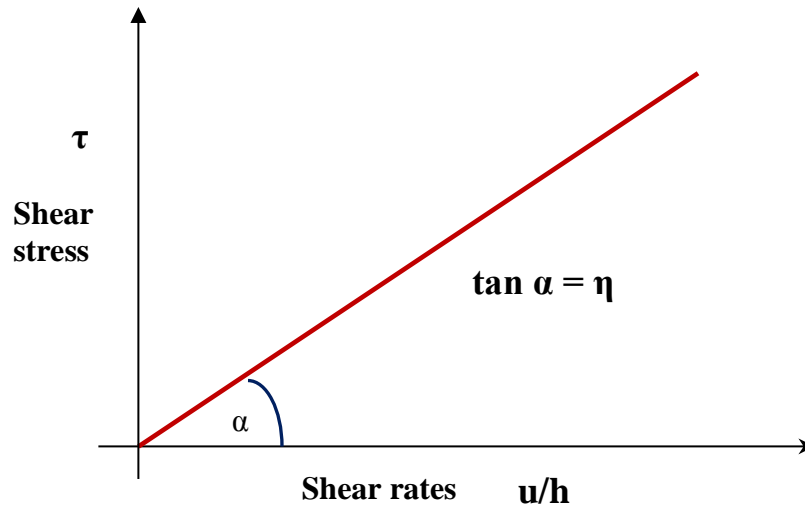


Figure 3.16 Shear stress- shear rate characteristic of a Newtonian fluid

Newtonian fluid assumption is valid up to shear rates of  $10^5$ - $10^6$  [ $s^{-1}$ ] for pure mineral oils. However the lubricant may behave as non-newtonian fluid in some applications at higher shear rate. In this case, the viscosity is not a constant and it will vary with the shear rate.

The mathematical model of cylinder liner and piston rings are usually based on Reynold's equation. The complete Reynold's equation is comprised of the elements hydrodynamic lubrication and the squeeze film lubrication with certain boundary conditions, which are described below.

### 3.1.1.12 Reynolds equation of hydrodynamic lubrication:

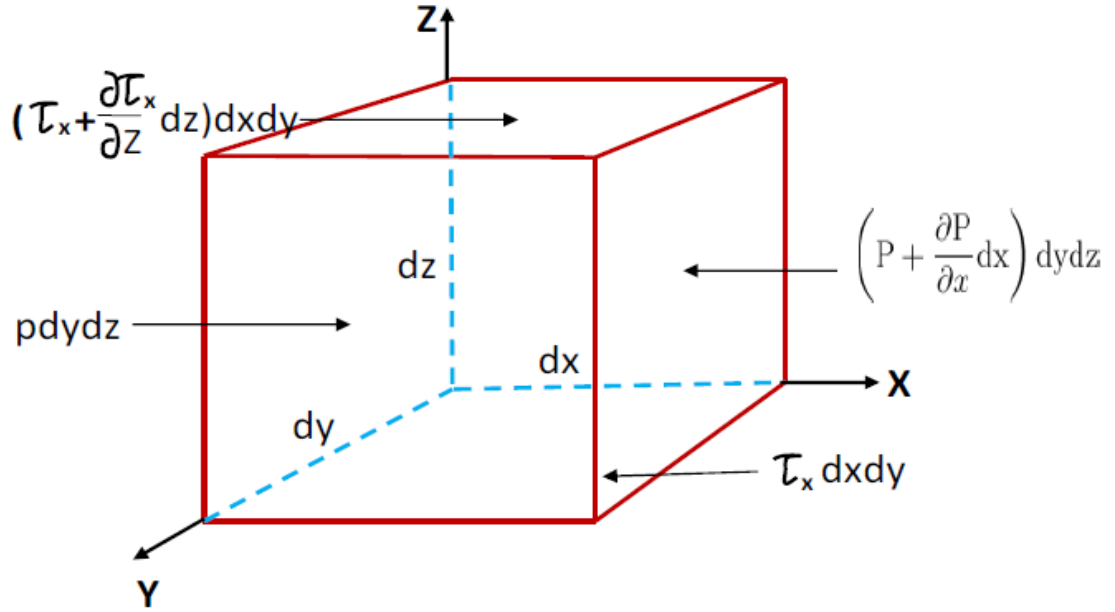


Figure 3.17 An element of fluid of hydrodynamic film in equilibrium position; 'p' is the pressure,  $\tau_x$  is the shear stress acting in the 'x' direction.

#### 3.1.1.12.1 Equilibrium of an element:

In the Figure 3.17, let us assume that the forces are acting initially in the 'x' direction only on a small element of fluid of a hydrodynamic film.

$$p dy dz + \left( \tau_x + \frac{\partial \tau_x}{\partial z} dz \right) dx dy = \left( p + \frac{\partial p}{\partial x} dx \right) dy dz + \tau_x dx dy \quad (3.15)$$

$$\frac{\partial \tau_x}{\partial z} = \frac{\partial p}{\partial x}, \text{ for forces acting in } x \text{ direction}$$

$$\frac{\partial \tau_y}{\partial z} = \frac{\partial p}{\partial y}, \text{ out of the page direction}$$

$$\frac{\partial p}{\partial z} = 0, \text{ as the pressure is constant through the film}$$

#### 3.1.1.12.2 Shear stress:

$$\tau_x = \eta \frac{u}{h} = \eta \frac{\partial u}{\partial z} \quad (3.16)$$

Where  $\tau_x$  is the shear stress acting in the 'x' direction; 'h' is the oil film thickness; 'u/h' is the velocity gradient.

### 3.1.1.12.3 Velocity in 'X' direction:

The velocity profile at the entry of the hydrodynamic film is shown in Figure 3.18. Entrain velocity is an important term for Reynold's hydrodynamic lubrication, which would be needed to develop the mathematical model. The relationship of the entrain velocity and the piston velocity is shown in the Equation 3.18.

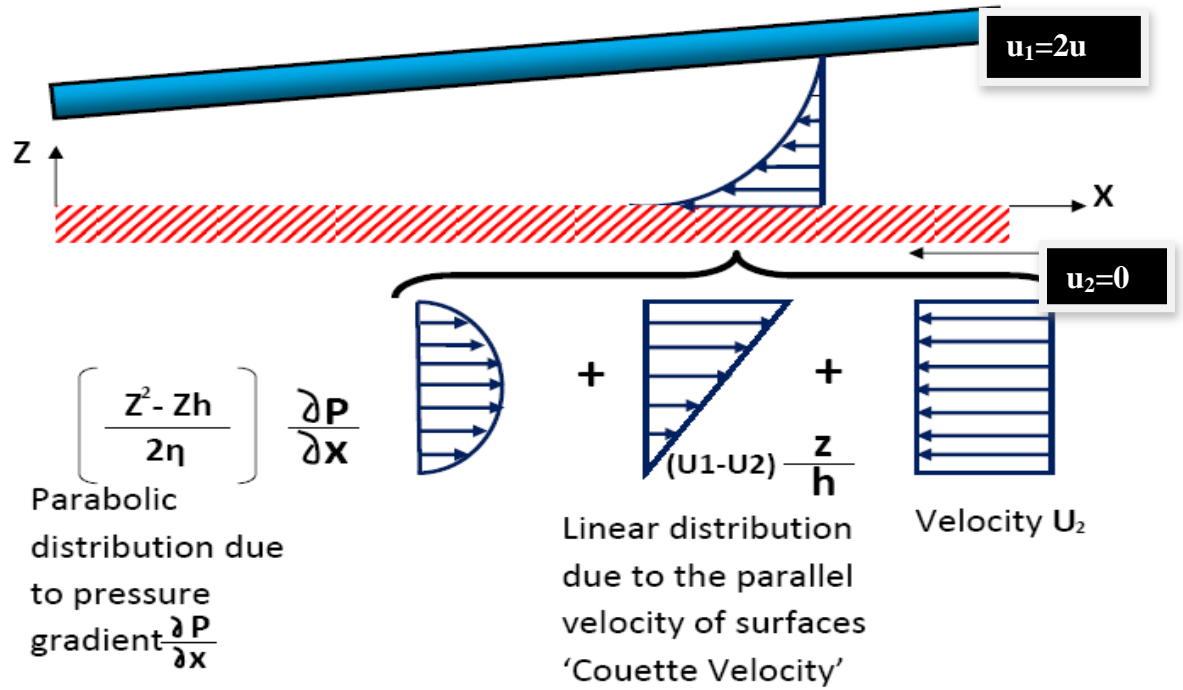


Figure 3.18 Velocity profiles at the entry of the hydrodynamic film

$$u = \left( \frac{z^2 - zh}{2\eta} \right) \frac{\partial p}{\partial x} + (u_1 - u_2) \frac{z}{h} + u_2 \quad (3.17)$$

In order to simplify, we consider  $u = \frac{U_1 + U_2}{2}$

$$\text{As } u_2 = 0, u = \frac{u_1}{2} \quad (3.18)$$

where  $u_1$  is the piston velocity against the crank angle.

#### 3.1.1.12.4 Continuity of flow in a column:

Reynold's equation for lubrication originates from the law of continuity of flow.

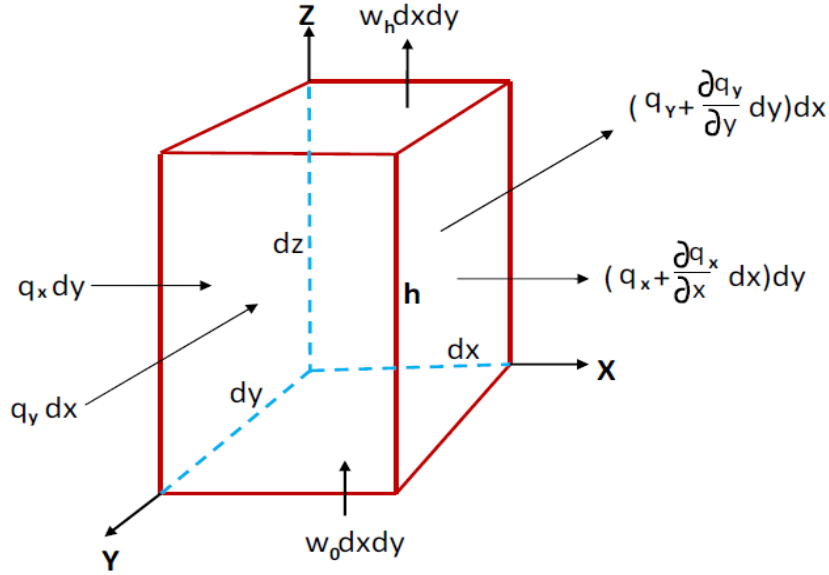


Figure 3.19 Continuity of flow in a column

The law of continuity of flow states that under steady state conditions, the inflow of liquid must be equal to its outflow from a control volume. We can write the following Equation 3.19 provided the density of the lubricant is constant:

$$q_x dy + q_y dx + w_0 dx dy = \left( q_x + \frac{\partial q_x}{\partial x} dx \right) dy + \left( q_y + \frac{\partial q_y}{\partial y} dy \right) dx + w_h dx dy \quad (3.19)$$

After simplifying, the equation of continuity becomes as:

$$\frac{\partial q_x}{\partial x} + \frac{\partial q_y}{\partial y} + (w_h - w_0) = 0 \quad (3.20)$$

Flow rate per unit length, 'q<sub>x</sub>' can be found from integrating the lubricant velocity profile over the film thickness, i.e.

$$q_x = \int_0^h u dz \quad (3.21)$$

Substituting for 'u' from velocity equation and after simplifying, the flow rate in 'x' direction:

$$q_x = -\frac{h^3}{12\eta} \frac{\partial p}{\partial x} + (U_1 + U_2) \frac{h}{2} \quad (3.22)$$

Substituting the above flow rate of equation 3.22 into the equation of continuity equation 3.20 yields:

$$\frac{\partial}{\partial x} \left[ -\frac{h^3}{12\eta} \frac{\partial p}{\partial x} + (U_1 + U_2) \frac{h}{2} \right] + \frac{\partial}{\partial y} \left[ -\frac{h^3}{12\eta} \frac{\partial p}{\partial y} + (V_1 + V_2) \frac{h}{2} \right] + (w_h - w_0) = 0 \quad (3.23)$$

**Full Reynold's equation:  $(U_1 + U_2) = u$**

$$\frac{\partial \left( \frac{h^3}{\eta} \frac{\partial p}{\partial x} \right)}{\partial x} + \frac{\partial \left( \frac{h^3}{\eta} \frac{\partial p}{\partial y} \right)}{\partial y} = 6 \left( u \frac{dh}{dx} + v \frac{dh}{dy} \right) + 12(w_h - w_0) \quad (3.24)$$

**Unidirectional velocity approximation. i.e.  $v = 0$**

$$\frac{\partial \left( \frac{h^3}{\eta} \frac{\partial p}{\partial x} \right)}{\partial x} + \frac{\partial \left( \frac{h^3}{\eta} \frac{\partial p}{\partial y} \right)}{\partial y} = 6u \frac{dh}{dx} + 12(w_h - w_0) \quad (3.25)$$

**Steady film thickness approximation. i.e.  $w_h - w_0 = 0$**

$$\frac{\partial \left( \frac{h^3}{\eta} \frac{\partial p}{\partial x} \right)}{\partial x} + \frac{\partial \left( \frac{h^3}{\eta} \frac{\partial p}{\partial y} \right)}{\partial y} = 6u \frac{dh}{dx} \quad (3.26)$$

**Infinitely long bearing approximation:**

Pressure gradient acting along 'y' axis can be neglected; i.e. ' $\partial p / \partial y = 0$ ' and 'h' is not a function of y f(y). Bearing is infinitely long in 'y' direction:

$$\frac{\partial \left( \frac{h^3}{\eta} \frac{\partial p}{\partial x} \right)}{\partial x} = 6u \frac{dh}{dx} \quad (3.27)$$

$$\frac{\partial \left( h^3 \frac{\partial p}{\partial x} \right)}{\partial x} = 6u\eta \frac{dh}{dx} \quad (3.28)$$

**Upon integration,**

$$h^3 \frac{dp}{dx} = 6u\eta h + C \quad (3.29)$$

To solve this, boundary condition is needed. It is assumed that at some point along the film, pressure is at a maximum. At this point, the pressure gradient is zero. i.e.  $\frac{dp}{dx} = 0$  and the corresponding film thickness is denoted as  $\bar{h}$ , Figure 3.20.

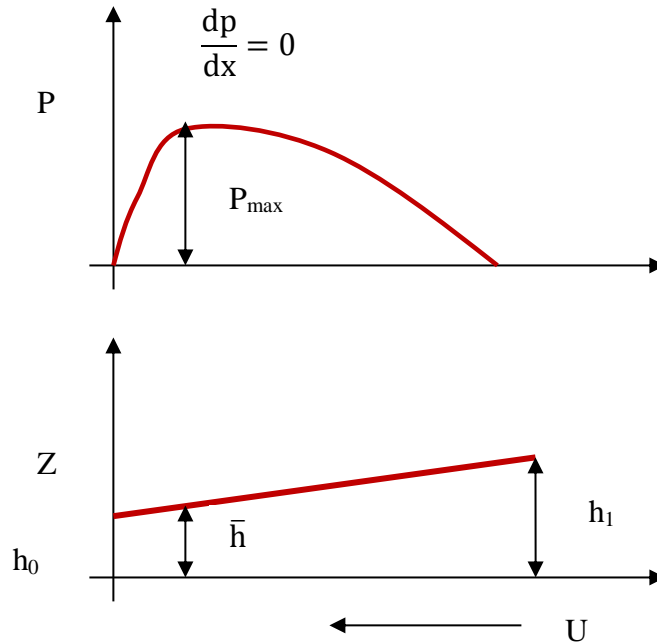


Figure 3.20 Max. pressure and the pressure gradient

$$C = -6u\eta\bar{h} \quad (3.30)$$

$$\frac{dp}{dx} = 6u\eta \frac{h - \bar{h}}{h^3} \quad (3.31)$$

It is to be noted that the velocity 'u' is assumed negative as shown in Figure 3.19.

#### **3.1.1.12.4.1 Lubricant flow:**

Lubricant flow plays very important role in the operation of a bearing. If adequate amount of oil is not supplied to the hydrodynamic contact, oil starvation would occur and will result in bearing failure. Sufficient amount of oil require to be supplied to the bearing so that the surfaces are fully separated by a hydrodynamic film.

The equations of the flow are formulated with the parameters of the bearing.  
It is also possible to optimize the flow of the lubricant.

When 'q<sub>x</sub>' and 'q<sub>y</sub>' of the flow equations 3.32 and 3.33 are integrated over the periphery of the bearing, lubricant leakage across the sides and the lengths of the bearing can be obtained.

$$Q_x = \int_0^L q_x dy \quad (3.32)$$

$$Q_y = \int_0^B q_y dx \quad (3.33)$$

As in the infinitely long bearing, side leakage of lubricants in the 'y' direction can be neglected, i.e. q<sub>y</sub> = 0; integration of the equation 3.32 will provide the lubricant flow in the bearing as follows:

$$Q_x = \int_0^L q_x dy \quad (3.32)$$

$$q_x = -\frac{h^3}{12\eta} \frac{\partial p}{\partial x} + (U_1 + U_2) \frac{h}{2} \quad (3.23)$$

With U<sub>1</sub> = U and U<sub>2</sub> = 0,

$$Q_x = \int_0^L \left( -\frac{h^3}{12\eta} \frac{\partial p}{\partial x} + \frac{Uh}{2} \right) dy \quad (3.34)$$

The boundary conditions are:

$$\frac{dp}{dx} = 0 \text{ at } h = \bar{h} \text{ (point of maximum pressure)}$$

Substituting the B.C. into the flow equation 3.34:

$$Q_x = \int_0^L \frac{U\bar{h}}{2} dy \quad (3.35)$$

Simplifying the equation after integration results in lubricant flow per unit length.

### 3.1.1.12.5 Reynold's equation for squeeze film:

As mentioned earlier, Reynold's appropriate equation for liner and piston lubrication has a second component, which characterizes the squeeze film, a time dependent film thickness.

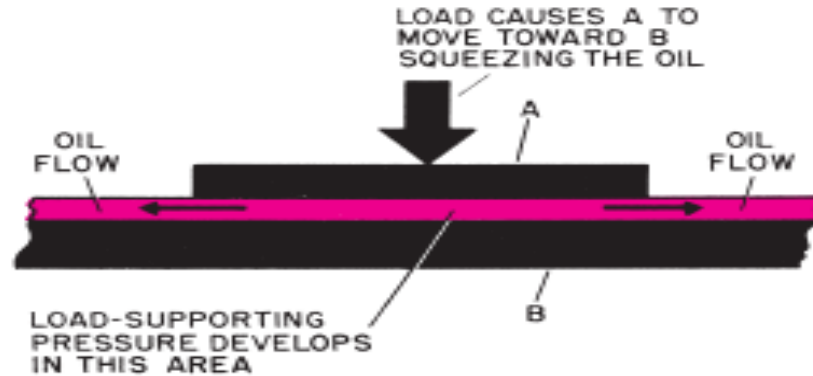


Figure 3.21 Squeeze film lubrication [153]

In this case it can be modeled for the load capacity under a time dependent film thickness, e.g.  $\partial h/\partial t$  is not equal to zero. Squeeze film is a term denoting film that sustains a negative  $\partial h/\partial t$ , i.e when the opposing surfaces are being squeezed together. An extreme useful characteristic of squeeze film is that they provide increased load capacity (although temporary) when a bearing is suddenly subjected to an abnormally high load like transient combustion forces. The squeeze film is always opposite in direction to the motion of either bearing surface. This is a form of damping; squeeze film forces contribute to the vibrational stability of a bearing. To analyze squeeze film forces, the term  $\partial h/\partial t$  is kept in the Reynolds equation and is given precedence over the film geometry term  $\partial h/\partial x$ .

The Reynolds equation for squeeze term is based on an isoviscous lubricant and zero entraining velocity, Equation 3.36.

$$\frac{\partial \left( h^3 \frac{\partial p}{\partial x} \right)}{\partial x} + \frac{\partial \left( h^3 \frac{\partial p}{\partial y} \right)}{\partial y} = 12\eta \frac{\partial h}{\partial t} \quad (3.36)$$

The equation 3.36 defines the hydrodynamic pressure field when the wedge effect is absent. It can be integrated in terms of a specified bearing geometry to provide load capacity, maximum pressure or any other bearing characteristic in terms of  $\partial h/\partial t$ . The 'squeeze time' means the time required for film thickness to reduce to



some critical minimum value. Squeeze time can also be obtained by integrating  $\partial h / \partial t$  with respect to time.

Two infinitely long parallel plates squeezed together are shown in the Figure 3.22.

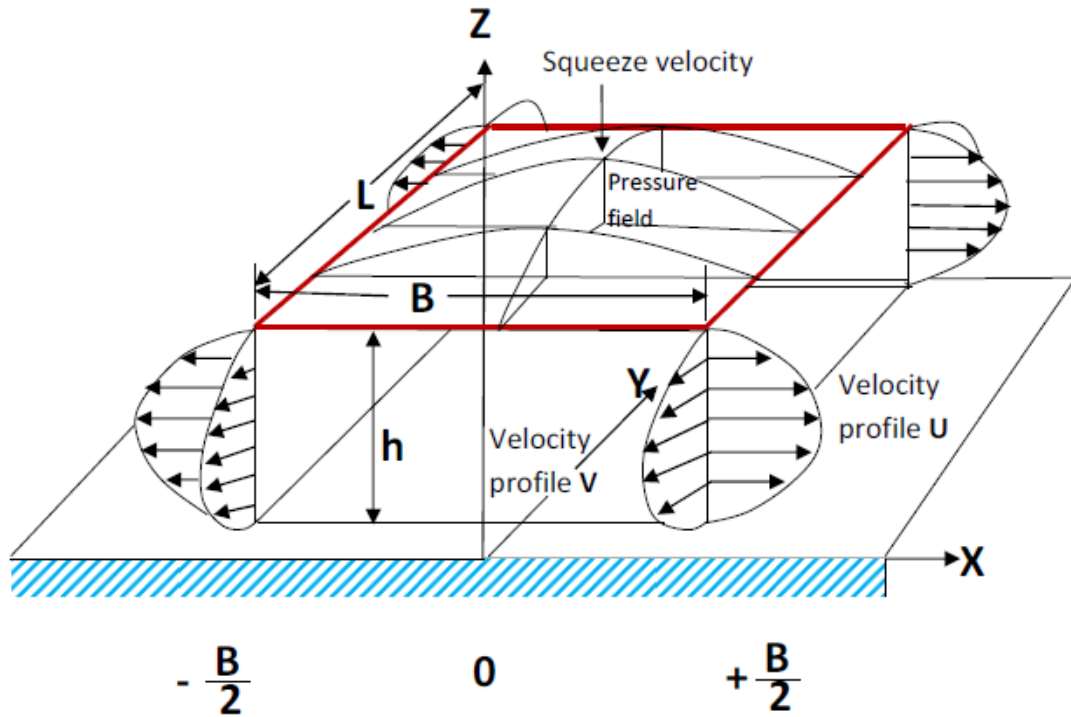


Figure 3.22 Squeeze film between two parallel plates

#### 3.1.1.12.5.1 Pressure distribution and load capacity:

For two parallel and infinitely long plates:

$$h \neq f(x)$$

$$\frac{\partial p}{\partial x} = 0$$

The Reynolds squeeze film equation

$$\frac{\partial \left( h^3 \frac{\partial p}{\partial x} \right)}{\partial x} + \frac{\partial \left( h^3 \frac{\partial p}{\partial y} \right)}{\partial y} = 12\eta \frac{\partial h}{\partial t} \quad (3.37)$$

reduces to:

$$\frac{d^2 p}{dx^2} = \frac{12\eta}{h^3} \frac{dh}{dt} \quad (3.38)$$

Integrating once:

$$\frac{dp}{dx} = \frac{12\eta}{h^3} \frac{dh}{dt} x + C_1 \quad (3.39)$$

and integrating once more:

$$p = \frac{6\eta}{h^3} \frac{dh}{dt} x^2 + C_1 x + C_2 \quad (3.40)$$

$C_1$  and  $C_2$  can be found from the boundary condition.

B.C. are:

$$P = 0 \text{ @ } x = \frac{B}{2} \quad (3.41)$$

$$\frac{dp}{dx} = 0 \text{ @ } x = 0 \quad (3.42)$$

Substituting B.C. in above Equations 3.39 and 3.40,

$$C_1 = 0 \quad (3.43)$$

$$C_2 = -\frac{6\eta B^2}{4h^3} \frac{dh}{dt} \quad (3.44)$$

Substituting  $C_1$  and  $C_2$  in pressure Equation 3.40:

$$P = \frac{6\eta}{h^3} \frac{dh}{dt} \left( x^2 - \frac{B^2}{4} \right) \quad (3.45)$$

And subsequently integrating the pressure Equation 3.40, the load/unit length:

$$\frac{W}{L} = \int_{-\frac{B}{2}}^{+\frac{B}{2}} \frac{6\eta}{h^3} \frac{dh}{dt} \left( x^2 - \frac{B^2}{4} \right) dx \quad (3.46)$$

$$\frac{W}{L} = -\frac{\eta B^3}{h^3} \frac{dh}{dt} \quad (3.47)$$

With changed boundary condition, the pressure and load equation changes accordingly. For piston ring solution, the boundary conditions are different as they are subjected to  $P_1$  and  $P_2$  pressure on either side of the ring. Considering a steady state fixed oil film thickness 'h' and  $X=0$  at the leading edge of the ring of ring height 'B', the above B.Cs are modified and solved accordingly:

For the piston ring, B.C are:

$$P=P_1 \text{ @ } x = 0 \text{ at the leading edge of the ring} \quad (3.48)$$

$$P=P_2 \text{ @ } x =B \text{ at the trailing edge of the ring} \quad (3.49)$$

and the pressure gradient

$$\frac{dp}{dx} = 0 \text{ @ } x = \frac{B}{2} \quad (3.50)$$

Substituting Equations 3.48, 3.49 and 3.50 in the Equations 3.40 and 3.39 of pressure and derivative of pressure equation yields the constants as:

$$C_1 = -\frac{6B\eta}{h^3} \frac{dh}{dt} \quad (3.51)$$

$$C_2 = P_1 \text{ or } P_2 \quad (3.52)$$

Substituting back 'C<sub>1</sub>' and 'C<sub>2</sub>' into the Equation 3.40 gives the pressure distribution as a function of dh/dt for the ranges of 'x' from 0~0.5B and 0.5B~B as follows:

$$|P|_0^{0.5B} = \frac{6\eta}{h^3} \omega \frac{dh}{d\theta} (x^2 - B) + P_1; \quad x = 0 \rightarrow 0.01 \quad (3.53)$$

$$|P|_{0.5B}^B = \frac{6\eta}{h^3} \omega \frac{dh}{d\theta} (x^2 - B) + P_2; \quad x = 0.01 \rightarrow 0.02 \quad (3.54)$$

where dh/dt of time domain =  $\omega \cdot (dh/d\Theta)$  of crank angle domain

$\omega$  = the angular velocity

$\Theta$  = crank angle

Integration the equation of the pressure distribution against the bearing area provides the load bearing capability of the ring and cylinder liner:

$$W = \int_0^L \int_0^B P \, dx \, dy \quad (3.55)$$

It can be expressed in load per unit length:

$$\frac{W}{L} = \int_0^B P \, dx \quad (3.56)$$

Substituting for 'p' from pressure distribution Equations 3.53 and 3.54:

$$\left[ \frac{W}{L} \right]_0^{0.5B} = \int_0^{0.5B} \left[ \frac{6\eta}{h^3} \omega \frac{dh}{d\theta} (x^2 - B) + P_1 \right] dx; \quad x = 0 \rightarrow 0.01 \quad (3.57)$$

$$\left[ \frac{W}{L} \right]_{0.5B}^B = \int_{0.5B}^B \left[ \frac{6\eta}{h^3} \omega \frac{dh}{d\theta} (x^2 - B) + P_2 \right] dx; \quad x = 0.01 \rightarrow 0.02 \quad (3.58)$$

and integrating yields:

$$\left[\frac{W}{L}\right]_0^{0.5B} = \frac{0.25\eta B^3}{h^3} \omega \frac{dh}{d\theta} - 0.5B^2 + 0.5P_1B; \quad x = 0 \rightarrow 0.01 \quad (3.59)$$

$$\left[\frac{W}{L}\right]_{0.5B}^B = \frac{1.75\eta B^3}{h^3} \omega \frac{dh}{d\theta} - 0.5B^2 + 0.5P_2B; \quad x = 0.01 \rightarrow 0.02 \quad (3.60)$$

### **3.1.1.12.6 Squeeze Time:**

Squeeze time can be defined as the time required for the lubricant film thickness between parallel surfaces to change between defined limits. Squeeze time can be obtained by rearranging the load capacity Equations 3.55 and 3.56:

$$dt = \frac{\eta B^3}{4h^3 \left\{ \frac{W}{L} + 0.5B^2 - 0.5P_1B \right\}} dh; \quad \left| \frac{W}{L} \right|_0^{0.5B} \quad (3.61)$$

$$dt = \frac{1.75\eta B^3}{h^3 \left\{ \frac{W}{L} + 0.5B^2 - 0.5P_2B \right\}} dh; \quad \left| \frac{W}{L} \right|_{0.5B}^B \quad (3.62)$$

The minimum lubricant film thickness in squeeze film lubrication is based on the combined surface roughness of the mating faces. For large bearings, it is based on the elastic deformation of the opposing faces.

### **3.1.1.12.7 Cavitation and squeeze effect:**

Cavitation occurs during positive and negative squeeze of a liquid lubricant in a system. Lubricant is incompressible. But as the cavitation creates bubbles in the lubricant and the bubbles can be compressed, cavitation has the effect on squeeze film forces. Bubbles can join and grow in size and change the squeeze characteristics of the system. The continuous presence of bubbles is owing to the higher rate of bubble formation against that of bubble dissolution.

The load bearing capacity is considerably reduced by the presence of bubbles. Hence the actual load bearing capacity of the bearing may be far lower than that of the calculated ones based on pure hydrodynamic theory with no effects of cavitation. In reality, the lubricant in a bearing is exposed to cyclic cavitation.

### **3.1.1.13 Gas pressure and Hydrodynamic pressure:**

In order to obtain the mathematical model for piston rings, balance of gas pressure and lubricants hydrodynamic pressure need to be balanced as described under section 3.1.2.1.2 The gas pressures are modeled as per the offset PV diagram (draw card) against various engine load. The pressure above and below the ring,  $P_1$  and  $P_2$  are determined from the labyrinth model (orifice and volume method) as follows:

$$\frac{P_m}{P_{m-1}} = \left( \frac{2}{\gamma + 1} \right)^{\frac{\gamma}{\gamma-1}} \quad (3.63)$$

where,

$\gamma$  is the ratio of specific heats at constant pressure and constant volume.

The oil film pressure are equal to the values of  $P_m$  and  $P_{m-1}$  at locations of entrance and exit of oil. [139]

### **3.1.2 Mathematical modeling of tribology method:**

In forming mathematical model for tribological method, four scenerios were considered. These are 1) Hydrodynamic and squeeze film combined 2) Boundary lubrication 3) Mixed (hydrodynamic and boundary) 4) No lubrication (full asperity contact). The models can be simulated from the generated equations and by giving variable inputs to the model as described in the Appendix 2 and the attached Excel file named ' Tribology model'. Through appropriate inputs, the generated model produces the graphs for oil pressure distribution, oil film thickness, coefficient of friction, friction force and load capacity against the crank angle of the engine.

#### **3.1.2.1 Piston ring 'hydrodynamic and squeeze film' combined lubrication mathematical model:**

Piston ring parameters predicted from Reynold's equation:

- *Pressure distribution*
- *Load capacity*
- *Friction force*
- *Co-efficient of friction*
- *Lubricant flow*

### 3.1.2.1.1 Piston ring bearing geometry: (*Film geometry of parabolic wedge*):

The Figures 3.23 and 3.24 film geometry can be considered for the hydrodynamic lubrication of the piston rings of internal combustion engine. The parabolic profile has the advantage that it tends to be self-perpetuating under wear since the piston ring tends to rock inside its groove during reciprocating movement and causes preferential wear of the edges of the ring.

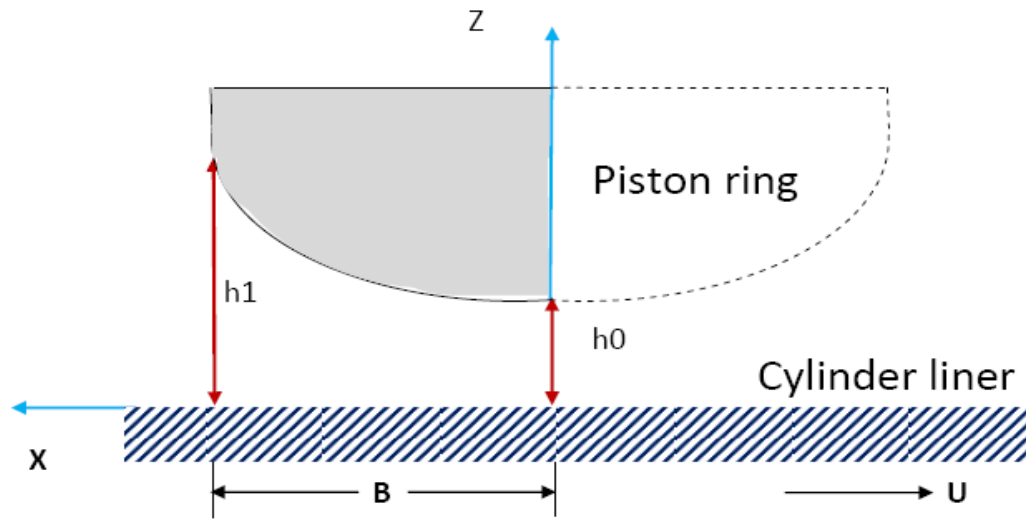


Figure 3.23 Geometry of the parabolic wedge bearing

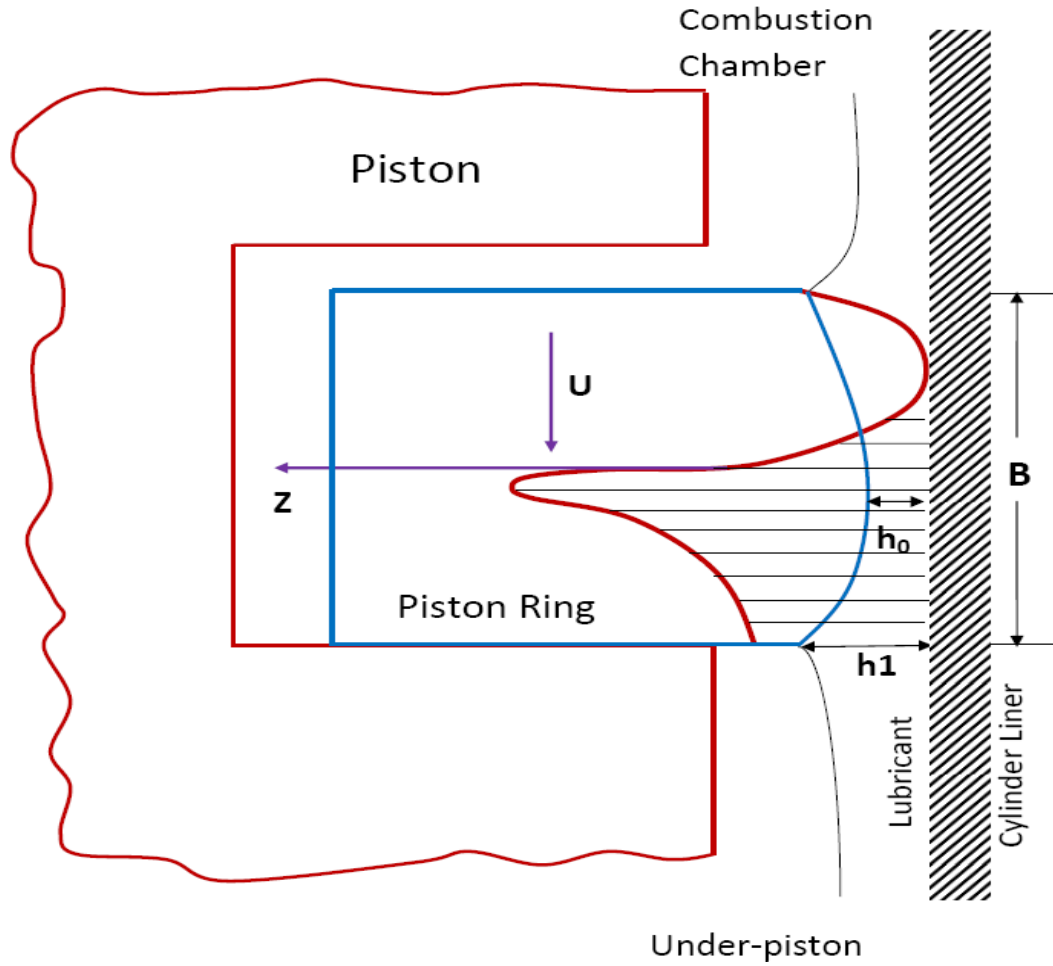


Figure 3.24 Application of geometry of parabolic wedge bearing in piston ring [132]

The film geometry is described by the Equation 3.64:

$$h = h_0 + (h_1 - h_0) \left( 1 - \frac{x}{0.5B_c} \right)^n \quad (3.64)$$

where,

$n$  is a constant and equals 2 for a simple parabolic profile

$B_c$  is the characteristic width, which is equal to ring height 'B' (m)

$x$  is the difference along the 'X' axis starting from the minimum film thickness (m)

Equation 3.64 can be rearranged by replacing  $\frac{h_1 - h_0}{h_0}$  with 'K' as:

$$h = h_0 + Kh_0 \left( 1 - \frac{2x}{B} \right)^2 \quad (3.65)$$

The appropriate form of the Reynolds equation for an incompressible lubricant, in which circumferential flow of the lubricant is neglected, is: [where  $(U_1 + U_2)/2 = u$ ]

$$\frac{\partial}{\partial x} \left[ \frac{h^3}{\eta} \left( \frac{\partial p}{\partial x} \right) \right] = 12u \left[ \frac{\partial h}{\partial x} \right] + 12 \frac{\partial h}{\partial t} \quad (3.66)$$

where the first term on the right hand side represents entraining velocity/action [ $u = (U_1 + U_2)/2$ ] of hydrodynamic lubrication and the second term the influence of normal velocities (squeeze-film action). If ' $\theta$ ' represents crank angle and the angular velocity of the engine is ' $\omega$ ', the latter term can be written more conveniently as  $12\omega(\partial h/\partial \theta)$ .

Since  $(h)$  is a function of  $(x)$ , i.e.  $h = f(x)$ , alone at a given instant, the Equation 3.66 can be integrated to yield:

$$\frac{\partial p}{\partial x} = 12\eta u \left[ \frac{1}{h^2} + \frac{\omega}{u} \left( \frac{\partial h}{\partial \theta} \right) \frac{x}{h^3} + \frac{C_1}{h^3} \right] \quad (3.67)$$

Further integration reveals the following general expression for pressure distribution within the lubricating film,  $P = P_z$ :

$$p = 12\eta u \left[ E + \frac{1}{R} \left( \frac{R\omega}{u} \right) \frac{\partial h}{\partial \theta} \cdot F + C_1 G + C_2 \right] \quad (3.68)$$

where,

$$E = \int \frac{dx}{h^2}; \quad F = \int \frac{x}{h^2} dx; \quad \text{and} \quad G = \int \frac{dx}{h^3} \quad (3.69)$$

where,

R      Crank radius (m)

h      Oil film thickness (m)

$p_z$       Hydrodynamic pressure (Pa)

u      Entraining velocity =  $(U_1 + U_2)/2$  (m/s)

E, F, G Constants

$\omega$       Angular Velocity of crank (rad/s)

$\eta$       Lubricant viscosity,  $\eta = f(\theta)$  is adjusted against the crank angle, as the liner temperature varies along the length of the cylinder.



It is essential to determine the cyclic variation of film thickness first, since other overall derived quantities such as friction and the 102et transport of lubricant between the ring and cylinder liner can then be derived.

The entraining velocity, Equations 3.9 and 3.66 and the inter-ring pressure Equation 3.63 are solved to yield 'u' and  $P_1$ ,  $P_2$  at each crank angle.

Substituting the value of 'h' with 'x' of Equation 3.65, the integrals E, F and G are found.

Then the integrals E, F and G have analytical solutions and hence the form of the pressure distribution are readily obtained for a given entraining velocity (u) and squeeze-to-entraining velocity ratio. The pressure distribution expression involves two constants of integration and the full determination of pressure thus calls for two boundary conditions, which is shown later in Equations 3.73 to 3.76.

$$E = \int \frac{dx}{h^2} = \int \frac{dx}{\left\{ h_0 + Kh_0 \left( 1 - \frac{2x}{B} \right)^2 \right\}^2}$$

$$= \frac{1}{4h_0^2} \left[ \frac{-B \tan^{-1} \left\{ \frac{(B-2x)\sqrt{K}}{B} \right\}}{\sqrt{K}} - \frac{B^2(B-2x)}{B^2 + K(B-2x)^2} \right] \quad (3.70)$$

$$F = \int \frac{x dx}{h^3} = \int \frac{x dx}{\left\{ h_0 + Kh_0 \left( 1 - \frac{2x}{B} \right)^2 \right\}^3}$$

$$= -\frac{1}{32h_0^3} \left[ \frac{3B^3(B-2x)}{B^2 + K(B-2x)^2} + \frac{2B^5\{K(B-2x) + B\}}{K\{B^2 + K(B-2x)^2\}^2} \right.$$

$$\left. + \frac{3B^2 \tan^{-1} \left\{ \frac{(B-2x)\sqrt{K}}{B} \right\}}{\sqrt{K}} \right] \quad (3.71)$$

$$\begin{aligned}
 G &= \int \frac{dx}{h^3} = \int \frac{dx}{\left\{ h_0 + Kh_0 \left( 1 - \frac{2x}{B} \right)^2 \right\}^3} \\
 &= \frac{1}{16h_0^3} \left[ \frac{3B^2(B-2x)}{B^2 + K(B-2x)^2} + \frac{2B^4(B-2x)}{\{B^2 + K(B-2x)^2\}^2} \right. \\
 &\quad \left. + \frac{3B \tan^{-1} \left\{ \frac{(B-2x)\sqrt{K}}{B} \right\}}{\sqrt{K}} \right] \quad (3.72)
 \end{aligned}$$

A representative form of the hydrodynamic pressure distribution in the partially filled clearance space between a piston ring face and cylinder liner is shown in the Figure 3.25.

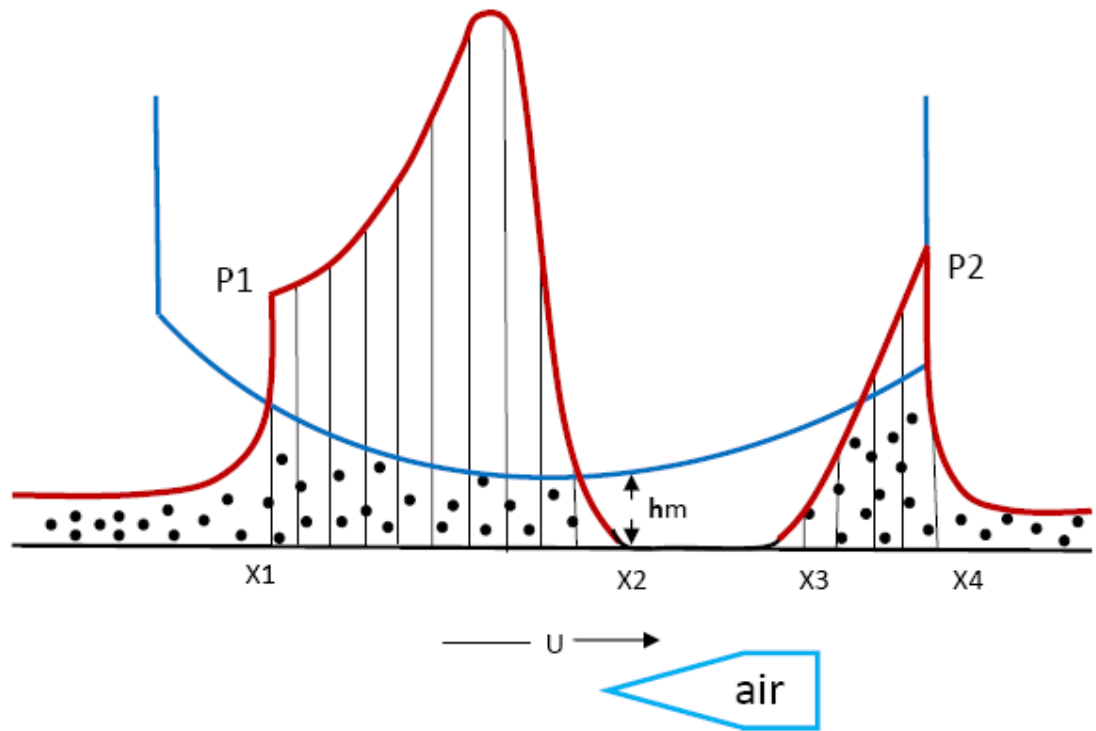


Figure 3.25 Hydrodynamic pressure distribution in a starved piston ring/liner conjunction

Now to find  $C_1$  and  $C_2$ , we need to use the boundary conditions on pressure and its derivative Equations 3.68 and 3.67.

$$P_z = P_1 \quad \text{at } x = x_1 = 0 \quad \text{Inlet} \quad (3.73)$$

$$P_z = 0 \text{ (or } P_2) \quad \text{at } x = x_2 \quad \text{Cavitation} \quad (3.74)$$

$$\text{and } \partial p / \partial x = 0$$

$$P_z = 0 \text{ (or } P_2) \quad \text{at } x = x_3 \quad \text{Reformation} \quad (3.75)$$

$$P_z = P_2 \quad \text{at } x = X_4 = B \quad \text{Outlet} \quad (3.76)$$

Where,  $P_z$  is the hydrodynamic pressure

The main region for the generation of hydrodynamic pressures which yield a fluid film force capable of balancing the instantaneous sealing force is located between  $X=X_1$  and  $X = X_2$ , Figure 3.25. At  $X_2$ , the pressure falls to the saturation pressure (atmospheric) for the lubricant, to create a ruptured or cavitated region. In the dynamic case, the cavitation zone starting point,  $X_2$  keeps changing. The double condition represented by the Reynolds boundary condition at  $X=X_2$ , on the pressure and its derivative locates  $X_2$ .

If the downstream pressure  $P_2$  exceeds the saturation pressure (atmosphere), a full lubricating film will reform to fill the clearance space at some point after  $X = X_2$ , i.e. at  $X=X_3$  to enable the hydrodynamic pressure to build up to  $P_2$  at the exit location,  $X=B$ . The pressure at  $X=B$  is thus equated to  $P_2$  and the Reynolds equation, with the previously determined value of  $C_1$ , is integrated until the pressure falls to atmospheric at  $X_3$ . The locations of  $X_2$  and  $X_3$  are thus determined and the magnitude of the hydrodynamic pressures established in the regions  $X_1$ - $X_2$  and  $X_3$ - $X_4$ .

Now, with known  $C_1$  and  $C_2$ ,  $P_z$  profile can be drawn with variable  $E$ ,  $F$  and  $G$  against the  $X$ -axis of the steady state crank angle condition with Equation 3.68.

The normal or squeeze film velocity required to generate hydrodynamic pressures,  $P_z$  capable of balancing the radial sealing force from the Equation 3.77 and Figure 3.26 is then established for the assumed, initial value of minimum film thickness at crank angle ( $\theta$ ).

### 3.1.2.1.2 Radial force balance:

The lubricant pressure balances against the radial gas pressure, which is used in the attached X-Cel lubrication model to produce simulated pressure profile, friction coefficient, film thickness and load capacity. The radial force balance on the rings is shown in Equation 3.77:

$$p_1(b - k) - p_2(l) - F_p - P_z + P_s = M \frac{d^2z}{dt^2} \quad (3.77)$$

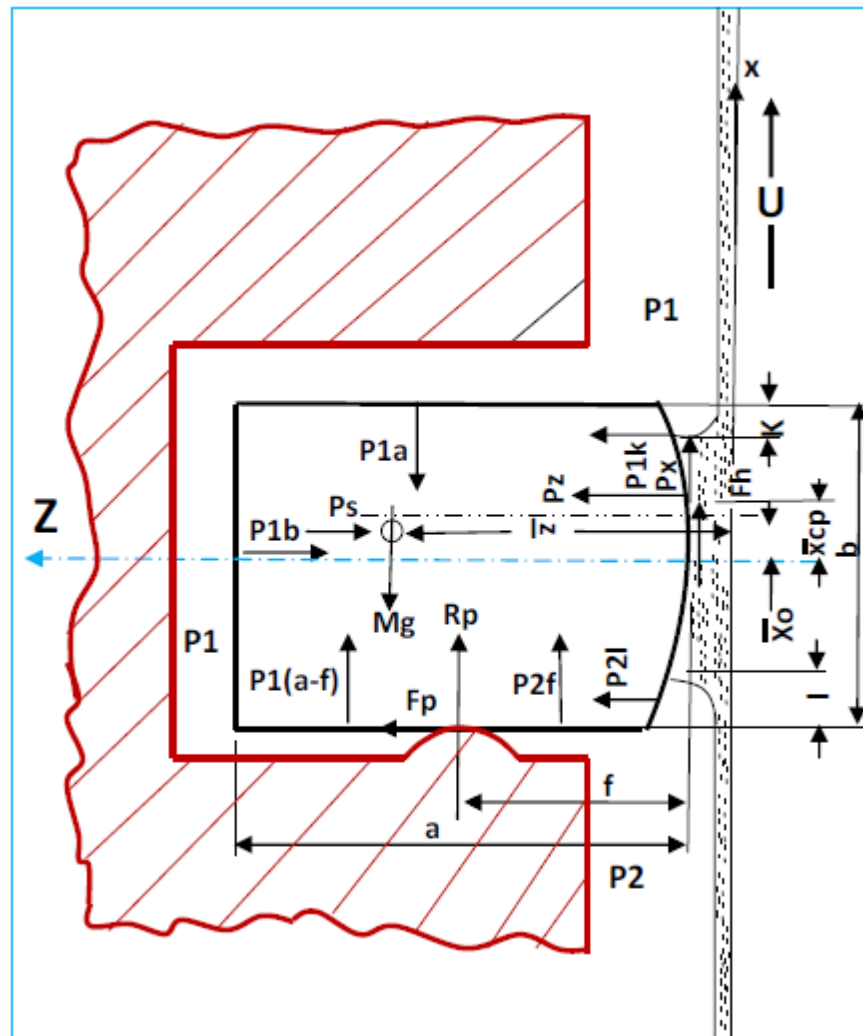


Figure 3.26 Forces acting on a piston ring at steady state condition

Where,

- a radial width of piston ring (m)
- b axial height of piston ring (m)

f	overhang of piston ring beyond effective pivot point (approximately equal to the distance from the pivot to the cylinder wall) (m)
k	exposed length of starved piston ring at top end of the ring face (m)
l	exposed length of starved piston ring at bottom end of the ring face (m)
p <sub>1</sub>	pressure above piston ring (Pa)
p <sub>2</sub>	pressure below piston ring (Pa)
x,z	axial and radial co-ordinates
$\bar{x}, \bar{z}$	location of piston ring centre of mass
$\bar{x}, \bar{z}$ x <sub>C.P.</sub>	axial location of resultant hydrodynamic normal force from mid plane of ring
F <sub>h</sub>	hydrodynamic shear force/unit circumferential length (radial) (N/m)
F <sub>p</sub>	ring pivot friction force/unit circumferential length (radial) (N/m)
M	mass of piston ring/unit circumferential length (Kg/m)
P <sub>s</sub>	spring (sealing) force/unit circumferential length (radial) (N/m)
P <sub>z</sub>	hydrodynamic normal force/unit circumferential length (radial) (N/m)
R <sub>p</sub>	piston/groove reaction force/unit length (axial) (N/m)

Once the hydrodynamic pressure is found, the load can be calculated by integrating it. The friction force and coefficient of friction can then be easily determined as shown under section 4.0.

### **3.1.2.2 Piston ring ‘boundary lubrication’ mathematical model:**

As per Greenwood model, during the boundary condition, the friction force between the piston ring and the cylinder liner:

$$\frac{F}{L} = \int_{x_{c1}}^{x_{c2}} a_{asp} P_c dx \quad (3.78)$$

where,

$a_{asp}$  is the friction coefficient governed by the surface properties

$x_{c1}$  and  $x_{c2}$  define the boundaries of the portion of the ring-liner surfaces that are in asperity contact for  $h/\sigma < 4$ .

$$P_c \left( \frac{h}{\sigma} \right) = K' E' \int_{\frac{h}{\sigma}}^{\infty} \left( z - \frac{h}{\sigma} \right)^{2.5} \phi(z) dz \quad (3.79)$$

$$K' = \frac{8\sqrt{2}\pi}{15} (\eta_a \beta_a \sigma)^2 \sqrt{\frac{\sigma}{\beta_a}} \quad (3.80)$$

where,

$\Phi(z)$  = the probability distribution of asperity heights

$h$  = mean separation of the two surfaces, i.e. oil film thickness

$\eta_a$  = asperity density per unit area

$\beta_a$  = asperity peak radius of curvature

$z_s$  = offset between the asperity height mean and the surface height mean

The composite Young's modulus and the composite standard deviation of asperity heights used by Greenwood and Tripp model are given by

$$E' = \frac{2}{\frac{1 - \nu_1^2}{E_1} + \frac{1 - \nu_2^2}{E_2}} \quad (3.81)$$

and

$$\sigma = \sqrt{\sigma_1^2 + \sigma_2^2} \quad (3.82)$$

respectively, where  $E_1$  and  $E_2$ , and  $\nu_1$  and  $\nu_2$  are the respective Young's modulus and Poisson's ratio of the two contacting surfaces, and  $\sigma_1$  and  $\sigma_2$  are the standard deviation of asperity heights of the two surfaces. The Greenwood and Tripp model assumes that the contact is elastic, and the asperities are parabolic in shape and identical on the contact surfaces [140].

Cylinder liners are pre-honed prior to putting into service. This pre-honing of liners allows them to trap oil within their honing cavities. Pre-honing can be plateau honed or slide honed. Various characteristics of cylinder liner surface such as roughness and the constants and calculated Greenwood and Tripp parameters of plateau honed and slide honed liners are shown in Table 3.2.

(a)		
	Plateau Honed	Slide honed
$R_q$ ( $\mu\text{m}$ )	0.84	0.49
$R_{pk}$ ( $\mu\text{m}$ )	0.25	0.28
$R_k$ ( $\mu\text{m}$ )	0.74	0.39
$R_{vk}$ ( $\mu\text{m}$ )	1.85	1.47
Sk	-2.79	-3.85
Ku	13.82	25.99
Honing angle	$35^\circ - 45^\circ$	$35^\circ - 45^\circ$
(b)		
	Plateau Honed	Slide honed
$\sigma$ ( $\mu\text{m}$ )	0.64	0.29
$\beta_a$ ( $\mu\text{m}$ )	29.2	27.6
$\eta \times 10^{10}$ ( $\text{m}^{-2}$ )	2.10	2.50
$Z_s$ ( $\mu\text{m}$ )	0.01	0.06
Sk	-2.95	-5.35
Ku	17.16	52.53
(c)		
$E'$	$1.75 \times 10^{11}$	Pa
$K'$	$2.396 \times 10^{-3}$	-

Table 3.2 (a) Characteristics of typical liner surfaces (b) Calculated Greenwood-Tripp Parameters (c) Typical Greenwood-Tripp Parameters

A typical asperity contact pressure against standard deviation of asperity heights of plateau honed, slide honed and an intermediate prorated one is shown in Figure 3.27.

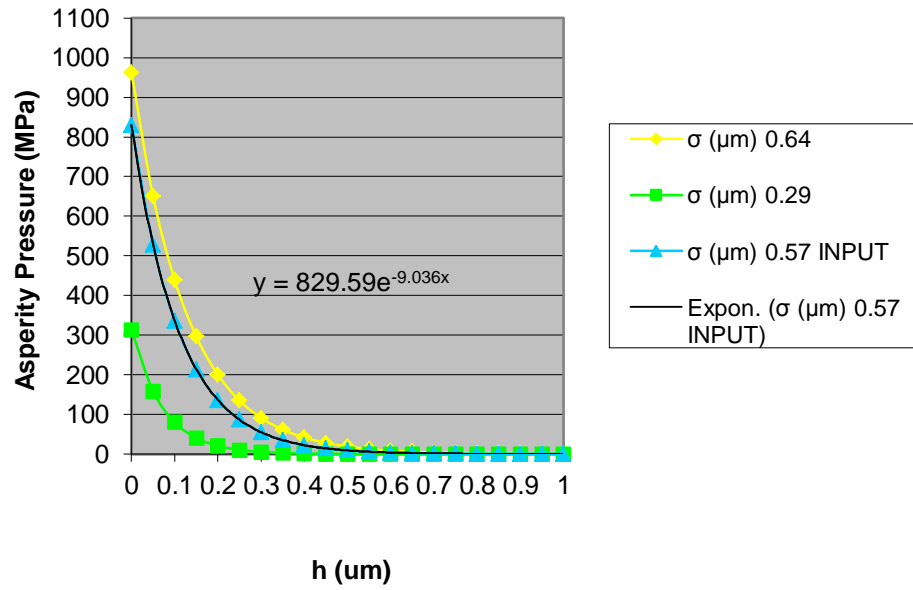


Figure 3.27 Asperity contact pressure against oil film thickness  
(adopted from data and interpolated) [147]

Gas pressure load from the back of piston ring:

$$\frac{W}{L} = P_1 B \quad (3.83)$$

Hence, Coefficient of friction:

$$\mu = \frac{F}{W} = \frac{\int_{x_{c1}}^{x_{c2}} a_{asp} P_c dx}{P_1 B} \quad (3.84)$$

### 3.1.2.3 Piston ring 'mixed lubrication' mathematical model:

In between the boundary and hydrodynamic lubricant lies a zone, where the lubrication is the combination of both boundary and hydrodynamic lubrication.

Many piston rings experience fluid-film lubrication for much of each operating cycle and hence their operating characteristics in these periods can be analyzed by conventional hydrodynamic theory. However, like many dynamically loaded reciprocating components, they also encounter mixed and boundary lubrication during the severe conditions of operation near TDC.

Furuhamma et al measured the variations of friction force during whole stroke of a piston. It indicated that the friction force of a piston ring comprised of two parts, the



hydrodynamic friction force due to mixed lubrication and the solid friction due to local asperity contact near TDC. [141]

The lubrication regime in the vicinity of the dead centres is a combination of boundary or mixed lubrication with an additional lubricant film squeeze effect, whilst during the piston mid-stroke regions hydrodynamic lubrication is prevalent. This has been established from both modeling [142, 25,143] and experimental work [144, 145, 146, 147].

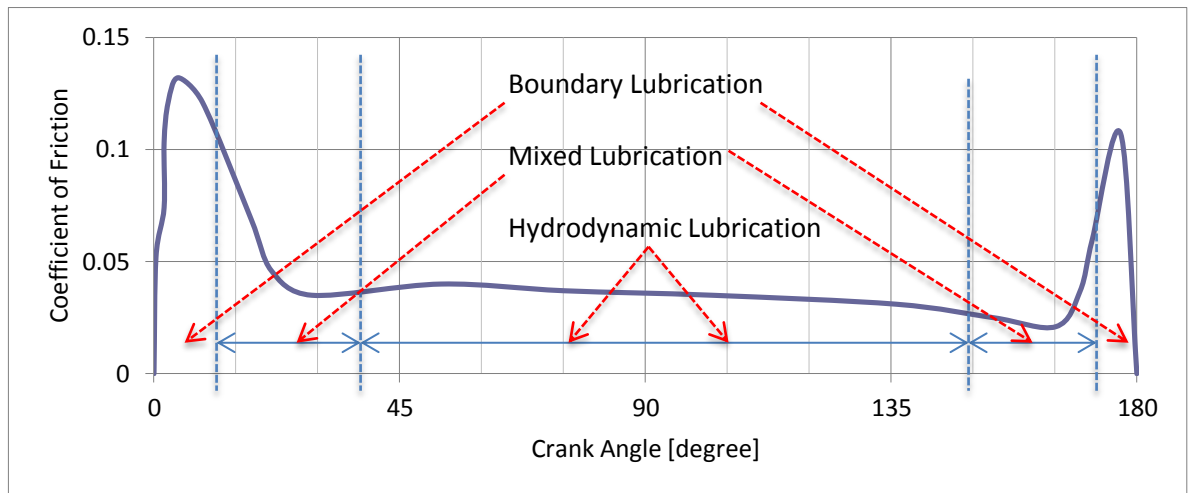


Figure 3.28 Different lubrication regimes encountered during an expansion stroke at 120r/min and 3 Kgf. [147]

By adding the boundary lubrication and hydrodynamic lubrication and apportioning the percentage according to their share with a drawn slopes of Figure 3.27 and 3.28 against crank angle, the friction force of mixed lubrication can be ascertained as in the Equation 3.85.

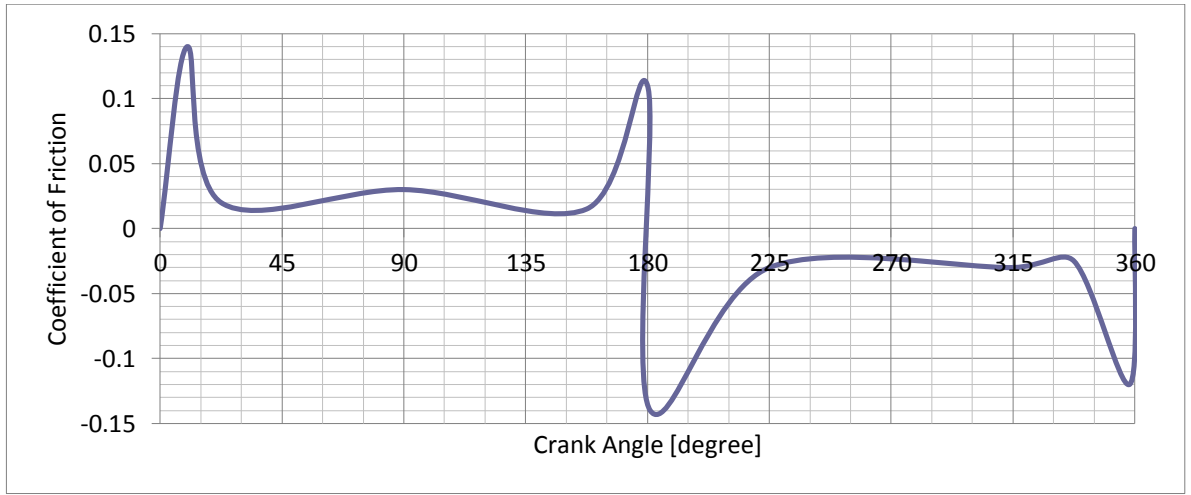


Figure 3.29 Friction results exhibiting 3 lubrication regimes [147]

$$\frac{F}{L} = m * \int_{x=0}^{x=B} \tau dx + (1 - m) * \int_{x_{c1}}^{x_{c2}} a_{asp} P_c dx \quad (3.85)$$

Where,

m and (1-m) are the ratio of hydrodynamic and boundary lubrication

B is the piston ring's vertical height

xc1 and xc2 define the boundaries of the portion of the ring-liner surfaces that are in asperity contact for  $h/\sigma < 4$ .

The coefficient of friction,  $\mu$  then can be calculated accordingly at various crank angles between the boundary and hydrodynamic lubrication.

#### **3.1.2.4 Piston ring 'No-Lubrication' mathematical model:**

When there is no lubrication, there is strong adhesion between the asperities of mating surfaces, which generates extreme frictional force and wear particles from the wiped asperities.

Under boundary lubrication, the coefficient of friction is defined as [28]:

$$\mu = \frac{\tau}{P_y} \quad (3.86)$$

where,

$\tau$  is the effective shear stress of the material (Pa)

$P_y$  is the plastic flow stress (yield pressure) of the material (Pa)

Effective shear stress is about 0.2 of the yield stress. Thus the coefficient of friction in boundary lubrication,  $\mu = 0.2$ .

The highest adhesion occurs between identical metals. The coefficient of friction between clean iron surfaces is very high, up to  $\mu = 3$ . The simple theory of adhesion fails to predict such high values of friction coefficient, and in order to explain this phenomenon, the process of asperity junction growth is considered. In the plastically deforming adhesion junction both normal and tangential stresses are involved.

To explain the 'asperity junction growth' process, we assume that initially there is a normal load acting on the asperity which is high enough for the asperity to plastically yield. Since the contact is in the 'plastic state', i.e., material flows, the contact area will be increased due to the tangential stress. Consequently, the normal pressure will be reduced owing to the increase in contact area (i.e. the same load is now carried by an increased area). The increased contact area will also be able to take larger tangential force. This increment or growth of tangential force and the contact area will continue until the material reaches its maximum (yield) shear stress. Coefficient of friction will also consequentially increase and the seizure of the mating parts will follow.

In precise terms, the mechanism of junction growth can be described by considering the Von Mises Yield Criterion. According to this criterion, a material will plastically deform when:

$$p_n^2 + 3\tau^2 = P_y^2 \quad (3.87)$$

where,

$p_n$  is the normal contact stress (pressure) (Pa)

$\tau$  is the effective shear stress in the contact (Pa)

$p_y$  is the plastic flow stress of the material (Pa)

As the normal stress ' $p_n$ ' and tangential stress ' $\tau$ ' together control the plastic yielding, we can write a relationship as follows:

$$p_n^2 + C\tau^2 = P_0^2 \quad (3.88)$$

where,

C is an arbitrary constant of approximate value of 10

$P_0$  is the plastic flow stress of the material when there is no tangential (frictional) force [Pa]

From the Equation 3.86, it can be seen that when the asperity experiences only a normal load, i.e.,  $\tau = 0$  then:

$$p_n = p_0$$

The stresses ' $p_n$ ', ' $\tau$ ' and ' $P_0$ ' can be expressed as follows:

$$p_n = \frac{W}{A_r} \quad (3.89)$$

$$\tau = \frac{F}{A_r} \quad (3.90)$$

$$P_0 = \frac{W}{A_{r0}} \quad (3.91)$$

where,

F is the friction force (N)

W is the normal force (load) (N)

$A_r$  is the actual area of contact in the presence of tangential force ( $m^2$ )

$A_{r0}$  is the actual area of contact in the absence of tangential force ( $m^2$ )

Substitution of Equations 3.89, 3.90 and 3.91 into Equation 3.88 gives:

$$\left(\frac{W}{A_r}\right)^2 + C \left(\frac{F}{A_r}\right)^2 = \left(\frac{W}{A_{r0}}\right)^2 \quad (3.92)$$

By rearranging the Equation 3.92, we obtain the relationship between the increase in actual contact area and the tangential force, i.e.:

$$\frac{A_r}{A_{r0}} = \left[1 + C \frac{F^2}{W^2}\right]^{\frac{1}{2}} \quad (3.93)$$

It is obvious from the Equation 3.93 that when the tangential force is increased, it results in increased adhesion as the actual area of contact grows, e.g. if  $C = 10$ , and the ratio of tangential force to normal force is 0.3, then the contact area will increase by 40 percent or a factor of 1.4. In clean surfaces, when the value of 'F' is

very high, the increase of the actual contact area is very obvious. When the tangential force is increased, the actual contact area also increases until the yield shear stress is reached at the asperities contact. That is when the macroslip occurs.

For high values of yield shear stress this condition is hard to reach because the increase in the contact area is almost matched by the increase in the tangential force as 'F' exceeds 'W',  $\frac{A_r}{A_0}$  tends to  $C^{0.5} \frac{F}{W}$ .

$$\frac{A_r}{A_{ro}} = C^{\frac{1}{2}} \frac{F}{W} \quad (3.94)$$

In contrast, it can be seen from Equation 1 that for small values of tangential forces and a limiting shear stress, the increase in 'A<sub>r</sub>' is negligible, so that the relationship  $\mu = \frac{\tau}{p_y}$  is approximately true.

In cases of extremely high adhesion and limiting interfacial asperity shear stress, the rate of increase in the real contact area with tangential force is sufficient to maintain an approximately constant asperity interface shear stress. This is because the ratio of tangential force to contact area does not change significantly so complete seizure of the sliding members can occur.

In cases of extremely high adhesion and limiting interfacial asperity shear stress, the rate of increase in the real contact area with tangential force is sufficient to maintain an approximately constant asperity interface shear stress. This is because the ratio of tangential force to contact area does not change significantly so complete seizure of the sliding members can occur (positive feedback loop).

### **3.2 Theory and modeling of thermoelectric method:**

#### ***3.2.1 Theory of thermoelectric method:***

The piston ring and liner undergoes boundary lubrication with approximate friction coefficient of  $\mu = 0.08$  near TDC and BDC owing to the low velocity. As the ring and liner surfaces rubs against each other under boundary conditions, the heat generated corresponds to the product of velocity, pressure and friction coefficient,

and it has to be dissipated by conduction into both bodies, thus raising their temperature.

If higher friction occurs in a particular spot, due e.g. to a momentary lack of lubrication or a speck of dirt, more heat is produced and the temperature of this spot will rise. It will expand, and a tiny bulge will be formed. This bulge will rub harder, produce more heat, and consequently grow further rubbing still harder, etc.

Now, if the rate of wear under such conditions is high enough to wear the bulge off as fast as it grows, conditions remain stationary and, as soon as normal lubricating is reestablished, the spot cools off and shrinks, producing a little scar. But if the rate of growth is faster than the wear rate, the bulge will rub more and harder, and will destroy lubrication completely. The temperature then rises above critical levels for welding, and scoring will result.

### **3.2.2 Mathematical modeling of thermoelectric method:**

The additional heat production is increased by greater values of rubbing speed, 'C<sub>m</sub>', friction coefficient, 'μ' and pressure, 'p':

$$\frac{dQ}{dx} = f C_m \mu p \quad (3.95)$$

In an one dimensional system, when piston ring is rubbing over the liner, the heat will be absorbed by both rings and liner. Total additional heat contained in the liner and rings is:

$$\Delta Q = f \rho c_{sp} \int_0^l (T_1 - T_0) dx \quad (3.96)$$

and the total elongation of the liner

$$\Delta l_t = \epsilon \int_0^l (T_1 - T_0) dx \quad (3.97)$$

By elimination we get

$$\Delta l_t = \epsilon \frac{\Delta Q}{f \rho c_{sp}} \quad (3.98)$$

If the boundaries of the system are assumed to be rigid, this thermal elongation must be taken up by wear and elastic compression of the liner.

$$\Delta l_t = \Delta l_{wear} + \Delta l_{elastic} \quad (3.99)$$

If the wear rate is sufficiently high, nothing is changed in the system geometry and the 'wear will prevent scuffing'. But if it is too low, the elastic compressions generate an additional contact pressure, which will in turn increase the friction heat and thus lead to an exponential growing friction. Assuming in the extreme case the wear to zero, we get the pressure rise

$$\Delta p = \Delta l_t \frac{E}{l_r} = \frac{\Delta Q \epsilon E}{f \rho c_{sp} l_r} \quad (3.100)$$

From equation 3.95 and the equality of the quantity of heat generated and the quantity of heat stored follows:

$$\Delta Q = \int_0^l dQ dt = \int_0^l f C_m \mu p dt \quad (3.101)$$

With equation 3.100, we obtain

$$\Delta p = \frac{\epsilon E}{\rho c_{sp} l_r} \int_0^l C_m \mu p dt \quad (3.102)$$

Assuming constant friction conditions, the integral solution is:

$$\begin{aligned} \Delta p &= \frac{\epsilon E}{\rho c_{sp} l_r} C_m \mu p \Delta t \\ \frac{\Delta p}{\Delta t} &= \frac{\epsilon E C_m \mu p}{\rho c_{sp} l_r} \end{aligned} \quad (3.103)$$

This rate of pressure rise characterizes the potential scuffing index and is related to  $T_t$ , the instantaneous temperature of liner and rings and

where,

f	Cross section of rubbing element	(m <sup>2</sup> )
l <sub>r</sub>	Length of liner and ring thickness	(m)
C <sub>m</sub>	Sliding speed (mean piston speed)	(m/s)
p	Pressure	(N/m <sup>2</sup> )

E	Young's modulus	(N/m <sup>2</sup> )
$\rho$	Density	(kg/m <sup>3</sup> )
$c_{sp}$	Specific heat	(J/kg. °C)
$\epsilon$	Coefficient of thermal expansion	(m/m.°C)
$\mu$	Coefficient of friction	(-)
Q	Stored energy	(J)
$\Delta p/\Delta t$	'Scuffing index'	(N/m <sup>2</sup> s)

In order to prevent scuffing, Equation 3.103 can be used with a set amplitude for the maximum rate of pressure rise. Accordingly, a maximum temperature  $T_t$  can also be derived. However, such dependence on the maximum temperature may be too late to prevent the onset of scuffing, as the reflected high temperature simply meant that the scuffing already is in progress. From the previous experience and the recorded temperature analysis of cylinder liners, it was discovered that, a series of fluctuating temperature pattern were always present prior to the onset of scuffing. It was also noted that full blown scuffing could be avoided, if some countermeasures are taken during this fluctuating temperature symptom, such as reducing the engine load and increasing the lubricant flow etc. It is then confirmed that the fluctuating temperature was related to the higher friction heat generated from the adhesive wear breaking of oil film on the liner surface and restoring the oil film with fresh supply of oil. This sporadic oil film breakage and restored film thickness was responsible for the temperature fluctuation. Hence, this fluctuating temperature pattern could be used as the early warning for scuffing detection.

Fluctuating temperatures were not found to be regular. Interval of wave peak, amplitude and mean temperature were also not fixed. Furthermore, when the gap or open end of the piston ring came in line with the temperature sensor, the temperature measured on the sensor rose. The temperature subsequently dropped when the ring end moved away from the sensor.

Hence, it was necessary to differentiate the fluctuating temperature from the ring-end temperature rise in order to create a mathematical function to assess the detection of scuffing. A Fourier series model was formulated for the analysis of the



series of fluctuating pattern against a specified period interval as shown in the Figure 3.30.

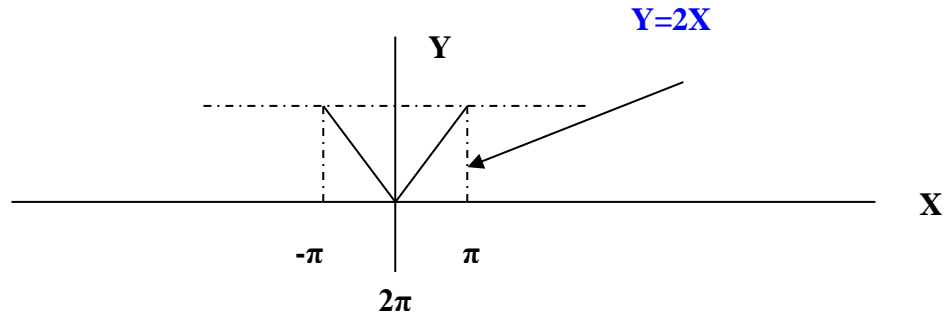


Figure 3.30 Fourier profile of temperature readings

$$y = f(x) \quad 0 < x < \pi$$

$$f(x) = f(x + 2\pi) \quad (3.104)$$

$$a_0 = \frac{1}{\pi} \int_0^{\pi} f(x) dx = \frac{2}{\pi} \int_0^{\pi} x dx = 2\pi \quad (3.105)$$

$$a_n = \frac{1}{\pi} \int_0^{\pi} f(x) \cos nx dx = \frac{4}{\pi} \int_0^{\pi} x \cos nx dx = 2\pi$$

Integration by parts:

$$\int u dv = uv - \int v du$$

Taking  $x = u$ ;  $du/dx = 1$ ;  $du = dx$

$dv = \cos nx$ ;  $v = (1/n) \sin nx$

$$a_n = \frac{4}{\pi} \int_0^{\pi} u dv = uv - \frac{4}{\pi} \int_0^{\pi} v du$$

$$a_n = \frac{4}{\pi} \left\{ \left[ \frac{x}{n} \sin nx \right]_0^{\pi} + \left[ \frac{1}{n^2} \cos nx \right]_0^{\pi} \right\} = \frac{4}{\pi n^2} (\cos n\pi - 1) \quad (3.106)$$

$\cos n\pi = 1$  (n even)

$\cos n\pi = -1$  (n odd)

$$a_n = 0 \text{ (n even)}; a_n = -\frac{8}{\pi n^2} \text{ (n odd)} \quad (3.107)$$

$$b_n = 0; \text{ since } f(x) \text{ is an even function} \quad (3.108)$$

So,

$$f(x) = \frac{1}{2} a_0 + \sum_{n=1}^{\infty} a_n \cos nx + b_n \sin nx$$

$$f(x) = \frac{1}{2} 2\pi - \frac{8}{\pi} \sum_{n=1}^{\infty} \frac{\cos nx}{n^2}$$

$$f(x) = \pi - \frac{8}{\pi} \left\{ \cos x + \frac{1}{9} \cos 3x + \frac{1}{25} \cos 5x + \dots \right\} \quad (3.109)$$

The solution of the fourier series for various values of 'x' is shown below in Figure 3.31.

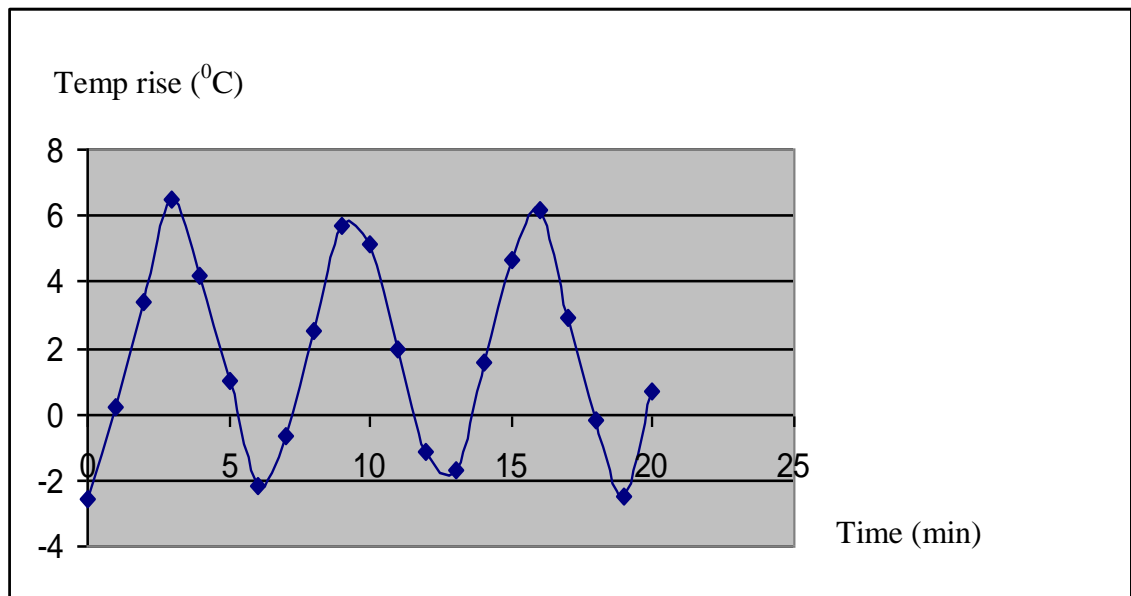


Figure 3.31 Fourier profile of temperature reading

### 3.3 Theory and modeling of eddy current method:

#### 3.3.1 Theory of eddy current method:

Eddy current is defined as the electric current induced within conductors owing to changing magnetic field in the conductor. In eddy current sensors, the eddy currents produce a magnetic field that opposes the field generated by the probe coil. The magnetic fields interaction varies with the distance between the probe and the target and is reflected in the voltage output. Eddy current sensor is also known

as inductive sensor. Unlike other sensors, they do not need a contact medium (couplant).

The goal of the research is to detect the scuffing on the piston rings and the liner, Figure 3.32. In order to achieve the penetration depth and the resolution for such defects, choice of appropriate mean diameter of excitation coil is vital. The optimum detection can be obtained only at certain frequency.

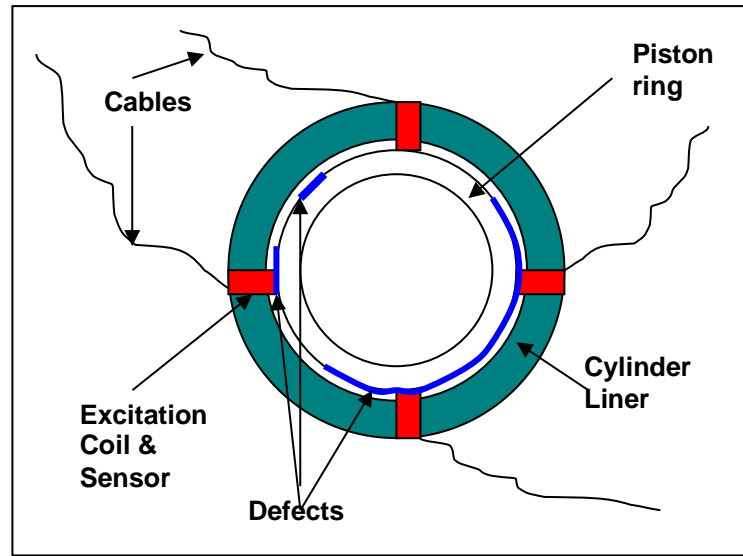


Figure 3.32 Eddy current sensor (ring/liner)

### 3.3.1.1 Effective Depth:

In eddy current sensor, the impedance of the coil changes as the distance between the target and the probe changes.

An eddy current sensor is useful for shallow depths in vicinity of its conductive target surface. Its effective depth is [148],

$$\delta_d = \frac{1}{\sqrt{\pi f_e \mu_m \sigma_c}} \quad (3.110)$$

Where,

$\delta_d$  is the depth

$f_e$  is the excitation frequency of the circuit

$\mu_m$  is the magnetic permeability of the target material

$\sigma_c$  is the conductivity of the target material

For inducing eddy currents in the material, the magnetic field of an eddy-current sensor has to penetrate the surface of the target. When the material is too thin, the target will have smaller eddy currents and consequently the target will generate a weaker magnetic field. This will reduce the sensitivity of the sensor and will result in to a smaller signal to noise ratio.

The material and the frequency of the sensor's oscillating magnetic field defines the depth of penetration of the magnetic field of the sensor. It could typically use a frequency of 1 to 2 MHz.

The transducer is effective only when the target material is at least three times thicker than the effective depth of the eddy currents, as the actual amplitude of the eddy current decreases quadratically with the distance.

### **3.3.1.2 Eddy current sensors:**

Eddy current methods, Figure 3.33, conventionally cover the frequency band up to approx.10 MHz.

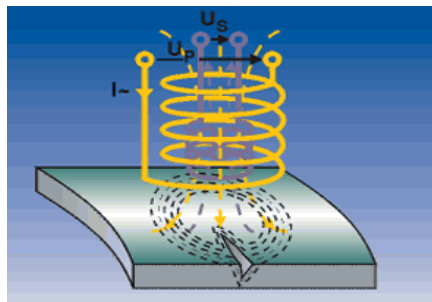


Figure 3.33 Eddy current sensor [39]

Sensors internal calibration is usually done in the factory. The calibration is material dependent. With regard to the recalibration of the sensor, it can be recalibrated in the field provided the type of the material is the same.

#### **3.3.1.2.1 Sensor Construction**

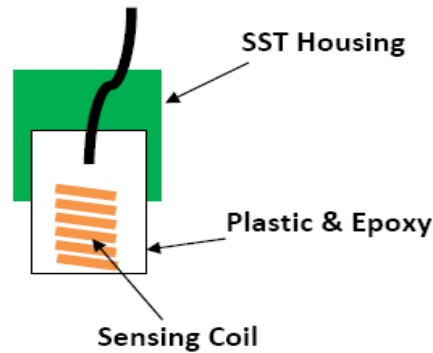


Figure 3.34 Eddy-Current Probe Construction

Sensing coil located near the end of the probe is the main functional piece of an eddy-current sensor. Alternating current is passed through the sensing coil that produces an alternating magnetic field, which sense the distance between the probe and the target. The coil resides within a plastic and epoxy capsule, which protrudes out of a housing made of stainless steel. This is because, unlike the capacitive sensors, magnetic field of an eddy-current sensor is not well focused and the protrusion of the epoxy covered coil allow the sensing field of the coil engage the target as shown in Figure 3.34.

#### **3.3.1.2.2 Spot Size, Target Size, and Range**

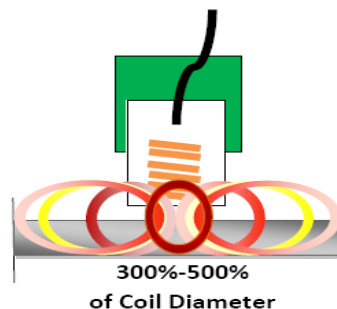


Figure 3.35 Eddy-Current probe spot size

The magnetic fields of an eddy current sensor produces a large spot size that is three times the diameter of the probe's sensing coil as shown in Figure 3.35. On the other hand, the ratio of the sensing distance to the sensing coil diameter is 1:3; e.g. for 1mm sensing range, the diameter of the sensing coil should be 3mm.

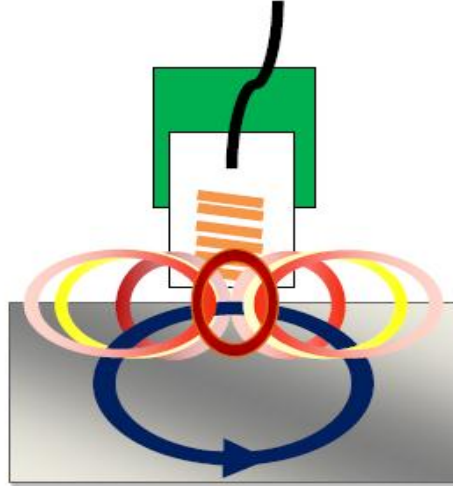


Figure 3.36 Magnetic field induces eddy current in conductive target

Magnetic field around the sensing coil of the eddy sensors is always maintained constant. As such, when the eddy currents produced in the target oppose the magnetic field of the sensing coil, the eddy sensor increases the current supply to its sensing coil for it to maintain its original magnetic field, Figure 3.36. Depending on the distance of the target from the probe, the required current in the sensing coil to maintain constant magnetic field will vary. The sensing coil current is converted to the output voltage, the value of which indicates the position of the target with respect to the probe.

#### **3.3.1.2.3 Target Materials and Rotating Targets**

Permeability and resistivity of the target material have strong influence on the strength of the eddy current. Different materials have different permeability and resistivity. Even for the same materials, these two properties can be different if they underwent different processing techniques; e.g. heat treatment, annealing.

Iron and steel are magnetic materials and they have high permeability, which can cause slight error for the eddy current sensor even within the same material. The

material's permeability changes somewhat around the microscopic cracks and material variations often present in the same material. High-resolution eddy-current sensors is able to detect these changes in the magnetic materials of very high permeability.

#### **3.3.1.2.4 Environmental Parameters: Temperature**

Eddy-current probes can operate in hostile environments within a temperature range of -25 to +125°C. If Teflon FEP cables are used instead of the standard polyurethane cables, eddy-current probes can measure the temperature up to +200°C. Capacitive probes, on the other hand, only have an operating range of +4 to +50 °C. Additionally, they are affected by condensation.

#### **3.3.1.2.5 Probe Mounting**

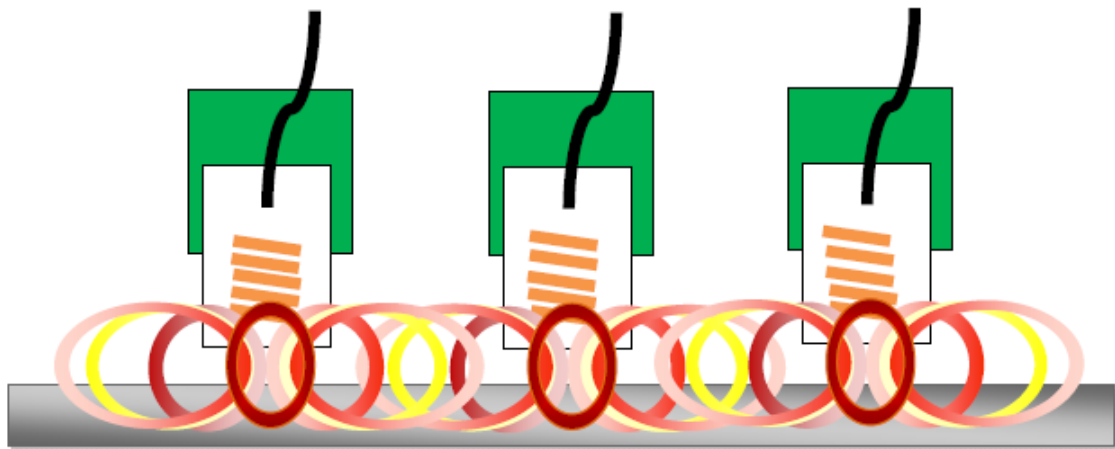


Figure 3.37 Interference of eddy-current probes mounted near each other

As the diameter of the magnetic field in eddy current sensor is more than three times that of the probe coil diameter, the magnetic fields will interact when multiple probes are mounted close to each other, as shown in the Figure 3.37. As a result, the sensor outputs will experience errors.

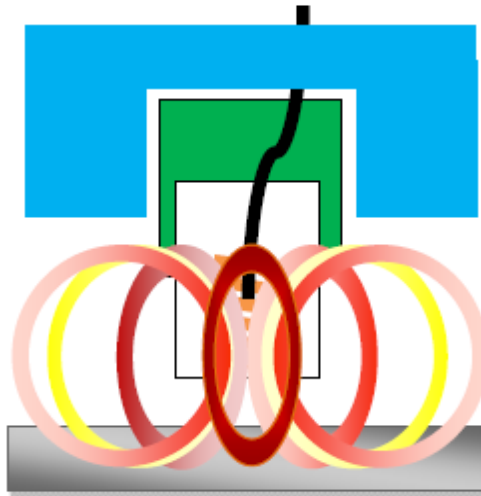


Figure 3.38 Mounting hardware can interfere with eddy probe magnetic field

There is also magnetic field behind the eddy-current probe. This magnetic field is present up to one and a half times the diameter of the coil. Metallic mounting hardware in this area will interact with the field and influence the sensor output as shown on the Figure 3.38. In such cases, sensors should be calibrated along with the mounting hardware.

#### **3.3.1.2.6 Error Sources**

Magnetic field in eddy current sensor can be changed by various factors other than the distance between the target and the probe. These factors produce error in the output signal.

Magnetic fields and sensor's output of eddy current are not influenced by nonmagnetic and nonconductive contaminants such as dust, sludge, water, and oil trapped between the eddy-current sensor and the target. Because of this, an eddy-current sensor is a suitable choice for a dirty or hostile environment, e.g. cylinder liner and piston ring condition monitoring.

#### **3.3.1.2.7 Linearity:**

The deviation of measured output from that of a straight line characteristics is termed as the linearity specification.



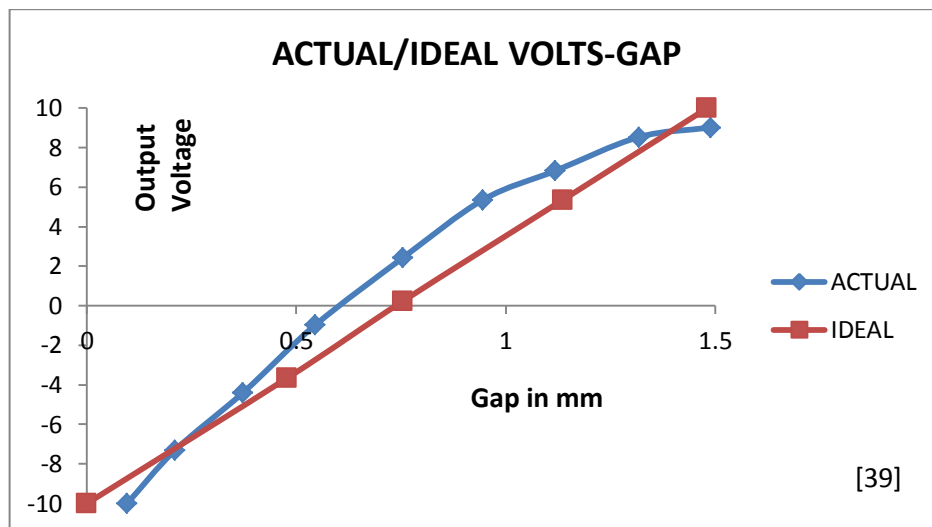


Figure 3.39 Linearity error band - Measured data deviates from the straight line  
(Data from reference)

Linearity error is calculated against the best fitting straight reference line of calibrated data using least squares fitting method as shown in Figure 3.39. The maximum deviation of the actual and the ideal line of a point is the linearity error. It is expressed in terms of percent of full scale; e.g, highest error of 0.003mm in the full scale calibration of 1mm, the linearity error is 0.3%.

#### **3.3.1.2.8 Effective Sensor Range:**

Effective range of an eddy current transducer, in practice, is the stated range offset from the target surface by 20%; e.g. an eddy current transducer of 2.0 mm range will be effective from 0.4 mm to 2.4 mm from the target surface.

The flat surface area of the target must be bigger than the diameter of the probe tip, otherwise the output signal will decrease.

#### **3.3.1.2.9 Cable length:**

Decision on cable length for eddy current sensors is very crucial, as cable length affects calibration. Hence, cable length alteration is not allowed once the sensors are ready to be installed for the specified application. Sensors are usually ordered with tailor made cable lengths to suit the needs of the installation.

### **3.3.1.2.10 Frequency range and power consumption:**

The bandwidths of eddy-current sensors lie between 10-15kHz. Nevertheless, bandwidths of as high as 80 kHz can be found in some eddy sensors.

An eddy-current probe consumes power between 40μW to 1mW.

Eddy-current sensors have many advantages compared to other non-contact sensors like optical, capacitive and laser.

- Tolerance of contaminants and dirty environments
- Not sensitive to material in the gap between the probe and target
- Much smaller than laser interferometers
- Less expensive than laser and capacitive sensors
- High frequency response

The disadvantages of Eddy-Current sensors are as follows:

- Extremely high resolution is required
- Large gap between sensor and target is needed
- Non linear relationship between distance and impedance of coil
- Temperature dependent
- Effective only on conductive material with adequate thickness

### **3.3.2 Mathematical Model of eddy current scuffing detection:**

Eddy sensors measurement of the roughness of the piston ring surface is used for the model. The monitoring of the roughness is then coordinated with the crank angle to determine the position of damage.

$$R_s = \int_{\theta=0}^{\theta=2\pi} r_s(\theta) d\theta \quad (3.111)$$

$$L_s = f(\theta)$$

where,

$R_s$  = average roughness integrated over a stripe and the piston stroke

$r_s$  = average roughness monitored per stroke over a stripe and piston stroke

$\theta$  = Crank angle

$L_s$  = Piston stroke as a function of crank angle

The roughness is then compared with the reference roughness measured and stored when the piston and liner were in good condition or in any other reference condition.

The software compares the longitudinal average roughness which is the integral of the roughness profile per stroke over the engine stroke. Greater the number of radially placed eddy sensors, greater is the accuracy of the roughness measurement.

The system allows the determination of deviations of average roughness in relation to the average reference roughness, and hence, allows the definition of alarm levels.

The sensors can give complimentary information such as oil film thickness, blocked piston rings and piston rings surface condition or profiles.

### **3.4 Theory and modeling of acoustic emission method:**

#### ***3.4.1 Theory of acoustic emission method:***

Acoustic emission method (AET) is known as one of the non-destructive testing methods. Other nondestructive test (NDT) methods are applied before or after loading of a structure. However, AET is generally applied during loading.

NDT techniques are differentiated on the basis the technique is applied and the type of information being received. The ultrasound method (UT) uses externally generated source signal and receiver to detect a defect in a specimen. AET, on the other hand, detects the elastic waves radiated by a growing fracture itself. Hence, AET is thought to be a "passive" non-destructive method, because it detects the defects as they develop during the measurement. Figure 3.40 shows the difference between "active" and "passive" NDT. In active methods, the source emitting the waves is usually applied to the material, Figure 3.40(a). On the contrary, the

sources are within the material in the passive method, Figure 3.40 (b); they quasi “produce” the test signal.

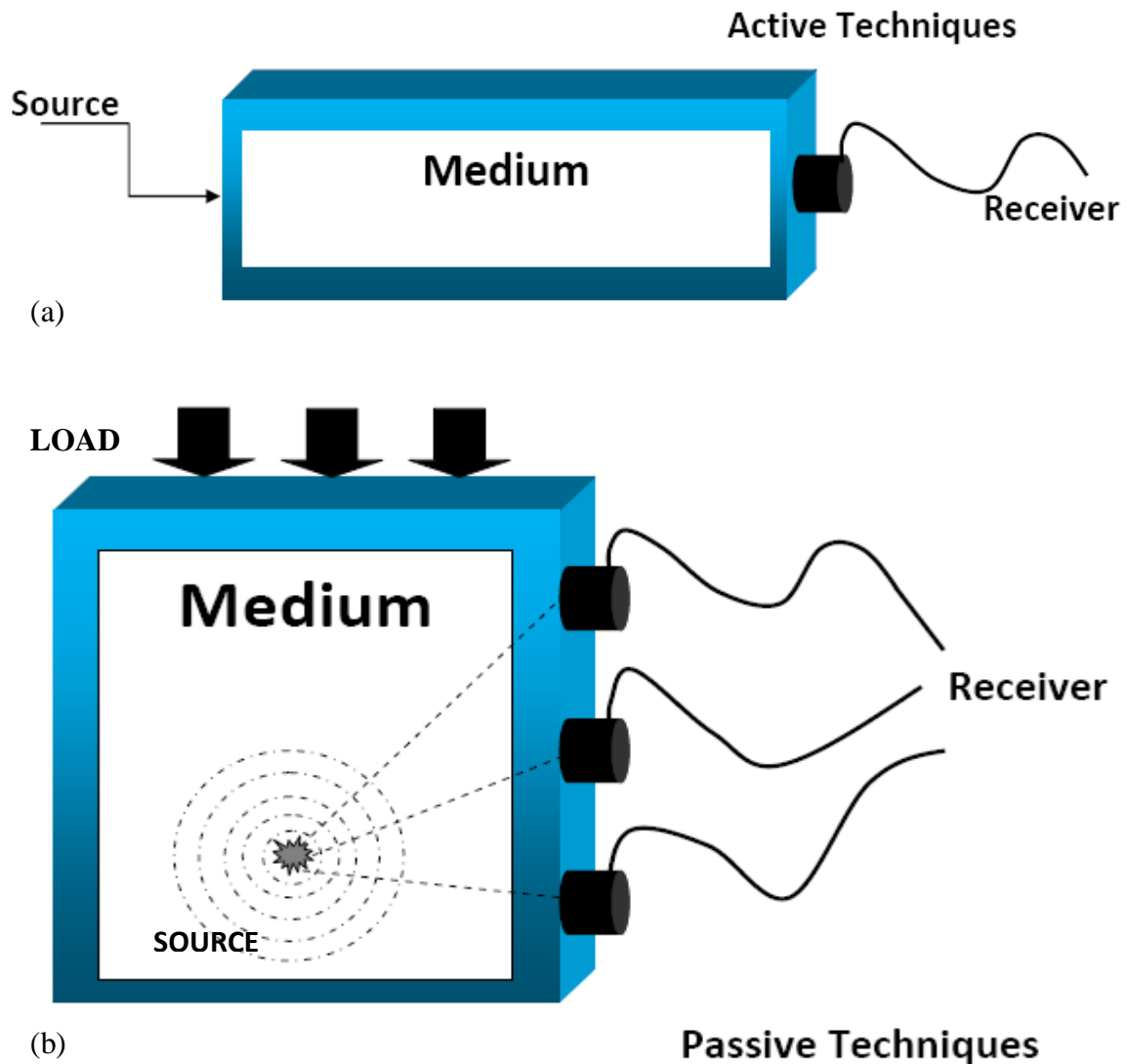


Figure 3.40 Comparison of NDT principles using active or passive techniques

Unlike other NDTs, in AET the damage processes in materials being tested can be observed during the entire load history. Only a few sensors are adequate for AET to observe the AE activity of a structure. The sensors can be attached to the surface of the specimen for the test period and do not have to be moved around for scanning point by point. Unlike some other NDTs, AET does not require access to both sides of the object being measured.

Materials response to stress can be elastic or plastic deformation. Elastic stress-strain relationship of materials is governed by Hooke's Law. AE picks up the non-elastic deformations in a material and hence only detects the new cracks and the extension of existing cracks or friction processes, which are often related to internal mechanical or thermal loads or external loads applied on the specimen. AE tests can be conducted under normal, service conditions or during a minor increase of the load. Because of this, AE is very useful in testing structures under real load conditions to record a potential failure development.

One of the demerits of the AET method is that a specific test is not truly reproducible owing to the nature of the signal source. Specimens of the same shape and same material properties may not always result in similar AE activities under load. Because of this AE test results should always be compared with other testing methods.

Another point of concern of acoustic emission is problems related to the influence of ambient noise and the weakening of signals, which results into low signal-to-noise ratio. Hence, AE needs highly sensitive sensors along with amplifiers and pre-amplifiers. It also needs powerful data processing method to detect the emissions, to localize them and to apply other superior methods or inversions.

#### ***3.4.1.1 Fundamentals of AE Measurement:***

Acoustic Emission (AE) can be classified into two types:

1. Continuous Emission (Metal friction/cutting)
2. Burst Signals (cracking)

In a material, failure process involves the release of stored strain energy and formation of cracks causing elastic waves, which are detected as AE waves. These AE waves propagate inside the material and are picked up by suitable AE sensors located on the outside surface of the material. Current AE devices are completely digitized other than the detection systems, which are still analog.

Kaiser's work on AE demonstrated that AE is an irreversible phenomenon. Damage mechanisms such as cracks release acoustic waves as the load or stress is increased and they initiate and propagate. If the load is released, and then gradually reapplied, no additional AE will be generated until the load exceeds its previous maximum value. Above the previous maximum value, existing damage may propagate or new damage may initiate, both of which may produce AE. This irreversible phenomenon of AE has been designated as the Kaiser effect. The Kaiser effect has been widely used in AE testing to determine information about previous maximum stress on a structure.

A standard AE detection system is illustrated in Figure 3.41. AE sensor picks up the AE waves, which changes the dynamic motions at the material surface into electrical signals. The signals are then amplified by a preamplifier and a main amplifier. As the signal-to-noise ratio of equipment is low, amplifier gain of 100 times is typically used and the amplifiers are often able to provide more than 1000 times gain. To reduce the noises, band pass filter is used. Band width of a few kHz to some 100 kHz or 1 MHz is used in the AE measurement of engineering materials.

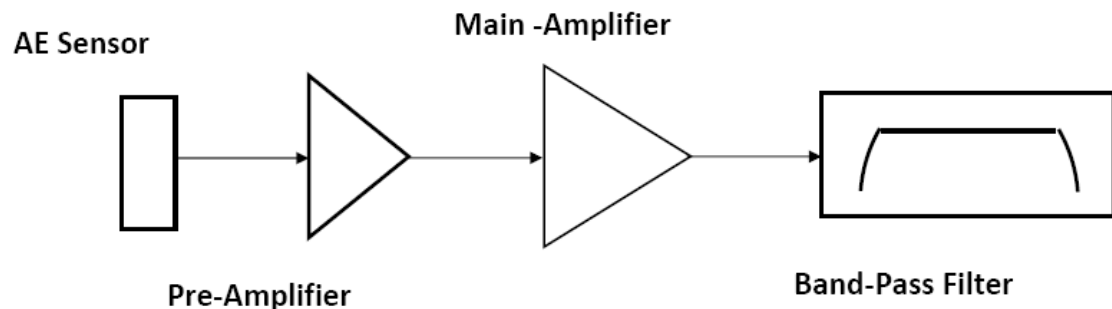


Figure 3.41 AE Detection System

AE waves are elastic waves in a solid. They are not sonic waves. The waves can be audible or inaudible, which depends on the frequency of the wave. Audible (acoustic) frequency is lower than 20 kHz. The frequency of wave higher than 20kHz is considered inaudible and is known as ultrasonic waves. Strictly speaking, AE waves are neither ultrasonic nor acoustic. Rationally, in cracking detection, AE waves are elastic waves from dislocation motions in the material. Hence, it can be

said that AE waves are not fully related with creating mechanisms, rather are responsible for the results of travel paths, media and the systems of detection.

#### **3.4.1.2 Factors Affecting AE Response:**

Factors that have effects on the relative amplitude of the AE response are shown in Table 3.3.

Factors increase acoustic emission response amplitude		Factors decrease acoustic emission response amplitude	
<ul style="list-style-type: none"> <li>• High Strength</li> <li>• High strain rate</li> <li>• Low temperature</li> <li>• Anisotropy</li> <li>• Non homogeneity</li> <li>• Thick Sections</li> <li>• Brittle failure (Cleavage)</li> </ul>	<ul style="list-style-type: none"> <li>• Material Containing discontinuities</li> <li>• Martensite phase transformation</li> <li>• Crack propagation</li> <li>• Cast materials</li> <li>• Large grain size</li> <li>• Mechanically induced twinning</li> </ul>	<ul style="list-style-type: none"> <li>• Low Strength</li> <li>• Low strain rate</li> <li>• High temperature</li> <li>• Isotropy</li> <li>• Homogeneity</li> <li>• Thin sections</li> <li>• Ductile failure (shear)</li> </ul>	<ul style="list-style-type: none"> <li>• Material without discontinuities</li> <li>• Diffusion-controlled phase transformations</li> <li>• Plastic deformations</li> <li>• Wrought materials</li> <li>• Small grain size</li> <li>• Thermally induced twinning</li> </ul>

Table 3.3 Factors that affect relative amplitude of acoustic emission response [149]

Various parameters can be obtained from the signal to assess the significance of an AE source and to read the AE signals. The signal waveform depends on the source type, source-to-sensor signal path, sensor properties and the measurement system. On the other hand, the parameters extracted from the signal depend on the type of the signal.

#### **3.4.1.3 Detection of AE:**

In the fracturing process of a material, stored strain energy is released and is consumed by newly developed surfaces, i.e. cracks and AE elastic waves are emitted, which propagate inside the material and are picked up by an AE sensor as shown in Figure 3.42.

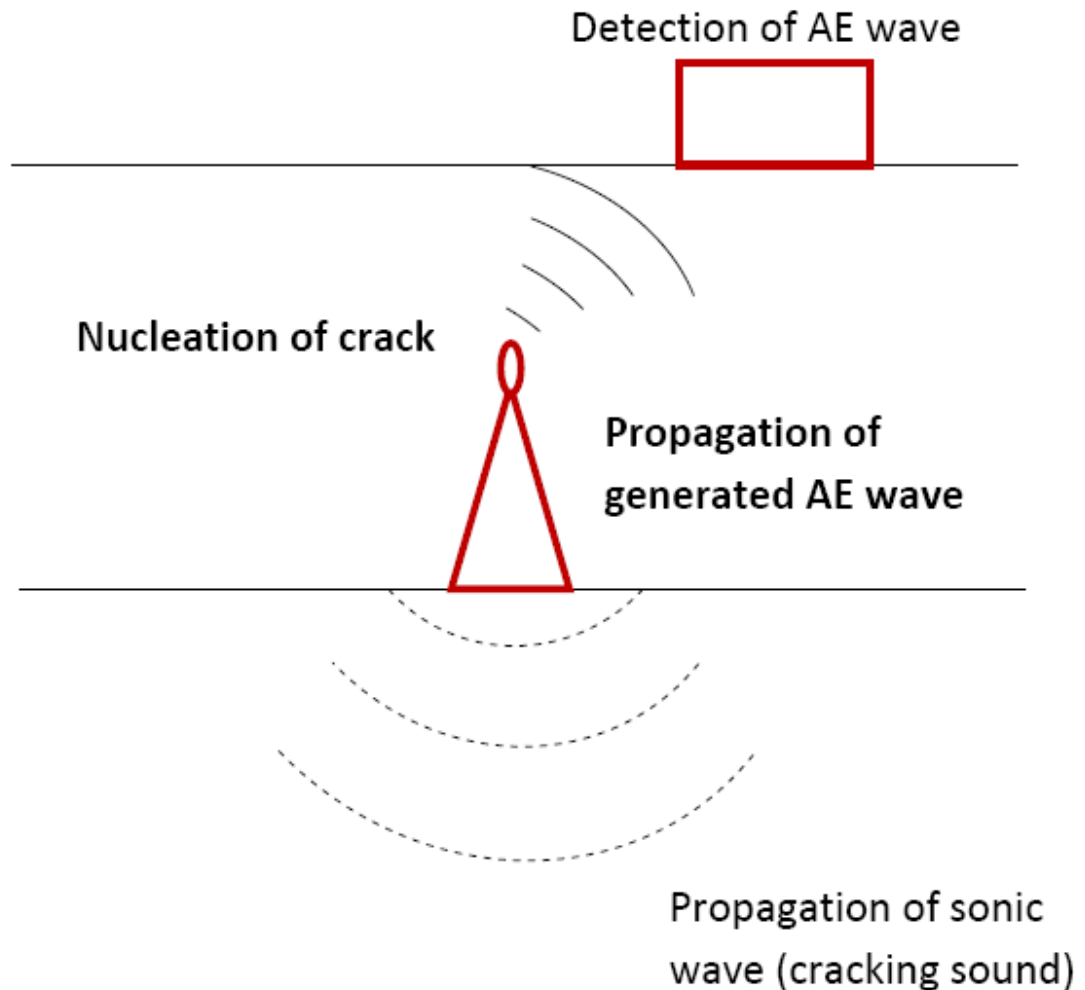


Figure 3.42 Detection of AE wave

In AE measurement, a contact type sensor is commonly used. Among other sensors, piezoelectric sensors have the best combination of low cost, high sensitivity, ease of handling and selective frequency responses.



As the amplitude of AE signals is low, coupling between sensors and a member plays very important role. Many methods are used for fixing the sensors to the structure namely adhesives or glue coupling materials and wax or grease are often used as couplants owing to their low impedance. If the structure is metallic, magnetic or immersion methods can be used. Or else, spring or rapid cement can also be used. In essence, coupling should cause least loss of signal energy. Acoustic impedance of the coupling must be lower than that of the testing material.

The sensitivity of AE sensor is expressed in output voltage per vertical velocity,  $1V/(m/s)$ . Estimated sensitivity is based on output voltage per unit pressure input ( $1V/mbar$ ).

#### ***3.4.1.4 Acoustic Wave properties:***

AE signals are weak and signal to noise ratio (SNR) is low. They are normally amplified twice as mentioned earlier. Band pass filter is used to reduce noises.

Signal triggering can be established by setting threshold. In trigger monitoring, only those signals the amplitude or voltage of which exceeds the threshold level are recognized as AE signals.

All acoustic wave devices are sensors. Devices employing surface acoustic waves (SAW) uses inter digital transducers to convert acoustic waves to electric signal and vice versa by exploiting piezoelectric effect.

Piezoelectricity means the generation of electric charges by applying mechanical stress and vice versa. Piezoelectric acoustic wave sensors apply an oscillating electric field to produce mechanical wave which propagates through substrate and then converted back to electric field for measurement. Typically SAW or acoustic sensors operate at 25-500 MHz. The sensitivity of a sensor is directly proportional to the propagation of energy perturb in the surface. Acoustic Wave sensor has proved to be more sensitive because of their larger energy density on the surface.

In the frequency bandwidth of 100 KHz to MHz of AE measurement, vibration occurs by fracture of crystallites, crack and growth. Vibration is related to collective

motion of group of atoms. Difference between low frequency and AE can be understood by following explanation. A defect is needed in bearing/any place which excites the vibration when rolling element is passing (if low frequency based sensor is to be used). But, in acoustic emission vibration is excited when crack is formed. Random ultra frequencies occurs at an early stage of fault i.e. just before seizure. Most sources of AE act as point sources. The point sources radiate energy in spherical wave fronts. Because of this, AE sensors can be placed in any place closer to the AE source and they can pick up the AE signals. On the contrary, direction of sensor is very crucial in the measurement of mechanical vibrations. Although AE measurement is non-directional, it is better to place the AE sensors closer to the expected emission source. Usually they are placed on the load side because every boundary surface affects damping on high frequency vibrational signal. Voltage in AE measurement is very low. Noise from environment affects AE measurement when the emission level from the source is low.

The frequency response of AE sensor is very non linear and hence it is not appropriate to measure the AE spectrum. So, narrow band pass filter is to be used normally in which central frequency is same as resonant frequency of sensor. As The sensitivity of piezoelectric AE sensors is highest at the frequency of around 150KHz. Therefore, those of the lower frequency until 100KHz can be filtered out.

Pulse count method in AE measurement is convenient because the size of measurement remains reasonable. On the other hand, in measurement of AE time signal, the data file can grow very large and the processing would be very difficult.

#### **3.4.1.5 AE Sensors:**

A transducer converts one form of energy into other form. On the contrary, a sensor converts any received signal into electrical signal only.

The sensitivity of a sensor is the indication of output changes of the sensor for the changes in the measured quantity. Highly sensitive sensors are able to measure very minor changes. Sensors also influence what is being measured. Making the sensor smaller enhances its effect on what is measured, which also gives other

benefits. Hence, micro sensors are produced with the help of MEMS technology. Micro sensors have better speed and sensitivity than those produced with macroscopic approaches. Ideal sensors should be sensitive to the measured property, but should not influence it. They should be insensitive to any other property in its application. Ideal sensors should be linear or logarithmic.

AE sensor is composed of a transducer, which is a microphone. The microphone converts sound (mechanical pressure wave) into an electrical signal. Any microphone or hydrophone has some basic structure of a pressure sensor. Acoustic sensors differ from pressure sensors such that an AE sensor doesn't need to measure constant or very slow changing pressure. Microphones use electromagnetic induction (dynamic microphone), capacitance variation (condenser microphone), piezoelectric group, or light change to convert mechanical vibration to an electrical voltage signal.

#### ***3.4.1.5.1 Piezoelectric Microphone:***

Piezoelectric microphones use piezoelectric elements and they are active transducers. Piezoelectric elements are elements that convert pressure into electrical signal directly. Hence no intermediate form of energy is produced. The common material used for the active element is mostly lead zirconate titanate (PZT), a piezoceramic, although it has been shown that other piezoactive materials such as polyvinylidene difluoride (PVDF) are equally feasible.

Based on the requirement of the user, specific microphone can be used. For the detection of scuffing, piezoelectric microphones can be used since these are economical compared to laser and fiber optic microphones. Their reliability and efficiency is also high when compared to carbon, condenser, electrets and inductive microphones.

#### ***3.4.2 Mathematical modeling of acoustic emission method:***

The equation of acoustic wave defines its propagation through a material. It is a partial differential equation of second order, which defines the development

of acoustic pressure ' $p_a$ ' or particle velocity ' $u_p$ ' as a function of position ' $r_p$ ' and time ' $t$ '. In one spatial dimension (position  $x$ ), the equation is:

$$\frac{\partial^2 p_a}{\partial x^2} - \frac{1}{c_s^2} \frac{\partial^2 p_a}{\partial t^2} = 0 \quad (3.112)$$

where,

$p_a$  is the acoustic pressure

$c$  is the speed of sound

If ' $c$ ' is a constant and independent of frequency (the dispersion-less case), then the solution of the equation is:

$$p_a = f_1(c_s t - x) + g_1(c_s t + x) \quad (3.113)$$

where,

' $f_1$ ' and ' $g_1$ ' are any two twice-differentiable functions. This is like the superposition of two waveforms travelling at the speed of ' $c_s$ '; one ' $f_1$ ' moving upwards and another ' $g_1$ ' downwards in the  $x$ -axis. An individual sinusoidal wave moving in a single direction can be explained by selecting one of the waves of ' $f_1$ ' and ' $g_1$ ' to be a sinusoidal; and the other in this case would be zero, which gives the form as:

$$p_a = p_{a0} \sin(\omega t \mp k_w x) \quad (3.114)$$

where

$\omega$  is wave's angular frequency

$k_w$  is the wave number

The equation of the wave is possible to be formulated from the equations of state, continuity and force.

The equation of state (ideal gas law):

$$PV = n_g R_g T \quad (3.115)$$

where,

$P$  is the pressure of the gas ( $\text{N/m}^2$ )

$V$  is the volume of the gas ( $\text{m}^3$ )

$n_g$  is the amount of substance of gas (moles)

T is the temperature of the gas (K)

$R_g$  is the ideal gas constant ( $J \cdot K^{-1} \cdot mol^{-1}$ )

In adiabatic process, pressure 'P' and density ' $\rho$ ' are related.

$$P = C_c \rho \quad (3.116)$$

Where,

$C_c$  is a constant

At their component level, we can write

$$C_c = \frac{\partial P}{\partial \rho} \quad (3.117)$$

$$P - P_0 = \left( \frac{\partial P}{\partial \rho} \right) (\rho - \rho_0) \quad (3.118)$$

The formula for adiabatic bulk modulus of a fluid is:

$$B_a = \rho_0 \left( \frac{\partial P}{\partial \rho} \right)_{adiabatic} \quad (3.119)$$

By substituting equation 3.119 into equation 3.118, we get equation 3.120:

$$P - P_0 = B_a \frac{(\rho - \rho_0)}{\rho_0} \quad (3.120)$$

' $s_d$ ' is the condensation, which is the ratio of the changed density and the original density as shown in Equation 3.121:

$$s_d = \frac{(\rho - \rho_0)}{\rho_0} \quad (3.121)$$

Substituting Equation 3.121 in Equation 3.120, we get the equation of state as shown in Equation 3.122:

$$P_a = B_a s_d \quad (3.122)$$

Where,

$P_a$  is the acoustic pressure ( $P - P_0$ ).

The equation of continuity (conservation of mass) in single dimension can be shown as in Equation 3.123:

$$\frac{\partial \rho}{\partial t} + \frac{\partial}{\partial x}(\rho u) = 0 \quad (3.123)$$

If the equation is made linear with mean and variable components, we get Equation 3.124 as:

$$\frac{\partial}{\partial t}(\rho_0 + \rho_0 s_d) + \frac{\partial}{\partial x}(\rho_0 u + \rho_0 s_d u) = 0 \quad (3.124)$$

As ambient density  $\rho_0$  is a constant and the product of the condensation and the velocity has a very small value, the Equation 3.124 can be written as Equation 3.125:

$$\frac{\partial s_d}{\partial t} + \frac{\partial}{\partial x} u = 0 \quad (3.125)$$

The equation of force, Euler's Force equation (conservation of momentum) in single dimension can be written as:

$$\rho \frac{Du}{Dt} + \frac{\partial P}{\partial x} = 0 \quad (3.126)$$

where  $\frac{D}{Dt}$  is the derivative of convection or material. This derivative is not located at a specific point. It moves with the medium.

Linearizing the variables, we get Equation 3.127 as follows:

$$(\rho_0 + \rho_0 s_d) \left( \frac{\partial}{\partial t} + u \frac{\partial}{\partial x} \right) u + \frac{\partial}{\partial x} (P_0 + p_a) = 0 \quad (3.127)$$

Reorganizing and ignoring the terms of small value of Equation 3.127, we obtain the force Equation 3.128 as:

$$\rho_0 \frac{\partial u}{\partial t} + \frac{\partial p_a}{\partial x} = 0 \quad (3.128)$$

Differentiating the continuity Equation 3.125 with time and the force equation 3.128 with space, we get Equation 3.129 and Equation 3.130 respectively:

$$\frac{\partial^2 s_d}{\partial t^2} + \frac{\partial^2 u}{\partial x \partial t} = 0 \quad (3.129)$$

$$\rho_0 \frac{\partial^2 u}{\partial x \partial t} + \frac{\partial^2 p_a}{\partial x^2} = 0 \quad (3.130)$$

After multiplying Equation 3.129 with  $\rho_0$ , subtracting it with Equation 3.130 and substituting the Equation of state 3.123, we get Equation 3.131 as follows:

$$-\frac{\rho_0}{B_a} \frac{\partial^2 p_a}{\partial t^2} + \frac{\partial^2 p_a}{\partial x^2} = 0 \quad (3.131)$$

Then the final Equation 3.132 emerges as follows:

$$\frac{\partial^2 p_a}{\partial x^2} - \frac{1}{c_s^2} \frac{\partial^2 p_a}{\partial t^2} = 0 \quad (3.132)$$

where,

$$c_s = \sqrt{\frac{B}{\rho_0}} \quad \text{is the speed of propagation}$$

#### 3.4.2.1 Mathematical Model:

The output from the sensor is electrical signal, obtained from mechanical pressure waves (sound), is amplified and filtered. We can represent the system response mathematically with a linear system as in Figure 3.43. Input function  $f(t)$  of mechanical motions are converted into output function  $g(t)$  of electric signals by transfer function  $L[f(t)]$  of AE sensor. Mathematical expression of the system is:

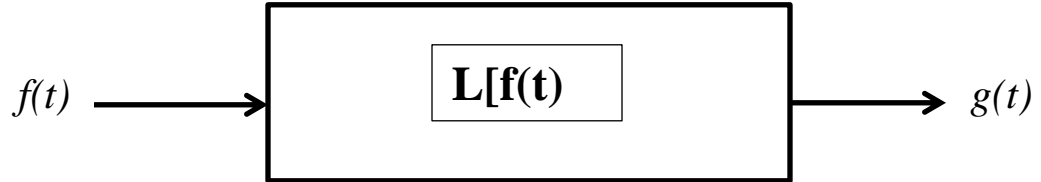


Figure 3.43 Linear System

$$g(t) = L[f(t)] \quad (3.133)$$

Dirac's delta function  $\delta(t)$  has a vital role. Equation 3.133 in a linear system will be:

$$g(t) = L[f(t) * \delta(t)] = f(t) * L[\delta(t)] \quad (3.134)$$

Where, the symbol (\*) represents the convolution.

Setting  $L[\delta(t)]$  as  $W(t)$ , we have,

$$g(t) = f(t) * W(t) \quad (3.135)$$

From Equation 3.136, it can be said that the sensor response  $g(t)$  is found from the convolution of the input  $f(t)$  with the impulse response of the system  $W(t)$ , as the input of the delta function results in the function  $L[\delta(t)]$  as the response of the system.

Convolution integral of the functions  $f(t)$  and  $W(t)$  can be expressed as:

$$g(t) = \int f(t - \tau) W(\tau) d\tau = f(t) * W(t) \quad (3.136)$$

With Fourier transform, we can write:

$$G(f) = \int g(t) e^{-j2\pi f t} dt = \iint f(t - \tau) W(\tau) d\tau e^{-j2\pi f t} dt \quad (3.137)$$

$$G(f) = F(f) W(f) \quad (3.138)$$

where,

$G(f)$ ,  $F(f)$  and  $W(f)$  are Fourier transforms of  $g(t)$ ,  $f(t)$  and  $W(t)$  respectively

$W(t)$  is the transfer function and  $W(f)$  is the function of frequency response. A calibration of AE sensor is equivalent to determination of function  $W(f)$ . On the other hand, it implies that frequency contents of AE waves are usually smeared by function  $W(f)$  of AE sensor. Thus, the absolute calibration means quantitative estimation of function  $W(t)$  or  $W(f)$ .

AE signals are weak and have noises. Hence, they are amplified and filtered. As a result, AE signal ' $a(t)$ ' recorded in the system shown in Figure 3.41 can be mathematically expressed as:

$$a(t) = W_f(t) * W_a(t) * W(t) * f(t) \quad (3.139)$$

where,  $W_f(t)$  and  $W_a(t)$  are transfer functions of the filter and the amplifiers. It is essential to know the significance of these functions in order to reduce their impact. Normally, the frequency responses of both the filter  $W_f(f)$  and the amplifier  $W_a(f)$  is flat or constant. Due to this, the frequency response or the transfer function  $W(f)$  or  $W(t)$  of AE sensor has considerable effect on the frequency contents of AE signals.

AE sensor voltage,  $V(t)$  is expressed as a function of the AE source mechanism, represented by a change in internal stress ( $\Delta\sigma_{jk}$ ), a propagation term given by the



spatial derivative of the Green's tensor ( $G_{ij,k}$ ) and the transducer response ( $T_r$ ). The Green's tensor is defined as the displacement components of an elastic medium of a given geometry at a specified receiver position, as a result of unit impulse forces along the coordinate axes at a given source position. Although the derivation of this theory is beyond the scope of this introductory text, the resulting equation is:

$$V(t) = \iint_{S_T} T_r(r, t - t') G_{ij,k}(r, r'_0, t' - t'') \Delta \sigma_{jk}(t'') dr dt'' \quad (3.140)$$

where the source is positioned at  $r'_0$  within the interior of the material, the receiver is positioned at 'r' on the surface of the material, and the transducer area is given by  $S_T$ .

$$V_{rms} = \sqrt{\frac{1}{\Delta t} \int_0^{\Delta t} V^2(t) dt} \quad (3.141)$$

The energy is given by,

$$E = \int_0^t V^2(t) dt \quad (3.142)$$

### 3.4.2.2 Signal Processing:

#### 3.4.2.2.1 Overall Process:

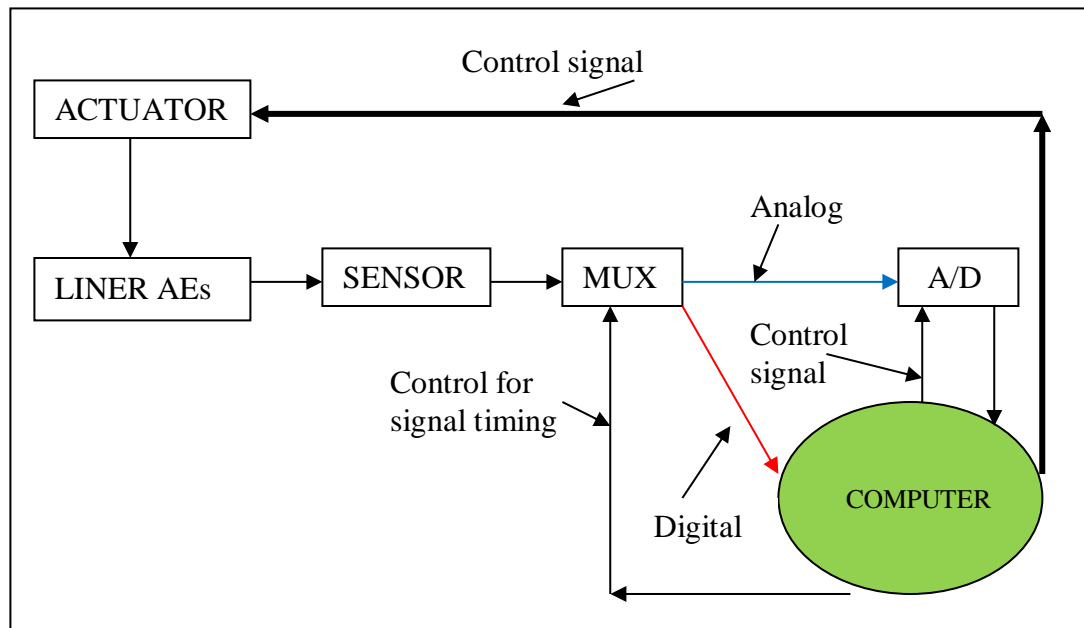


Figure 3.44 Overall process

(AES: Acoustic Emission Source, MUX: Multiplexer, A /D: Analog to Digital Converter)

The Figures 3.44 and 3.45 illustrate that liner of a cylinder acts as an acoustic source. The acoustic emission is sensed by acoustic sensor. If output of the sensor is digital, it is multiplexed (output of all sensors accumulated and various processes such as pre process, BSS/ICA, post process are carried out).

Finally, the outputs of individual sensors are displayed in computer. This computer can provide command signal to actuator to take necessary action to prevent excessive damage.

If the output from sensor is analog, it is essential to convert analog to digital. This operation is performed by analog to digital converter (A/D converter). In our case, if friction arises between liner and piston, AE can be observed in the place where friction occurs and it would be sensed by an acoustic sensor.

After other processes, the command signal from computer reaches the actuator. The actuator applies extra lube oil on the liner surface or reduces the engine load accordingly.

### 3.4.2.2.2 AE Sensor:

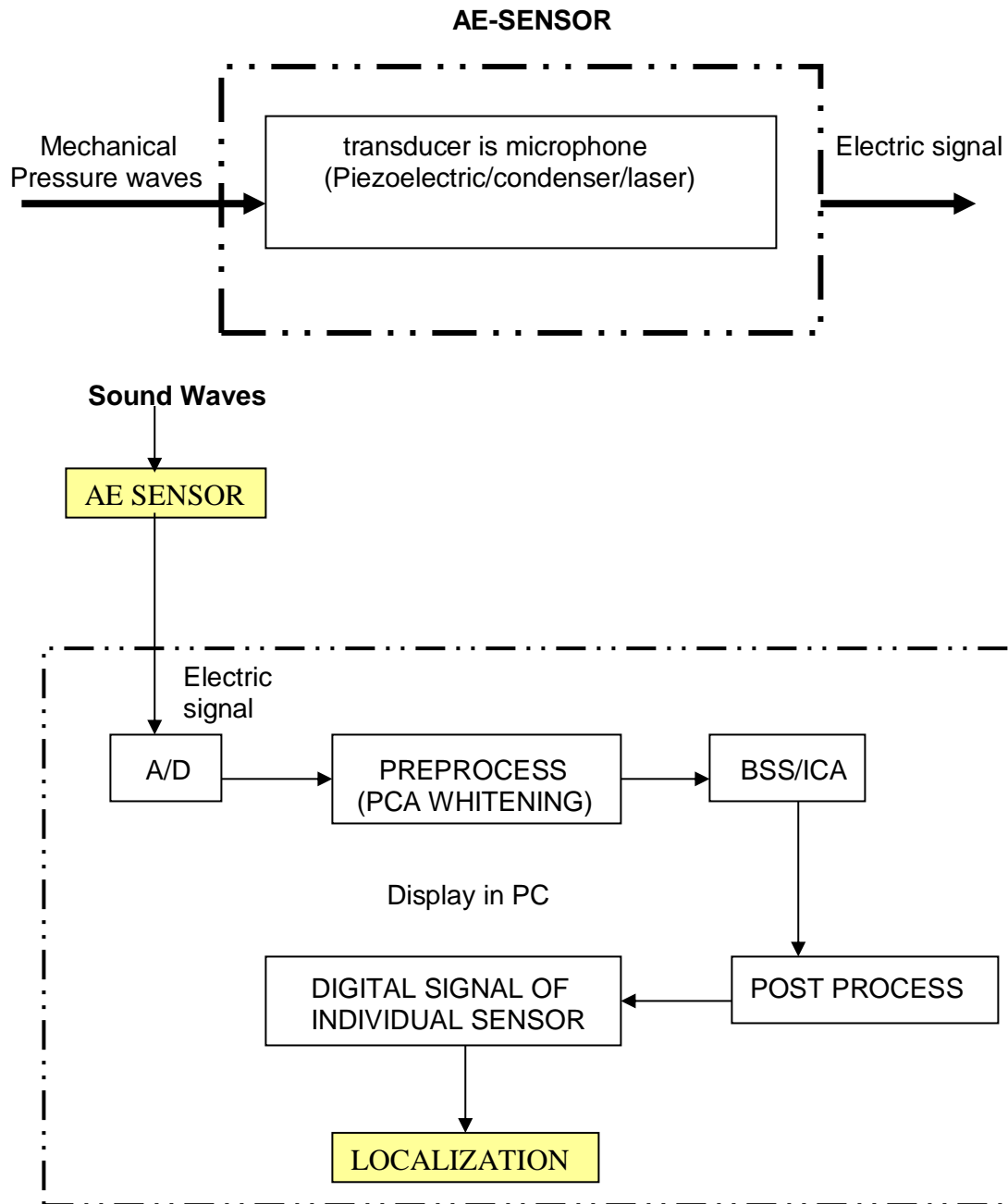


Figure 3.45 Signal Processing

### 3.4.2.2.3 Blind Source Separation (BSS):

#### Overview:

The overview of essential areas in blind separation of convolutive sources can be illustrated via schematic, figure 3.46 as follows:

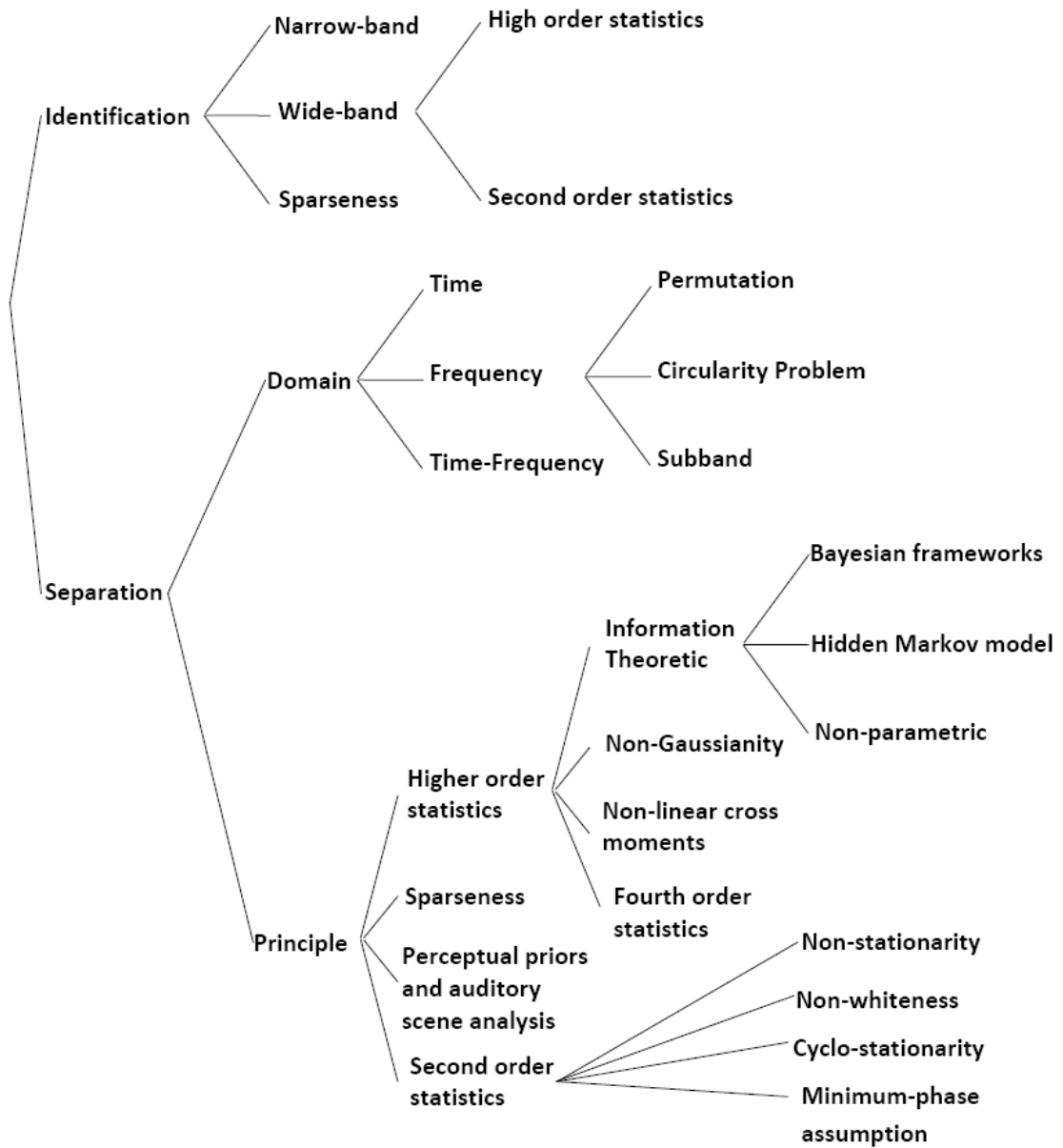


Figure 3.46 Overview of BSS [149]

The overall process that takes place in BSS can be expressed as follows:

Step 1:  $X = AS + V$  (Observation / Sensor Output)

Step 2:  $X = AS$  (Preprocessing)

Step 3:  $Y = WX$  (ICA-Independent Component Analysis)

Step 4:  $WA = I$  (Postprocessing implies that  $W=A^{-1}$ )

Where,

X: Observation, A: Mixing Matrix (Channel), S: Source, V: Noise, W: Unmixing Matrix, I: Identity Matrix.

#### **3.4.2.3 Source Localization:**

It is essential to spot out the place where AE occurs. Because, that's the place where some irregularities would have been occurred in the liner. AET use localization techniques in order to find the emission source. Testing object's geometry and requirement of one, two or three dimensions of resolution decides which methods would be applicable for localizing the AE events. Source location determination is an inverse problem.

The location of the source can be worked out from the time differences when the elastic wave was radiated by the fracture and when was received by each sensor. The origin of source of acoustic emission lies in its time,  $t_0$  (start of the rupture) and its place in Cartesian coordinates  $(x_0, y_0, z_0)$ . The calculated location is at a point in space and time where the fracture originated. The first elastic wave the sensor picks up is the compressional wave (P-wave). For cases, where the shear wave (S-wave) is picked up, it can be used instead of P-wave or else can be combined with P-wave. Nevertheless, in AE analysis, it is quite hard to detect S-wave. The S-wave can be concealed in the coda of the P-wave, if the source and the receiver are only a few wavelengths away from each other and the near field effects, incomplete separation of P-wave and S-wave, will be experienced. As the motion of particles of S-wave and P-wave are normal and parallel respectively to the direction of propagation, a P-wave sensor is not intended to identify S-waves.

For any localization (1D, 2D or 3D), it is required to know the onset times, the positions or coordinates of sensors and the velocities of the compressional and shear wave, provided it is detected. If a homogeneous material is used, the direct ray path between the source and the receiver can be used for the computation of the location of the source. On the other hand, if a layered or a heterogeneous material is used, the effects of the material on wave propagation and the ray path ought to be accounted for calculating an accurate localization.

In our case, let us consider homogeneous material. One dimensional localization is sufficient to identify the emission source, because the resolution provided by one dimension is enough for our analysis. Two and three dimensional localizations are widely used in medical applications.

#### ***3.4.2.3.1 1-Dimensional Localization:***

Zone location method can be used to locate the source of acoustic emissions. In this method, the idea is not to find the precise source coordinates of AE, rather the localization accuracy depends on detecting a signal and the radius or the zone of the sensitivity range of the sensor. Localization accuracy in 1-dimensional localization is also affected by the geometry of the structure, which is being tested. The principle behind zone localization method is very simple, though it is not so precise. The location of the source is closest to the particular sensor that receives the signal first among other sensors. In Figure 3.47, an example of 8 sensors distribution is shown.

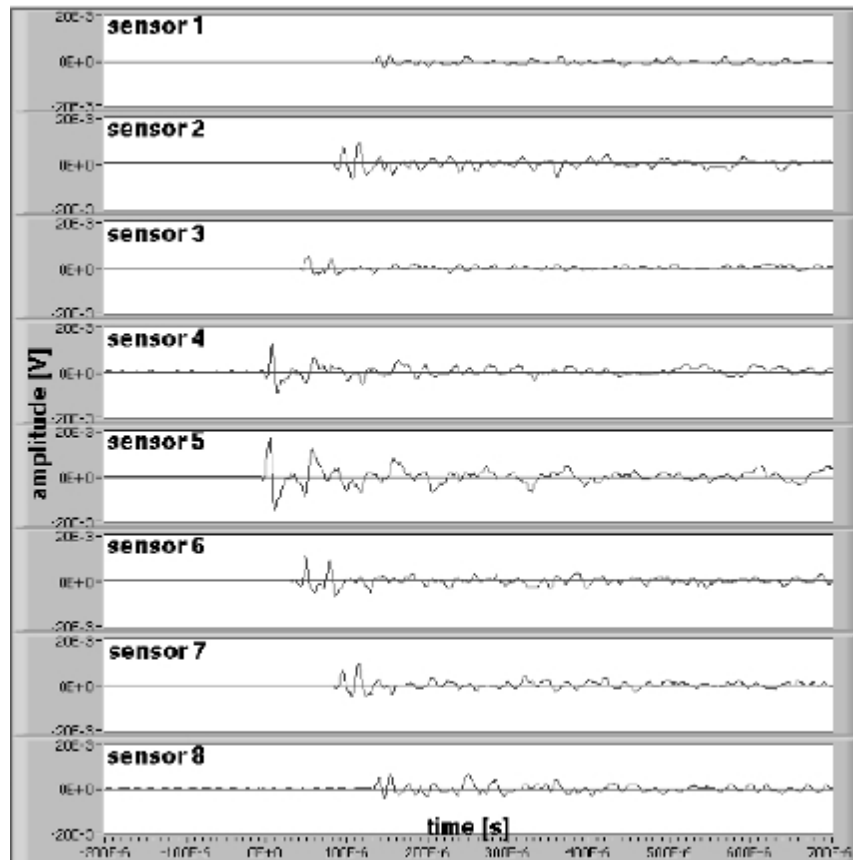


Figure 3.47 Sample output from array of (8) sensors.

Let us consider a situation that array of (8) sensors are placed along the sides of the liner of a diesel engine, the coordinates of which are known. The sensors show variation in their outputs, based on which, it is possible to determine the AE source. Sensor 4 records the signal first, which is followed by the sensor 5.

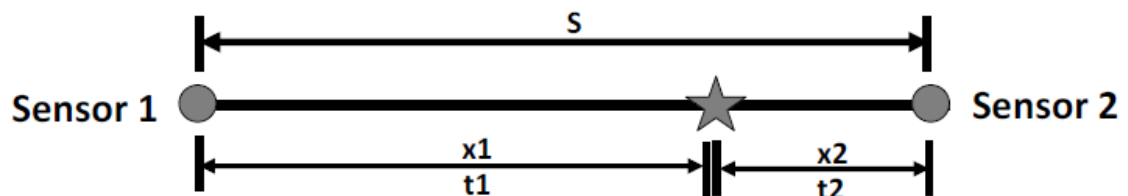


Figure 3.48 Principle of a 1-dimensional localization

Example of 1-dimensional localization is shown in Figure 3.48. The location of the emission source is shown by the star sign.

Given:

s        Distance between the two sensors  
 $t_1, t_2$     Onset time at each sensor  
 $v$         Sound velocity of the material

To find:

$t_0$         Source time  
' $x_0$ '.    1-D source location

The distances ' $x_1$ ' and ' $x_2$ ' from the emission source to the sensors are:

$$v * (t_1 - t_0) = x_1 \quad (3.143)$$

$$v * (t_2 - t_0) = x_2 \quad (3.144)$$

$$s = x_1 + x_2 \quad (3.145)$$

Inserting Equation 3.145 into Equation 3.143 or 3.144,  $t_0$  ,  $x_1$  ,  $x_2$  and source location, ' $x_0$ ' against the two sensors can be found.

Finally the location of AE source can be found out using the following expression.

$$v * t_0 = x_0 \quad (3.146)$$

#### **3.4.2.3.2 2-Dimensional Localization:**

The 2-D localization method is more accurate than that of 1-D zone method. In a 2-D localization, ' $x_0$ ' and ' $y_0$ ' coordinates of the source are determined. 2-D localization is often called a planar localization as it lacks in the information of the depth and the source location of it is called epicenter. This method is suitable for objects of smaller thickness and where the source coordinates are only needed in two directions.

In the 2-D localization method, minimum 3 sensors are required. The velocity is considered constant. As the 3 sensors record 3 different arrival times  $t_1$ ,  $t_2$  and  $t_3$  of the compressional wave, it is possible to obtain the epicenter by hyperbola approach. In order to find the epicenter, the arrival time difference between two sensors needs to be analysed. If the time difference is constant on a particular hyperbola, this simply ascertains the location of epicenter on that hyperbola and the corresponding sensor coordinates as the foci of the hyperbola; e.g. Figure 3.49, epicenter lies on the  $t_2 - t_1$  hyperbola and is at the intersection of the 3



hyperbolas and the sensor coordinates of  $t_1$  and  $t_2$  are the foci of the  $t_2 - t_1$  hyperbola.

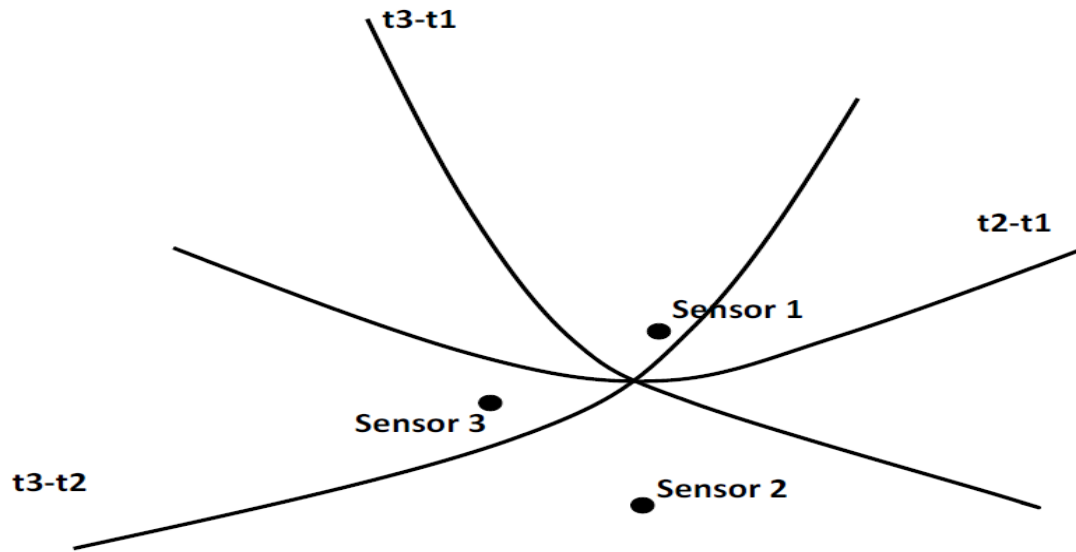


Figure 3.49 Two-Dimensional localization using hyperbola method

If the 3 hyperbolas do not intersect at a point, it simply means that there are errors in the measurement. In that case, it would demand more than 3 sensors and the application of statistical method to improve the accuracy of the measurement.

#### **3.4.2.3.3 Optimization:**

The number of sensors to be placed in the liner of a large diesel engine would be more in number. If more sensors are used, the accuracy and the resolution of the AE source would be higher. On the other hand, incorporating more sensors would also make the system more expensive. In order to optimize the system, broadband sensors can be used. These broadband sensors operate in a wide band of frequency. This results in the reduced cost as the number of sensors used is less. On the other hand, more accuracy and high resolution of AE source localization cannot be expected by using the broad band sensors.

Adaptive Beam Forming (ABF) can be applied at mixing model to receive source signals at sensors. By using ABF technique, sensor array collects spatial samples of propagating source signals. Parameters in beamformer are adjusted to form a

spatial pattern with a dominant response for the directions of interest while the response for the positions of interfering signals is minimized.

Pros of ABF:

1. Spatial selectivity
2. Utilizing available geometric information

Cons of ABF:

1. Cross-talks (Inter Symbol Interference-ISI)
2. Only second-order statistics utilized

By combining convolutive BSS with ABF, their advantages can be combined while their weaknesses can be compensated with each other. In normal cases, BSS is viewed as multiple ABF's. Combination of ABF mixing model and BSS separation system is shown in Figure 3.50.

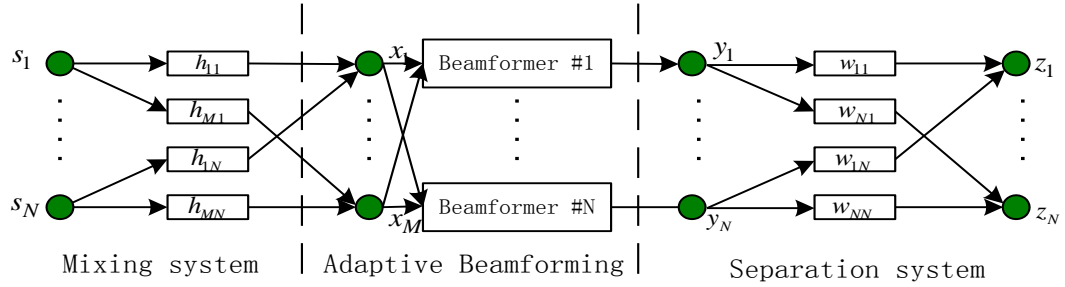


Figure 3.50 System structure for proposed approach

Different beamforming algorithms can be selected in the first stage to get the best beam pattern. Different convolutive BSS algorithms can be selected, such as time domain, frequency domain, higher-order based algorithms etc., in the second stage to get the best separation result. Hence, combined Adaptive Beamforming and Blind source separation improves the performance of separation process.

### **3.5 Summary of modeling of scuffing detection methods:**

Four methods have been modeled for the detection of scuffing of cylinder liner and piston rings.

Out of the four, the first method is the tribology model, which was extensively studied and evaluated in order to identify all variables and coefficients against various loading of a real slow speed marine engine. The full model is captured in the attached X-cel file and Appendix 2. By inputting the variables, such as engine RPM, engine load and lubrication feed rate etc; the simulation takes place and the necessary diagrams are drawn automatically for the hydrodynamic pressure distribution, oil film thickness, coefficient of friction, force and load against the whole range of crank angle.

For the other three detection methods, the generated mathematical models have been physically experimented on the test bench and engine to confirm the validation of the results against those of the models. Necessary error elimination have been incorporated in the experiments to ensure the accuracy of the obtained results.

## Chapter 4. Experimental Tests

---

### 4.1 Analytical simulation of tribology model:

Analytical simulation of the developed hydrodynamic lubrication model on the cylinder liner and piston ring of a vessel equipped with an Wartsila Sulzer 10RTA84C engine rated 55100BHP at 102RPM was carried out. Details of the engine and experiment condition are shown in Table 4.1.

Cylinder Liner Bore	844mm (4mm worn out)
Piston ring height	20mm
Engine RPM	90
Engine Load	80%
Lubricating Oil	CLO70 TBN

Table 4.1 Detail specification of the engine and experiment condition

The tribology model for simulation is in the attached Excel file named, 'Tribology model', as attached and its usage is described in Appendix 2. In this simulation, the input data are keyed in as per the Table 4.1. The output generated from the model are the hydrodynamic distribution, the oil film thickness, coefficient of friction and load, which are obtained against any desired crank angle of that particular RPM and load of the engine. Necessary corrections are made to take into account of the temperature effect on the viscosity of the lubricant, which affects the hydrodynamic lubrication.

### 4.2 Field test of thermoelectric sensor:

The field test was conducted on a cylinder of the main propulsion engine of a panamax container ship equipped with the engine as mentioned in section 4.1. Two 'K' type Chromel (+ve) – Alumel(-ve) thermocouples of temperature range of -200°C to +1200°C were fitted on the upper part of the running surface of the cylinder liner, Figure 4.1.

The depth of the measuring point was around 10mm from the liner inner surface. The sensors were fitted on the fuel injection pump side and exhaust side (180°

apart). A hybrid recorder and thermocouples were connected by compensation wires through a junction box.

The hybrid recorder changed the voltage of thermocouple to the value signal of temperature. It also changed the sensor signals of a load indicator position and engine speed to the processable data in order to refresh the reference points.

Temperature readings were obtained for the engine running at 85%MCR. Original cylinder lubrication feed for the unit was 0.87g/bhp/h. The feed rate for the unit was gradually reduced to 0.42g/bhp/h in order to detect the onset of scuffing due to starved lubrication.

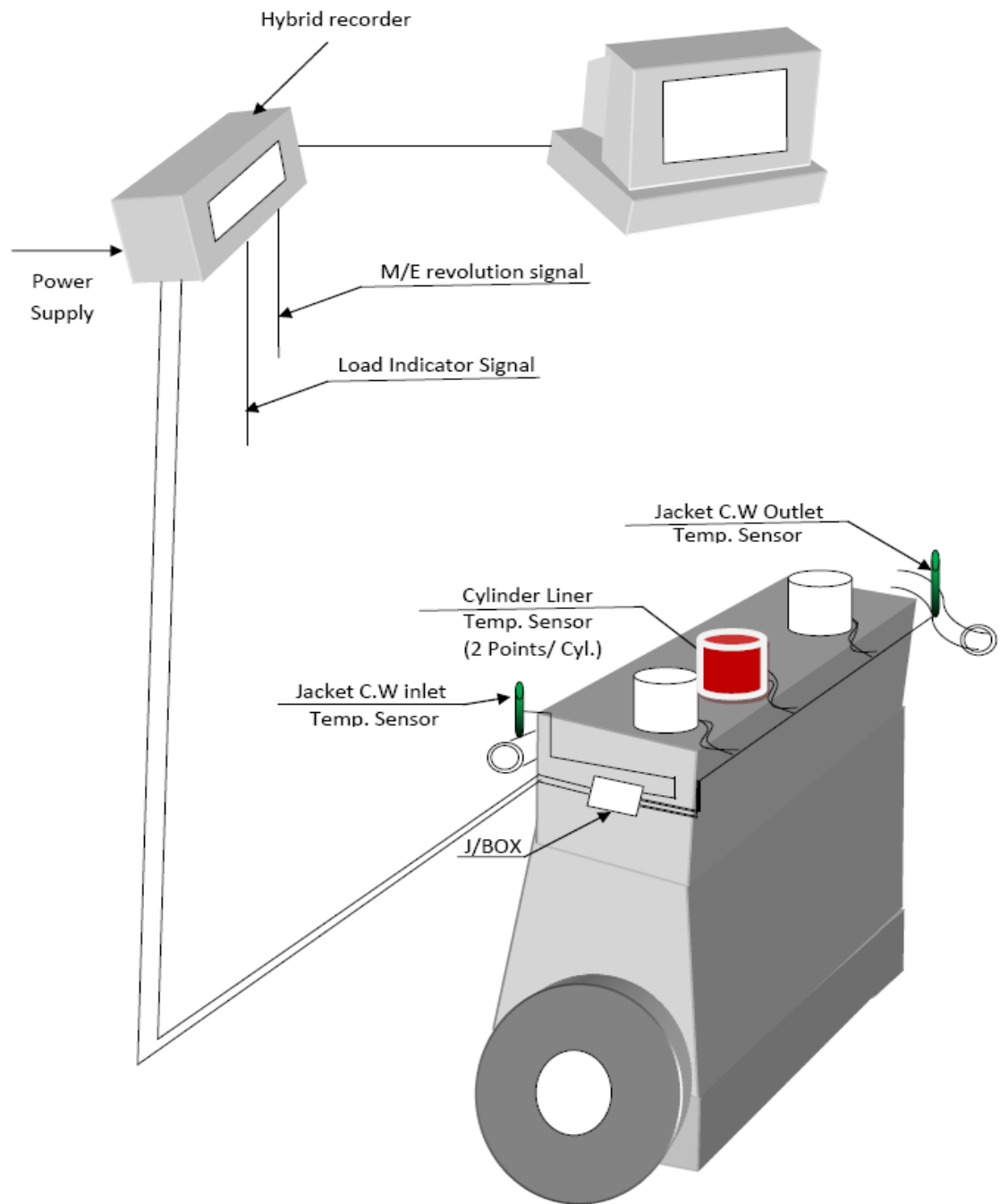


Figure 4.1 Physical hardware system of liner temperature monitoring

### **4.3 Field test of eddy current sensor:**

#### **4.3.1 Jig Test:**

##### **4.3.1.1 Materials:**

It is best to carry out the jig test on a real piece of the components to replicate the wear and scuffing in the real field. In this aspect, an used piece of cylinder liner was prepared to be used in the jig test. The following are the dimensions of the cut piece of the liner:

Length: 0.7 m

Sector: Sectors of 60° (which gives a contact width of approximately 0.6 m).

Rings: New piston rings were cut in pieces approximately the same like that of the liner piece in terms of sectors.

At first, material analysis was conducted on the cutout sample of used cylinder liner to establish metallurgical properties and chemical composition of a typical cylinder liner in operation.

The metallurgic characterization of the specimens was carried out, i.e. metallographic microscopic photos showing the grain, an electronic microscopic analysis to characterize the bonds, a chemical composition from the top and bottom of the specimens (because of elements migration to the surface) and analysis of physical properties. The electronic micrograph and surface photographs were done with an amplification of maximum 100 X.

The examined cylinder liner sample had relatively homogenous microstructure of essentially graphite flakes in pearlite matrix with ~5% (phosphide) eutectic hard phase. There were no significant variations in the hardness and chemical compositions across the wall thickness of the cylinder liner. The metallurgical properties and chemical compositions of the examined sample were considered normal for gray cast iron material used for cylinder liner application.

##### **4.3.1.2 Scope of analysis work included the following:**

- (i) Surface metallographic examination
- (ii) Sectional metallographic examination
- (iii) Hardness test

- (iv) Energy dispersive x-ray (EDX) spectrometry
- (v) Chemical Analysis

#### **4.3.1.2.1 Surface metallographic examination:**

Surface metallographic examination was carried out on representative area at the internal wall surface of the cylinder liner sample. The examination was conducted by surface replication technique on the following surface condition.

- (i) Original surface – without polishing and etching (Figure 2, Appendix 1)
- (ii) Original surface – after light polishing and etching (Figure 2, Appendix 1)
- (iii) Polished surface – after polishing to a depth of 0.1mm (Figure 3, Appendix 1)

The original surface had scuffing marks and surface (micro) seizure in forms of networks of micro fissures propagating along the graphite flakes and the eutectic hard phase (Figure 2, Appendix 1). Polishing of the internal wall surface to a depth of 0.1mm revealed no significant indication of seizure / fissuring (figure 3, Appendix 1). The microstructure essentially revealed graphite flakes in pearlite matrix with ~5% eutectic hard phase.

#### **4.3.1.2.2 Sectional metallographic examination:**

Sectional metallographic examination was conducted transversely across representative areas of the cylinder liner sample. The examination was carried out at depths of ~0.1mm, 1mm and 10mm below the surface of the cylinder liner for assessing possible microstructure variation (depth wise). The selected sections were mounted, ground, polished and etched to reveal the microstructure. Representative micrographs of the examined locations are shown in Figures 4 to 6, Appendix 1.

The cylinder liner had a microstructure of essentially graphite flakes in pearlite matrix with ~5% (phosphide) eutectic hard phase. There was no significant variation in microstructures of the examined locations at various depths below the surface of the cylinder liner.



#### **4.3.1.2.3 Hardness test:**

Hardness test was performed on the transverse section of the cylinder liner sample using a Krautkramer MIC10 hardness tester. The hardness test results are shown in Table 4.2

LOCATION	HARDNESS (HV)						Standard Dev (%)
	#1	#2	#3	#4	#5	Average	
Near surface	356	359	341	340	348	349	2.46
Mid-wall portion	338	356	356	348	347	349	2.14

Table 4.2 Hardness values of the specimen

The examined locations at different depths below the surface of the cylinder liner generally revealed no significant variation in hardness.

#### **4.3.1.2.4 Energy dispersive X-Ray (EDX) spectrometry:**

EDX analysis was conducted on the cylinder liner sample at various depths below the surface. The EDX analysis was performed using an OXFORD EDX analyzer coupled to a Hitachi S3400 SEM, which is summarized in the following table 4.3.

SAMPLE cylinder liner	CHEMICAL COMPOSITION (wt %)						
	C	Si	Mn	P	S	Cr	Mo
Near surface	2.5	1.10	0.72	0.18	0.04	0.06	0.20
Mid-wall	2.5	1.10	0.70	0.16	0.04	0.06	0.19

Table 4.3 Chemical composition of specimen

Note: EDX analysis only indicates main alloying elements. Trace elements present in the base material could not be detected by EDX – refer to chemical analysis results.

The elements detected from EDX analysis were essentially the main alloying elements of the (gray) cast iron base material of the cylinder liner sample. There was no indication of significant variation in elemental compositions at the various examined locations of the cylinder liner.

#### **4.3.1.2.5 Chemical analysis:**

Chemical analysis was conducted on the base material of the cylinder liner by wet analysis method. The chemical analysis results are shown in Table 4.4.

The cylinder liner sample was relatively homogeneous in nature as indicated by the minimal variation in chemical compositions across the wall thickness of the liner.

<b>SAMPLE</b>	<b>ELEMENTAL COMPOSITION</b>	<b>FIGURE(Appendix 2)</b>
0.1mm below surface	Major: Iron and carbon Minor: Silicon and manganese	7
1mm below surface	Major: Iron and carbon Minor: Silicon and manganese	8
10mm below surface	Major: Iron and carbon Minor: Silicon and manganese	9

Table 4.4 Elemental composition of specimen

The material analysis of the cut piece of the cylinder liner was necessary to understand the implications of scuffing in the metallurgy of the surface of the liners and make possible recommendations or improvements with materials, as needed. It was also essential to perform a proper characterization of the specimen to pick the most appropriate eddy sensor and as we can only compare things that are comparable.

Upon metallurgical analysis, it was found that the used piece of cylinder liner conforms to that of a liner used in the engine, where the field test was carried out later.

#### 4.3.1.3 Fabrication of test jig:

A jig, Figure 4.2 was fabricated to evaluate the possibility of using eddy current sensors to monitor the piston ring roughness in service.

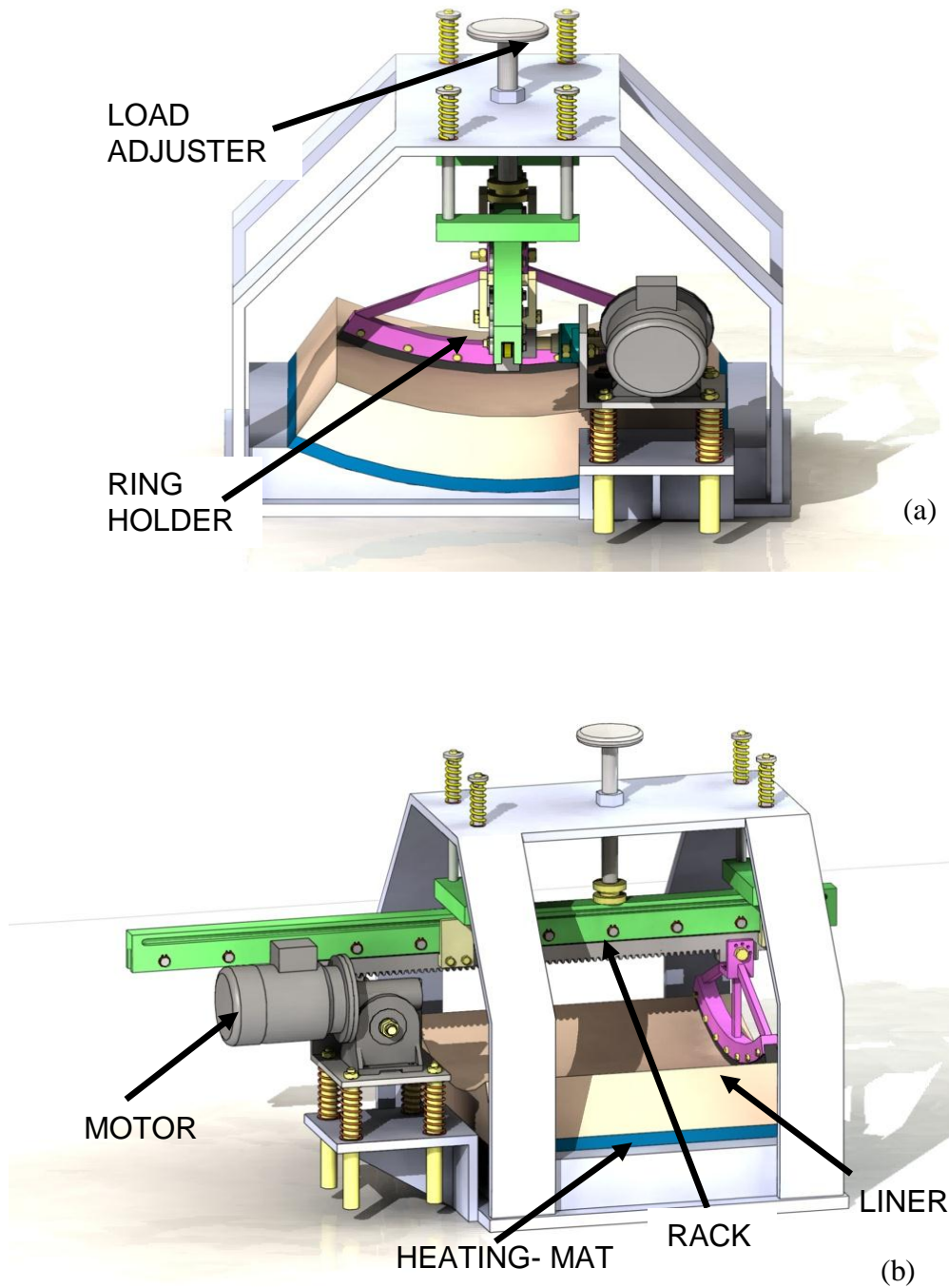


Figure 4.2 Test Jig for eddy current sensor analysis (a) front view (b) side view

The sensors used on the test jig were same as what were placed on the engine cylinder liner during the field test. The jig has the variable speed mechanism, a load measuring system and a lube system. It has an oil bath with appropriate temperature setting of the heating mat. The distortion at the back of the liner arising from the applied force on its wall through the ring was measured. This was measured by the vertical motion amplitude. This vertical motion had some effect on the set loading of the ring/liner wall.

The jig allowed control of the load on the piston ring, on the linear speed of the ring over the liner, liner temperature, piston ring angle, temperature and evidently the oil flow.

#### ***4.3.1.3.1 Load Cell Calibration (approximate):***

The load cell was calibrated on the hydraulic press using the hydraulic pressure indicated on the manometer to calculate the approximate force on the load cell. The hydraulic press suffers from a leakage meaning that it could not maintain pressure. To make a measurement, the hydraulic pressure was increased and then an attempt was made to stabilize the load cell reading against the leak by pressing down on the pump handle to compensate for the leak. Once the reading was more or less stable this was noted along with the manometer reading.

There were two different instruments available for measuring the load cell output. One was a dedicated strain gauge instrument MVP2555 and the other was a combined thermocouple/strain gauge instrument TC-31K. The latter required an external power supply. The MVP2555 used an a.c. excitation voltage but the power supply voltage used for the TC-31K was 5V d.c. In fact, the excitation voltage for the MVP2555 was a sine wave of about 4.8kHz, 3.6v pk-pk. The MVP2555 gave an output in mV/V regardless of what units are set in the instrument. To get an equivalent output using the TC-31K, the mV output were divided by the excitation voltage (5V in our case). It was observed that the two instruments gave a different zero-load reading for the same sensor. However, by zeroing the readings the results were comparable (that is to say that the slope of a linear regression was the same).

The pressure was converted from Bar to Pascals and then the approximate force was calculated using  $\text{Force} = \text{pressure} \times \text{Area}$ , where the area is the cross-sectional area of the hydraulic ram of the press.

$$\text{Force} = p\pi r^2$$

Where,  $p$  is the pressure and  $r$  is the radius of the hydraulic ram ( $\sim 0.05\text{m}$ ).

$$\text{Force} = p \times 0.0079$$

Figure 4.3 shows a graph of zeroed load cell output (in mV/V) versus press pressure (bar) and approximate force. From the equation of the line and the error band, the pressure equals 0.66806 times the load cell output with an error margin of 2.8%.

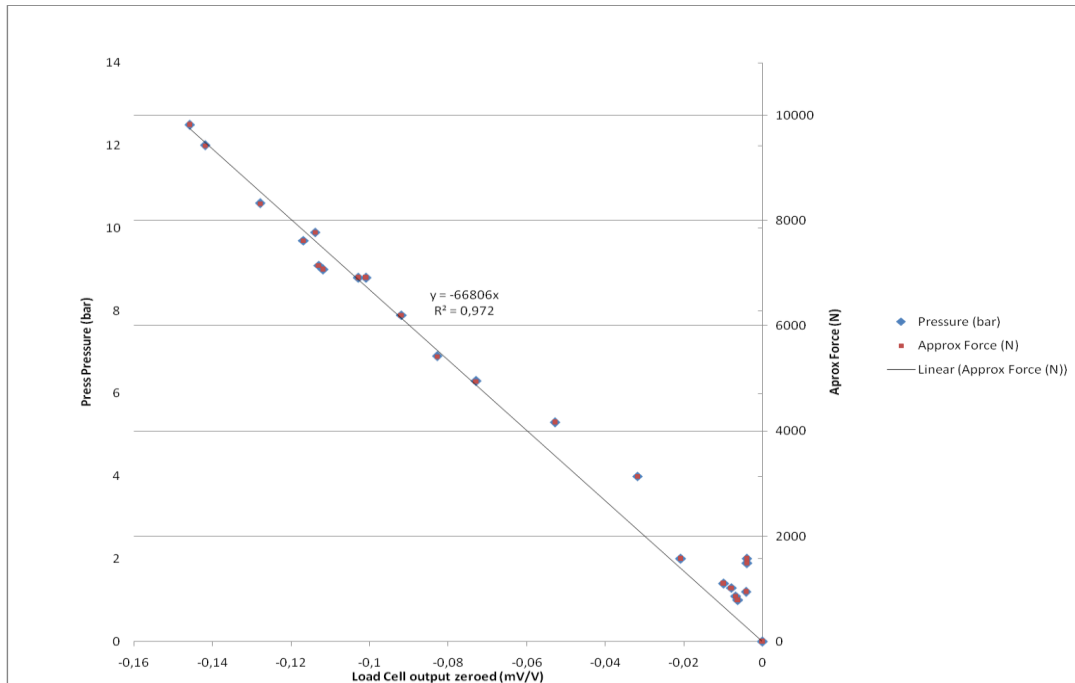


Figure 4.3 zeroed load cell output Vs pressure

To take a measurement with the load cell and the TC-31K instrument, first of all, it was necessary to take a no-load reading. When taking a reading from the load cell, the no-load reading needed to be subtracted first, and then the values were to be divided by the power supply voltage to get the values in mV/V. The value was then multiplied by 66,800 to give the approximate load in Newtons.

#### **4.3.1.3.2 Jig test analysis:**

The sensor was placed inside a Teflon carrier. The Teflon carrier was tapped to take the sensor screw thread. The Teflon carrier was fixed to a slightly curved strip of metal which acted as a spring to hold the Teflon carrier against the liner surface. The spring was attached to the piston ring carrier by a bolt. There were five bolts at different positions on the liner carrier, giving five positions for the eddy current sensors.

The surface of the liner corresponding to the first position was altered by adding some physical features. Ultimately the features were: a slot 1.9mm wide and 0.3mm deep; another slot 0.9mm wide and about 0.15mm deep; a shallow slot filed with a hand file; an area 30mm wide ground with a power tool having a maximum depth of about 0.1mm.

For initial testing metal strips were taped to the liner to give a position reference. These can be seen in the Figure 4.4. The features A, B and C are the 0.3mm slot; the 0.15mm slot and 0.1mm slot respectively seen against the reference line. The readings confirmed the ability of the jig to measure physical roughness.

The optical sensor signal showed pulses between 200 and 300 samples. These correspond to the rising edges on the signal from the optical sensor. The rising edges from the optical sensor signal were used as a trigger input to the microcontroller which causes an interruption in the software. Due to hardware limitations it was not possible to measure the analogue optical signal without compromising the number of samples taken. Initially the optical sensor gave an imprecise signal but this was rectified by using a wider strip of reflective material on the Teflon sensor carrier (the width of the strip was changed from ~5mm to ~25mm). In fact the reflective strip covered the whole of the Teflon sensor carrier.

The sampling time was 2ms. The approximate distance covered in one sample was 0.25mm. There was some variation as the motor accelerated at the beginning and end of each run.

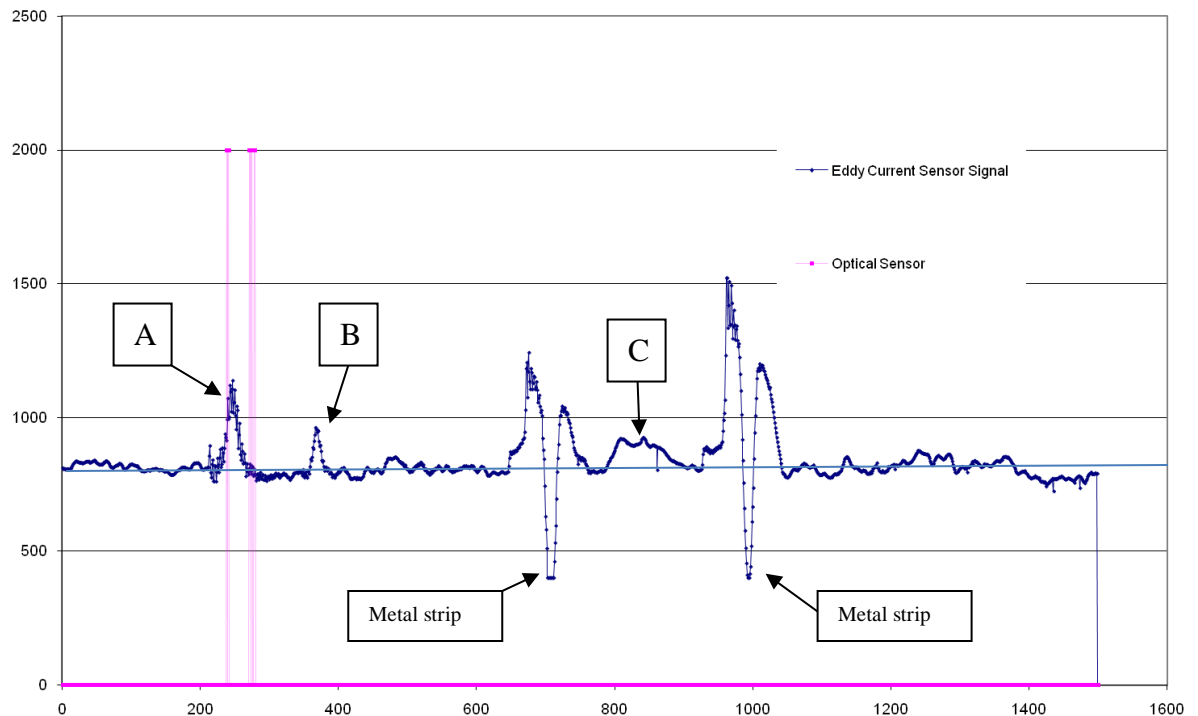


Figure 4.4 Marked 3 features for testing accuracy of measurement

#### **4.3.1.3.3 Potential issues with the test jig:**

The sensor can be inadvertently moved in a number of ways.

After loading, the spring strip of metal may become bent upward, or the Teflon sensor may be at an angle with the surface of the liner.

After changing the position of the sensor it may not line up exactly with the previous position.

The sensor distance may change with position along the length of the liner due to the pressure of the ring causing the liner to move.

The speed can be changed up to “50%” of its rated speed, above which the carriage may hit the end of travel.

The motor controller stops the motor due to overheating after a few runs at the minimum speed (“0%”) but will run at “50%” for at least 300 strokes. It is thought

The maximum error between the obtained readings and the three physical features was within the range of +/-3%.



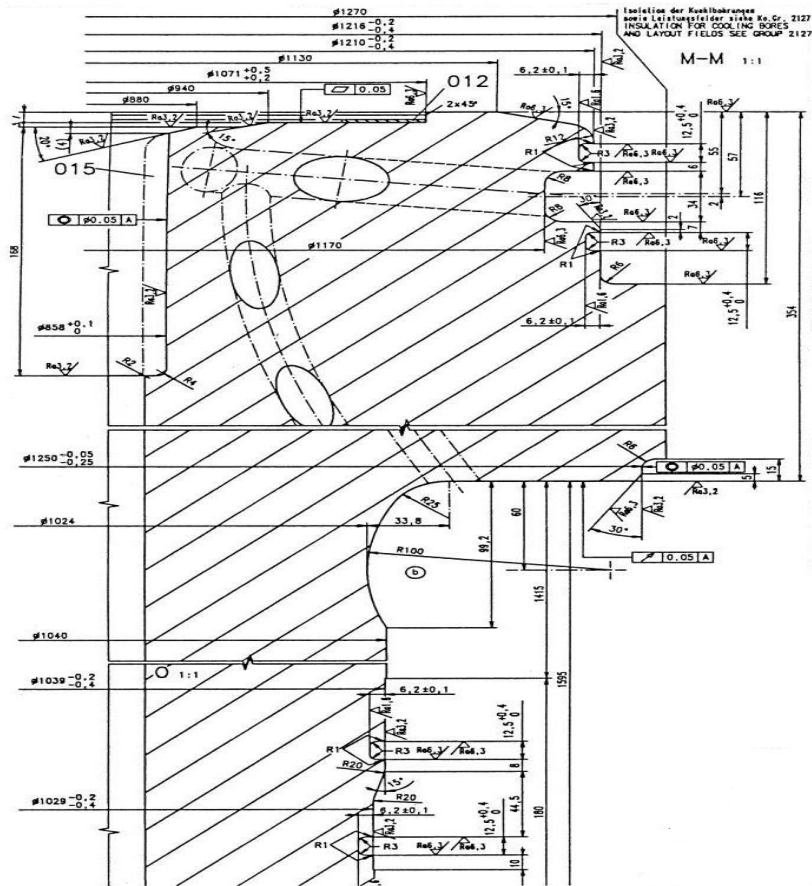


Figure 4.6 Liner details of the specimen

The firing order of the engine is as follows:

1, 6, 7, 3, 5, 10, 9, 2, 4, 8

Eddy current sensors were installed on the unit number 4, as it had the highest liner wear of 3.02 mm against 44,500 running hours. The maximum liner wear tolerable for this engine is 3.5 mm.

The Material Specification of the cylinder liner and piston are as follows:

#### 4.3.2.1.1 Piston crown:

Material 16 CrMo 4 4

Composition: C 0.13-0.20; Si 0.15-0.35; Mn 0.50-0.80; P 0.035; S 0.035; Cr 0.90-1.20; Mo 0.40-0.50; Ni ≤0.40

#### **4.3.2.1.2 Cylinder liner:**

Material Grey Cast Iron with Lamellar Graphite GJL-250

Composition: C 3.3; Si 1.2; Mn 0.5; P 0.25%; S  $\leq 0.06$ ; Cu 1.4; V  $\leq 0.15$ ; B 0.02

Hardness: 180-230HB

#### **4.3.2.1.3 Piston skirt:**

Material Grey cast iron GJL-250; FC250; HT250

Composition: C 3.4; Si 1.3; Mn 0.6; P 0.30-0.40, S max 0.12;

Hardness: >180HB

The material composition is important in order to pick up the most appropriate Eddy sensor.

#### **4.3.2.2 System Concept:**

Four eddy current sensors as shown in the figure 4.7 were placed 90 deg to the BDC of the piston stroke. The sensors scanned the surface of the piston from its crown to the bottom of skirt.

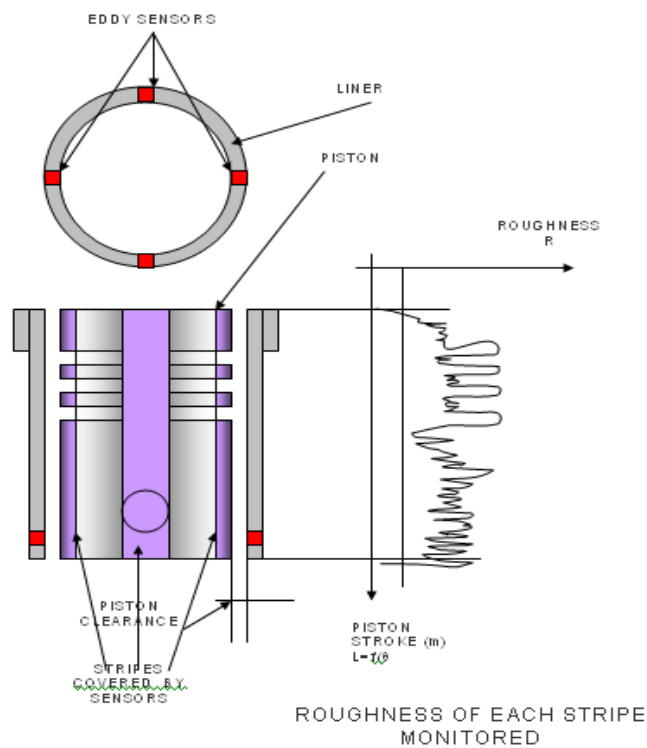


Figure 4.7 System concept

#### 4.3.2.3 System architecture:

The system architecture is shown in the Figure 4.8, which consisted of the following:

Four Eddy sensors per cylinder

Power supply

Sensors excitation

Signal amplifiers

Encoder

Pressure sensor

Data acquisition system

Software for electronic main processing and analysis unit

Computer

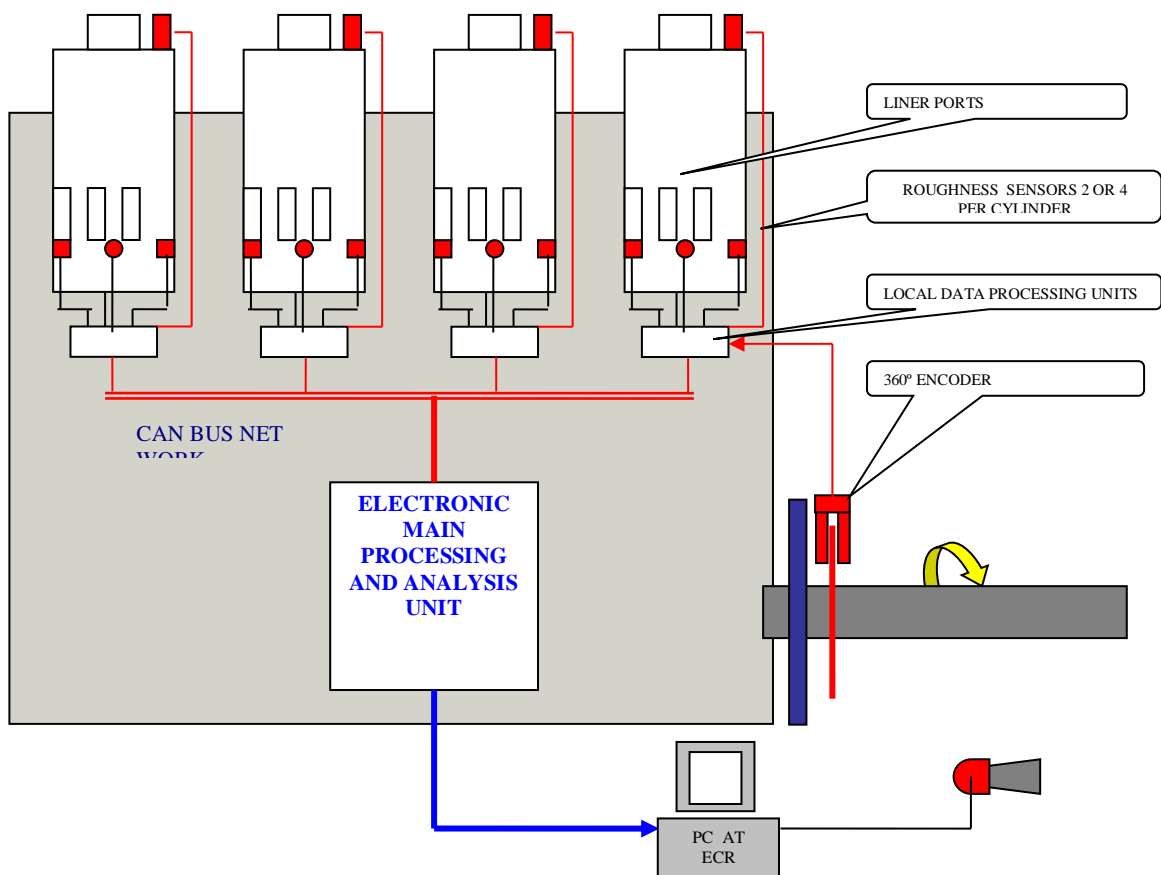


Figure 4.8 Block diagram for the whole system for 4 cylinders

Figure 4.9 show the actual picture of the cylinder liner lying on the floor. It shows the location of the installation of the four eddy sensors around its periphery, which are just above the scavenge ports of the liner.



Figure 4.9 Cylinder Liner

Figure 4.10 shows the three of the four holes with the bolting arrangements, which were drilled around the cylinder liner periphery above the scavenge ports in order to install the eddy sensors.



Figure 4.10 Cylinder liner sensor holes (shown 3 of 4holes)  
(4 sensor holes were drilled onto the liner above scavenge ports)

Figure 4.11 shows the encapsulated eddy sensor along with the length of cable to be connected with the electronic main processing and analyzing unit

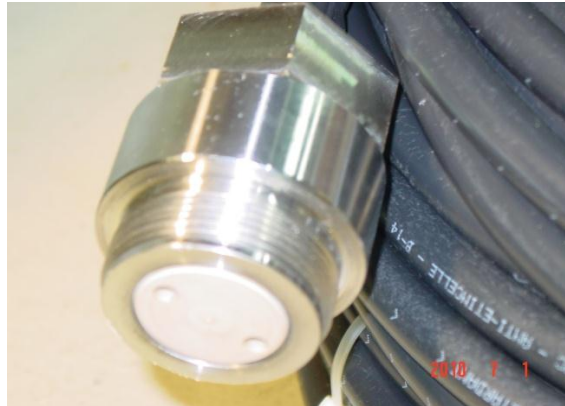


Figure 4.11 Four encapsulated sensors fitted to the four liner holes

Figure 4.12 shows the pictorial view of the eddy sensors fitted to the cylinder liner

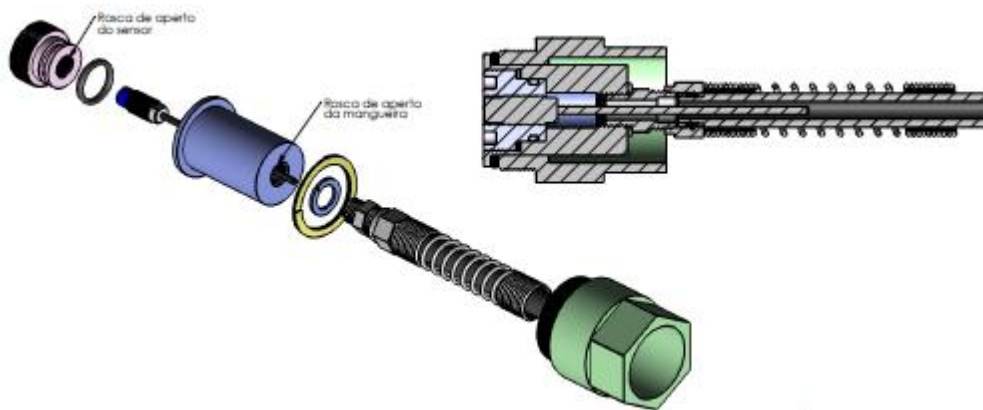


Figure 4.12 Pictorial view of the eddy sensor

Figure 4.13 (a) and (b) shows the detailed sectional drawings of the eddy sensors in vertical and horizontal positions.

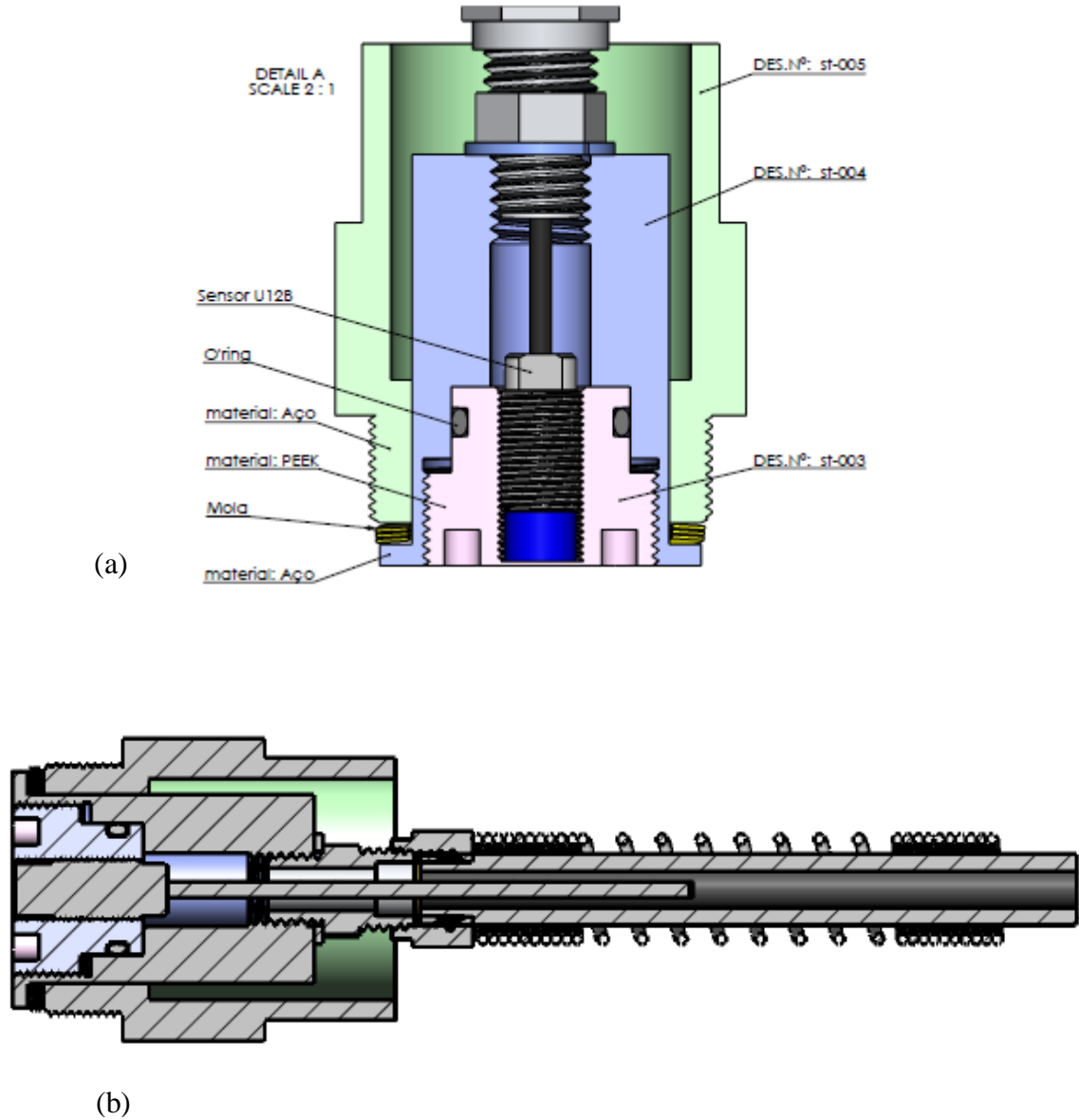


Figure 4.13 Sensor sectional drawing with cable

#### **4.3.2.4 Engine Load and Cylinder pressure:**

Cylinder pressure diagrams as shown in Figure 4.14 were taken of unit 4 of the engine with engine performance analyzer of Figure 4.8 at different loads and the distance reference points of each load were formed, as the load of the engine exerts load at the back of the piston ring, which will affect the distance reading between the cylinder liner and the piston rings.

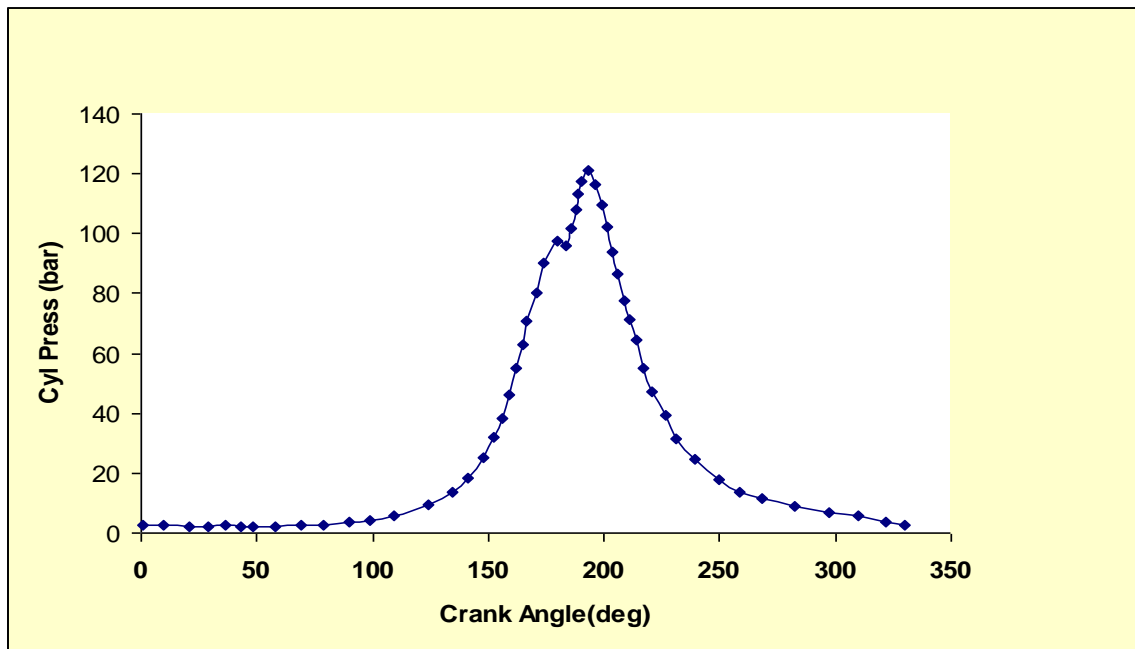


Figure 4.14 Crank Angle/Cylinder Pressure from Performance Analyzer @ 85% MCR

With the data entry of ring thickness, ring diameter and the ring gap, the ring's normal pressure was superimposed onto the combustion pressure measured from the unit as shown in Figure 4.15.

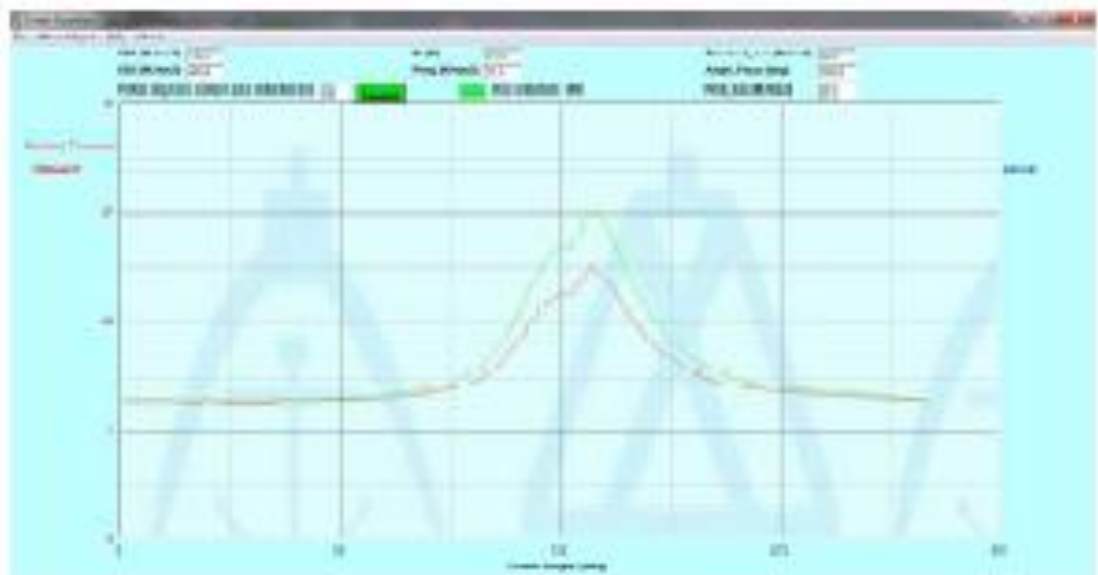


Figure 4.15 Pressure angle diagram from Liner guardian software (developed from present study)

#### 4.3.2.5 Software development and system variables: (numerical & graphical display):

With the collection of the data, all values were converted to the crank angle as shown in the Figure 4.16. All values were referenced to the TDC from 0° to 180°. The unit for averaged roughness was the value of 1 micron. The roughness coverage of the transducers ranged from 0 ~ 3500 microns.

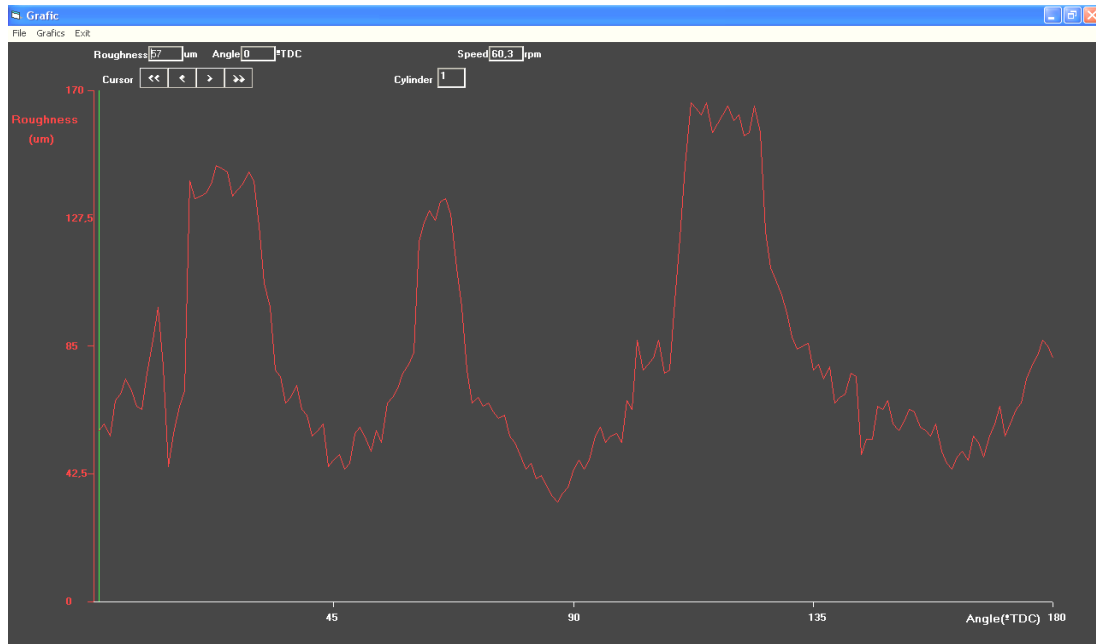


Figure 4.16 Aligning Angle against roughness

The values of roughness were read for each crank angle, as well as the engine revolution and the piston linear speed for each sample points of the cylinder.

The software was developed. The information the system measured were: reference Ra (Rar); in service Ra (Ras); difference (Rar-Ras); Standard deviation of (Rar-Ras); rate of increase of the standard deviation (Rar-Ras); alarm levels from deviation; time stamp, number of strokes, rpm and cylinder pressure profile.

In summary: The system monitors the following variables:

- Roughness from sensor 1 as a function of time/crank angle, i.e.  $R_a = f(t)$  or  $f(\theta)$



- Roughness from sensor 2 as a function of time /crank angle, i.e.  $R_a = f(t)$  or  $f(\theta)$
- A delta value between the reference roughness profile (previously recorded) and any actual roughness data
- For each set of data an average roughness number
- For each set of data a standard deviation
- RPM to work out the piston speed
- Cylinder pressure to work out the compression and expansion pressures of the piston rings against the liner and its groove as a function of crank angle
- Calculated MEP, measured peak pressure and Rate of Pressure Rise as this is fundamental for piston ring collapse monitoring
- All the data set with a time and date stamp
- A liner temperature measurement to relate to the viscosity of the lubricant
- A boost air pressure (optional) to measure load
- Acquisition of data is initiated by the request on the software

The data capturing software configuration is shown in Figure 4.17. The engine and the cylinders were named. The experience names were defined as the data collection points of the sensors, i.e. Forward, Aft, Port and Starboard. Under the acquisition type, the variables were recorded, such as 25%, 50%, 75% and 92% load, Heavy Fuel or MDO operation, Various sulphur content, Reduced CLO feed etc. The example of the names of the acquisition types given was HFO/1.45%S/75%Load /0.72g/bhp/h CLO. The acquisition timings and the period were captured by initiating the acquisition. On the right hand side the stored / saved experiments were retrieved.

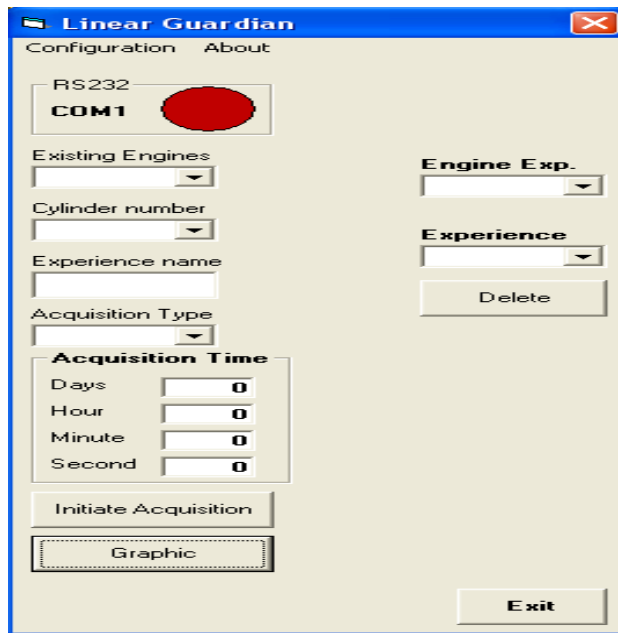


Figure 4.17 Developed data capturing software configuration

For the measuring system, the pressure combustion traces were synchronized with the rest of the measurements.

#### **4.4 Field test of AE sensor:**

##### **4.4.1 Lab test:**

##### ***4.4.1.1 Development and Characterization of AE Sensor:***

Two types of AE sensors were selected. One was the commercial sensor from Kistler and the other one was developed in-house. The bandwidth of the in-house sensor was from 0.5-10kHz, while that from Kistler was from 10kHz-200kHz.

##### ***4.4.1.2 Development of Electronics and Data Acquisition Hardware:***

The AE system used the self developed high bandwidth, high fidelity pre-amplifier. The AE system used was a National Instrument digitizer that was USB based and hence could be connected to a laptop or a desktop for data acquisition.

The throughput of the USB 2.0 interface was tested and found to be sufficient. The software for Data acquisition has been developed and tested.

#### **4.4.1.3 Fabrication of test rig:**

Schematic of the prepared test rig is shown in the Figure 4.18.

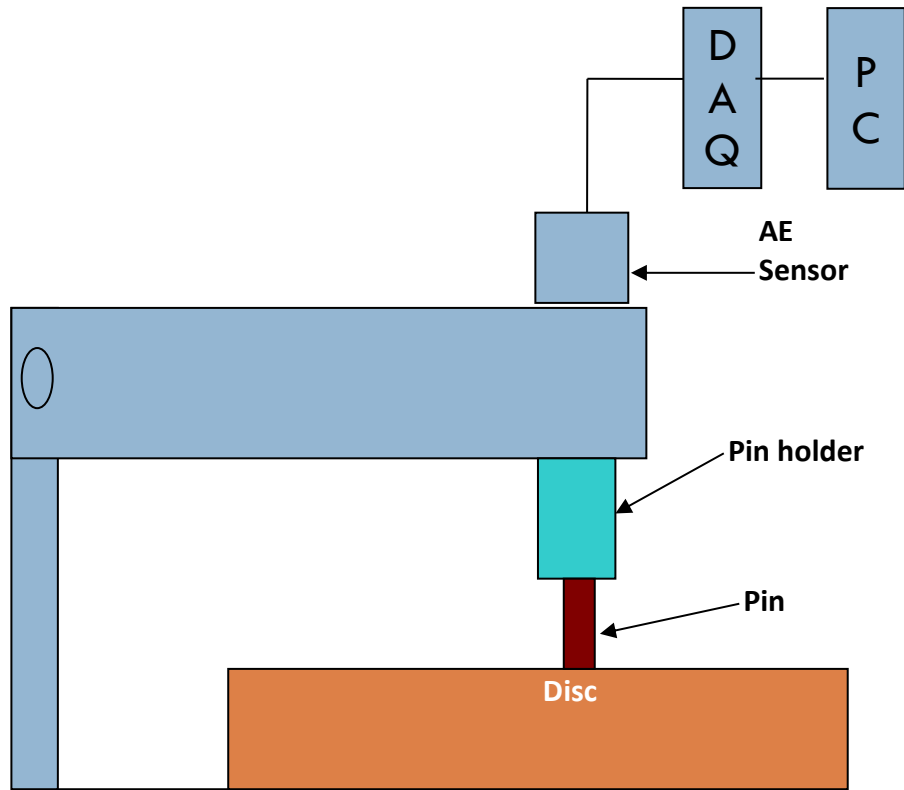


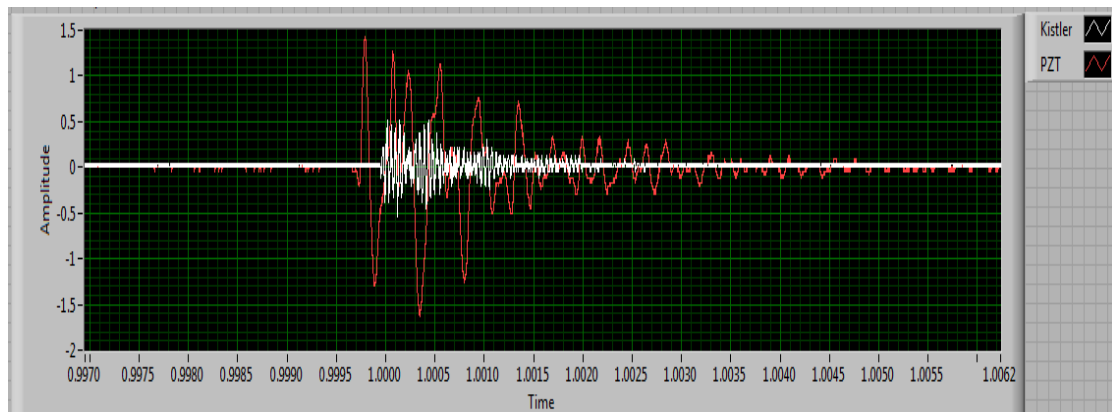
Figure 4.18 Schematic of test rig

#### **4.4.1.4 Integration of Hardware and Sensor:**

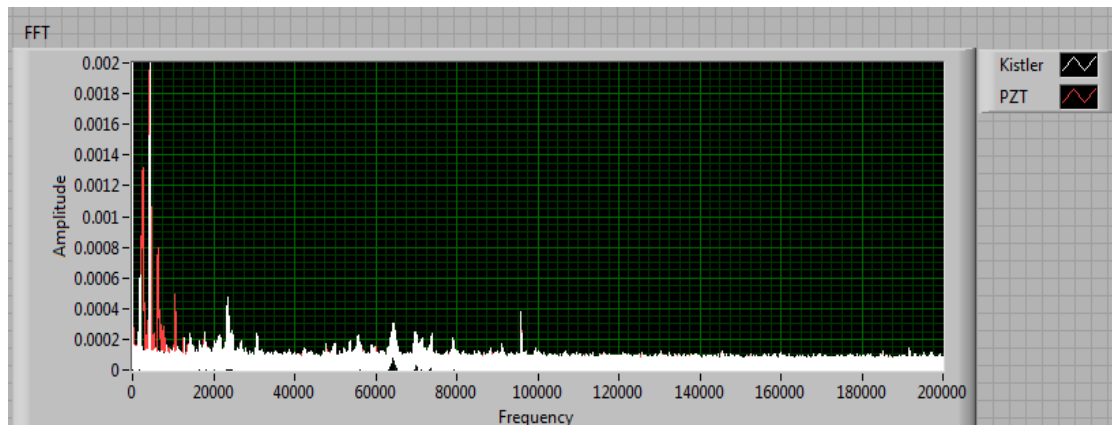
The data acquisition system and the sensor system have been integrated and tested. Several issues regarding the interfacing have been solved and the system has been tested in the test rig.

#### **4.4.1.5 Test rig preliminary data analysis:**

The performance of the in-house sensor using PZT crystal was compared with that of the Kistler sensor. The pencil load break test data of these two sensors against time and frequency are shown in Figure 4.19 (a) and (b) respectively.



(a)



(b)

Figure 4.19 Pencil load break test data of Kistler and in-house PZT crystal sensor against (a) time (b) frequency

The pencil test data confirmed that the in-house sensor can register amplitudes and system gain of sufficient magnitude against voltage. Secondly, it confirmed the accuracy of the source location setup by indirectly determining the actual value of the acoustic wave speed for the object being monitored.

The performance of the aluminum and mild steel pin on stainless disc were tried out at 4 different speeds (50, 100, 150 and 200 RPM). The preliminary data and analysis of aluminum and mild steel pins on stainless steel disc are shown in Figures 4.20 and 4.21 respectively.

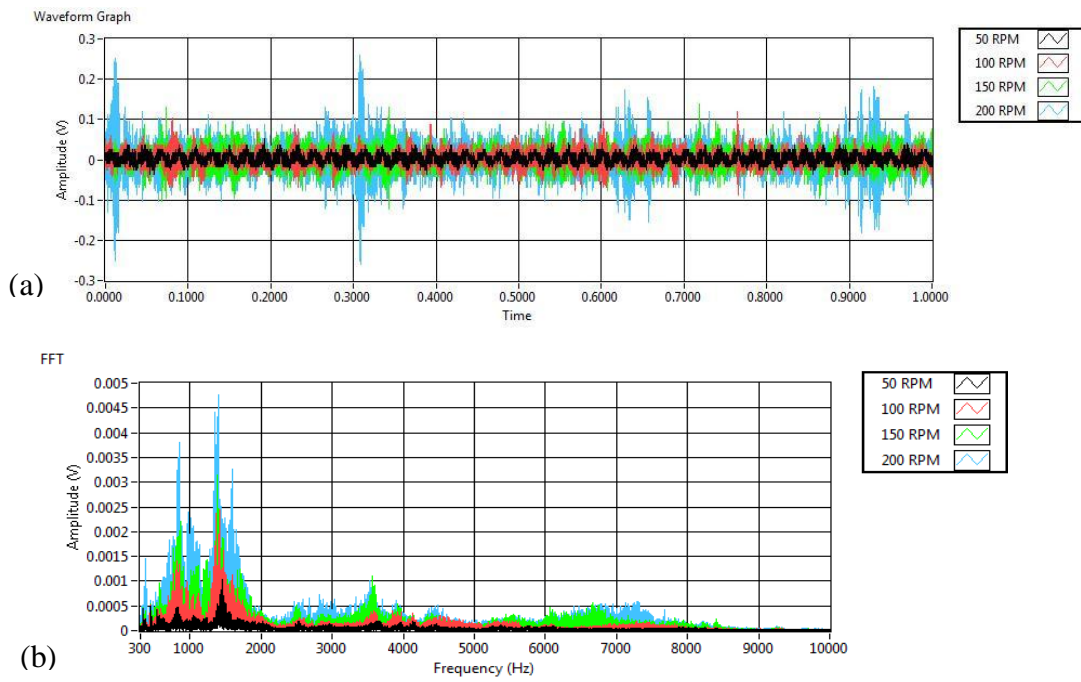


Figure 4.20 Preliminary test data of Aluminum pin on stainless steel disc

(a) time (b) frequency

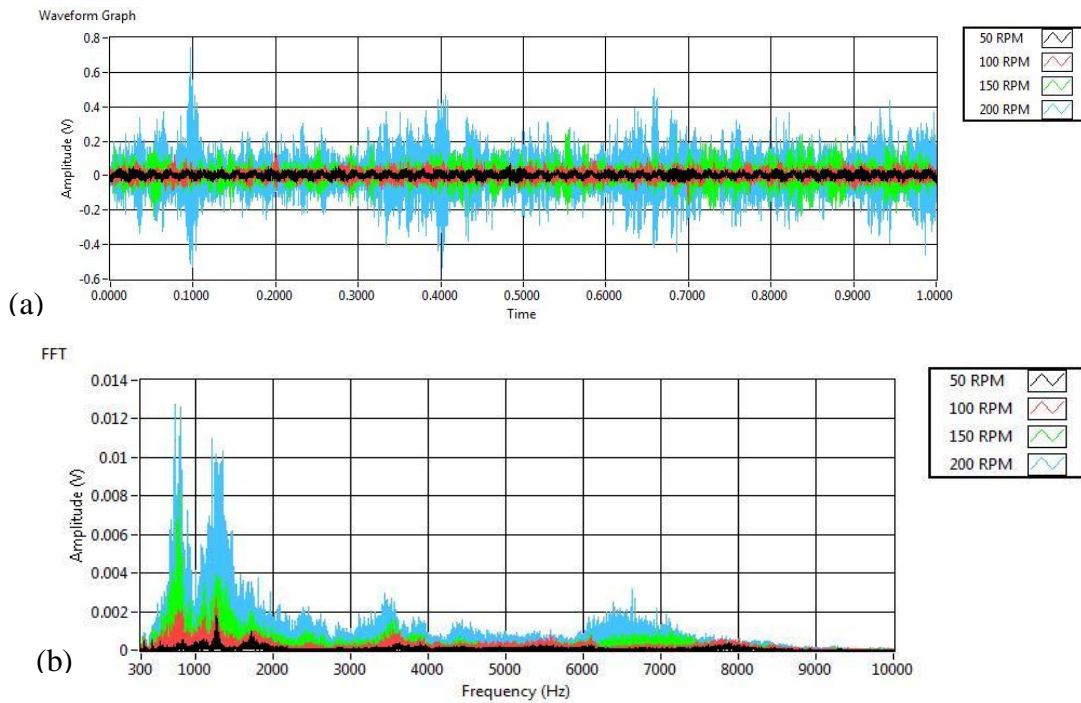


Figure 4.21 Preliminary test data of mild steel pin on stainless steel disc

(a) time (b) frequency

The preliminary data and analysis of mild steel pins on stainless steel disc with and without lubrication were carried out as shown in Figure 4.22.

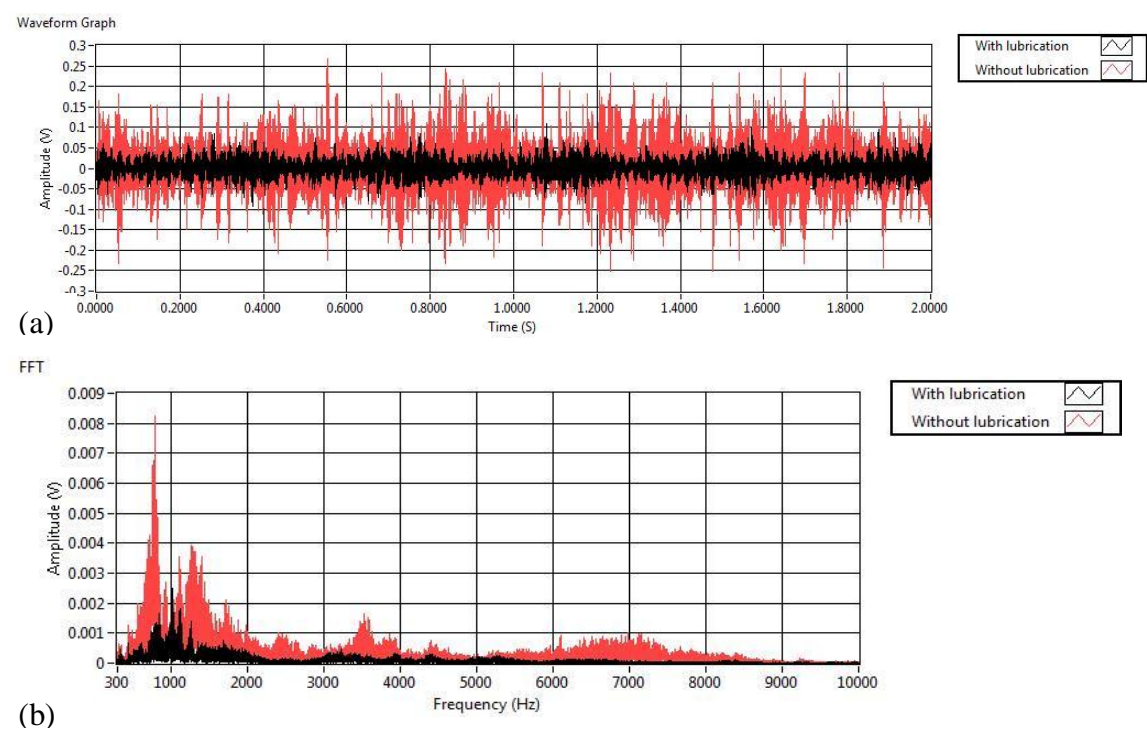


Figure 4.22 Preliminary test data of mild steel pin on stainless steel disc with/without lubrication (a) time (b) frequency

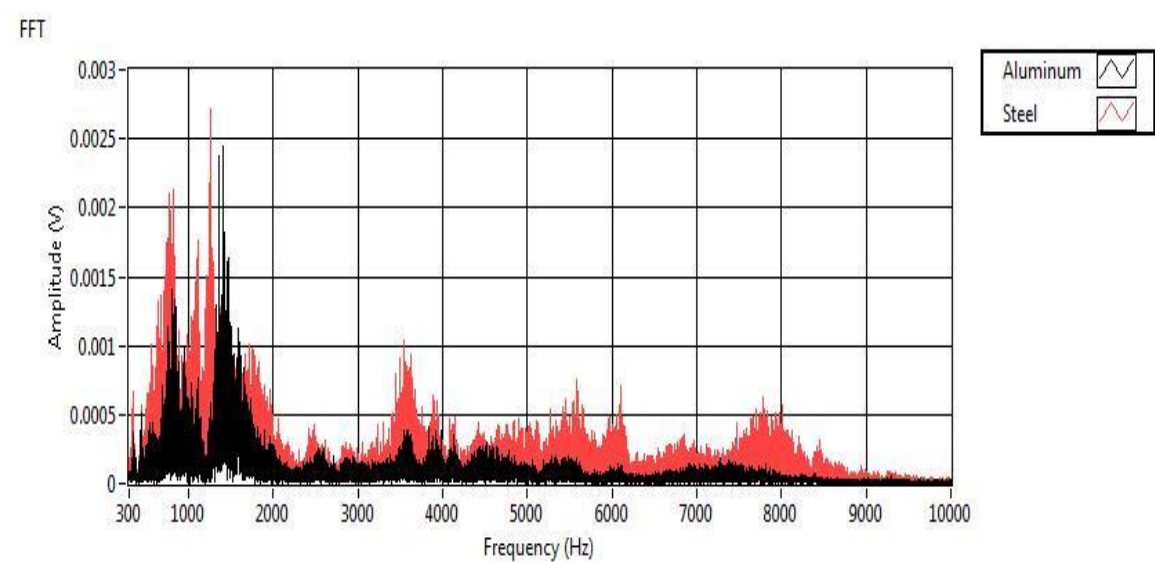
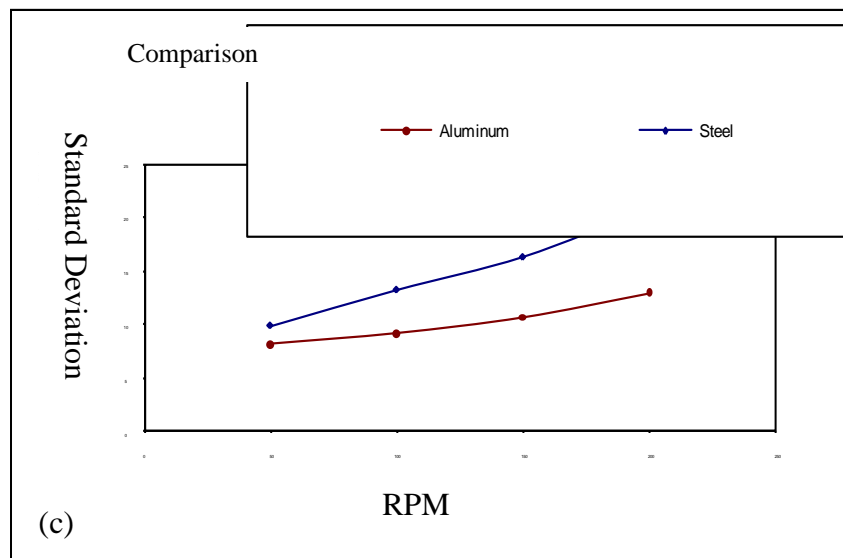
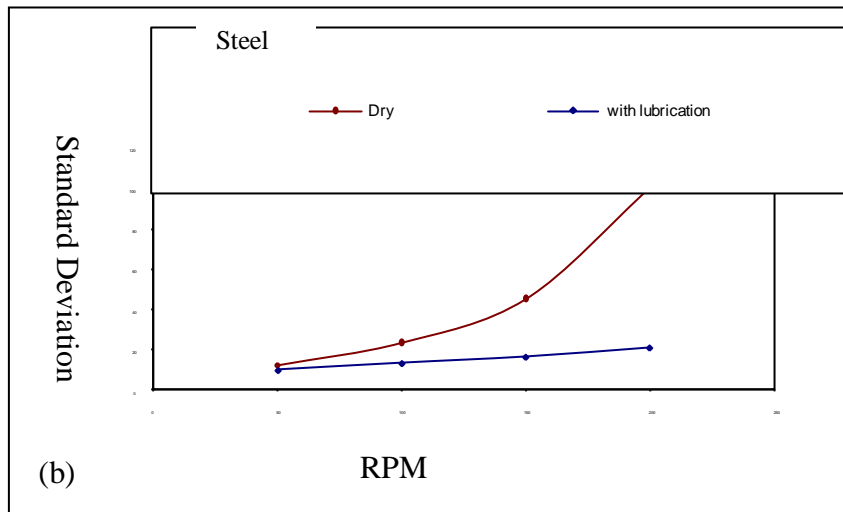
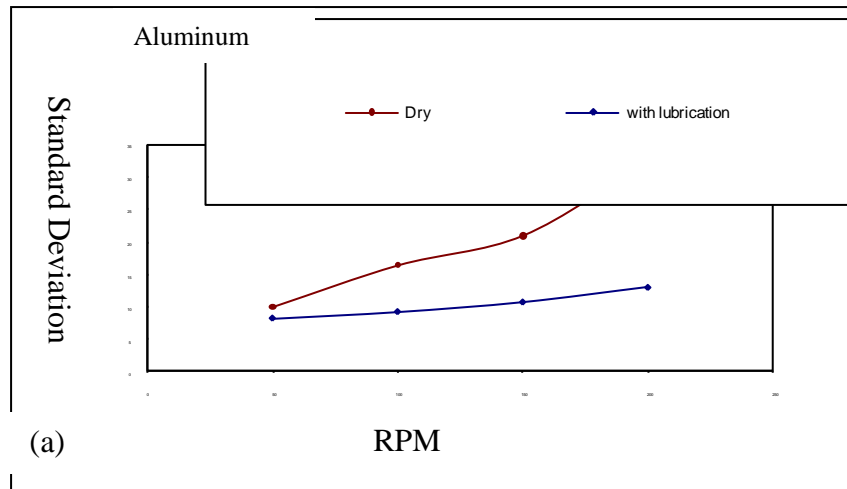


Figure 4.23 Comparison of AE amplitudes of aluminum and mild steel pins



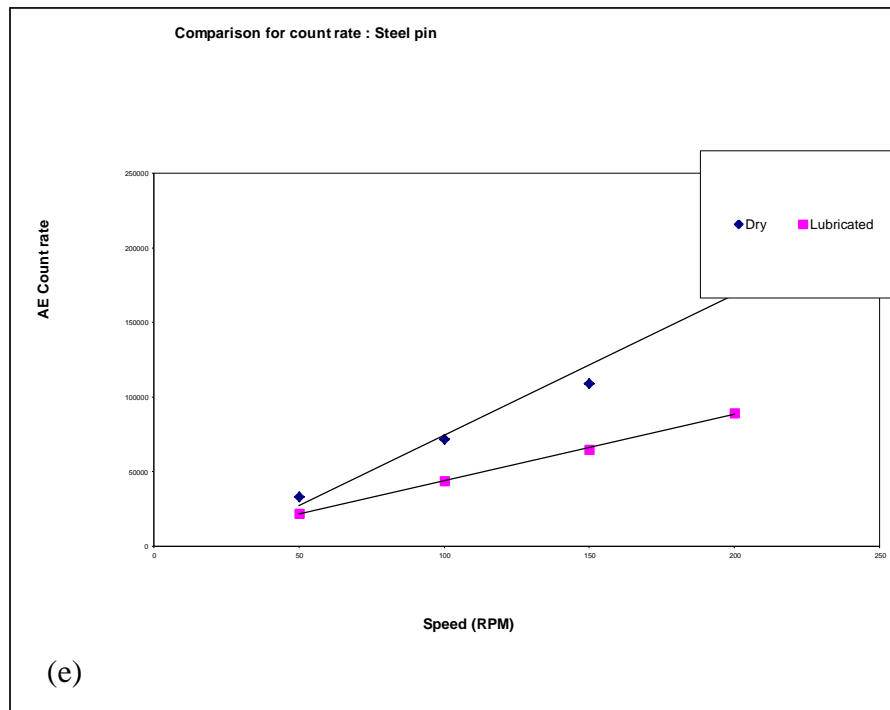
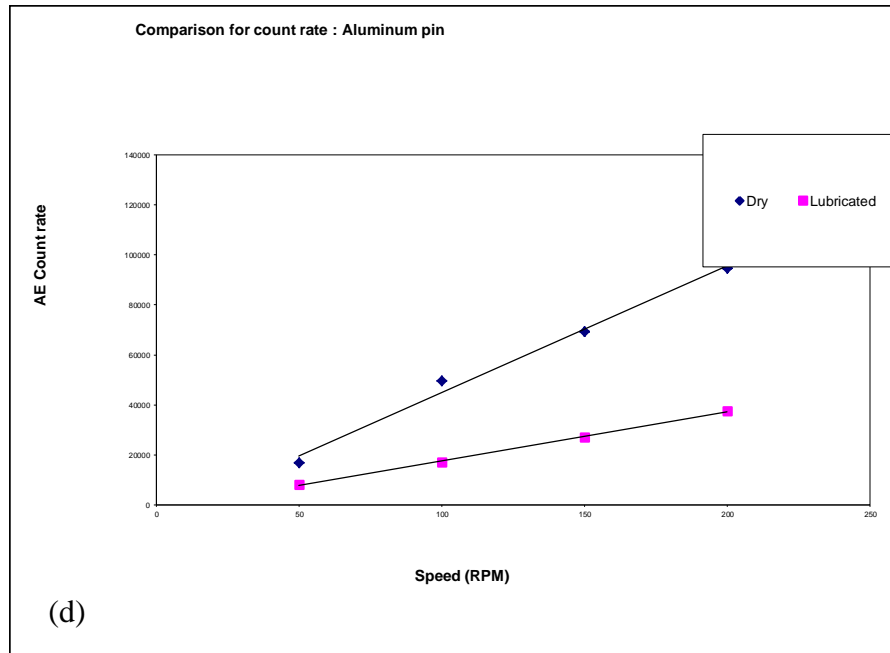


Figure 4.24 Preliminary statistical data analysis of aluminum and mild steel pin on stainless steel disc (a) SD-Aluminum (b) SD- Mild steel (c) Comparison of SD (d) AE count rate-Aluminum (e) AE count rate-Mild steel



The difference of amplitudes of aluminum and steel pin on stainless steel disc is shown in Figure 4.23. Standard deviations of aluminum and steel pin against various speeds are shown in Figure 4.24 (a) and (b) respectively and their comparison is shown in (c). Comparison for AE count rate of aluminum and steel pin against various speed are shown in (d) and (e). From this statistical analysis, the suitability of the steel pin was concluded for the in-house sensor and the experiments.

#### 4.4.2 Engine Test:

##### 4.4.2.1 Sensor mounting locations:

A four stroke, air cooled, single cylinder motor cycle engine was used for the experiments. Commercially available broad band AE sensors from Kistler Instrument Corporation (8152B211) with a frequency range of up to 1 MHz were used for acquiring the data. An 8 bit high speed digitizer from NI (NI USB-5133) with a maximum sampling rate of 100 MHz was used for data acquisition.

Two sensors were mounted on the fin of the engine cylinder as shown below in Figure 4.25 and 4.26. These were tested over several hours each and found that both sensors do not degrade over the period of testing.

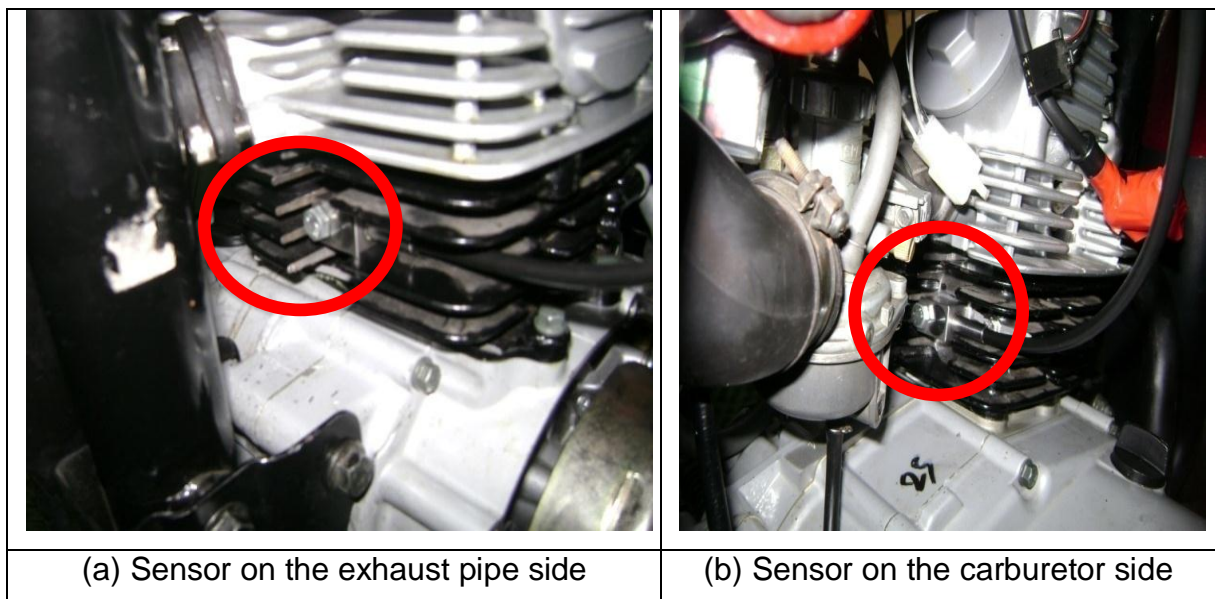


Figure 4.25 Sensor locations

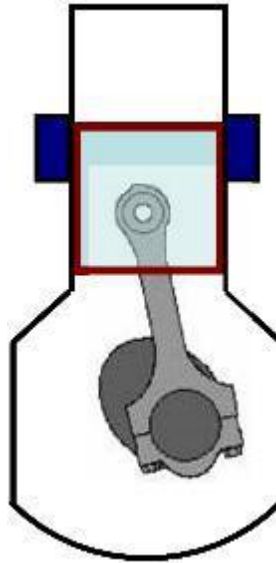


Figure 4.26 Schematic of sensors location

The AE data was then collected for four different speeds of the engine for different simulated fault conditions. The data was sampled at one MHz and the duration of each record was one second. The collected data was transformed from time domain to crank angle domain by using the reference data collected using a magnetic field speed sensor from 2D data recording systems. Figure 4.27 shows the sample of the data collected for one engine cycle for the sensor mounted on thrust side. It can be clearly seen that the sensor records four continuous type of AE event that correspond to the four strokes of the piston.

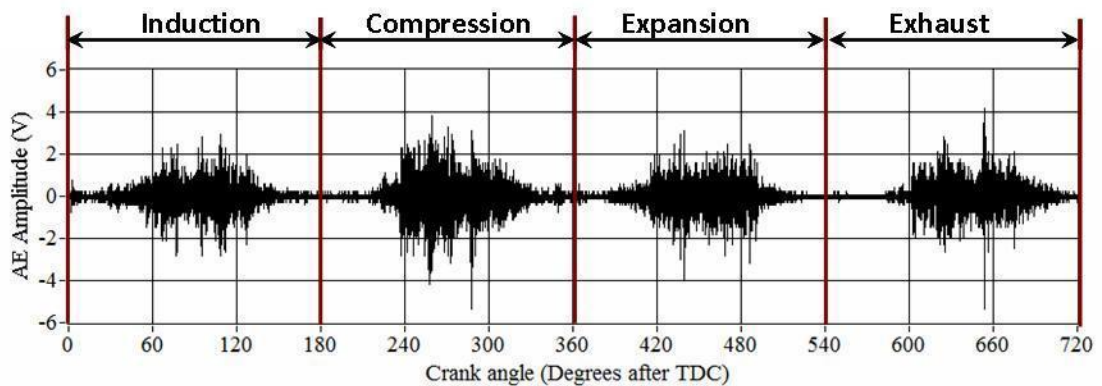


Figure 4.27 Sample data of one engine cycle acquired using sensor-1

Details of Sensor and instrumentation used are as follows:

- In-house PZT sensor (200 KHz natural frequency)
- Kistler, piezotron – 8152B211

Frequency range : up to 1 MHz

Sensing element : Piezoelectric ceramic mounted on steel-diaphragm

Output voltage :  $\pm 2$  V Full scale

Current : 4 mA

Excitation voltage: 30 V

DAQ : NI 5133, 8 bit, Max sampling rate: 100 MHz

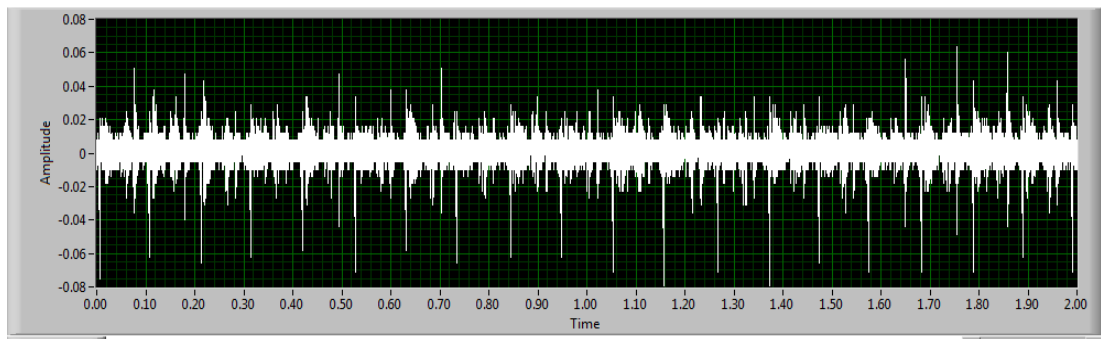
#### ***4.4.2.2 Data collected on Single Cylinder Engine:***

The data was collected for two sets of piston rings, a fresh set and a set of worn out rings. The details are given in the table 4.5 below.

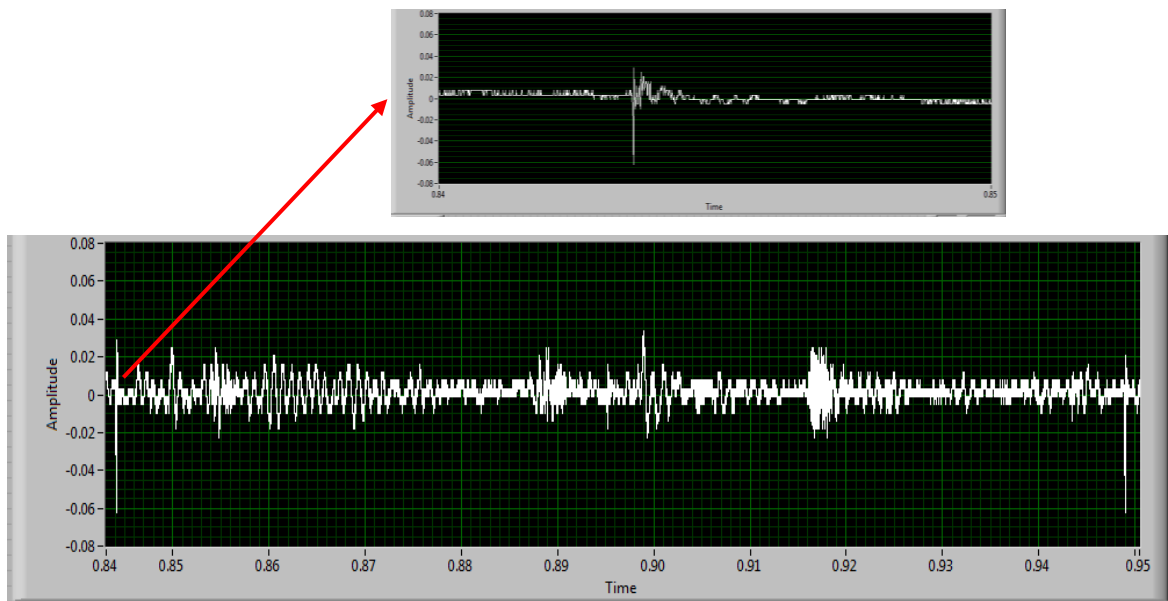
	Close end gap	
	First ring	Second ring
Fresh sample	0.13	0.15
Worn out rings	1.168	0.635

Table 4.5 Close end gaps of rings

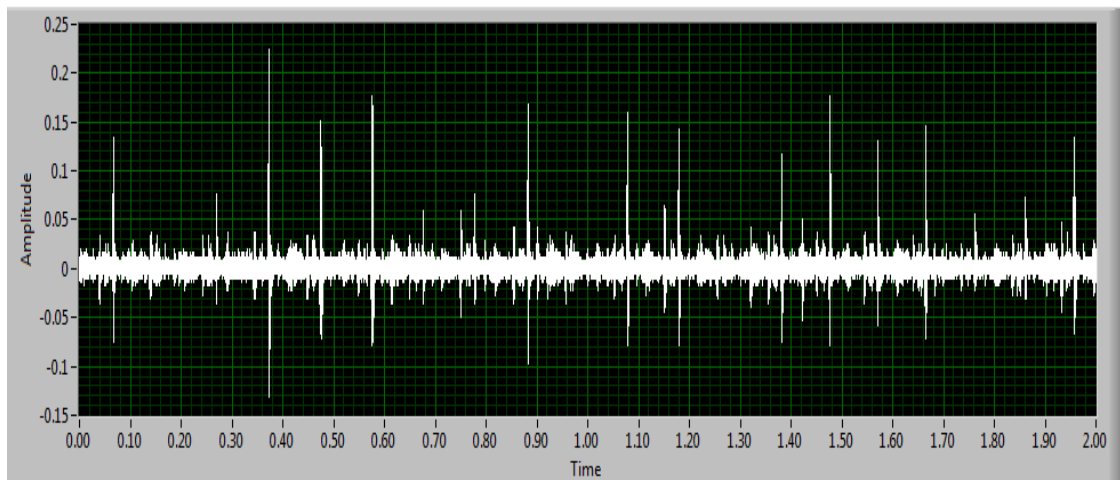
The data was collected by motoring the engine using a chassis dynamometer. One set of data was collected on the running engine as well. The data was collected at four different speeds of the engine at 4th gear i.e. 30, 40, 50 and 60 km/h. The corresponding engine RPM were 2660, 3550, 4440 and 5320 respectively. Data from in-house PZT sensors and Kistler sensors of the spark plug side and opposite spark plug side are shown in Figures 4.28 and 4.29 respectively.



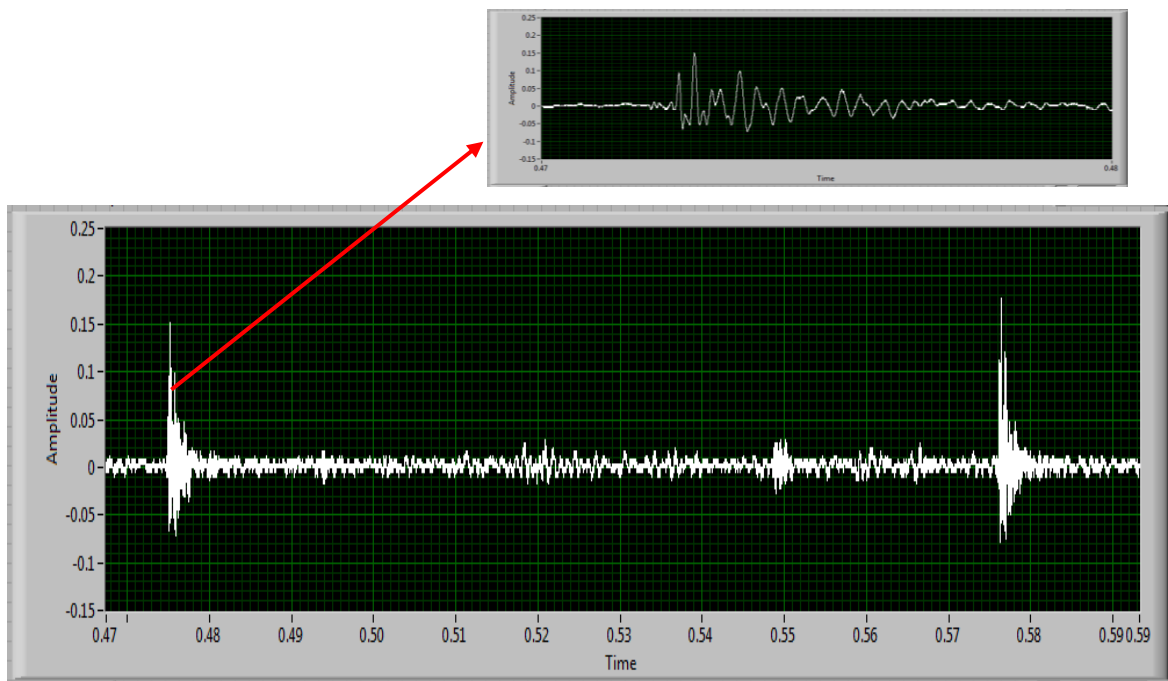
(a)



(b)

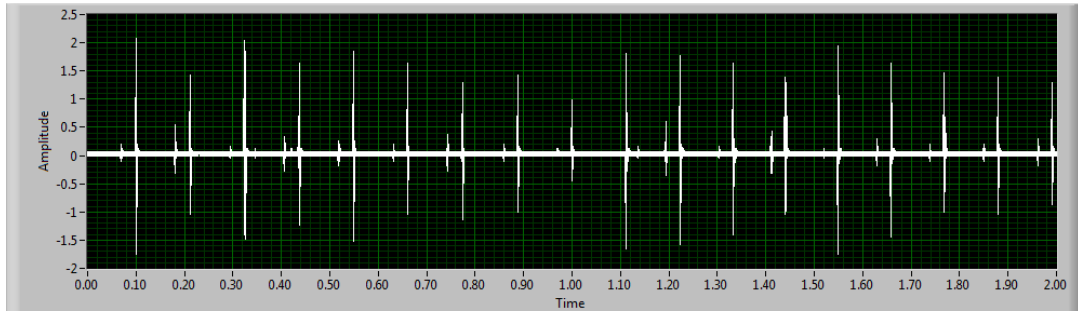


(c)

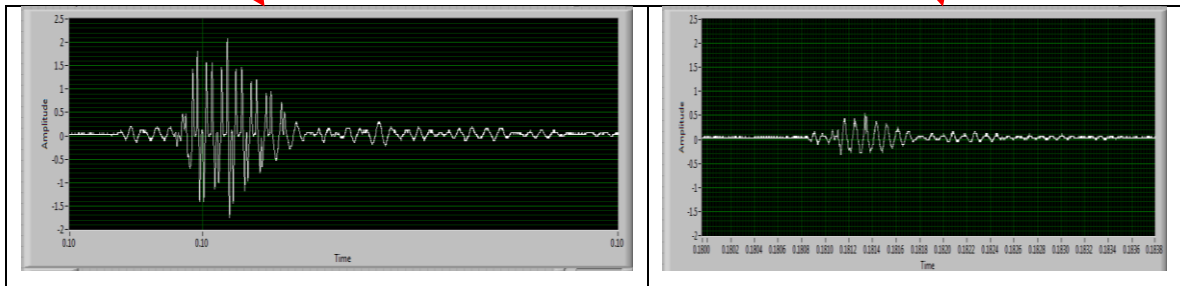
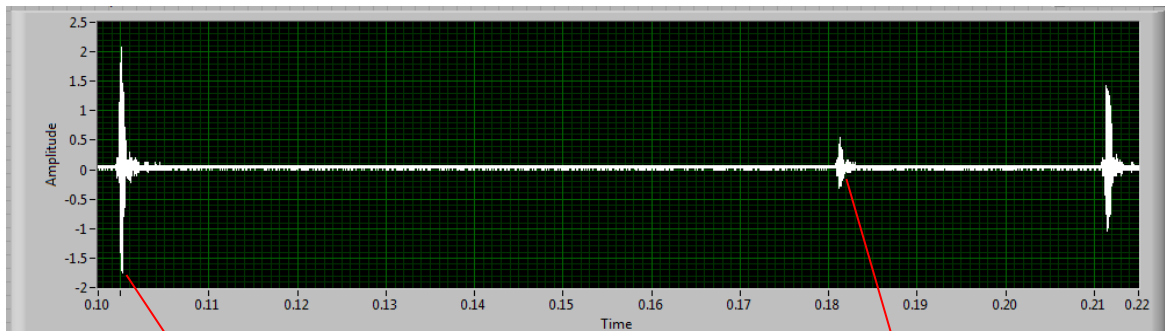


(d)

Figure 4.28 Data from in-house PZT sensors (a) Sensor output from Spark plug side, (b) Zoomed in view (c) Sensor output from opposite side of Spark plug (d) Zoomed in view



(a)



(b)

Figure 4.29 Data from Kistler sensors (a) Sensor output from opposite side of Spark plug (b) Zoomed in view

From the comparison of the spectrum of the acoustic signals of in-house PZT sensor and Kistler sensor, it is obvious that in-house sensor captures more information and events of the combustion process than that from Kistler sensor. Hence, in-house PZT sensor was used for the rest of the experiment.

#### 4.4.2.3 Methodology followed:

Figure 4.30 shows the methodology followed for the study. A reference data was collected by assembling all the good parts on a new engine. This reference data was used for comparison with the data collected for different simulated fault conditions. The test engine was then intentionally introduced with different fault conditions that can occur in the components of the interest, the piston ring and cylinder wall interface. The three fault conditions induced included (1) worn out piston rings, (2) worn out piston and (3) oil starved condition at the ring/wall interface. The worn out piston rings had the closed end gap increased by 67% higher than the allowed limits. In case of worn out piston the clearance between the piston and cylinder wall was 22.45% higher than the design specifications. The oil starved condition between piston and the cylinder wall was simulated by running the engine after draining the lubricating oil from the engine completely. The AE data was acquired for these induced fault conditions and analyzed to understand the features in the signature of the data that highlight the respective fault condition.

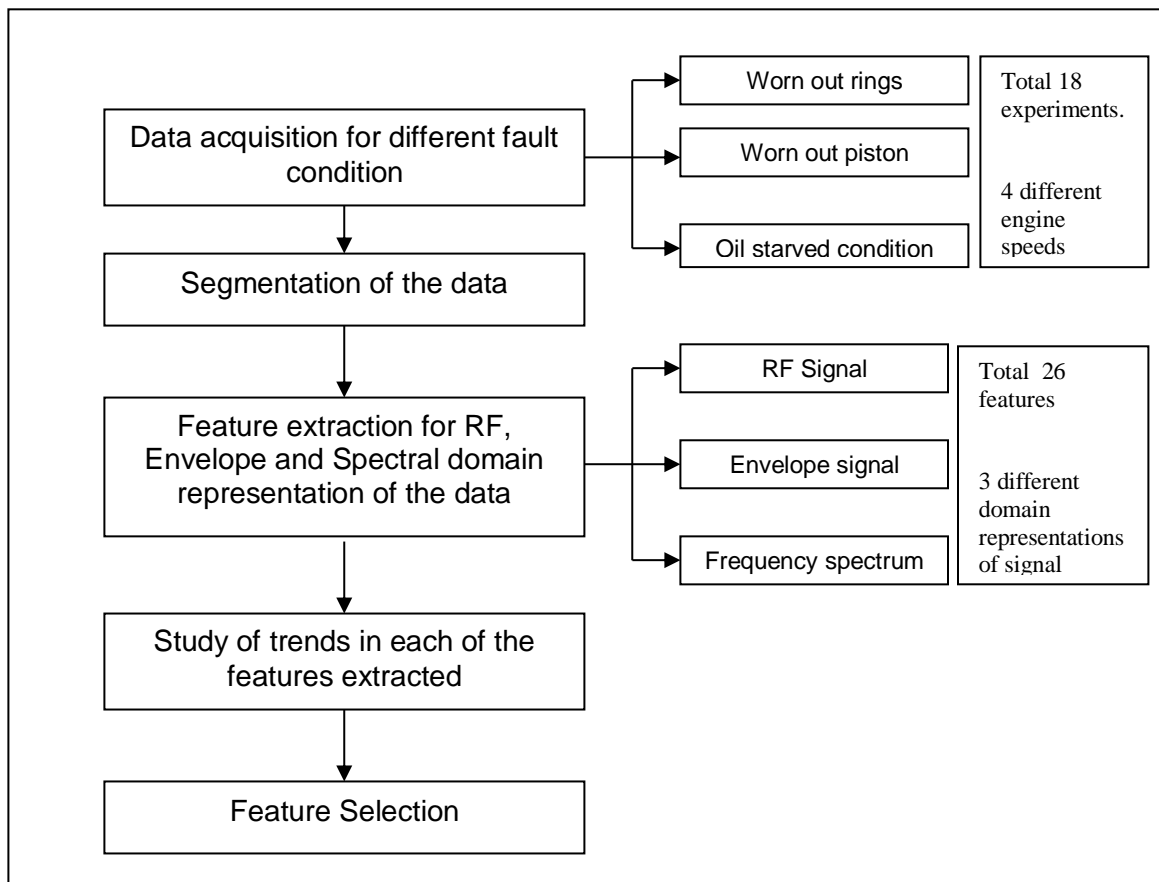


Figure 4.30 Methodology followed for the study

#### ***4.4.2.4 Development of Digital Signal Processing (DSP) Algorithms:***

The algorithm has the following features and is developed and tested:

- Time domain gating and feature selection
- Frequency domain feature selection
- Hilbert Transform feature selection
- STFT feature Selection
- Wavelet features



## Chapter 5. Results and Discussions

---

### 5.1 Tribology model results and discussions:

The tribology model was developed, which can be found in the attached Excel file named, 'Tribology model'. The usage of the model is described under Appendix 2. Three conditions of hydrodynamic, boundary and mixed lubrication are discussed. 'No lubrication' is the extreme case, which the engine would hardly face in the real world and in such scenario, the engine seizure would occur immediately owing to very high coefficient of friction. Hence, it is excluded from the discussion.

#### 5.1.1 Hydrodynamic lubrication:

In order to find the hydrodynamic pressure which balances the combustion chamber pressure on piston ring at various crank angle, the constants  $C_1$  and  $C_2$  need to be determined against the boundary conditions. A simplistic approach was made to find  $C_1$  and  $C_2$  for equation 3.67 considering the values of  $x_1 = 0$ ,  $x_2 = B/2 = 0.01$ ,  $x_4 = B = 0.02$  (where  $B = 0.02\text{m}$ , the ring height).

##### 5.1.1.1 To find constants $C_1$ and $C_2$ :

For  $C_1$  :

@  $x = x_2 = 0.01$ ,

$$\frac{\partial p}{\partial x} = 0$$

$$\frac{\partial p}{\partial x} = 12\eta u \left[ \frac{1}{h^2} + \frac{\omega}{u} \left( \frac{\partial h}{\partial \theta} \right) \frac{x}{h^3} + \frac{C_1}{h^3} \right] = 0$$

$$\text{Hence, } C_1 = -h_0 - \frac{\omega}{u} \left( \frac{\partial h}{\partial \theta} \right) * 0.01 \quad (5.1)$$

For  $C_2$ :

@  $x = x_1 = 0$ ,  $P_z = P_1$ , we need to find  $E$ ,  $F$  and  $G$  for  $x = 0$ ;

$$E = -\frac{1}{4h_0^2} \left\{ \frac{B \tan^{-1}(\sqrt{K})}{\sqrt{K}} + \frac{B}{K+1} \right\} \quad (5.2)$$

$$F = -\frac{1}{32h_0^3} \left\{ \frac{3B^2 \tan^{-1}(\sqrt{K})}{\sqrt{K}} + \frac{2B^2}{K(K+1)} + \frac{3B^2}{K+1} \right\} \quad (5.3)$$

$$G = -\frac{1}{16h_0^3} \left\{ \frac{3B \tan^{-1}(\sqrt{K})}{\sqrt{K}} + \frac{2B}{(K+1)^2} + \frac{3B}{K+1} \right\} \quad (5.4)$$

Hence, by putting the values of E, F, G and  $C_1$  in the pressure Equation 3.68:

$$\begin{aligned} C_2 &= \frac{P_1}{12\eta u} - E - \frac{\omega}{u} \left( \frac{\partial h}{\partial \theta} \right) F - C_1 G \\ &= \frac{P_1}{12\eta u} + \frac{1}{4h_0^2} \left\{ \frac{B \tan^{-1}(\sqrt{K})}{\sqrt{K}} + \frac{B}{K+1} \right\} + \frac{1}{32h_0^3} \left\{ \frac{3B^2 \tan^{-1}(\sqrt{K})}{\sqrt{K}} + \frac{2B^2}{K(K+1)} + \frac{3B^2}{K+1} \right\} \\ &\quad * \frac{\omega}{u} \left( \frac{\partial h}{\partial \theta} \right) + \frac{1}{16h_0^3} \left\{ \frac{3B \tan^{-1}(\sqrt{K})}{\sqrt{K}} + \frac{2B}{(K+1)^2} + \frac{3B}{K+1} \right\} \\ &\quad * \left\{ -h_0 - \frac{\omega}{u} \left( \frac{\partial h}{\partial \theta} \right) * 0.01 \right\} \end{aligned} \quad (5.5)$$

#### 5.1.1.2 $P_z$ Profile:

Now, with known  $C_1$  and  $C_2$ ,  $P_z$  profile can be drawn with variable E, F and G against the X-axis of the steady state crank angle condition with Equation 3.68:

$$p = 12\eta u \left[ E + \frac{1}{R} \frac{R\omega}{u} \left( \frac{\partial h}{\partial \theta} \right) F + C_1 G + C_2 \right]$$

The hydrodynamic oil pressure profile is divided in two sections over the X-axis as 1 and 2, which are subjected to gas pressure  $P_1$  and  $P_2$  at their initial points. The equation of the divided X-axis is shown in Equations 5.6 and 5.7.

$$P_{z1} = 12\eta u \left[ E + \frac{\omega}{u} \left( \frac{\partial h}{\partial \theta} \right) F + C_1 G + C_2 \right] \quad (5.6)$$

For  $x = 0 \rightarrow 0.01\text{m}$  and  $C_2$  is based on gas pressure  $P_1$ .

$$P_{z2} = 12\eta u \left[ E + \frac{\omega}{u} \left( \frac{\partial h}{\partial \theta} \right) F + C_1 G + C_2 \right] \quad (5.7)$$

For  $x = 0.011 \rightarrow 0.02\text{m}$  and  $C_2$  is based on gas pressure  $P_2$ .

The liner temperature varies along the length of the cylinder and it was therefore necessary to determine the axial distribution of liner temperature. In any event, it was necessary to determine the relationship between the effective lubricant viscosity and crank angle,  $\eta = f(\theta)$ , which was earlier shown in Equation 3.11 and used in the X-cel file.

#### **5.1.1.3 Hydrodynamic pressure distribution:**

In order to derive the hydrodynamic pressure distribution, an initial estimate was made of the minimum film thickness at  $30^\circ$  crank angle after TDC and the hydrodynamic pressure was found to be balanced with the radial force Equation 3.77. And the initial squeeze film velocity enabled an estimate to be made of the film thickness at the next increment  $(\theta + \delta\theta)$  of crank angle. The integrated Reynolds Equation 3.68 was then solved at  $(\theta + \delta\theta)$  until the force balance Equation 3.77 was once again satisfied and a new estimate of the squeeze film velocity established. The trapezium rule, Equation 5.8 was then applied to calculate the minimum film thickness at  $(\theta + \delta\theta)$  based upon the film thickness at  $(\theta)$  and the squeeze film velocities at  $(\theta)$  and  $(\theta + \delta\theta)$ :

$$h_{(\theta + \delta\theta)} = h_\theta + 0.5 \left[ \left( \frac{\partial h}{\partial \theta} \right)_\theta + \left( \frac{\partial h}{\partial \theta} \right)_{\theta + \delta\theta} \right] \delta\theta \quad (5.8)$$

This cycle of calculations is repeated as necessary until the film thickness changes by a quantity smaller than some specified tolerance.

The calculation then advances to the next crank angle and in this way it is possible to march out the complete engine cycle to yield the cyclic variation in film thickness.

The hydrodynamic pressure distribution at 270° crank angle after TDC in the partially filled clearance space between the modeled piston ring face and cylinder liner (as in the attached model file) is shown in the Figure 5.1 below.

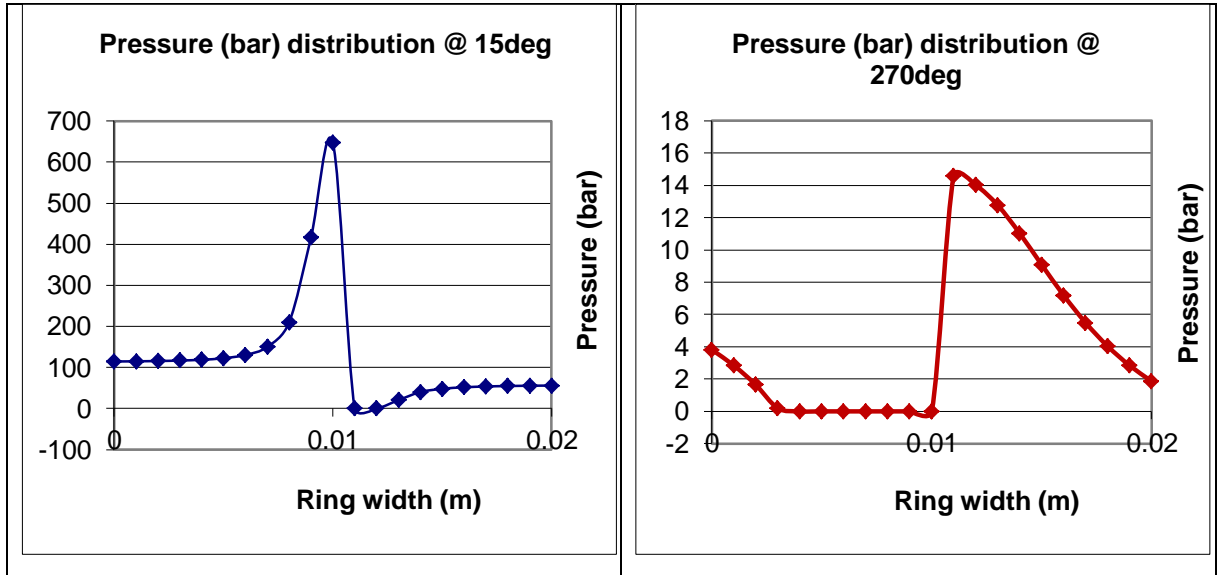


Figure 5.1 Hydrodynamic pressure distribution in ring/liner conjunction

#### 5.1.1.4 Oil film thickness profile:

The cyclic variations of the oil film thickness were mapped out, with the model file, for the entire engine cycle as shown in Figure 5.2 below. The co-relation of hydrodynamic pressure of Figure 5.1 and the oil film thickness of Figure 5.2 is obvious. Near to the TDC and BDC, the film thickness is the least owing to the inadequacy of the hydrodynamic condition.

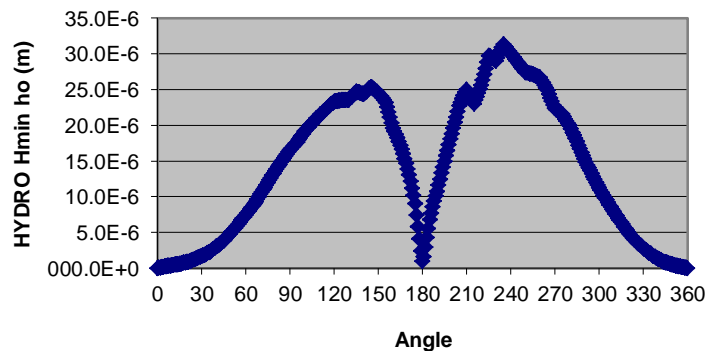


Figure 5.2 Film thickness against crank angle

### 5.1.1.5 Load, Friction Force and Co-efficient of friction:

#### 5.1.1.5.1 Load:

Load was calculated by integrating the pressure distribution curve.

$$\frac{W}{L} = \int_0^B P_z dx \quad (5.9)$$

The area under the pressure distribution curve can be calculated by the trapezoidal rule as follows:

$$\frac{W}{L} = \frac{x_1 - x_0}{2} \{P_0 + 2(P_1 + P_{x-1}) + P_x\} \quad (5.10)$$

Load against the crank angle is shown in Figure 5.3.

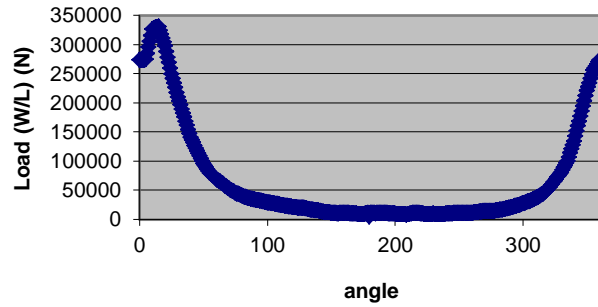


Figure 5.3 Load against crank angle

#### 5.1.1.5.2 Friction force:

$$u = \left( \frac{z^2 - zh}{2\eta} \right) \frac{\partial p}{\partial x} + (U_1 - U_2) \frac{z}{h} + U_2$$

$$\frac{du}{dz} = (2z - h) \frac{1}{2\eta} \frac{dp}{dx} + \frac{u}{h}$$

$$\tau_x = \eta \frac{u}{h} = \eta \frac{\partial u}{\partial z} = \frac{1}{2} (2z - h) \frac{dp}{dx} + \frac{u\eta}{h}$$

with  $z = h$ ,

$$\tau = \frac{h}{2} \frac{dp}{dx} + \frac{u\eta}{h}$$

$$\frac{F}{L} = \int_0^B \tau dx = \int_0^B \left( \frac{h}{2} \frac{dp}{dx} + \frac{u\eta}{h} \right) dx = \int_0^B \left( \frac{h}{2} \frac{dp}{dx} \right) dx + \int_0^B \frac{u\eta}{h} dx$$

The first half of the equation is solved by integration by parts and:

$$\begin{aligned} \frac{F}{L} &= \frac{h_0 + Kh_0 \left(1 - \frac{2x}{B}\right)^2}{2} P_{(x)} - \int_0^B P_{(x)} Kh_0 \left(-\frac{2}{B} + \frac{4x}{B^2}\right) dx \\ &\quad + \int_0^B \frac{u\eta}{h_0 + Kh_0 \left(1 - \frac{2x}{B}\right)^2} dx \\ &= \frac{h_0(K+1)}{2} P_2 - \frac{h_0(K+1)}{2} P_1 + \frac{Bu\eta \cdot \tan^{-1}(\sqrt{K})}{h_0\sqrt{K}} \end{aligned} \quad (5.11)$$

at  $x=0$ ;  $P_{(x)} = P_{(0)} = P_1$

at  $x=B$ ;  $P_{(x)} = P_{(B)} = P_2$

#### **5.1.1.5.3 Coefficient of friction:**

Coefficient of friction is then found as:

$$\mu = \frac{F/L}{W/L} \quad (5.12)$$

Coefficient of friction for hydrodynamic condition against crank angle is shown in Figure 5.4 below:

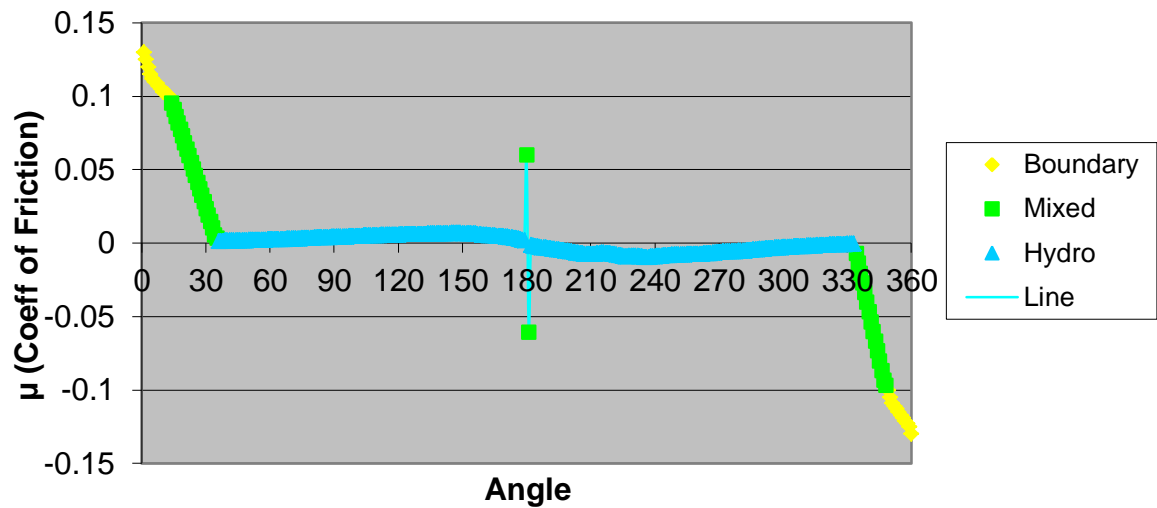


Figure 5.4 Coefficient of friction against crank angle (Viscous shear contribution)

It should be noted that the predicted film thickness generally falls below the composite surface roughness of the ring and liner near one or both of the dead centre positions. This implies that boundary lubrication conditions then apply.

#### 5.1.1.6 Lubricant Volume:

Minimum oil film thickness,  $h_m$  is related to the volume rate of flow of lubricant per unit circumferential width by the expression,  $Q_x = \frac{U h_m}{2}$ .

#### 5.1.1.7 Multiple compression ring:

The analysis of a multiple compression ring configuration is carried out with the assumption of continuity of flow as shown in the following Figure 5.5:

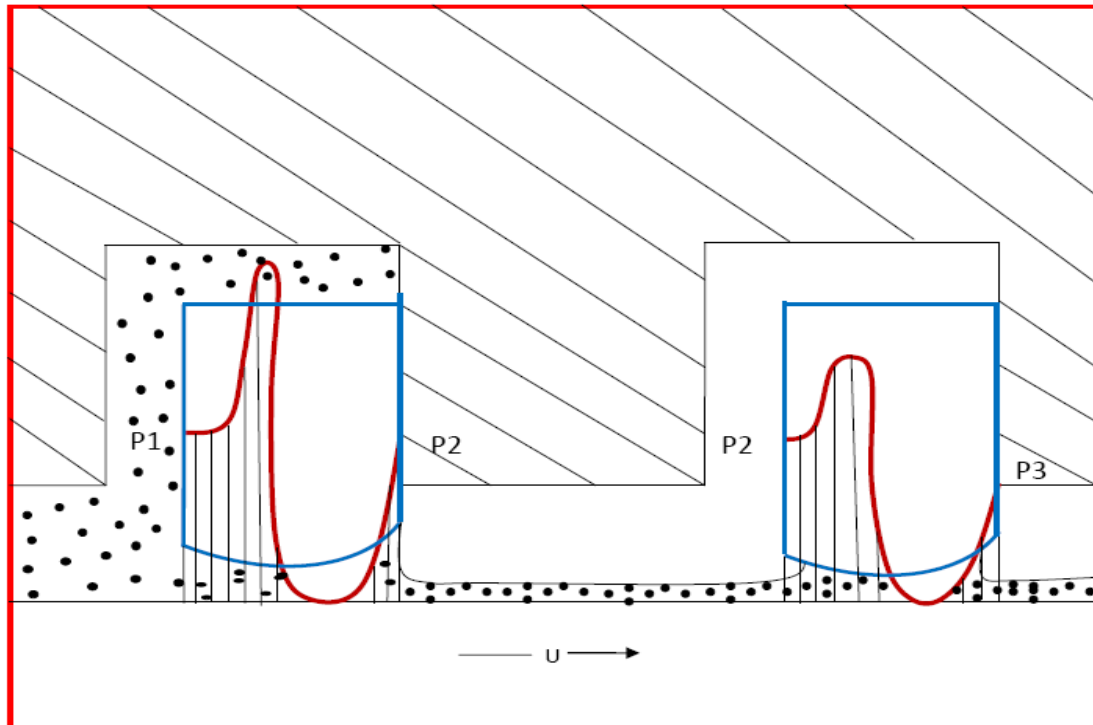


Figure 5.5 Multiple ring pack [21]

#### 5.1.1.8 Limitation of the model:

The model was made for the top ring only. The lubricant transported within the oil film beneath each ring is but one contribution to the total flow, since oil may pass through the ring gap.

It was assumed that the lubricant available to the  $n^{\text{th}}$  ring was equal to that passing beneath the leading ring  $(n+1)^{\text{th}}$  or  $(n-1)^{\text{th}}$  in any stroke.

If the ring lifts from its seat on the groove flank a relatively large volume of oil may also pass the ring from the inter-ring volumes. However, this phenomenon is usually observed near TDC with large ring inertia and light loads at high speed. Ring lift has been analysed by Ruddy et al, Ruddy B.L. [150, 151]. But for slow speed engines, the load remains unidirectional and should not have the lifting effect.

All rings were assumed to be parabolic after considerable amount of running hours.

The concept of lubricant starvation to the analysis of each ring was also applied.



The model assumed symmetry between the piston and cylinder bore and a steady ring geometry. In reality the forces and associated moments acting on the ring will cause the ring section to twist by an amount, which varies throughout the cycle and will influence the hydrodynamic performance of piston rings. [152]

The dynamic ring distortion was not considered in the model. The effective geometry of the ring face presented to the cylinder liner may also be affected by thermal and elastic distortions of the piston and liner and also by wear of the ring groove flanks and the liner. Such distortion may affect piston ring lubrication.

Cylinder bores are not strictly circular in section as assumed. There are errors of shape, ovality produced at manufacture to anticipate shape changes in the running engine, assembly deformations and changes in elastic/thermal distortions throughout each cycle. The elastic distortions created by bolting of the cylinder head generally have a pronounced effect upon cylinder bore profiles.

In distorted bores the film thickness varies circumferentially, but the circumferential pressure gradients are still small compared with axial gradients and hence 'no side leakage, form of Reynolds equation as used can be retained.

#### **5.1.2 Boundary Lubrication:**

The coefficient of friction in the boundary lubrication near to TDC and BDC could be found by solving the Equation 3.78 with various values of roughness of the rings and liner. The contribution of the total coefficient of friction from boundary lubrication could be 14~15 times more [139] than that of the hydrodynamic ones as shown in Figure 3.28 and 3.29. This value of coefficient of friction changes with the number and configuration of the asperities comes in contact owing to the change of oil film thickness separating the ring and liner surfaces.

#### **5.1.3 Mixed Lubrication:**

By using Equation 3.85, the percentage of hydrodynamic and boundary lubrication can be allocated against the slope of the mixed zone of the Figure 3.29.

## 5.2 Thermoelectric analysis- Results and Discussions:

The temperature reading of the cylinder liner no.4 was recorded at 70% engine load against the cylinder oil feed rate of 0.72g/bhp/h, Figure 5.6. The regular fluctuation of temperature of liner surface, as shown in Figure 5.6, is considered normal. Even when the engine load was changed, the temperature also changed smoothly. Occasional high temperature readings were noted. These occasional high peak or spike temperature readings indicated the passing of piston ring gap against the sensor. The goal was not to capture these spikes. Rather our interest was in capturing fluctuating wave pattern.

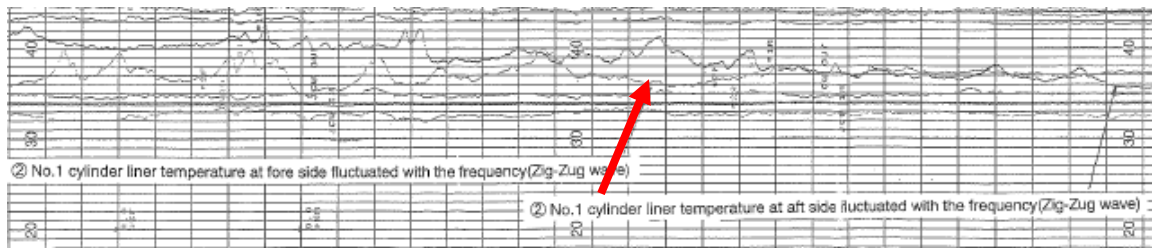


Figure 5.6 Fluctuating temperature of the cylinder liner

At the same 75% engine load, as the cylinder oil feed rate were being reduced from 0.72g/bhp/h to 0.42g/bhp/h, the temperature readings were thoroughly studied in order to discover the precursor of scuffing. Until the feed rate was reduced to 0.42g/bhp/h, normal cylinder liner temperature curves were found to be very smooth and plain.

The fluctuating temperature phenomenon was then recognized, at reduced feed rate of cylinder oil, by the inclination and the amplitude of the temperature data curve, figure 5.7. Such fluctuating temperature with the number of peaks in the limited period from a block of sample potentially indicates onset of scuffing.

Average temperature of these fluctuating waves at 0.42g/bhp/h cylinder oil feed rate was found to be usually higher than the temperature reading of normal condition against the same load.

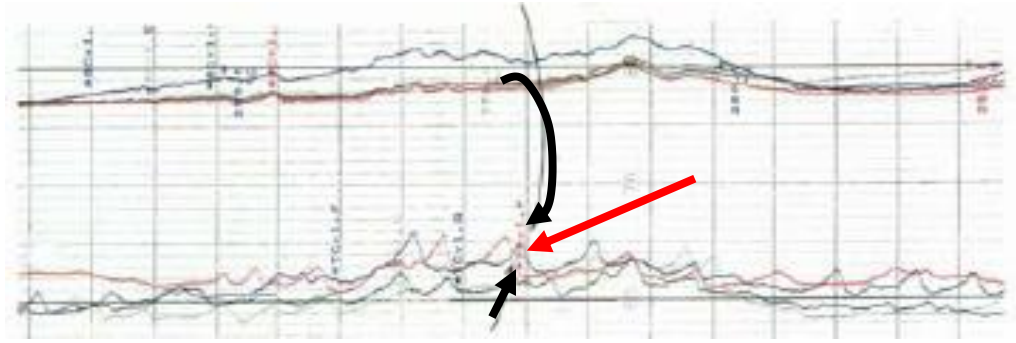


Figure 5.7 Sinusoidal wave (Liner Temperature fluctuates frequently)

The above field data of Figure 5.6, were then checked against the earlier developed mathematical function, Equation 3.109 and its profile, Figure 3.31 and depicted in Figure 5.8 below.

$$f(x) = \pi - \frac{8}{\pi} \left\{ \cos x + \frac{1}{9} \cos 3x + \frac{1}{25} \cos 5x + \dots \right\} \quad (3.109)$$

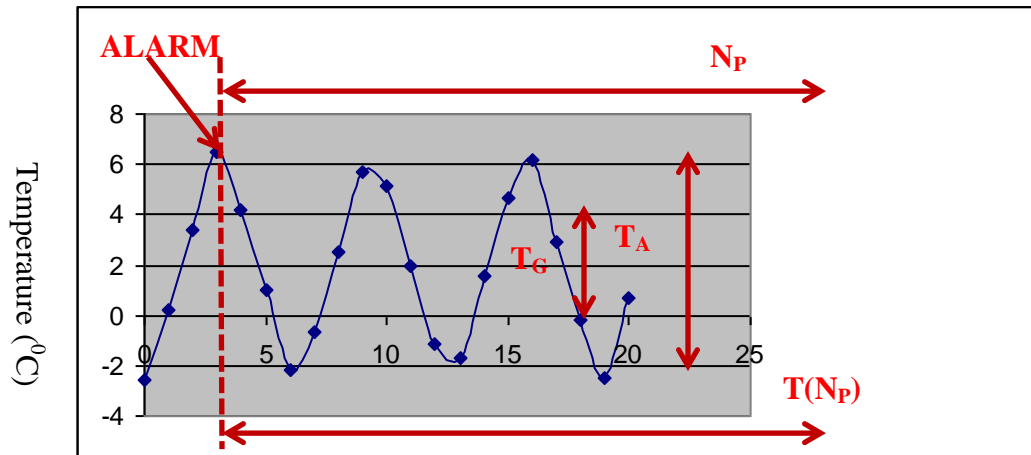


Figure 5.8 Fourier profile of temperature reading

There was close matching of the modeled wave pattern with the wave pattern discovered from the field data. The prediction of onset of scuffing is then possible by analyzing the set spectrum of fluctuating temperature reading block and setting a periodical limit with threshold amplitude of  $T_t$ , discussed earlier.

$$\frac{\Delta p}{\Delta t} = \frac{\epsilon E C_m \mu p}{\rho c_{sp} l_r} \quad (3.103)$$

As was mentioned under modeling, the rate of pressure rise of Equation 3.103 characterizes the potential scuffing index and is related to  $T_t$ , the instantaneous temperature of liner and rings and the series of fluctuating temperature pattern, breaking and restoring oil film, were always present prior to the onset of scuffing. This sporadic oil film breakage and restored film thickness was responsible for the temperature fluctuation.

Now, with such a pattern wave of temperature, a character or the boundary condition can be built around it to define the precursor of scuffing. The building block of such precursor,  $T_A$ ,  $T_G$ ,  $N_P$ ,  $T(N_P)$ , figure 3.31 above, can be set as follows, which would point towards the onset of scuffing:

$T_A > 8^\circ\text{C}$  more than normal average

$T_G > 4^\circ\text{C/minute}$

$N_P > 4$  times

$T(N_P) > 25$  minutes

Where,

$T_A$  = Amplitude of the peak temperature

$T_G$  = Gradient of temperature rise

$N_P$  = Number of peaks

$T(N_P)$  = Time period for the block of  $N_P$

Additionally, with some imposed boundary conditions, two secondary alarms can be set. Usual maximum temperature of a liner is around  $200^\circ\text{C}$ . Hence, an alarm can be activated if the liner temperature reaches  $220^\circ\text{C}$  or more and remain at that level for more than 5 minutes, as shown in the Figure 5.9. Momentary high temperature is usually due to ring end passing through the temperature sensor point.

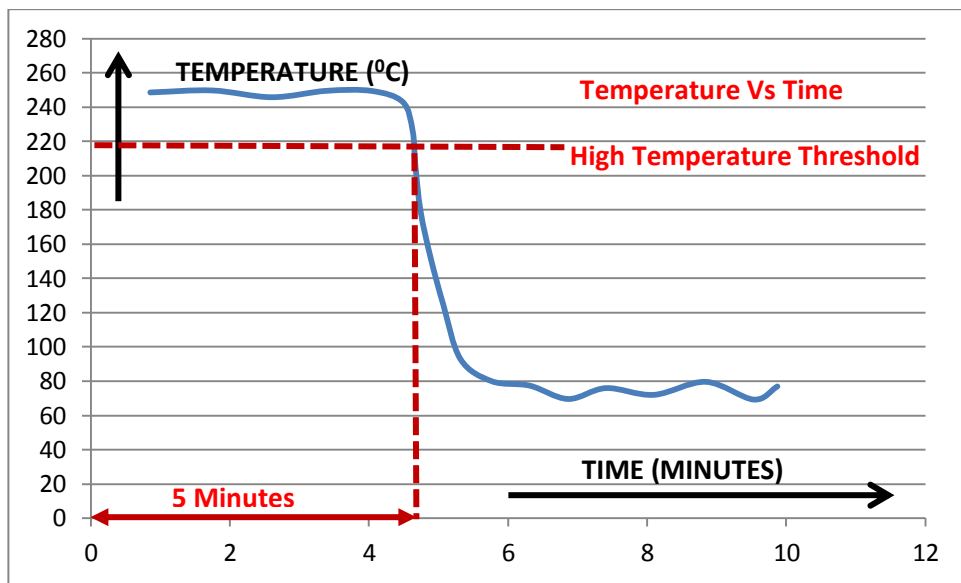


Figure 5.9 Cylinder liner high temperature alarm

The other alarm can be provided for the cylinder liner temperature deviation. The alarm can be activated when the liner temperature of a particular unit exceeds more than a threshold value against the average liner temperature of the engine. If the average liner temperature of the engine is 150°C for a particular load and if any of the unit of the engine experiences liner temperature more than 40°C that of the average and remain at that level or higher more than 10 minutes, the alarm can be activated, Figure 5.10.

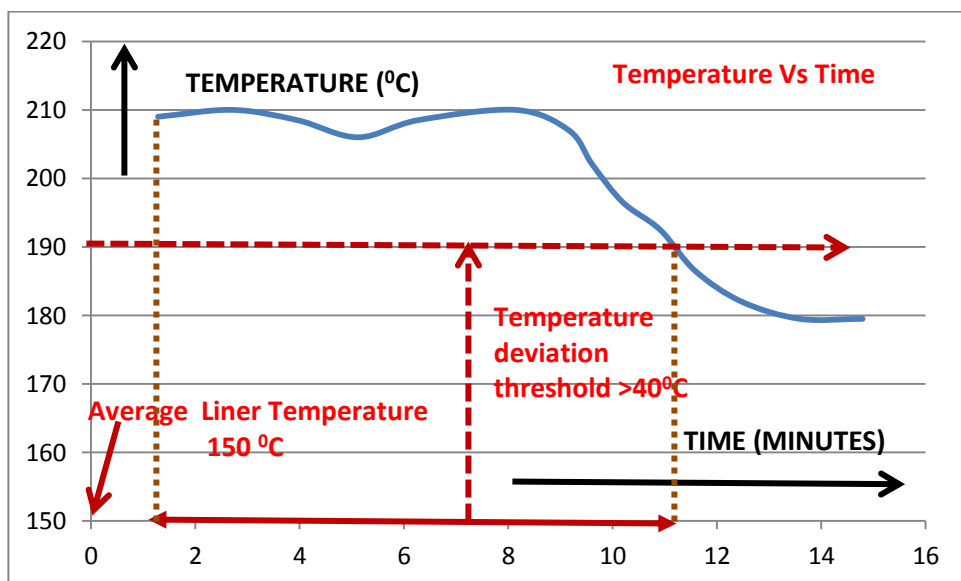


Figure 5.10 Cylinder liner temperature deviation alarm

So, overall, there could be three kinds of alerts: a) high temperature b) high temperature deviation and c) zigzag wave. The setting of these three will depend on an engine type.

### 5.3 Eddy Current Analysis –Results and Discussions:

#### 5.3.1 Baseline tests:

A series of baseline results were taken to establish a reference for comparison with later results after the liner showed some wear. These were taken with no contact between the piston ring and the liner.

10 baseline tests were taken in each direction (i.e. sensor moving from left to right and from right to left) for position 1. There was very little variation from one test run to the next. The two large slots and the ground area were identifiable. An example for position 1 is given in Figure 5.11. The features A, B and C correspond to the features A, B and C in Figure 4.4.

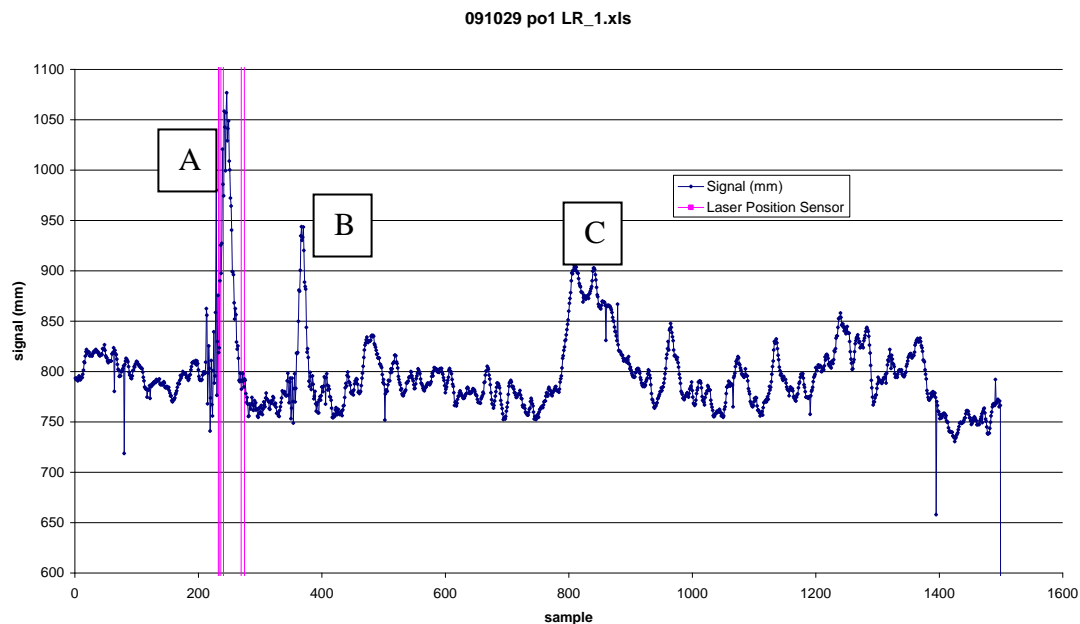


Figure 5.11 Baseline test of eddy sensor jig analysis

Baseline tests were taken at all 5 positions (both directions) including a repeat of the tests at position 1. The results were analysed, which showed little variation from test to test.

### 5.3.2 Wear tests:

The piston ring was loaded and the “liner Guardian” was run for 30 strokes (i.e. 15 left to right and 15 right to left) without any lubrication between the ring and the liner. Before the piston ring was loaded a no-load reading was taken from the load cell. The following Table 5.1 and 5.2 are the readings from the load cell.

Signal	Value	Units
Excitation voltage	5.0	V
Zero load reading	-4.240	mV
On load reading	-4.449	mV
Zeroed output (calculated)	-0.259	mV
Converted to mv/V (calculated)	-0.052	mV/V
Approximate Force (calculated)	3500	Newtons

Table 5.1 Load cell readings with no load

The piston ring was loaded and the load cell readings were as follows:

Signal	Value	Units
Excitation voltage	5.0	V
Zero load reading	-4.217	mV
On load reading	-4.486	mV
Zeroed output (calculated)	-0.269	mV
Converted to mv/V (calculated)	-0.0538	mV/V
Approximate Force (calculated)	3600	Newtons

Table 5.2 Load cell readings after ring was loaded

The load varied with stroke up to 4.9mV which equates to about 9000 Newton force. During this time the Liner Guardian was run for ~100 dry strokes. The surface was then sprayed with WD-40, a low viscosity oil.

The ring was loaded again with ~5800 Newtons and the liner was run for 150 strokes at higher speed (set speed denoted as 50% on the LG software). It is to be noted that at speeds greater than “50%” the ring came close to the edge of the liner at the right hand side limit of travel. Readings were taken at all positions.

The ring was loaded again with ~7000 Newtons and 300 strokes were made at “50%” speed.

After this another 100 strokes were made with a ring force of ~6500 Newtons.

Readings were taken for each position in both directions. 3 tests were made for each position in each direction. The result of the measurements after each increasing number of strokes at position 5 is shown in Figure 5.12.

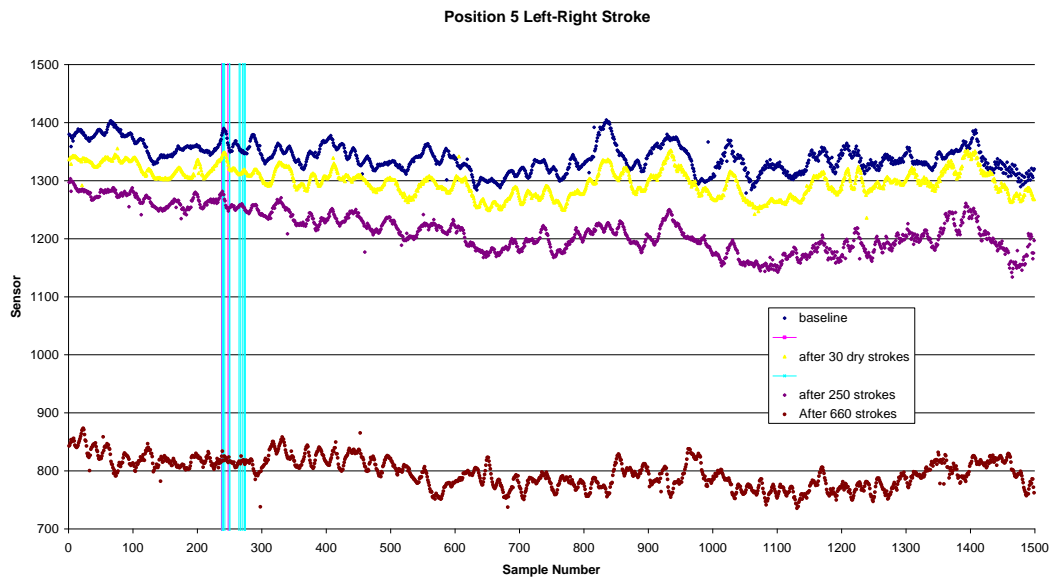


Figure 5.12 Roughness profile at stepped number of strokes

Whilst it could not be concluded that any linear substantial wear has been detected after 650 strokes, it could be observed that roughness pattern was maintained. However, the smoothing of the surface with the increased number of strokes confirmed the ability of the Liner Guardian to capture the discrimination of the surface.

When installed on the engine, the sensors operate in a non moving location (the engine cylinder liner) exactly the opposite of the condition tested on the test jig, i.e., moving sensor over the stationary liner.



### 5.3.3 Sensor output from engine cylinder 4:

The output of the 4 sensors of the cylinder no.2 (new cylinder liner and rings as reference) and cylinder liner no. 4 for testing the mathematical model were both taken at 75% MCR, 83 RPM. The no.4 cylinder liner had maximum wear of 3.02mm. The reference cylinder no.2 had the cylinder oil feed of 0.7g/bhp/h and that of the unit no.4 was reduced to 0.45g/bhp/h. The following outputs, Figure 5.13 (a) and (b), were received from opposite sensors of 1 and 3 of the unit no.4

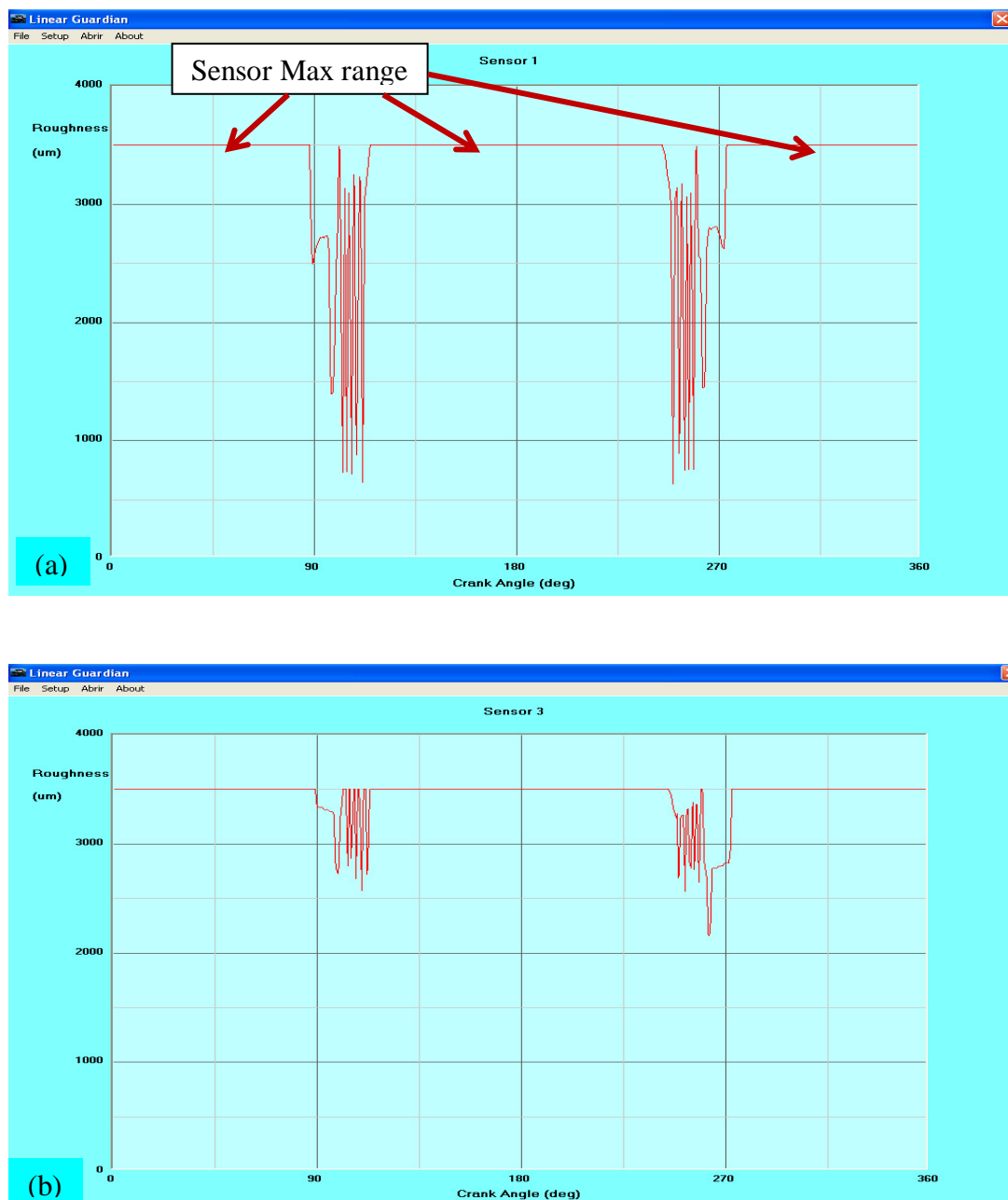
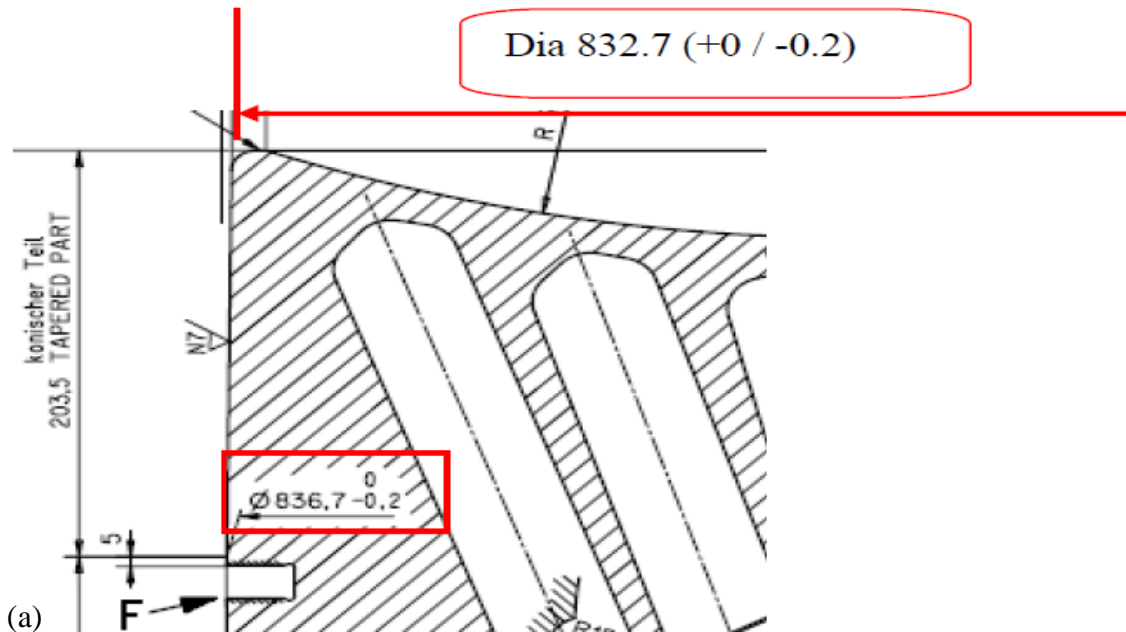
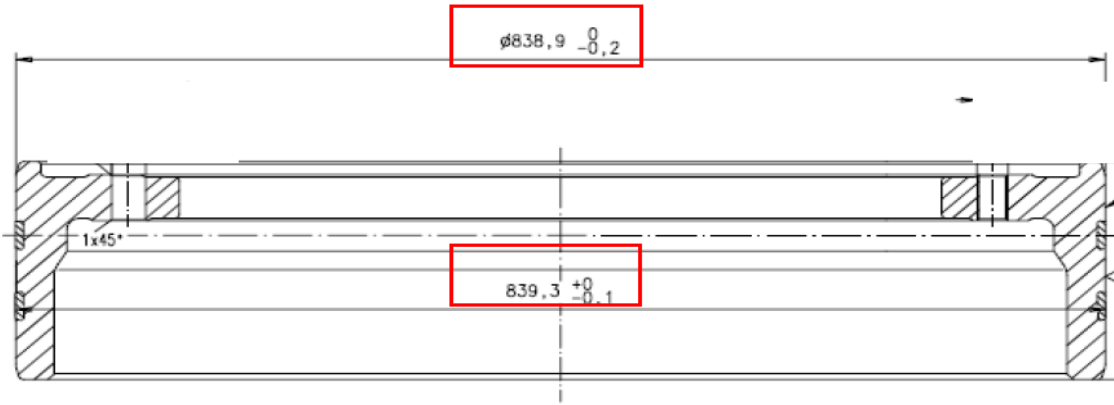


Figure 5.13 Outputs (a) of sensor1 (b) of sensor 3 from engine cylinder unit no.4

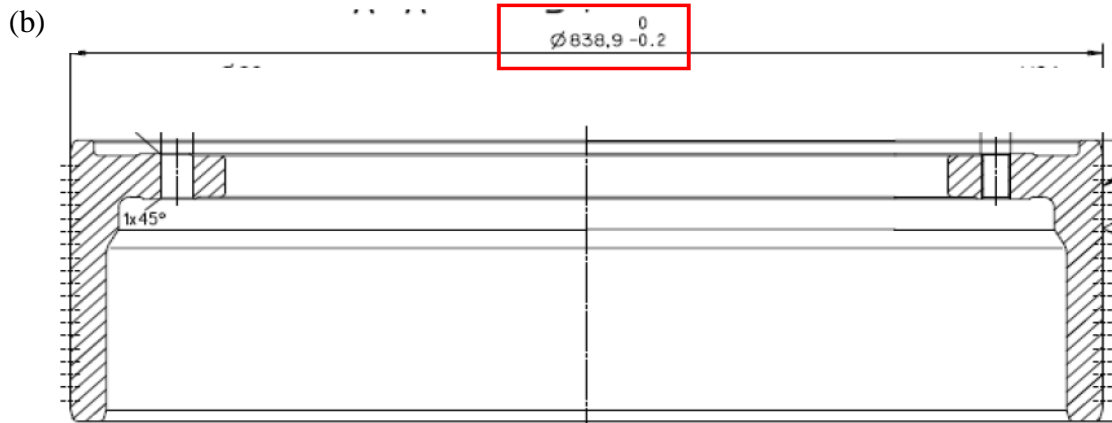
The maximum range of the eddy sensor is 3.5mm is reflected on the output graph as a flat line. The gap between the piston crown ring land and cylinder liner, Figure 5.14 (a), which is  $\{ 840 (+0.23/-0.0)+3.02-836.7(0.0, -0.2)\}$ mm = approx.6.32 (0.0, 0.43)mm. In addition to this 6.32mm gap, there is additional 2mm distance between the sensor head and the cylinder liner surface. As the eddy sensor is unable to register readings beyond 3.5mm, it fails to register the gap readings of the ring land, which is 8.32mm. Piston crown is further away from the ring land and hence the gap is more than 8.32mm. As the liner wear itself is 3.02mm and adding the 2mm depth of the sensor and the cylinder liner surface, it is minimum 5.02mm. Hence the readings of the skirt and the copper band 5.14 (b, c) also could not be registered, though their diametrical figure is higher than that of piston crown and ring land.

Standard new liner tolerance = dia 840mm (+0.23 / -0.0)





New execution piston skirt with 2 copper bands.



Previous skirt execution without copper bands

(c)  
Figure 5.14 Gap between crown and cylinder liner (a); skirt dimensions (b, c)

In this study, our interest is to study the ring surface, which is in contact with the liner and hence is within the range of eddy sensor's capability even with the 2mm gap between the cylinder liner and the piston ring. Eddy current sensors measured the distance between the sensor and the ring surface, Equation (5.13),

$$D' = d' + h(\theta) + R_a(\theta) \quad (5.13)$$

where,

$D'$  = the total distance between the sensor and the ring surface;

$d'$  = distance of the sensor head from liner surface; (2000 micron)

$h(\theta)$  = hydrodynamic oil film thickness at angle  $\theta$  (15-20 micron, reference fig 5.2)

$R_a(\theta)$  = ring roughness at angle  $\theta$

To be more precise, the Equation 5.13 should have catered for the original machine cut roughness of the rings. It is assumed to have no significant impact in the roughness reading, as the acceptable morphology of the ring is only the valleys, Figure 5.15 and additionally, the rings were already run in for a considerable time prior to taking the readings.

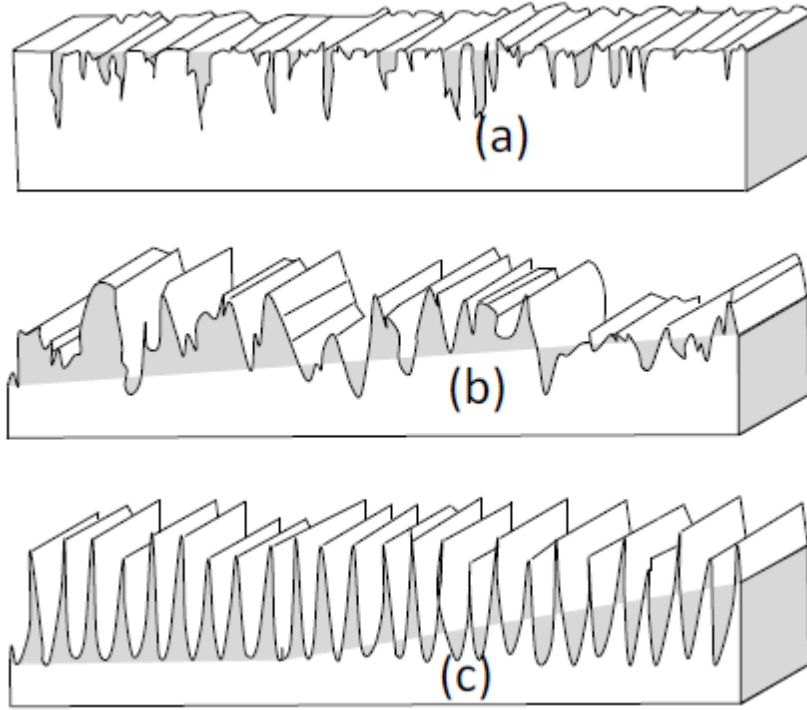


Figure 5.15 Different surface morphologies of rings and liner with same  $R_a$  values

(a) acceptable morphology with valleys but no peaks

(b) and (c) not acceptable morphologies

All distance values were measured against the crank angle and referenced to the TDC from  $0^\circ$  to  $180^\circ$ . Actual piston rings surface distance against the sensors was then segregated against the crank angle as follows:

$$R_d = \frac{1}{L_s} \int_{\theta=90^\circ, 240^\circ}^{\theta=120^\circ, 270^\circ} r_d(\theta) d\theta \quad (5.13)$$

where,

$R_d$  = average distance over a stripe

$r_d$  = average distance monitored per stroke over a stripe and piston stroke

$\theta$  = Crank angle

$L_s$  = Piston stroke as a function of crank angle

The average distance was calculated from the opposite side sensor outputs of cylinder number 2 and the reference standard deviation ( $SD_R$ ) was formed. This  $SD_R$  was then compared with the subsequently measured actual standard deviation ( $SD_A$ ) of the cylinder no.4. The deviation of these two standard deviation ( $SD$ ), Figure 5.12 reflects the wear of the cylinder liner and the piston rings. As the liner wears out, in a way, the distance between the sensor head and the ring is shortened after a long time. This needs to be corrected time to time. But as the rings become rough in scuffing within a short time, the eddy sensors actually registers the surface roughness instantly by sensing the distance of the peaks and the valleys, created by the scuffing process. In that sense, the rate of the increment of  $SD_A$  is vital and a sudden high rate serves as an indicator of scuffing. Through real experiments, by scuffing a liner, it will be possible to determine the rate at which the scuffing commence and this can be considered as the index of scuffing detection,  $SD_S$ . In our case, the test was not extended to scuff the liner and hence,  $SD_S$  is not reflected in the Figure 5.16.

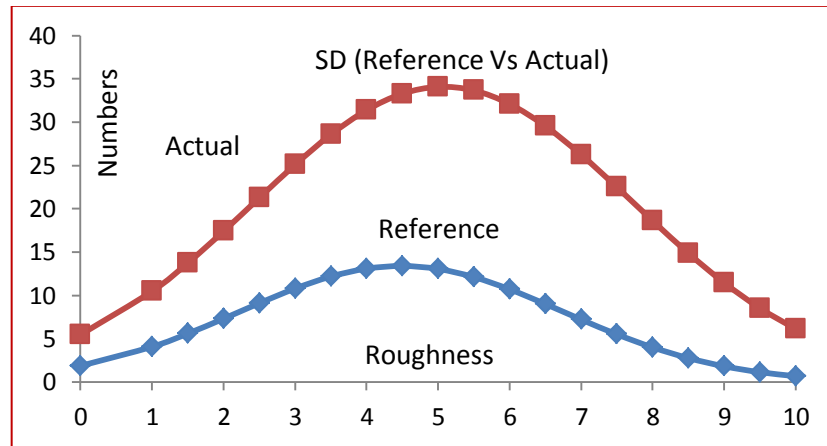


Figure 5.16 Variation of standard deviation of roughness

Additionally, any increase of roughness from  $SD_R$  towards  $SD_S$  will affect the asperity contact of boundary and mixed lubrication. If the average roughness of the

liner is assumed to be mirror image that of the rings, these values can form the composite roughness. With the composite roughness and oil film thickness in hand, the coefficient of friction of boundary and mixed lubrication can be readily solved by Equations 3.84 and 3.85.

#### **5.3.4 Notes on data analysis:**

It is to note that magnetic field will be maximum above the defect.

$$H_{mean} = \frac{H_{max}}{2\pi(\mu_m - 1)H_{initial}} \quad (5.14)$$

$$= \frac{z_d}{x_d^2 + z_d^2} - \frac{z_d + h_d}{x_d^2 + (z_d + h_d)^2} \quad (5.15)$$

where,

‘H<sub>mean</sub>.’ - mean value of magnetic field above the flaw

‘H<sub>max</sub>.’ - magnetic field maximum above the flaw

‘H<sub>init</sub>.’ - magnetic field coming from the source

‘μ<sub>m</sub>’ - magnetic properties parameter

‘z<sub>d</sub>’ - gap between probe and surface of an object

‘x<sub>d</sub>’ - distance between probe position and defect position on the surface

‘h<sub>d</sub>’ - depth of the defect.

The distance between two defects is denoted by Δx<sub>d</sub>. In a case where many defects are identified in a target material, the defect depth evaluation gets high error Δ of influence of neighbouring defects on the inspected surface. It can then be calculated as follows,

$$\Delta = \frac{A_f - A_d}{A_f} \quad (5.16)$$

where,

$\Delta$  – Error

$A_f$  – Flaw detector data for group of defects

$A_d$  - Flaw detector data for a defect

Flaw detector data depended on magnetic fields are changing their numbers of  $\Delta x$ . It could be either negative or positive. If it is -ve, the real number of defect depth could appear much higher and defect danger estimation will rise up in that case. If error  $\Delta$  is +ve, it is possible to get smaller number of defect depth evaluation.

#### **5.4 Acoustic emission analysis- results and discussions:**

The collected data was analyzed in both time as well as frequency domains.

##### ***5.4.1 Time domain analysis:***

##### ***5.4.1.1 Comparison between reference condition and worn out rings:***

The data collected for different simulated fault conditions were compared with the reference data. Figure 5.17 shows comparison between reference condition and worn out piston rings for one engine cycle. The amplitude of AE signal for worn out piston rings can be observed to be higher as compared to the reference condition. This is due to the change in geometry of the piston ring as it wears out. The piston rings have a tapered end that comes in contact with the cylinder wall as shown in Figure 5.18a. The tapered portion of the rings starts to wear out as they are put in to service under certain harsh conditions and the area of contact between the piston rings and cylinder wall starts to increase as shown in Figure 5.18b. The magnified views of Figures 5.18a and 5.18b are shown in the Figure 5.18c. This increased area of contact results in increased AE activity and leads to the higher amplitudes of signals. Also, a sharp rise in signal amplitude at approximately 600° before TDC in every upward stroke of the piston can be seen for worn out piston rings. This is due to the piston slapping against the cylinder walls as a result of increased clearances between piston and cylinder wall.

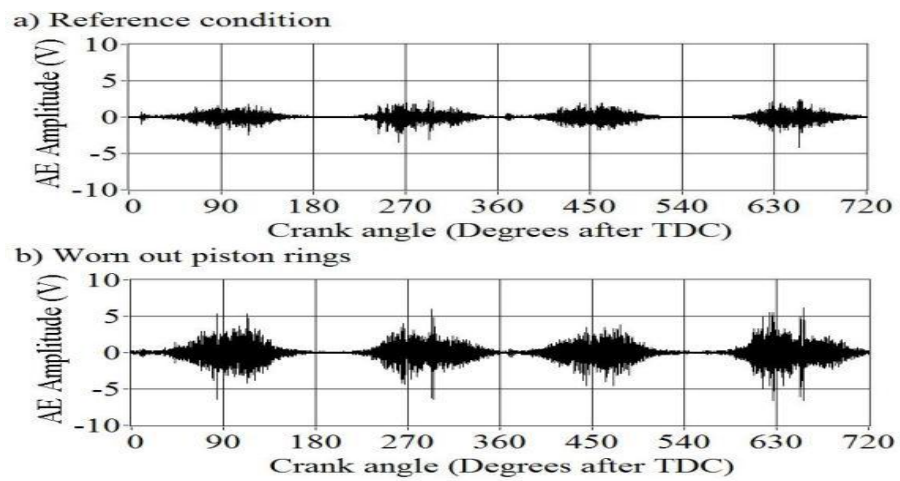


Figure 5.17 Comparison of reference condition (a) and worn out piston rings (b)

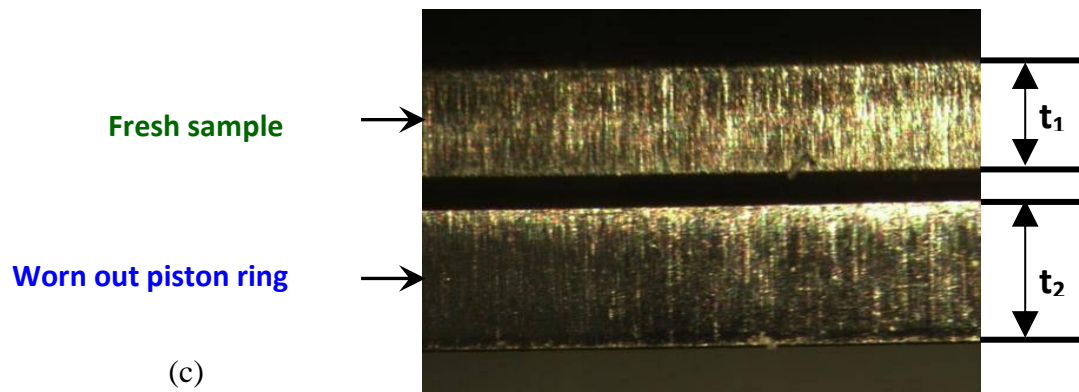
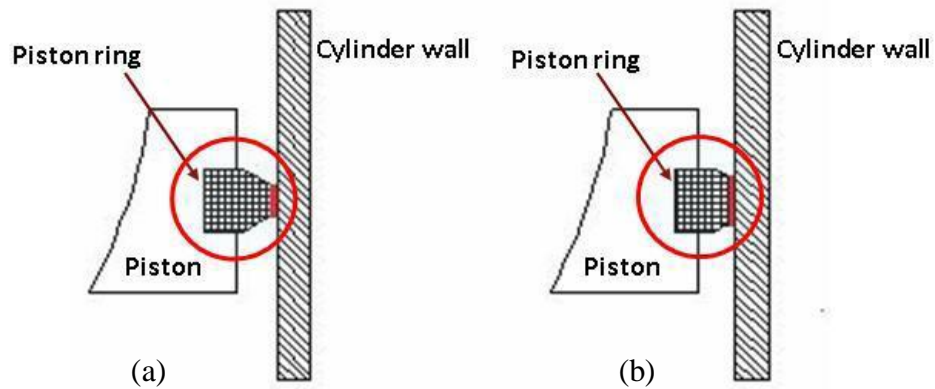


Figure 5.18 (a) Fresh piston ring contact area (b) Worn out piston ring contact area (c) 40X Magnified view of piston ring contact area between fresh and worn-out piston rings.  $t_2 > t_1$ : An increase of approximately 34% in contact patch.



#### 5.4.1.2 Comparison between reference condition and worn out piston:

Figure 5.19 shows comparison between the reference condition and worn out piston. The amplitude of the signal during all four strokes of the piston was observed to reduce as compared to the reference condition. The clearances between piston and cylinder wall starts to increase as both piston and rings starts to wear out. Once this wear exceeds certain level, the uniform contact between piston and cylinder wall is lost resulting in lower AE.

Also, as seen in the case of worn out piston rings, a sharp rise in signal amplitude at approximately  $600^\circ$  before TDC in every upward stroke of the piston can be observed for worn out piston condition. This is due to piston slap as explained above. An increase in AE amplitude near TDC before the start of every expansion stroke was observed in case of worn out piston. This is due to the contact between piston and the cylinder wall near TDC. The increased clearances results in tilted motion of the piston and hence the chances of sudden contact between piston and cylinder wall increases resulting the increased AE amplitudes in the region.

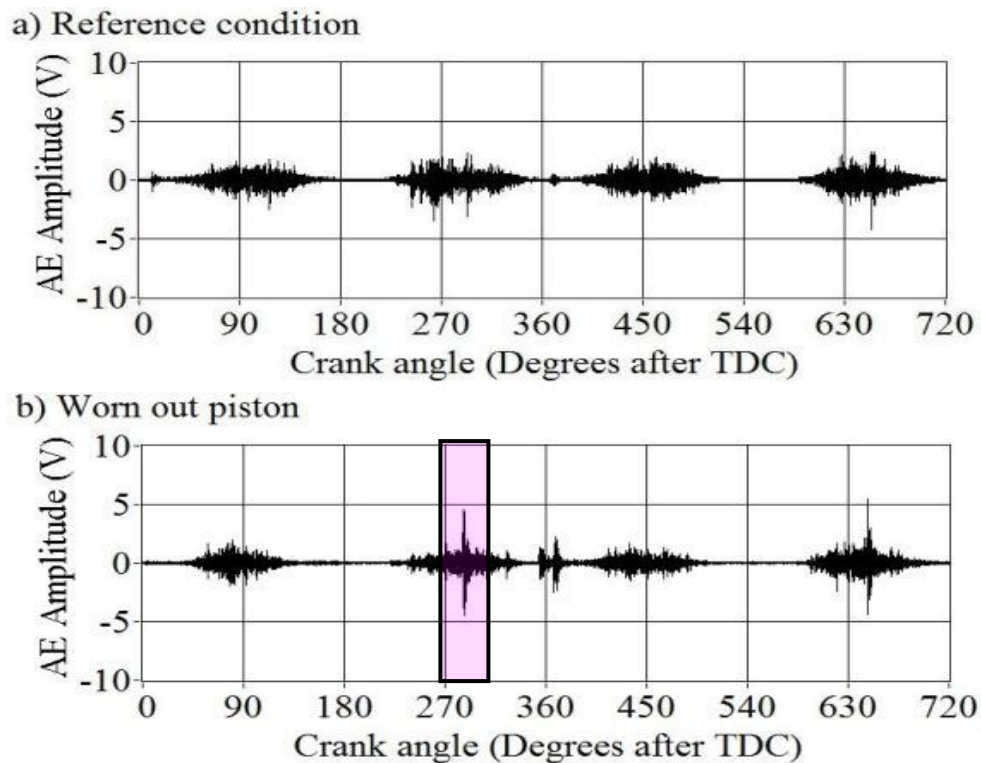


Figure 5.19 Comparison of reference condition(a) and worn out piston (b)

#### 5.4.1.3 Comparison between reference condition and oil starved condition:

Figure 5.20 shows the effect of oil starved conditions at the ring-wall interface on the signature of the collected data. The data shown on top of the Figure 5.20 is for the reference condition consisting of all new parts with specified amount of lubricating oil in the engine. The signal shown at the bottom is for an intentionally induced fault condition of oil starvation in the region of ring-wall interface. It is evident from the data that the AE amplitude corresponding to all the four strokes of the piston in a cycle increases for the case of oil starved conditions. A closer look at the data shows one more interesting feature being developed in the data. The signal in a small window after TDC shows an increase in amplitude for oil starved condition of the engine. The friction between piston rings and cylinder wall is highest near the dead centers when stroke reversal of piston occurs. In case of absence of proper lubricating oil film between the piston ring and cylinder wall, there is metal to metal contact between the pair and hence the intensity of signal increases.

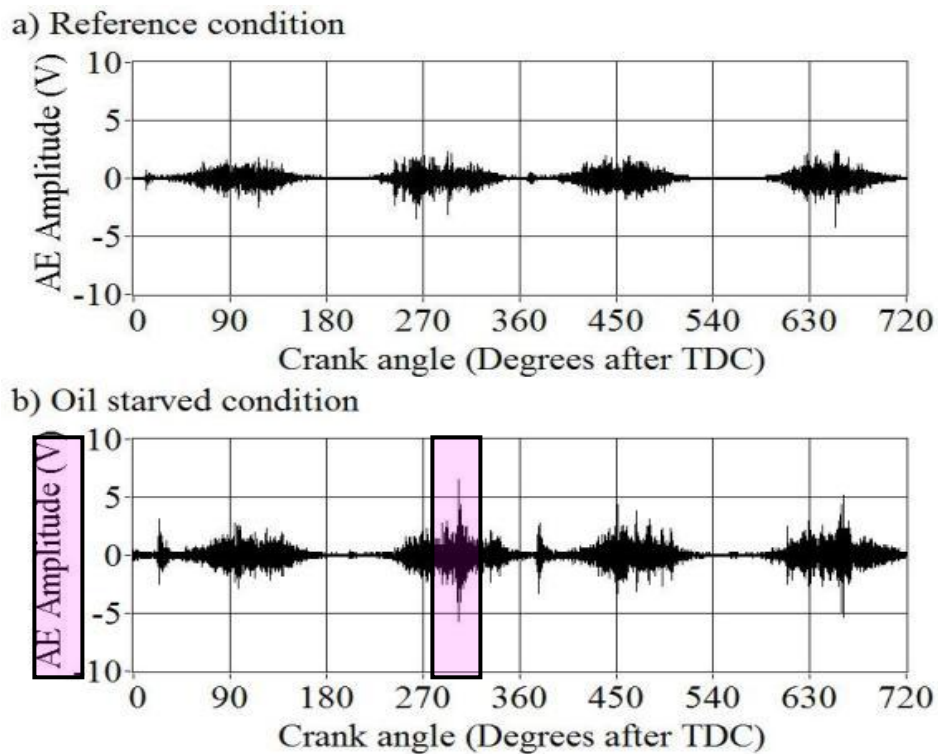


Figure 5.20 Comparison of reference condition (a) and oil starved condition (b)

#### 5.4.2 Frequency domain analysis:

In traditional spectral analysis the discrete Fourier transform is used to represent the frequency domain of the collected data. The discrete Fourier transform of the signal reflects the spectral content of the entire signal over time but does not indicate at what time or crank angle the spectral content occurs. It is evident from the time domain analysis of the collected AE data that the time or crank angle at which certain events occur for different induced fault\_conditions is important. Hence using discrete Fourier transform is not sufficient to identify features related to different induced fault conditions. To overcome this difficulty a linear time-frequency analysis tool called Short Time Fourier Transform (STFT) was used.

The Short-time Fourier transform (STFT) is also known as the windowed Fourier transform. STFT multiplies the signal with a window function and then divides the time-domain input signal into few separated or overlapped blocks. After that discrete Fourier transform is applied to each block. Window functions are also known as sliding windows. In window function, the amplitude tapers progressively and smoothen the edges toward zero. Since each block has different time periods, the developed STFT shows the signals at each corresponding time period. The following Equation 5.17 was used for computing the STFT:

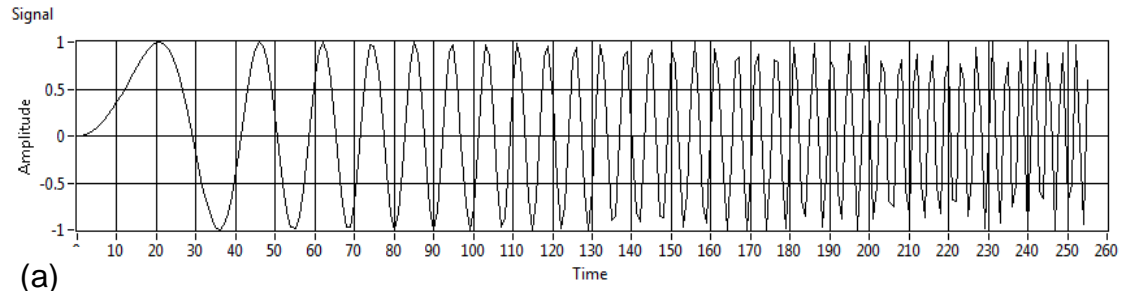
$$STFT[m, n] = \sum_{j=mdM-\frac{L_w}{2}}^{mdM+\frac{L_w}{2}-1} x_j \gamma^* [j - mdM] e^{\frac{-j2\pi in}{F_B}} \quad (5.17)$$

where,

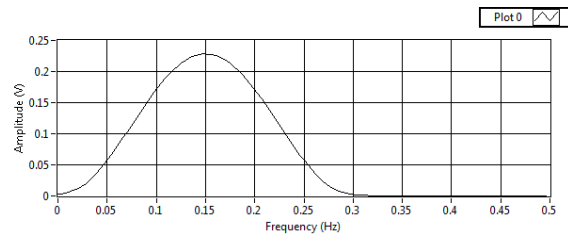
m, n	time, frequency
dM	time step (length of filter)
L <sub>w</sub>	window length
x <sub>j</sub>	signal
γ*	window function
[j – mdM]	delay
2πn = ω	
i	order of filters, 1 <sup>st</sup> , 2 <sup>nd</sup> , 3 <sup>rd</sup> etc
F <sub>B</sub>	frequency bins (Total order of filter)

Sample of signal, FFT and STFT is shown in Figure 5.21.

### SIGNAL:



### FFT:



### STFT:

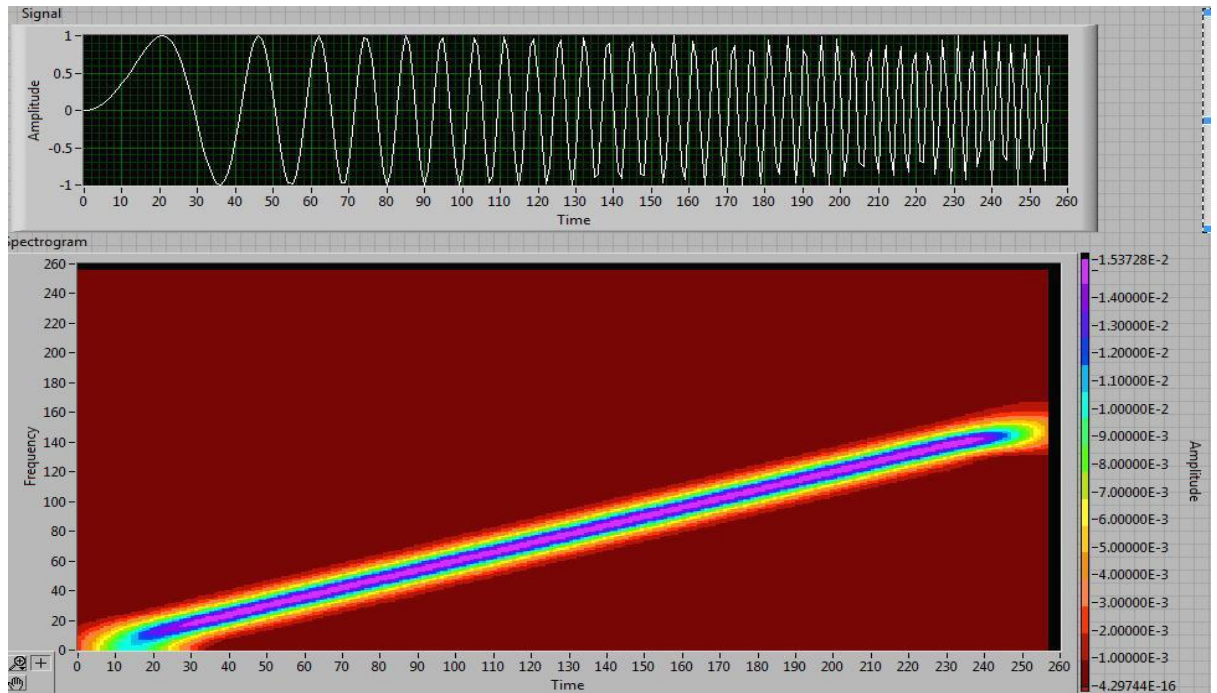


Figure 5.21 Samples of Signal (a), FFT (b) and STFT (c)

Figures 5.22 and 5.23 show the STFT for one engine cycle for reference condition and worn out piston ring samples respectively.

It can be clearly seen that the major amount of data lies in the frequency band of 50 kHz to 175 kHz. However higher amplitude high frequency components up to 275 kHz can be seen in STFT of the worn out samples.

The STFT for other fault conditions were also computed. The STFT for worn out piston is shown in Figure 5.24. It can be clearly seen that signal amplitude is less as compared to reference condition. Also signal amplitude increases near TDC that has a frequency band ranging from 50 kHz to up to 150 kHz.

Figure 5.25 shows STFT for the fault condition of oil starved conditions. The STFT of the data shows a wider frequency bandwidth (ranging from 10 kHz to 150 kHz) signal in a small window of approximately  $300^\circ$  after TDC. This is due to the metal to metal contact between piston ring and cylinder wall in absence of lubricating oil film between them as explained earlier.

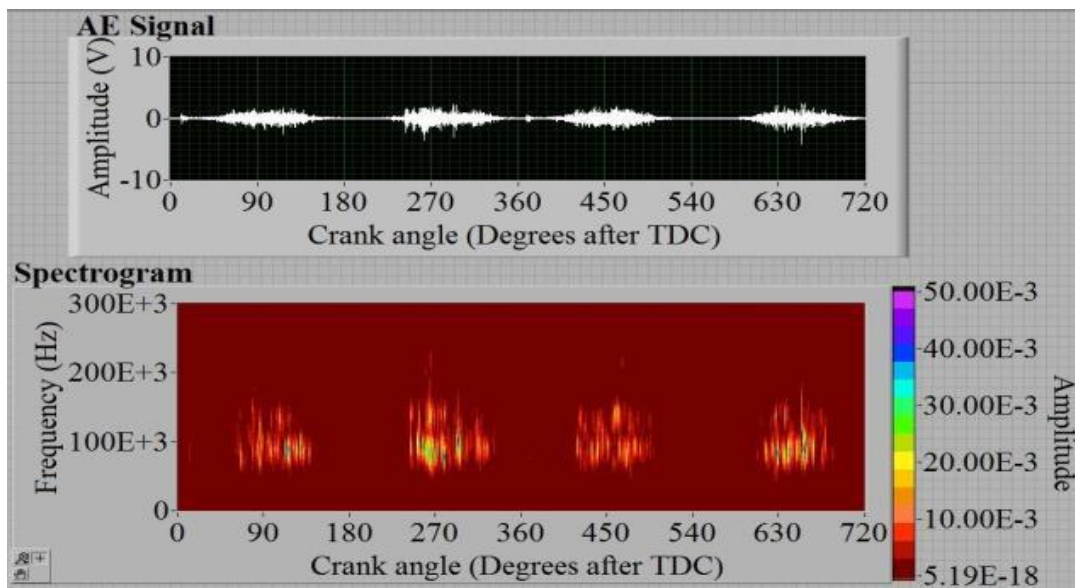


Figure 5.22 STFT of the data reference condition



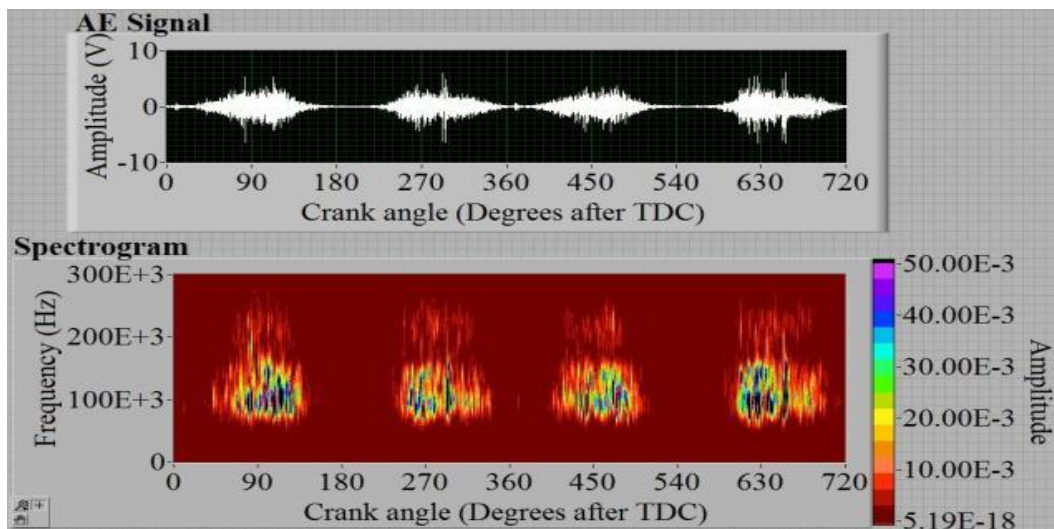


Figure 5.23 STFT of the data for worn out rings

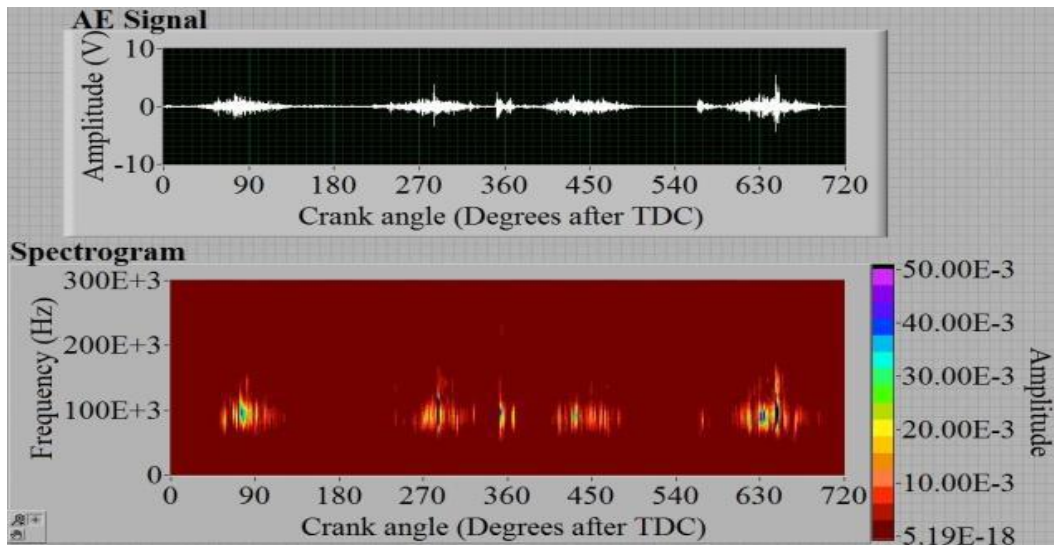


Figure 5.24 STFT of the data for worn out piston

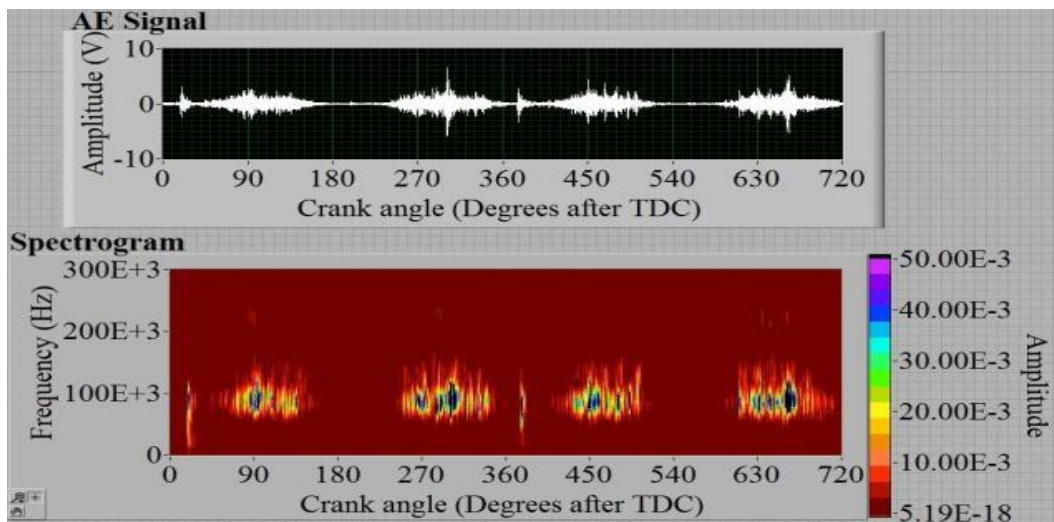


Figure 5.25 STFT of the data for oil starved condition

#### 5.4.2.1 Segmentation of data:

The AE data acquired for different induced fault conditions consisted of several number of engine cycles depending on the engine speed. It was also observed that the signature of the data for each simulated fault conditions showed unique features such as increase in amplitude in certain portions of the engine cycle. In order to gain a better understanding of the AE events in general and their correlation with the simulated fault conditions, the data for one engine cycle was split into different segments based on the direction of piston motion as well as the events occurring near TDC. Figure 5.26 shows one such engine cycle being divided in to six different segments. Table 5.3 gives the details of the segments extracted from each cycle of engine.

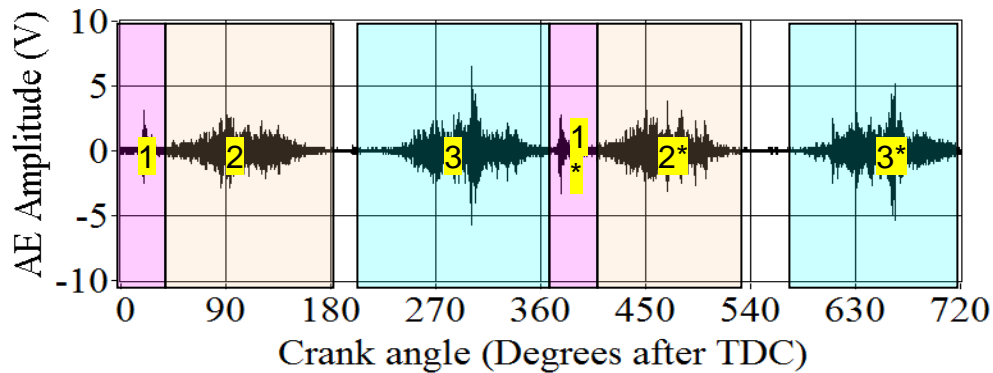


Figure 5.26 One engine cycle showing different segments

Segment Number	Description	Direction of piston movement
1	Near TDC	Downward
2	Induction stroke	Downward
3	Compression Stroke	Upward
1*	Near TDC after firing	Downward
2*	Expansion Stroke	Downward
3*	Exhaust Stroke	Upward

Table 5.3 Details of the segments extracted

#### 5.4.2.2 Feature extraction:

The segments extracted from each cycle were processed to compute a number of features in order to gain a better understanding of the effect of different simulated fault conditions on signature of collected AE data. The features were computed for all the segments of the full data length for three different domains of the signal namely, Raw signal RF, Envelope of the signal and Frequency spectrum FFT of the signal as shown in Figure 5.27 (a), (b) and (c) respectively. A total of 26 features were extracted and are as tabulated in Table 5.4.

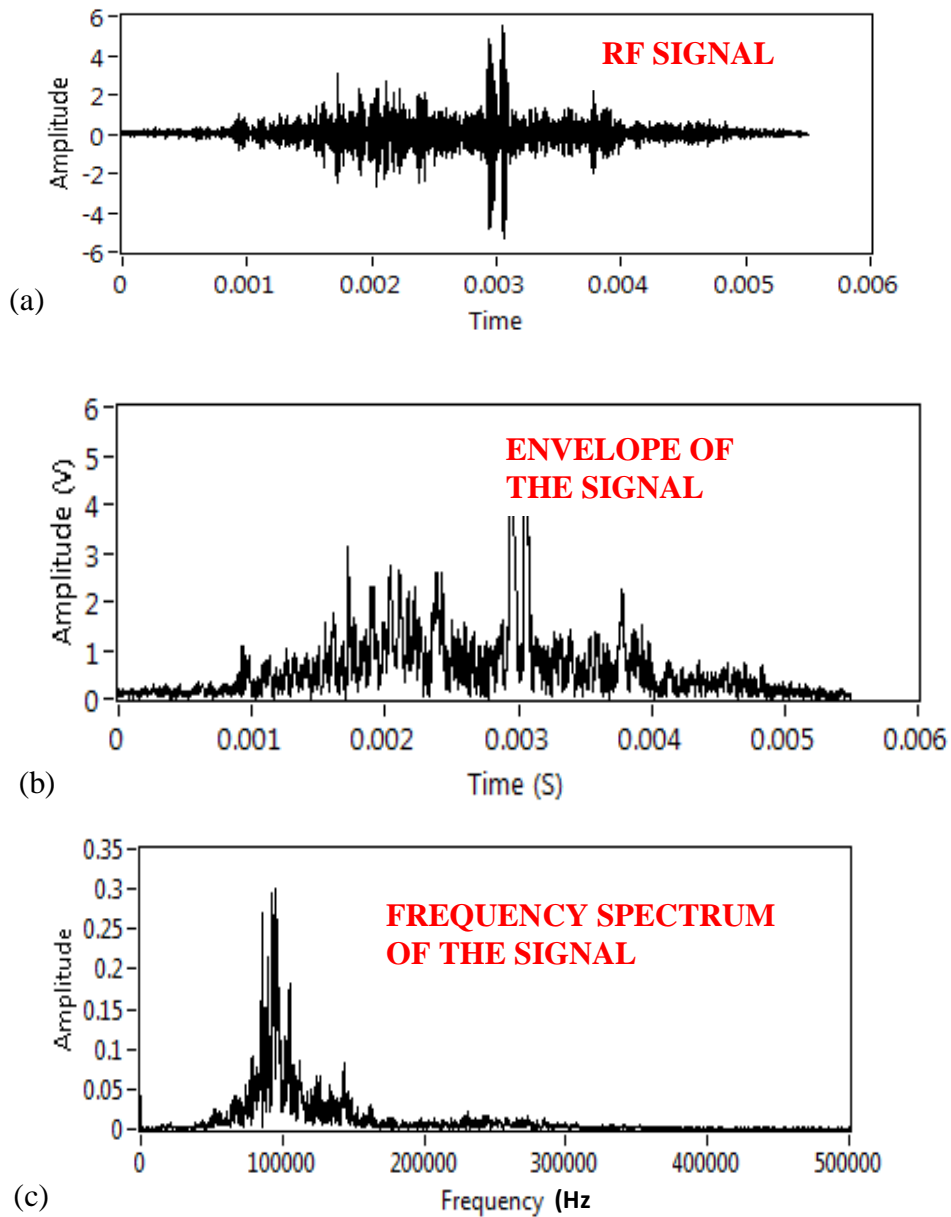


Figure 5.27 Three domains of signal



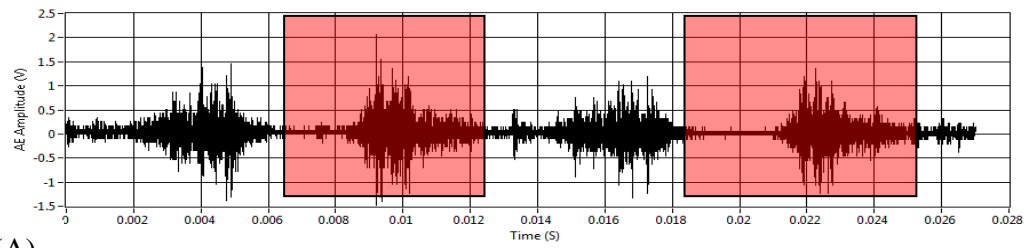
<b>RF FORMAT</b>	<b>ENVELOPE FORMAT</b>	<b>SPECTRAL FORMAT</b>
Positive Peak	Positive Peak	Fundamental Frequency
Negative Peak	Peak to Peak	Amplitude
Peak to Peak	Mean	Total Harmonic Distortion (THD)
Mean	Standard Deviation	Total Harmonic Distortion + Noise (THD + N)
Standard Deviation	Skewness	
Skewness	Kurtosis	
Kurtosis	Median	
Median	Mode	
Mode	Positive Peak/Mode	
	Rise Time	
	Fall Time	
	AC estimate	
	DC estimate	

Table 5.4 Features extracted for different domains of the signal

The features computed for each segment for different fault conditions were compared and the trends were studied. The envelope domain was observed to indicate the differences between different fault conditions more strongly as compared to RF domain. The spectral domain features were found to have no strong correlation between the features of different fault conditions. The comparison plots shown in Figures 5.28, 5.29 and 5.30 contain amplitudes of different features with respect to stroke number. The two consecutive stroke numbers in each plot on the abscissa refer to the two consecutive segments (for example 1, 1\*, 2, 2\* and 3, 3\*) in a cycle. Thus the number of strokes in each plot depends on the engine speed. The comparison plots shown are for some of the envelope domain features extracted from the data collected using one of the sensors at an engine speed of 4150 rpm. Similar trends were observed for a number of RF as well as envelope domain features for the data collected using both the sensors for all the four different speeds of the engine.

Figure 5.28 shows comparison between features for reference condition and worn out piston rings for segments 3 and 3\* (Upward movement of the piston comprising of compression and exhaust strokes). The amplitude of features like standard deviation was observed to vary from high to low alternatively for all the strokes of the piston. This trend was observed for both upward as well as downward movements of the piston. The consecutive points on the comparison plots as discussed earlier correspond to compression and exhaust strokes. Hence it can be concluded standard deviation of the signal is high for all the compression strokes as compared to exhaust strokes. This trend can be explained as follows. The piston ring conforms to the cylinder wall and moves in the ring groove, sealing off the combustion chamber from the crankcase. The sealing ability of the ring depends on many factors like ring and wall conformability, pre-tension of the ring and gas force distribution on the ring back face. The gas force acts on the back face of the rings and helps in its better contact with cylinder wall as shown in Figure 5.31. The arrows in Figure 5.31 indicate the gas force acting on the piston ring. The gas forces acting on the back face of the piston rings is higher during expansion and compression strokes as compared to induction and exhaust strokes respectively. This results in higher amplitude signals for expansion and compression strokes as compared to induction and exhaust strokes of the piston respectively. Hence, the signal is observed to alternate between low and high for both upward and downward movement of the piston.

Table 5.5 gives the details of different fault conditions and the corresponding features that indicate their presence. An increase in the amplitude of these features indicates the presence of the respective fault condition. It can be clearly seen from the table that higher order statistical features like Skewness and Kurtosis indicate the presence of fault conditions like worn out piston and oil starved condition. It can also be observed that a number of features are common to different fault conditions and hence it is difficult to classify and assign an increase or decrease in the features accurately to a particular type of fault condition. In order to overcome this difficulty the frequency domain information was used.



(A)

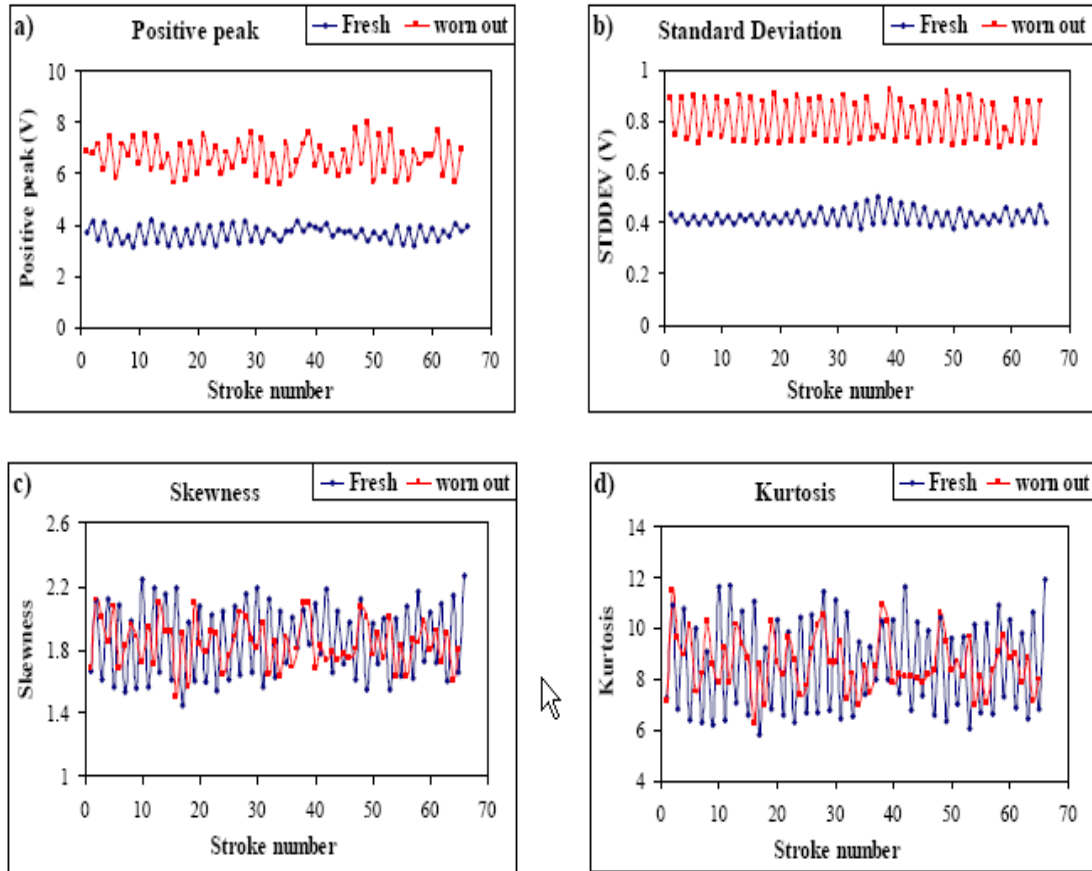


Figure 5.28 (A) segment 3 and 3\*. Comparison of features between reference condition and worn out piston rings a) Positive peak, b) Standard deviation, c) Skewness, d) Kurtosis.

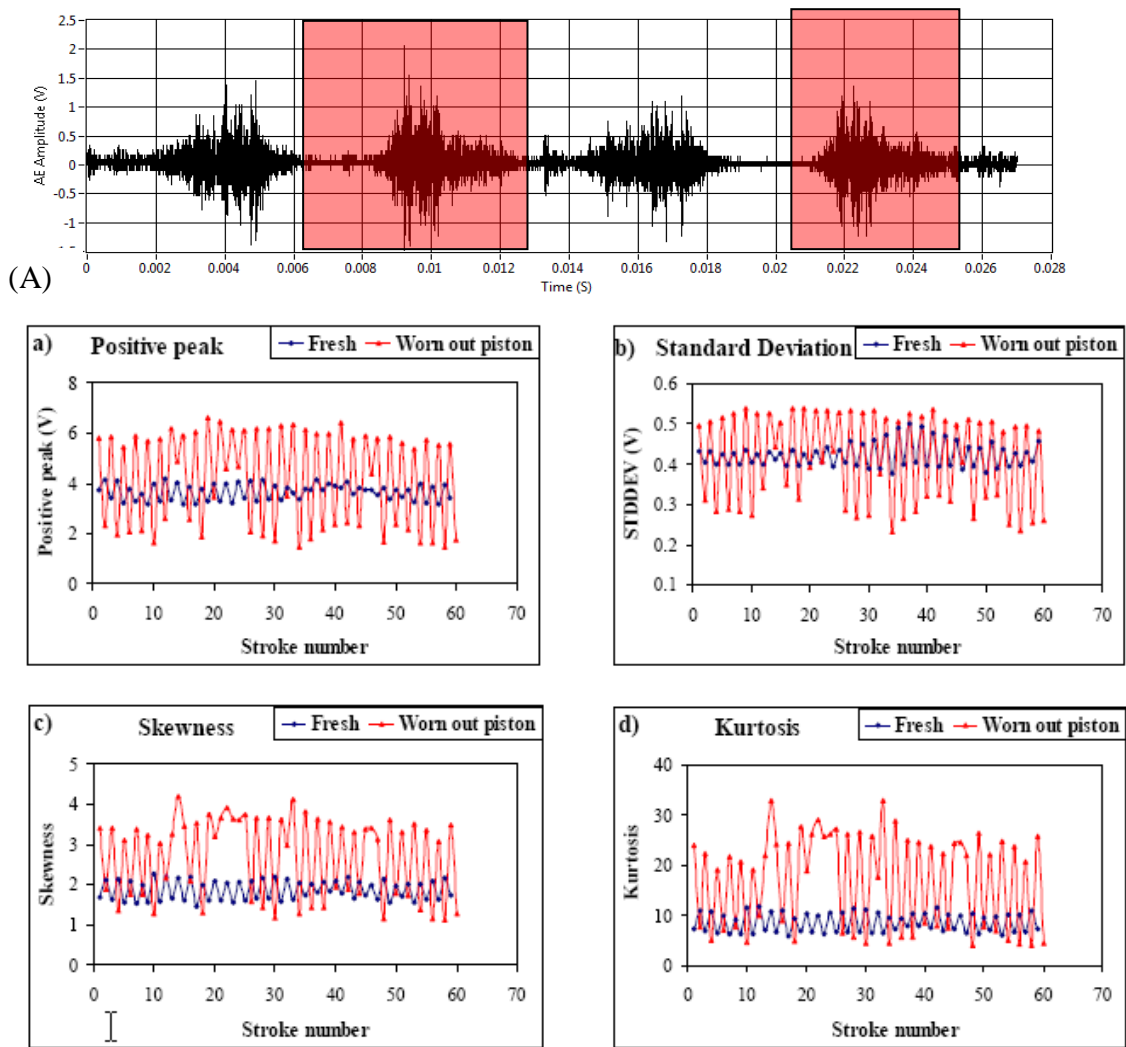
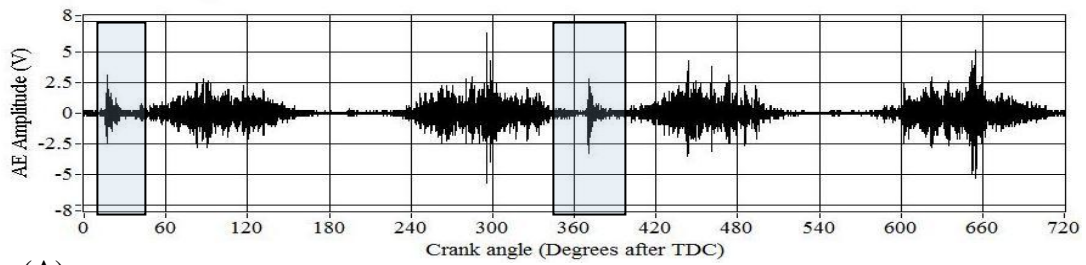


Figure 5.29 (A) segment 3 and 3\*. Comparison of features between reference condition and worn out piston a) Positive peak, b) Standard deviation, c) Skewness, d) Kurtosis.



(A)

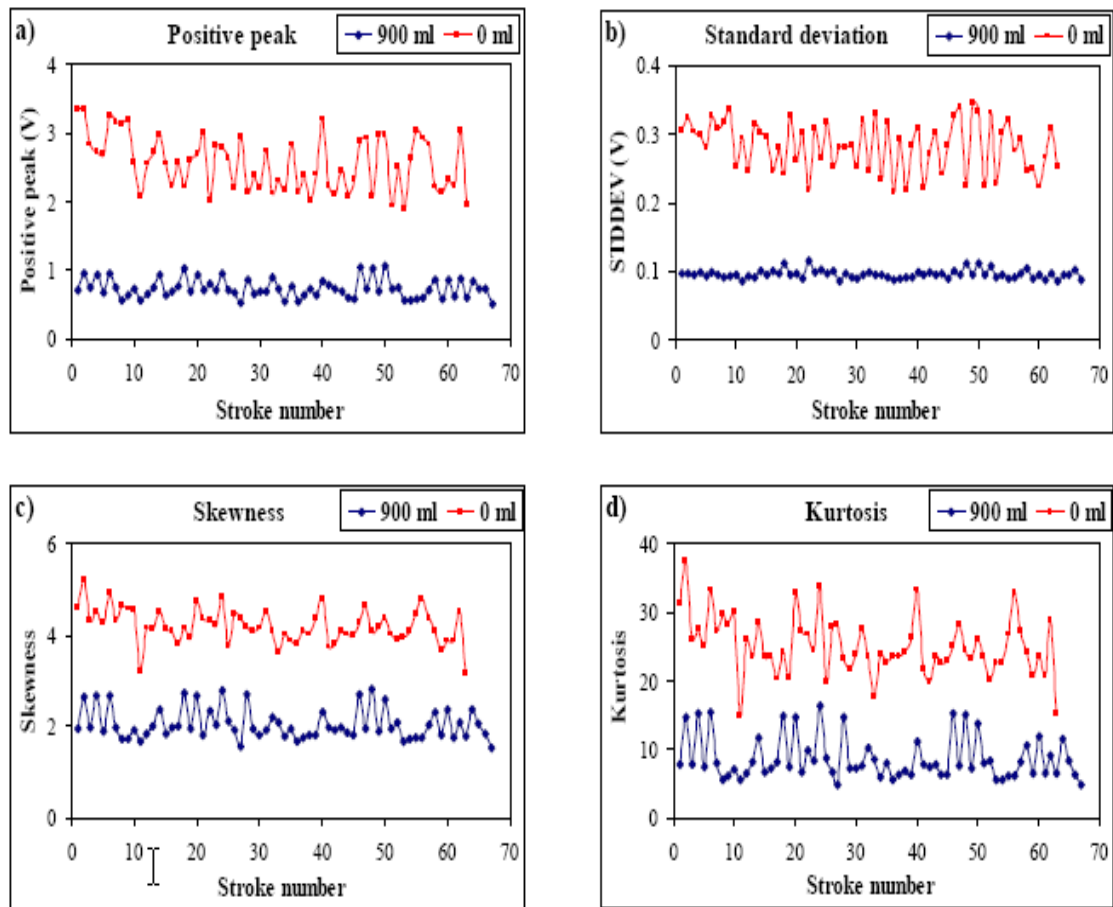


Figure 5.30 (A) segment 1 and 1\*. Comparison of features between reference condition and oil starved condition a) Positive peak, b) Standard deviation, c) Skewness, d) Kurtosis.

Worn out piston ring		Worn out piston		Oil starved condition	
RF	Envelope	RF	Envelope	RF	Envelope
Positive peak	Positive peak	Positive peak	Positive peak	Positive peak	Positive peak
Peak-to-Peak	Mean	Peak-to-Peak	Peak-to-Peak	Peak-to-Peak	Peak-to-Peak
Standard deviation	Standard deviation	Standard deviation	Standard deviation	Standard deviation	Standard deviation
	Median	<i>Skewness</i>	<i>Skewness</i>	<i>Skewness</i>	<i>Skewness</i>
	Mode	<i>Kurtosis</i>	<i>Kurtosis</i>	<i>Kurtosis</i>	<i>Kurtosis</i>
	Positive peak/ mode		Positive peak/ mode		Positive peak/ mode
	AC estimate		AC estimate		Median
	DC estimate		DC estimate		Mode
					AC estimate

Table 5.5 Different fault and corresponding features that indicate their presence

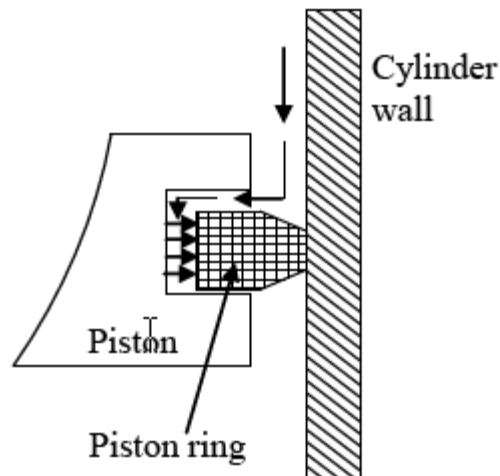


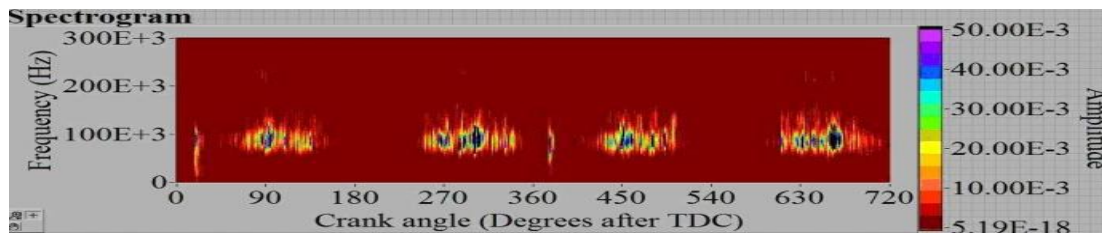
Figure 5.31 One engine cycle showing different segments

It can be observed from the STFT of the data as discussed that the frequency contents for each fault condition varies in range as well as occurrence ( i.e. at what crank angle the frequency contents occur).

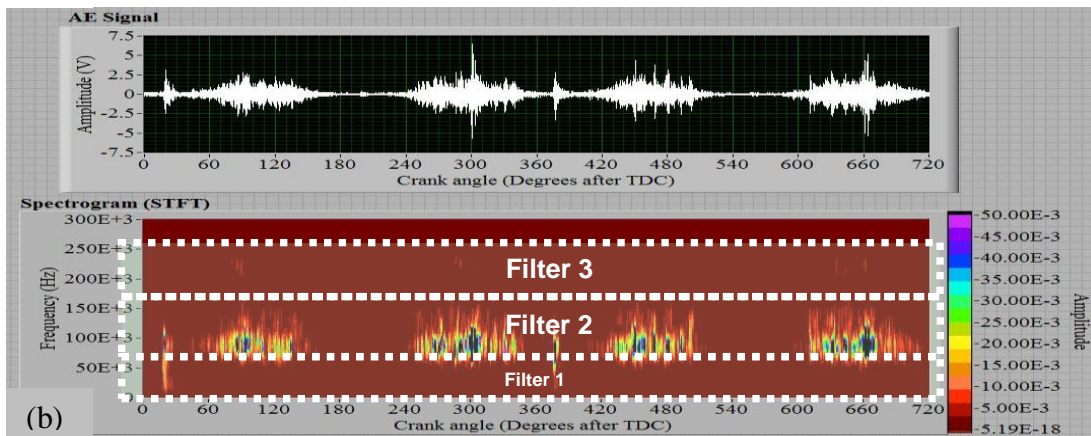
In order to understand these trends clearly and to classify the features accurately the frequency spectrum of the signal was divided into three different bands. This

was done by applying three stages of band pass filters to the raw data, a lower band ranging from 0-50 kHz (Filter 1), a mid band ranging from 50-175 kHz (Filter 2) and a higher band ranging from 175-275 kHz (Filter 3). Figure 5.32 shows STFT of the data and the three band pass filters applied to it.

These three different band pass filtered data was further processed to compute all the 26 features as discussed earlier. The features thus computed for different fault conditions were compared with reference condition. Figures 5.33, 5.34 and 5.35 show comparison between standard deviation of the envelope domain data, for different fault conditions for Filters 1, 2 and 3 respectively. It can be observed from the figures that data in the frequency range of 0-50 kHz, for segments near TDC (1 and 1\*), show higher amplitudes for oil starved condition as compared to other fault conditions. The data in the frequency range of 50-175 kHz, for segments near TDC (1 and 1\*), shows higher amplitude for worn out piston as compared to other fault conditions. Similarly the data in the frequency band of 50-175 kHz as well as 175-275 kHz, for segments 2, 2\* and 3, 3\* show in increase in amplitude for worn out piston rings as compared to other fault conditions.

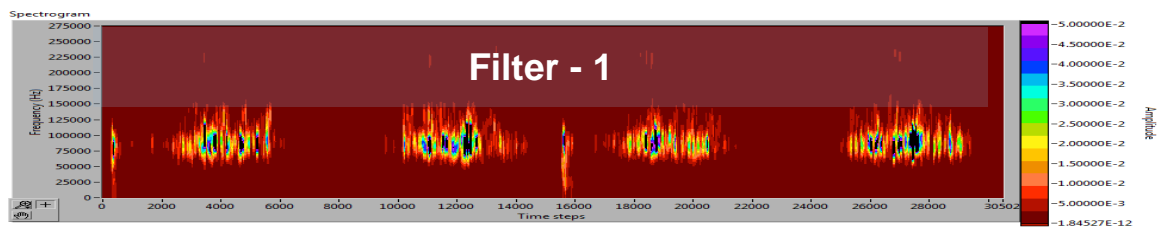


(a)



(b)

Figure 5.32 STFT of data showing (a) original (b) different frequency bands and filters applied



(A)

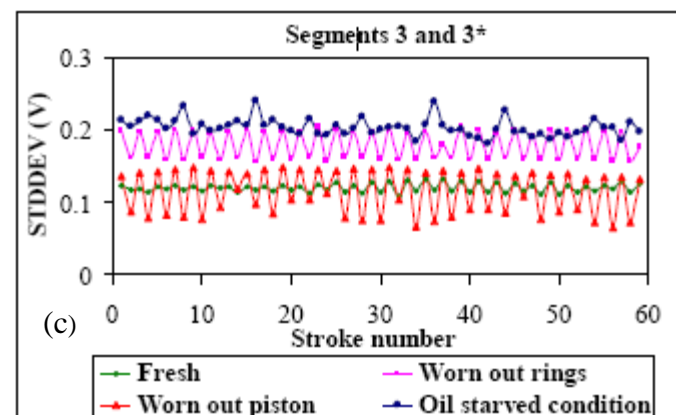
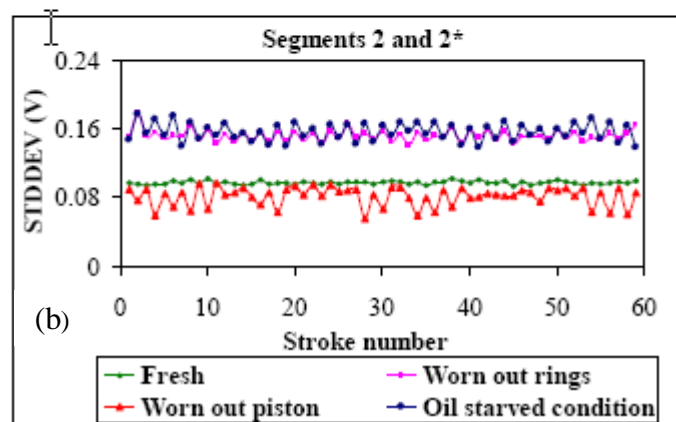
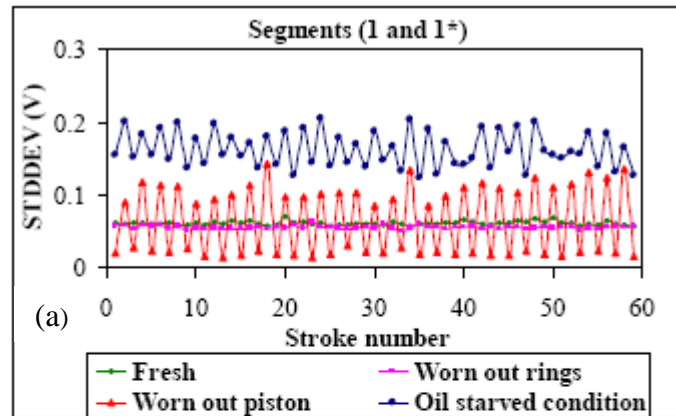
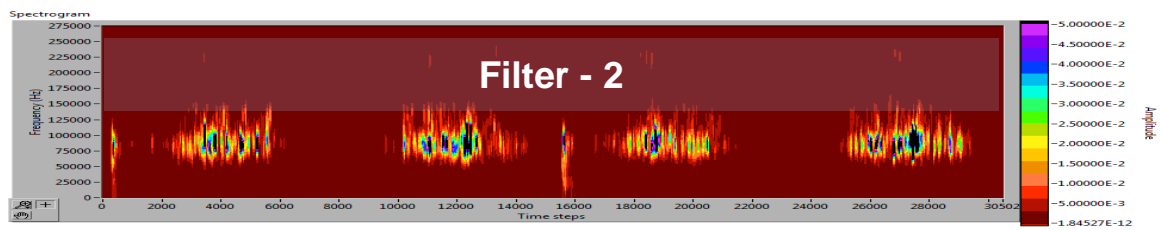


Figure 5.33 (A) Frequency band 0-50 kHz near TDC. Comparison of standard deviation of segments 1 and 1\* (a); 2 and 2\* (b); 3 and 3\* (c) in the frequency band of 0-50 kHz in the segments near TDC.





(A)

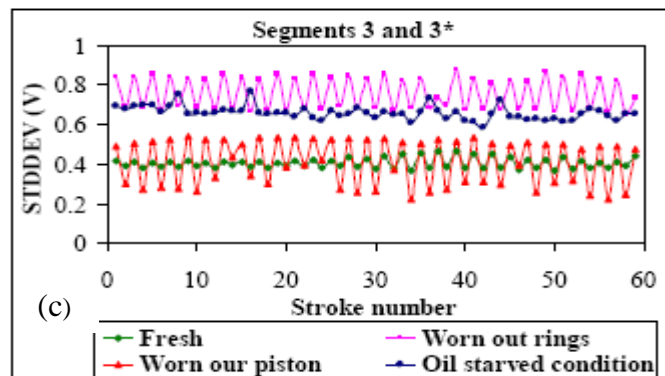
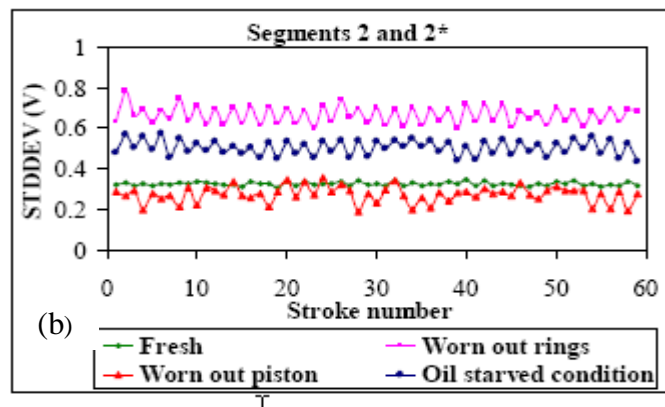
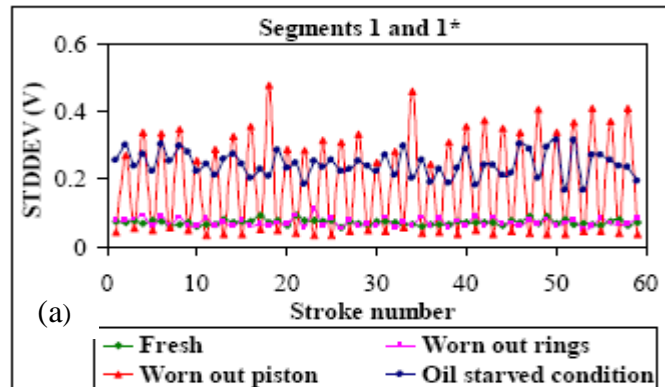
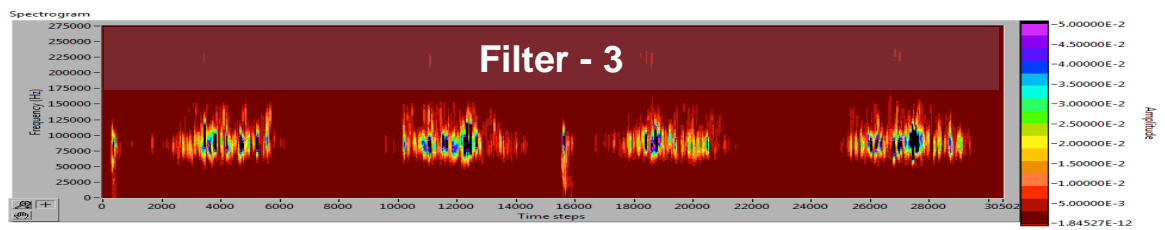


Figure 5.34 (A) Frequency band of 50-175 kHz. Comparison of standard deviation of segments 1 and 1\* (a); 2 and 2\* (b); 3 and 3\* (c) in frequency band of 50-175 kHz



(A)

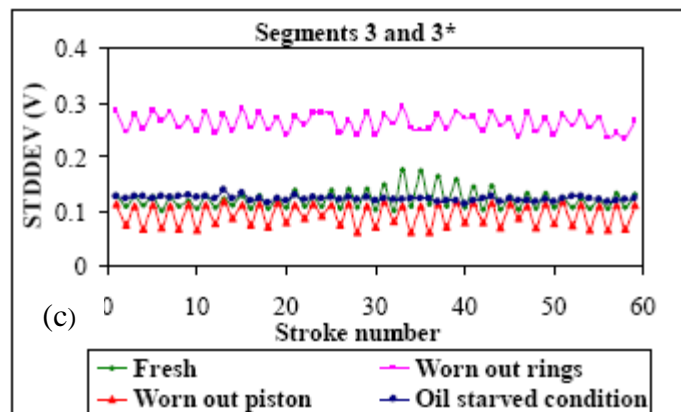
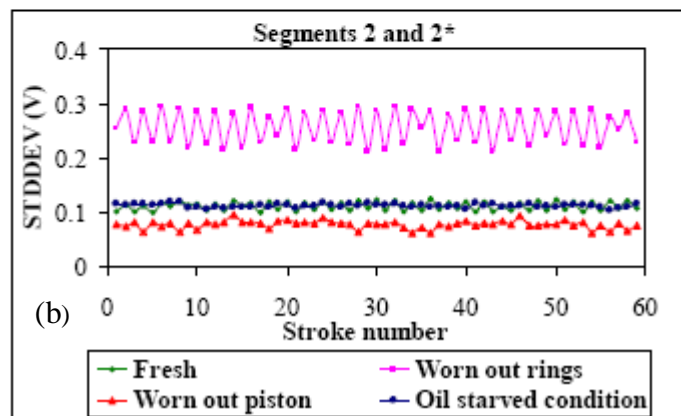
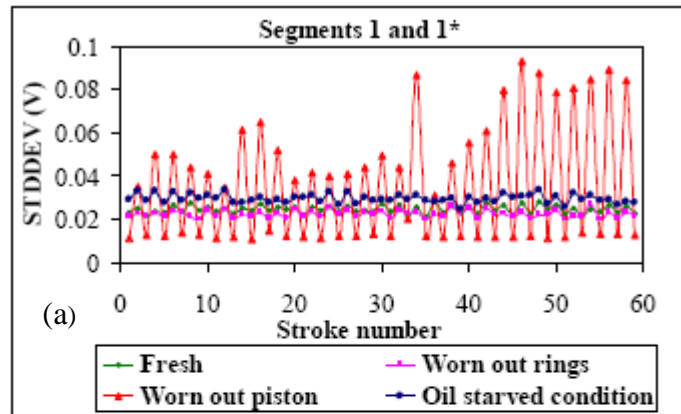


Figure 5.35 (A) Frequency band of 175-275 kHz. Comparison of standard deviation of segments 1 and 1\* (a); 2 and 2\* (b); 3 and 3\* (c) in frequency band of 175-275 kHz

Hence it can be concluded from the results of frequency analysis that it is important to look at the different segments and frequency bands in order to accurately detect different fault conditions.

The trends observed for each fault condition were verified by repeating the experiments and analyzing the data as per the methodology followed. All the trends observed in the initial experiments were observed to repeat consistently for all the three induced fault conditions.

Table 5.6 tabulates the result of the observations drawn from the segmentation in frequency domain. It can be clearly seen from the table that worn out piston ring fault condition can be detected by increase in amplitude of key features in the frequency band of 175-275 kHz during both downward as well as upward movements of the piston. The fault condition of worn out piston can be detected by increase of key features in the frequency band of 50-275 kHz in the segments near TDC. The oil starved condition can be detected by looking at the increase in the key features in the frequency band of 0-50 kHz in the segments near TDC.

<b>Segments</b>	<b>Frequency Band</b>	<b>0-50 Hz</b>	<b>50-175 Hz</b>	<b>175-275 Hz</b>
<b>1 and 1* (Segments near TDC)</b>		Oil starved condition	Worn out piston	Worn out piston
<b>2 and 2* (Downward movement of piston)</b>		Oil starved condition/ Worn out piston rings	Oil starved condition/ Worn out piston rings	Worn out piston rings
<b>3 and 3* (Upward movement of piston)</b>		Oil starved condition/ Worn out piston rings	Oil starved condition/ Worn out piston rings/ Worn out piston	Worn out piston rings

Table 5.6 Consolidated results of frequency domain analysis

## Chapter 6. Conclusion and Future work

---

Unlike corrosive wear, adhesive wear is not a slow, controllable and predictable one. Once the adhesive wear starts, it damages the engine in an accelerated manner and the whole engine is damaged within a short span of time. Hence, it is of utmost importance to discover the adhesive wear at its prenatal stage. Adhesive wear of an engine originates from many factors.

Incidents of adhesive wear (scuffing) have increased over the last few decades due to the continued development of large-bore, two-stroke engines. During this time, the IMEP for engines has increased from 13 to 19.5 bar with peak firing pressures similarly rising from 90 to 150 bar. Hence, it can be said that newly designed engines operate on a knife edge with little or no apparent reserve for out-of-the-normal operation.

Although the occurrence of scuffing is generally associated with extreme conditions of temperature or pressure, there are a number of other possible causes such as the presence of water in the scavenge air, carbon deposits on piston crown lands and in ring grooves and even the fuel injection patterns and combustion characteristics. Among all factors contributing to the scuffing, piston ring behaviour plays the major role. It involves piston ring pack design, operation condition, running-in, material, leakages and pressure distribution. The other important contributing factor is the lubricants, its characteristics, mode of lubrication and even its delivery method.

As the contributing factors of the adhesive wear are known and many of these can be modeled, many of these design and operational factors have been addressed in order to reduce or diminish the possibility of the onset of adhesive wear. In this regard, piston ring material and design and optimized lubrication plays crucial role. In principle, anything that helps the ring to maintain its correct sealing conditions should be facilitated and the operating conditions must be eased. It is necessary to preclude distortions, excessive pressures and temperatures, maintain satisfactory lubricating conditions, eliminate blow-by, and apply correct cooling.

Despite the improvement in design and operation to combat scuffing, the problem still persists. In this regard, detection of scuffing at natal stage or finding the appropriate precursor is very vital.

Scuffing can be detected by analyzing and monitoring the hydrodynamic lubrication variables, such as oil film thickness, coefficient of friction and load analysis.

Conventional method of trying to detect scuffing through traditional temperature sensor like thermocouple is inadequate. Normal cylinder liner temperature curves are very smooth and plain. Depending on the engine load, the temperature changes smoothly. Occasional high peak or spike temperature reading indicates the passing of piston ring gap against the sensor. These spikes are not responsible for onset of scuffing. From numerous data acquisition, it was discovered that many blocks of fluctuating wave pattern data of sensor output indicated the breaking and reforming of oil film thickness, which can serve as a potential scuffing indicator. The fluctuating temperature phenomenon was recognized by the inclination and the amplitude of the temperature data curve. The goal was to capture such fluctuating wave blocks.

A Fourier series model was formulated for the analysis of the series of fluctuating pattern against a specified period interval. The real data from the field were checked against the developed mathematical function and found the matching of the pattern. The number of peaks and the period of the sample blocks were analyzed. The prediction of onset of scuffing is then possible by analyzing the set spectrum of fluctuating temperature reading block and setting a periodical limit with a threshold amplitude.

Yet, it is argued that scuffing detection by temperature sensing should be considered as the last safety barrier, as temperature effect is the after effect of the scuffing and it solely depends on the localized condition and the material's thermal status.

Eddy current is known to detect material flow at the micro scale. With proper built in compensation, the system can detect the deviation of roughness of the piston

ring surfaces, which can serve as the precursor of onset of scuffing. Such roughness gauging through eddy sensors picks up scuffing symptom at the very early stage long before the temperature sensors detection capability. As the measured roughness is based on the distance between the rubbing surfaces of the liner and the ring, it encompasses the oil film thickness and hence has the potential to measure it.

Owing to different lubrication model (hydrodynamic, mixed and boundary), different minimum oil film thickness in different regions of the piston stroke guards the rings and the liner against scuffing. Hence, eddy current analysis of scuffing detection was mathematically modeled and analyzed to understand the ring and liner behaviour through the various model of lubrication over the entire length of the cylinder liner. The software was developed, with which the standard deviation of the current average roughness could be measured against the standard deviation of the reference average roughness. Predefined value of deviation of the said two standard deviations and the rate of increase of such deviation can then serve as the precursor of the scuffing and can be termed as scuffing index against the cylinder pressure profile.

Yet, the number, location and the range of the eddy current detectors on a cylinder liner could be limited and at that, they measure the small section of the ring and lubrication condition. Eddy current sensors need to be mounted on the cylinder liners against the rings exposed surface and hence is considered as an intrusive method. They are prone to be damaged by the sliding rings and is more so when the liner is worn out. These constraints may serve as the limiting factors for the usage of eddy current analysis.

Acoustic emission method, though is ideal to predict scuffing before its onset, needs intelligent analysis to isolate the scuffing signals from other routine and unusual events of the operating engine. It also needs to distinguish adhesive wear from other controllable and uncontrollable wears. Owing to its non-intrusive characteristics, it certainly has competitive advantages against others. On the other

hand, it is subjected and prone to more noise mixing. Feature extraction is the important part of the detection process.

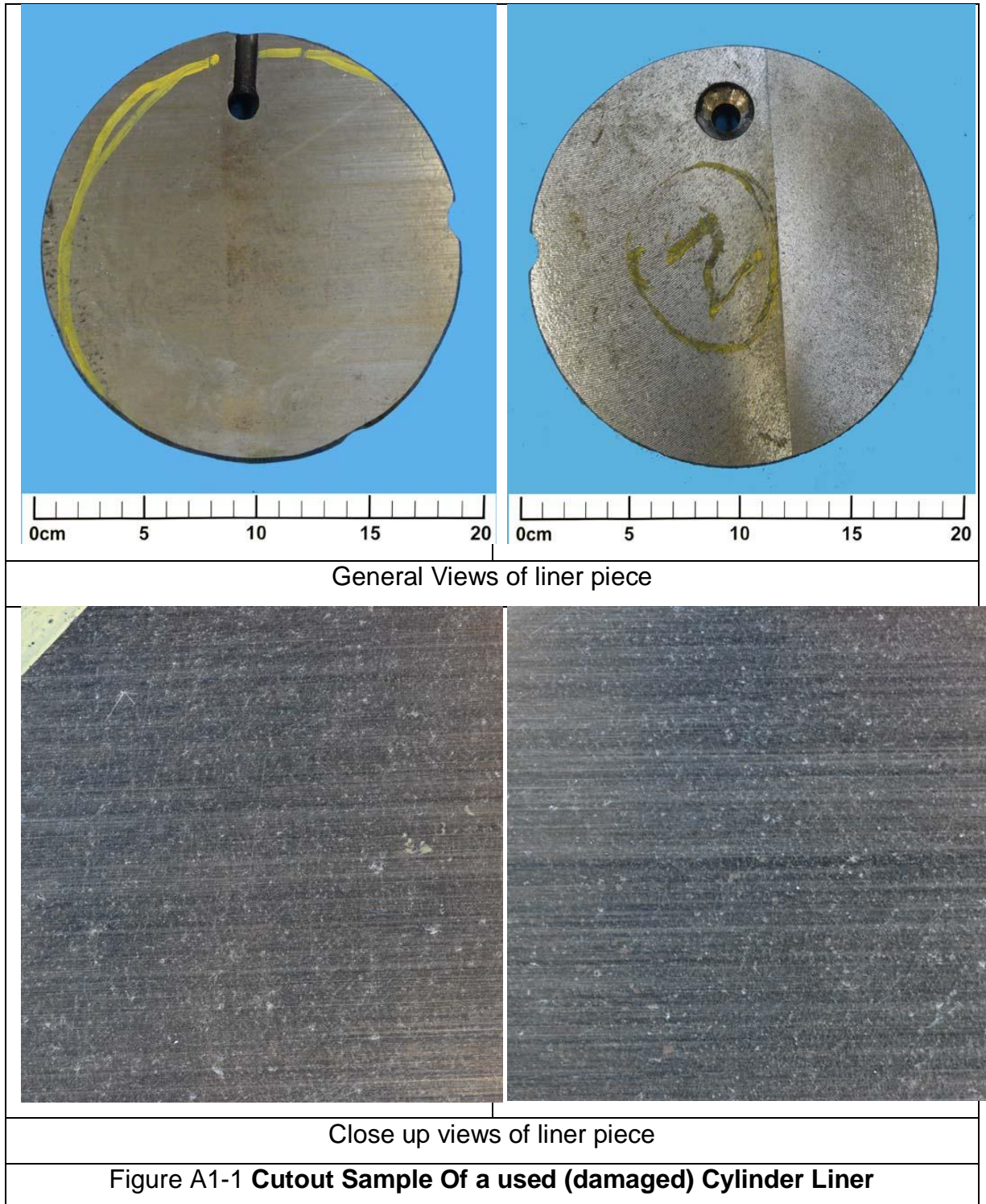
An acoustic emission based methodology for detecting three major fault conditions at the piston – cylinder wall interface was developed. These are piston wear, ring wear and oil starvation. The methodology was based on signature analysis of the collected AE data for the three simulated fault conditions. A total of 26 features were computed for each stroke of the piston for the full length of the data collected. The trends of these features were studied for different fault conditions. The fault condition of any type can be quickly detected by looking at the time history of collected data. Any variation in the amplitude of the collected AE signal indicates the presence of a fault in an engine. Hence the first check point is to compare the time history of the data with the reference data (Data collected for a good engine at the start of its service life without any faults). However classification of the extracted features is necessary in assigning certain features to a particular type of fault accurately. This is done by combining the frequency domain analysis with the trend analysis of features. The spectral content of the signal was divided in to three bands: low, mid and high, each ranging from 0-50 kHz, 50-175 kHz and 175-275 kHz respectively. This was done based on the presence of data for different fault conditions in these bands of frequencies. Henceforth, detection of oil starvation, which leads to the onset of scuffing is clearly found from the frequency bin.

To summarise on the detection method, it can be stated that the best method of detection of the onset of cylinder liner scuffing at natal stage is possible through acoustic emission analysis coupled with thermocouple, which serves as a secondary protection.

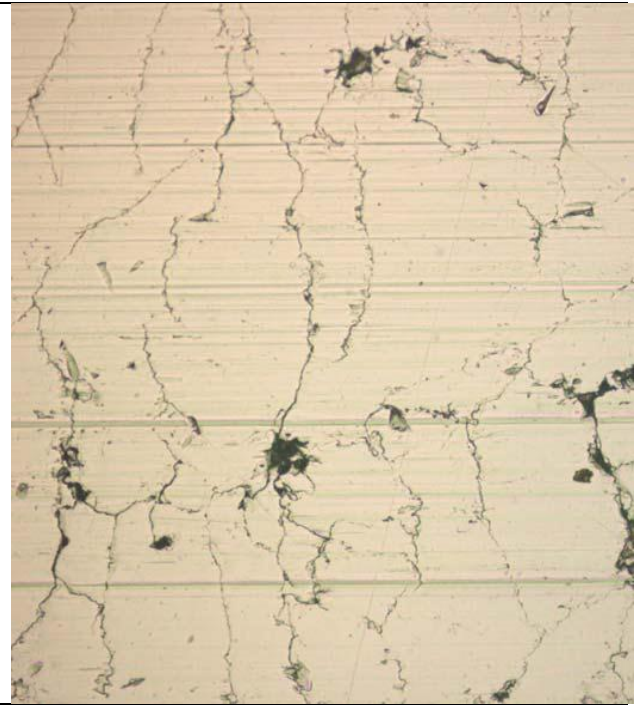
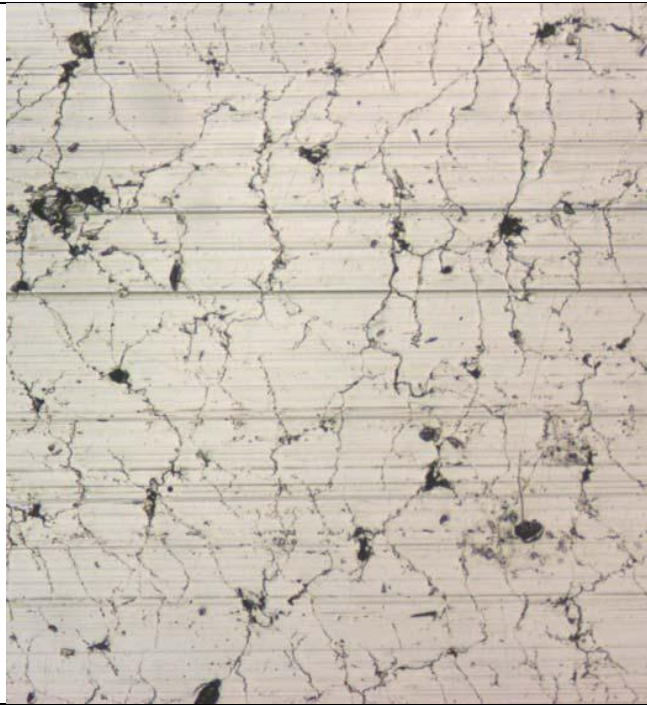
Acoustic emission analysis for the detection of scuffing has very high potential, which was shown through the field test on a four stroke engine. However, future work is needed to carry out more field tests under various loading condition on a slow speed marine diesel engine in order to understand the various event alignment and the non-routine detection, such as scuffing.

## APPENDIX 1

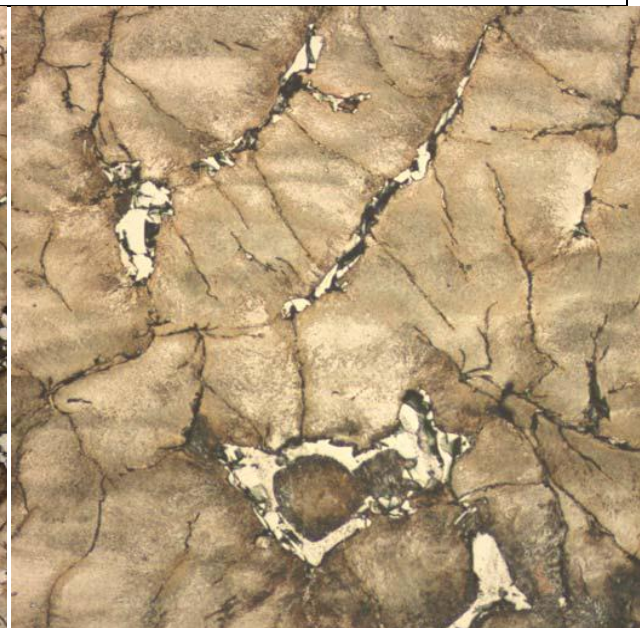
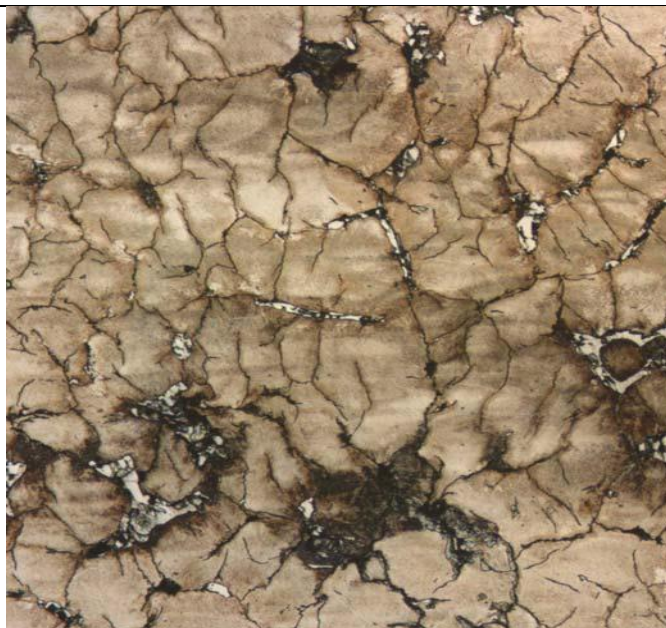
Details of the material analysis of the cut piece of the liner, which was eventually used in the fabricated jig for the lab run of the eddy current detection system is shown below:







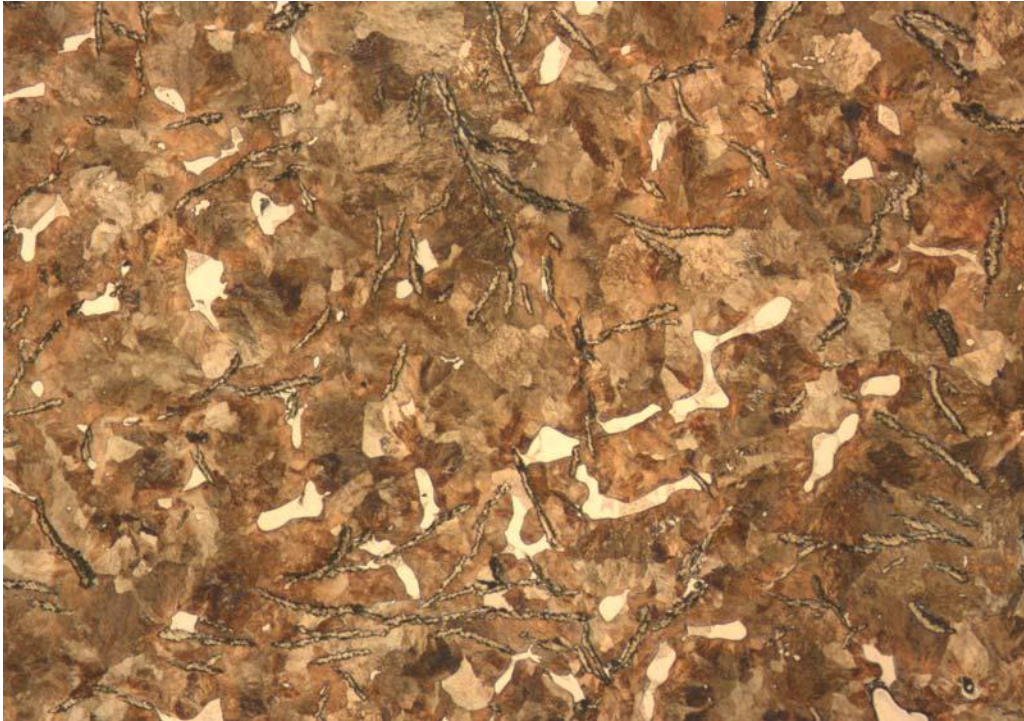
Replicated micrograph at 50X (left) and 100X (right) magnifications – before etching



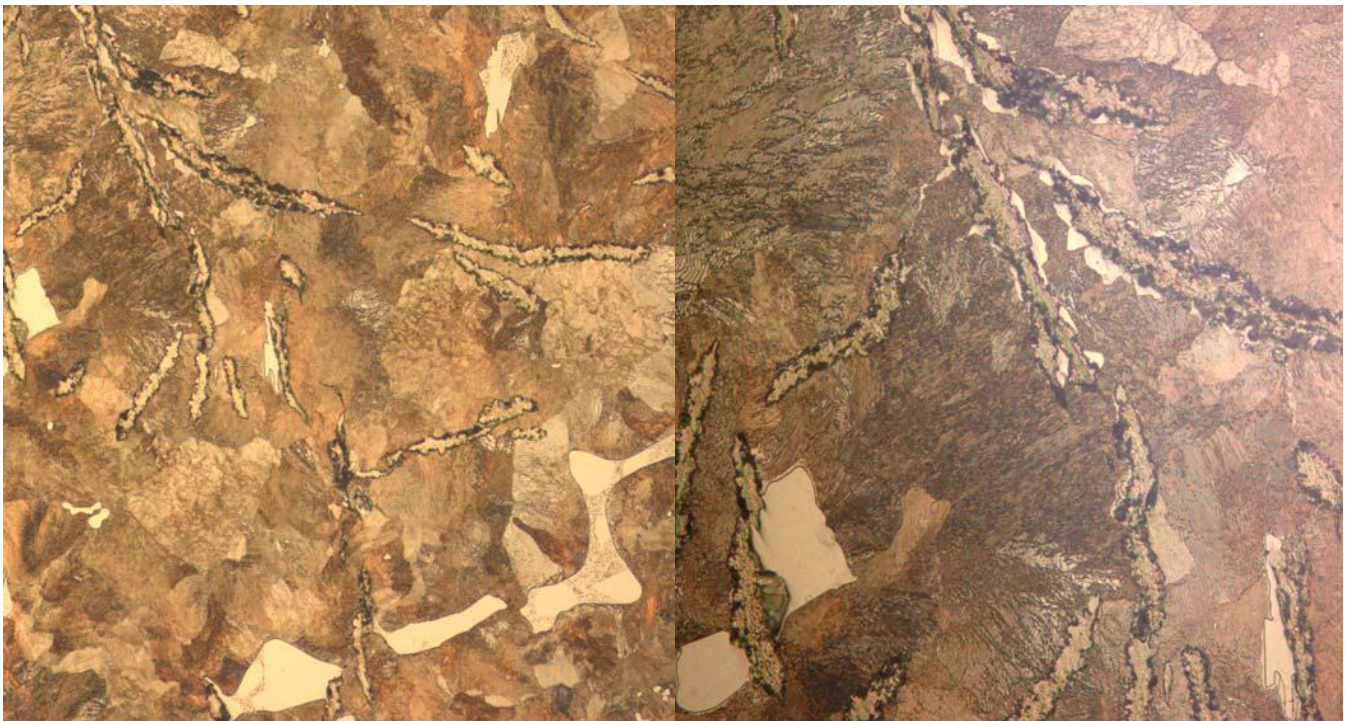
Replicated micrograph at 50X (left) and 100X (right) magnifications – after light polishing and etching

**Figure A1-2 Surface Metallography – Original Surface (As-Received and After Light Polishing & Etching).** The examined location had scuffing marks and surface (micro) seizure in the form of networks of micro fissures propagating along the graphite flakes and the eutectic hard phase.





Replicated micrograph at 50X magnification



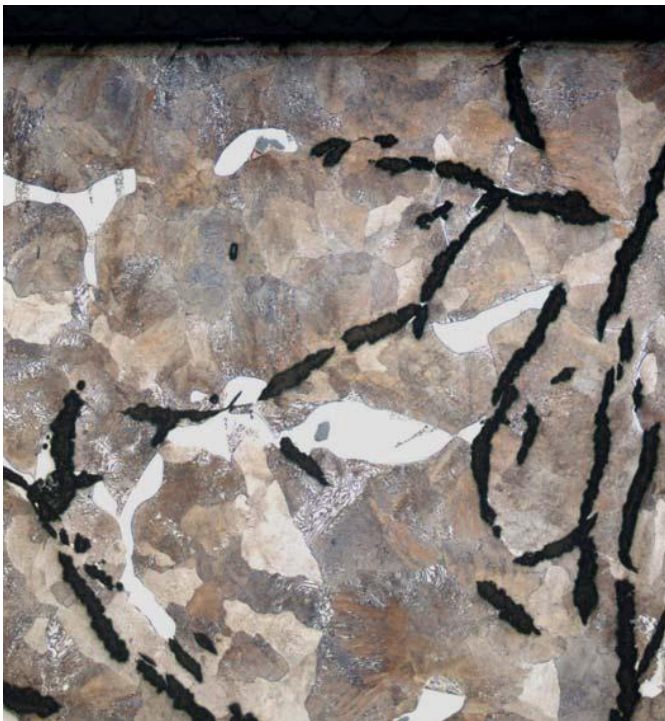
Replicated micrographs at 100X (left) and 200X (right) magnifications

Figure A1-3 **Surface Metallography – 0.1mm Below Surface.** No indication of seizure / fissuring was observed after polishing to a depth of ~0.1mm. The microstructure essentially revealed graphite flakes in pearlite matrix with ~5% eutectic hard phase.





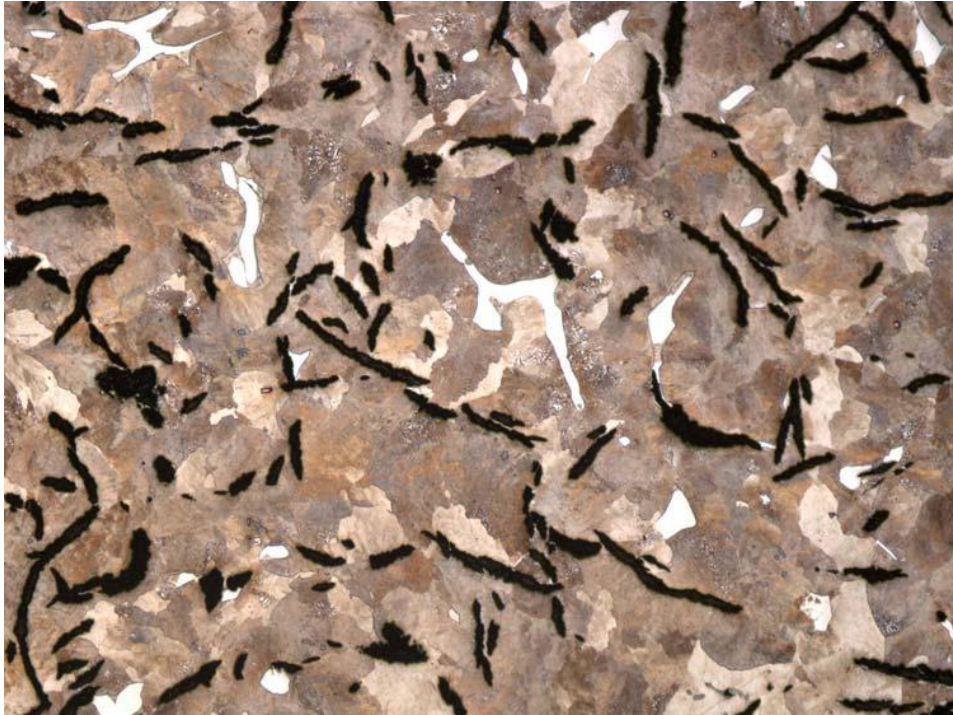
Micrograph at 50X magnification



Micrographs at 100X (left) and 200X (right) magnifications

Figure A1-4 **Sectional Metallography – Below Surface**. The examined location had a microstructure of essentially graphite flakes in pearlite matrix with ~5% (phosphide) eutectic hard phase.





Micrograph at 50X magnification



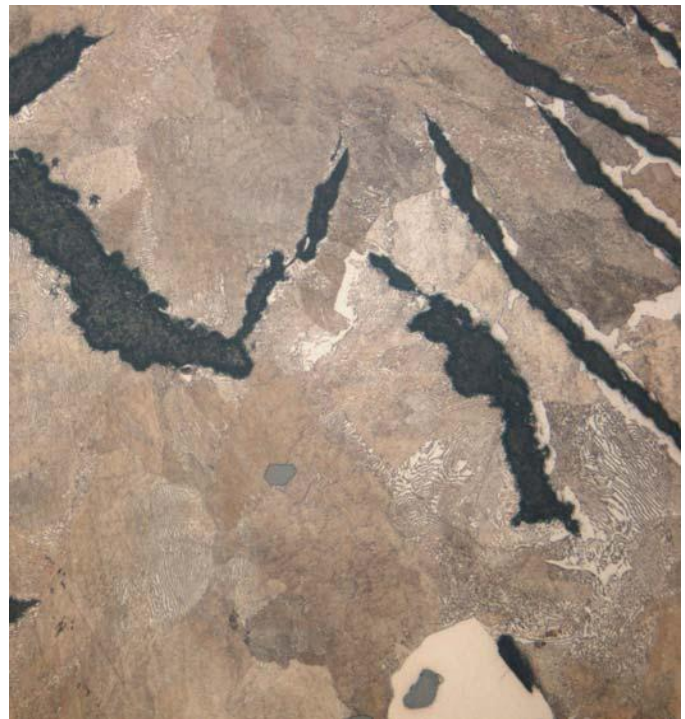
Micrographs at 100X (left) and 200X (right) magnifications

Figure A1-5 **Sectional Metallography – 1mm Below Surface**. The examined location had a microstructure of essentially graphite flakes in pearlite matrix with ~5% (phosphide) eutectic hard phase.





Micrograph at 50X magnification



Micrographs at 100X (left) and 200X (right) magnifications

Figure A1-6 **Sectional Metallography – 10mm Below Surface**. The examined location had a microstructure of essentially graphite flakes in pearlite matrix with ~5% (phosphide) eutectic hard phase.

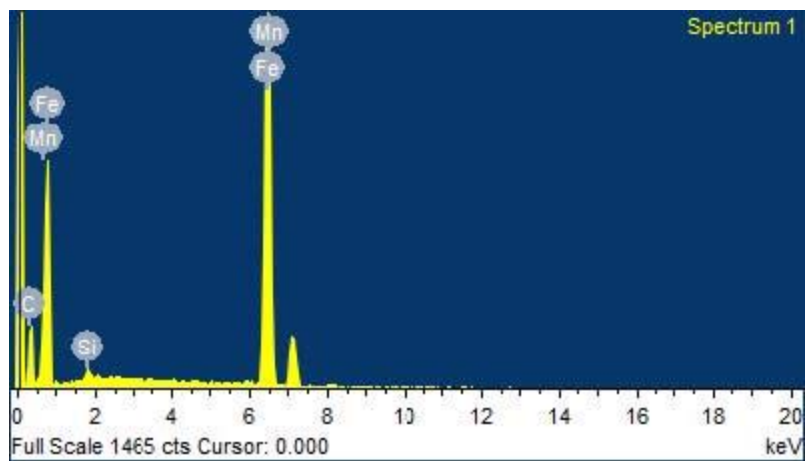
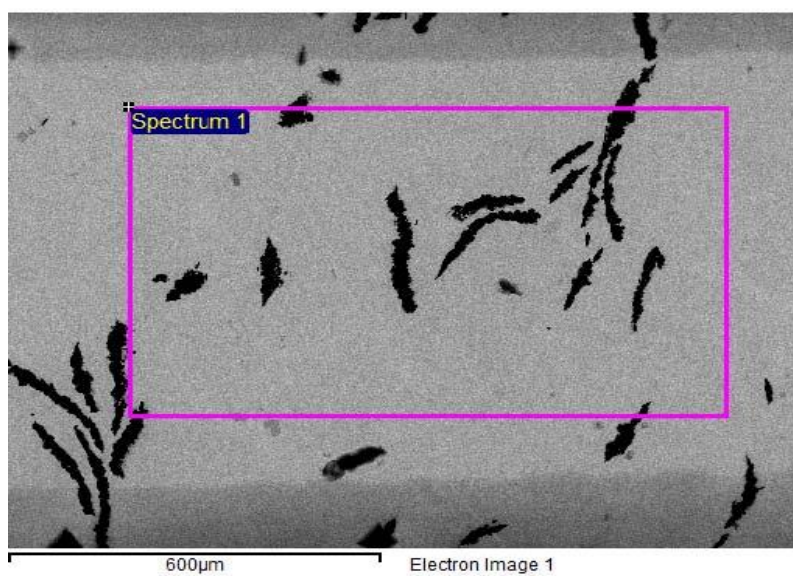


Figure A1-7 **EDX Spectrum – Below Surface.** EDX analysis of the base material at ~0.1mm below the surface revealed major presence of iron and carbon with minor presence of silicon and manganese.



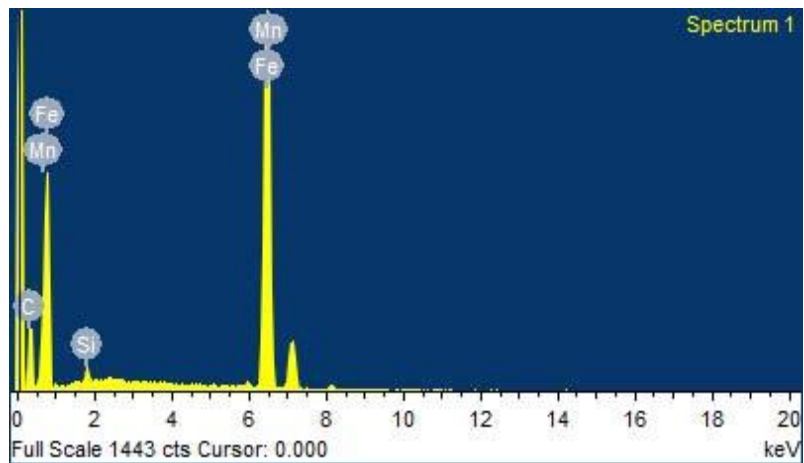
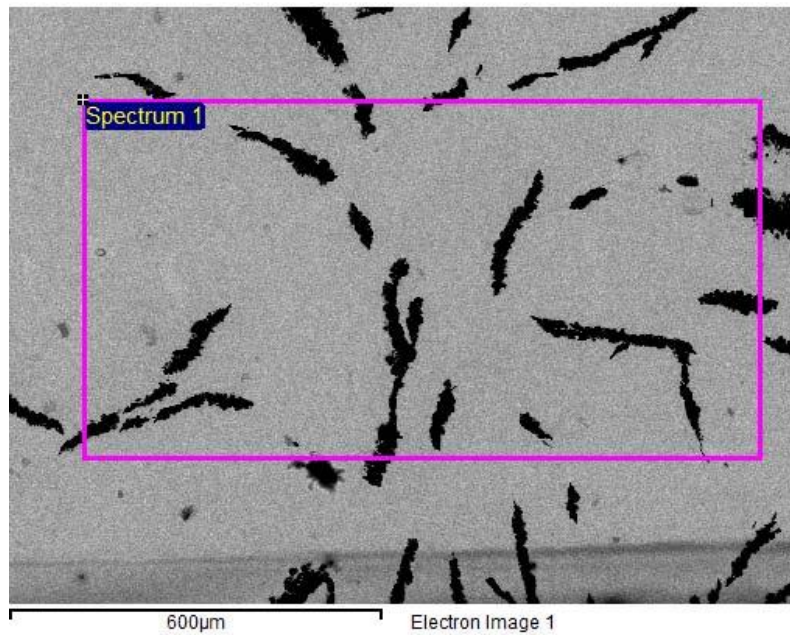


Figure A1-8 **EDX Spectrum – 1mm Below Surface.** EDX analysis of the base material at ~1mm below the surface revealed major presence of iron and carbon with minor presence of silicon and manganese.

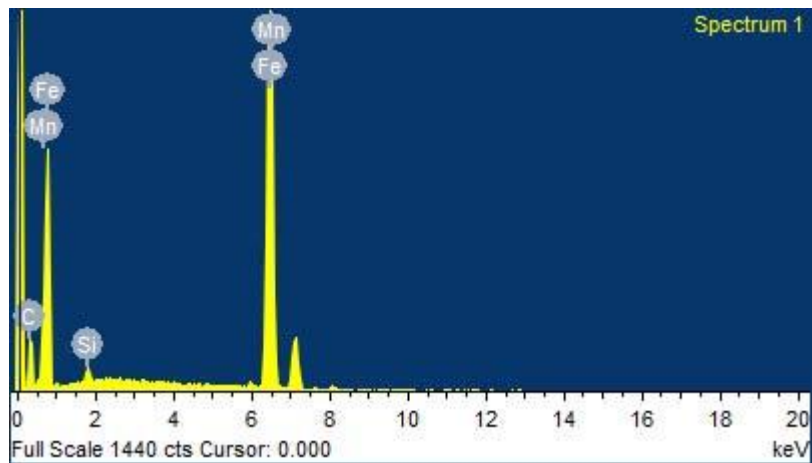
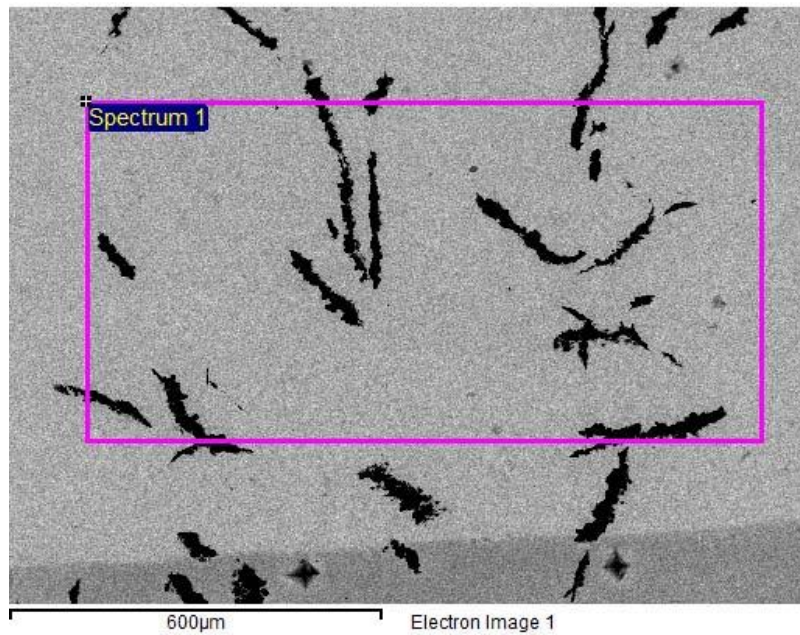


Figure A1-9 **EDX Spectrum – 10mm Below Surface**. EDX analysis of the base material at ~10mm below the surface revealed major presence of iron and carbon with minor presence of silicon and manganese.

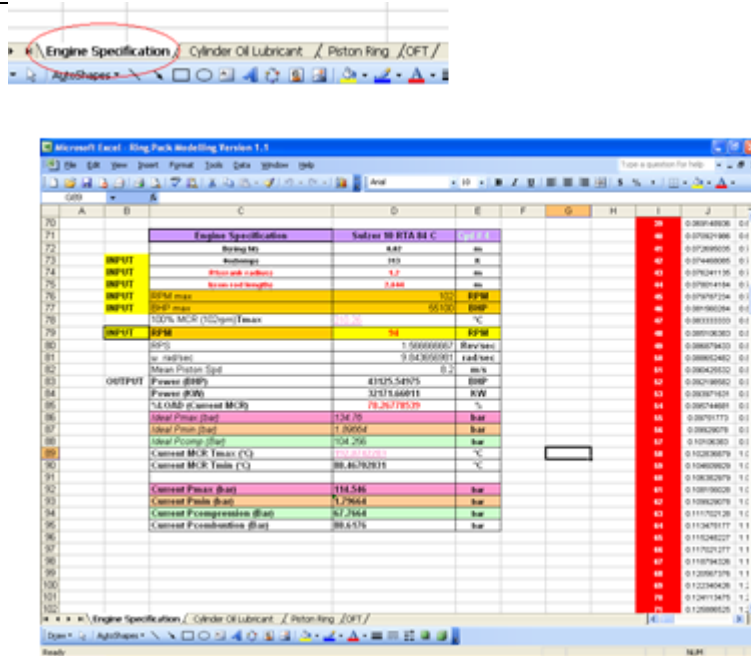


## APPENDIX 2

### Manual for tribological model for the detection of onset of scuffing

# User Manual

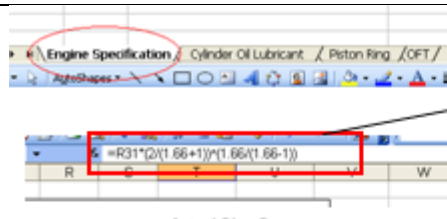
## Ring Pack MODEL Version 1.1



Cell	A	B	C	D	E	F	G	H	I	J
70										
71			Engine Specification	Sulzer RTA 96 C	1.0	1.0			0.00145506	0.1
72			Ring ID	8.87	in				0.070421986	0.1
73	INPUT		Ring ID	110	in				0.072895005	0.1
74	INPUT		Ring ID coefficient	1.7	in				0.074400005	0.1
75	INPUT		Ring ID coefficient	1.04	in				0.070421986	0.1
76	INPUT		Ring ID coefficient	1.04	in				0.070421986	0.1
77	INPUT		Ring ID coefficient	1.04	in				0.070421986	0.1
78	INPUT		Ring ID coefficient	1.04	in				0.070421986	0.1
79	INPUT		Ring ID coefficient	1.04	in				0.070421986	0.1
80			Ring ID	1.000000007	Revised				0.00079400	0.1
81			Ring ID	0.043000001	rad/sec				0.00000000	0.1
82			Ring ID	0.2	in				0.00000000	0.1
83	OUTPUT		Power (kW)	41025.54975	BHP				0.00000000	0.1
84			Power (kW)	31015.66815	BHP				0.00000000	0.1
85			% Load (Current MCR)	78.26778539	%				0.00000000	0.1
86			Ideal Pump (bar)	134.78	bar				0.00000000	0.1
87			Ideal Pump (bar)	1.00004	bar				0.00000000	0.1
88			Ideal Pump (bar)	104.256	bar				0.00000000	0.1
89			Current M-C Tmax (°C)	134.78	°C				0.00000000	0.1
90			Current M-C Tmin (°C)	88.4676718	°C				0.00000000	0.1
91			Current M-C Tmid (°C)	111.546	°C				0.00000000	0.1
92			Current Power (bar)	134.78	bar				0.00000000	0.1
93			Current Power (bar)	1.00004	bar				0.00000000	0.1
94			Current Power (bar)	104.256	bar				0.00000000	0.1
95			Current Power (bar)	104.256	bar				0.00000000	0.1
96			Current Power (bar)	104.256	bar				0.00000000	0.1
97			Current Power (bar)	104.256	bar				0.00000000	0.1
98			Current Power (bar)	104.256	bar				0.00000000	0.1
99			Current Power (bar)	104.256	bar				0.00000000	0.1
100			Current Power (bar)	104.256	bar				0.00000000	0.1
101			Current Power (bar)	104.256	bar				0.00000000	0.1
102			Current Power (bar)	104.256	bar				0.00000000	0.1

Fill in the engine design specification and current service parameter

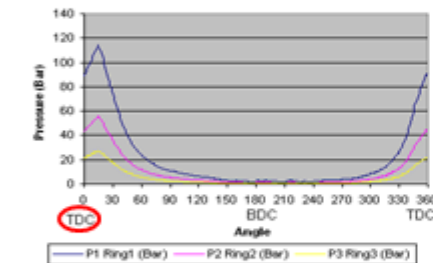




$$P_1 \left( \frac{2}{1.66 + 1} \right)^{\frac{1.66}{1.66 - 1}}$$

$$\frac{P_m}{P_{m-1}} = \left( \frac{2}{\gamma + 1} \right)^{\frac{\gamma}{\gamma - 1}}$$

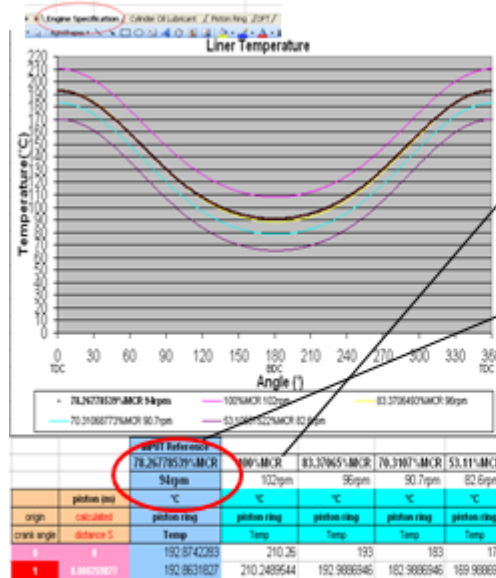
1. INPUT required RPM (65-102 rpm)
2. View the change in Pressure
3. P1 @ 15° = Pmax



Bar	in N/m <sup>2</sup>	Bar	in N/m <sup>2</sup>	Bar	in N/m <sup>2</sup>
measured		calculated		calculated	
P1	P1	P2	P2	P3	P3
3	88.6176	8.0E+05	43.2520114	4.3E+05	21.11099482
9	90.34916	9.03E+05	44.09649347	4.409649347	21.52278233
9	92.07472	9.21E+05	44.94017553	4.494017553	21.93456985
1	93.80328	9.38E+05	45.7838576	4.57838576	22.34635736
4	95.53184	9.55E+05	46.6275396	4.66275396	22.75814487

Engine Specification		Solve to RTA B4 C	Exp 1.1
INPUT	Boring In	8.42	in
INPUT	Stroke	163	in
INPUT	Piston web width	1.2	in
INPUT	Stroke web length	2.844	in
INPUT	RPM max	102	RPM
INPUT	100% MCR (102rpm) Tmax	567.92	°C
INPUT	RPM	75	RPM
OUTPUT	rpm	5600000.07	Revised
OUTPUT	rpm	9.043050011	rad/sec
OUTPUT	Mean Piston Spd	0.2	m/s
OUTPUT	Power (kW)	43125.54975	kW
OUTPUT	Power (hp)	57971.66811	hp
OUTPUT	100% MCR (102rpm) Tmax	567.92	°C
OUTPUT	Current MCR Tmax (°C)	567.92	°C
OUTPUT	Current MCR Tmin (°C)	88.46782831	°C
OUTPUT	Current Pmax (bar)	114.546	bar
OUTPUT	Current Pmin (bar)	7.7664	bar
OUTPUT	Current Compression Ratio	17.2644	
OUTPUT	Current Combustion Ratio	88.6376	

Input RPM and Output is generated for pressure



Engine Specification		Solve to RTA B4 C	Exp 1.1
INPUT	Boring In	8.42	in
INPUT	Stroke	163	in
INPUT	Piston web width	1.2	in
INPUT	Stroke web length	2.844	in
INPUT	RPM max	102	RPM
INPUT	100% MCR (102rpm) Tmax	567.92	°C
INPUT	RPM	75	RPM
OUTPUT	rpm	5600000.07	Revised
OUTPUT	rpm	9.043050011	rad/sec
OUTPUT	Mean Piston Spd	0.2	m/s
OUTPUT	Power (kW)	43125.54975	kW
OUTPUT	Power (hp)	57971.66811	hp
OUTPUT	100% MCR (102rpm) Tmax	567.92	°C
OUTPUT	Current MCR Tmax (°C)	567.92	°C
OUTPUT	Current MCR Tmin (°C)	88.46782831	°C
OUTPUT	Current Pmax (bar)	114.546	bar
OUTPUT	Current Pmin (bar)	7.7664	bar
OUTPUT	Current Compression Ratio	17.2644	
OUTPUT	Current Combustion Ratio	88.6376	

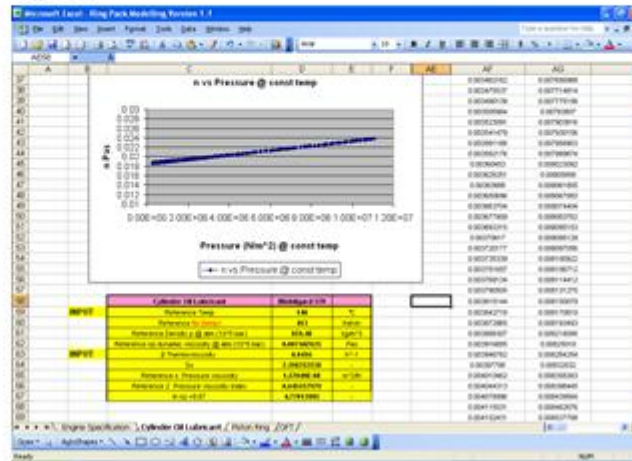
Liner Temperature		Exp 1.1
INPUT	70.26778529°MCR 90rpm	70.26778529°MCR 90rpm
INPUT	100°MCR 102rpm	100°MCR 102rpm
INPUT	83.3706572°MCR 90rpm	83.3706572°MCR 90rpm
OUTPUT	calculated	calculated
OUTPUT	acceleration	acceleration
OUTPUT	140.8081329	192.8742283
OUTPUT	140.7754797	192.8629229
OUTPUT	140.6775437	192.8290125
OUTPUT	140.5143956	192.7725151

1. INPUT required RPM (65-102 rpm)
2. View the change in Temp MAX  
Temp MIN

Input RPM and output is generated for the profile of cylinder liner temperature

Engine Specification \ Cylinder Oil Lubricant \ Piston Ring \ O/F /

$$\alpha * p = [\ln \eta_0 + 9.67] \left\{ \frac{[T-138]}{[T_0-138]} \right\}^{\frac{-(\delta[T_0-138])}{\ln \eta_0 + 9.67}} * (1 + 5.1 * 10^{-9} * P_{\text{azradial}})^{\frac{(0.6+0.965 \log_{10} \eta_0) * 10^{-8}}{(5.1 * 10^{-9} (\ln \eta_0 + 9.67))} - 1]}$$

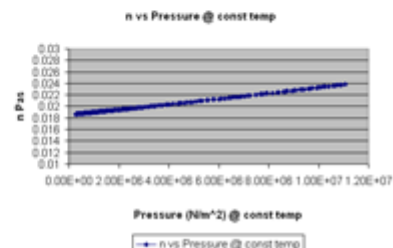
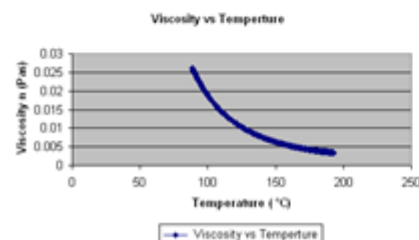


Engine Specification / **Cylinder Oil Lubricant** / Piston Ring / GFT /

	Cylinder Oil/Lubricant	Mobilgard 570
INPUT	Reference Temp	140
	Reference $\rho_0$ (temp)	403
	Reference Density $\rho_0$ at atm (10 <sup>-5</sup> bar)	859.48
	Reference $\eta_0$ dynamic viscosity at atm (10 <sup>-5</sup> bar)	0.002447625
INPUT	$\rho$ Thermodynamic	0.8014
	So	2.398252538
	Reference s: Pressure viscosity	1.57049E-04
	Reference Z: Pressure viscosity index	0.455557979
	In $\eta \rightarrow 0.67$	4.77013805

- [illegible]

1. INPUT **RPM** from Engine Spec Tab
2. View the change in  $\eta_R = \eta^* e^{\alpha^* p}$
3. Due to change in Temp & Pressure



249

$$p_1(b-k) - p_2(\ell) - F_p - P_z + P_s = M \frac{d^2 z}{dt^2} = 0$$

	TOP 10			
INPUT	of time (roughness)	0.5	gms	
OUTPUT	rising roughness	0.27		
	a composite roughness	5.6847E-07	ms	
	of boundary (a) 0.1713	5.6847E-07	ms	
INPUT	of boundary coefficient of friction	0.1		
INPUT	of time (a) 0.1713	2.2729E-06		
INPUT	of time coefficient of friction	0.001		
	of boundary (a) 0.1713	2.2729E-06		
	Density	7890	kg/m <sup>3</sup>	
INPUT	Rising time	0.62		
INPUT	Rising time for P10	0		
INPUT	Rising time for P10	0		
INPUT	Rising time	0.62		
INPUT	Rising time	0.62		
INPUT	P10 spring pressure	0.001	kg/cm <sup>2</sup>	
	a g value	0.001		
INPUT	coefficient of friction	0.1		
	top area of ring	0.000022	m <sup>2</sup>	
	vol. of ring	0.000000	m <sup>3</sup>	
	area of ring	4E-007	m	
	area of ring	0.000001	m <sup>2</sup>	
	dia of piston	0.02		
	dia of piston	0.02		
	dia of piston	0.02000		
INPUT	Force of piston	0.0001	N	
INPUT	Force of piston	0.0001	N	

**Engine Specification**

g1-g2	Force act on 1/2 mass of ring + ring act	$\mu$ r/ric coeff	g1				
in N	Fp in N	Fp in N	in N/m2	bar			Non
	Friction force	per dip					Radial Load
total force	total Fp		Pz	Pz			W/L
67509.48183	8793.948183	339697.2501	8.59E+06	85.963091577			1.72E+05
65825.77783	8528.37783	344188.8862	8.78E+06	87.5900542			175120.1084
70588.08954	7058.08954	352940.4782	9.02E+06	89.21615263			178432.3883
7191.24715	7191.24715	359562.0883	9.30E+06	90.87233105			181744.8628
72236.73966	7223.673966	366183.6983	9.52E+06	92.52649949			185056.839
74581.06187	7456.106187	372505.3083	9.82E+06	94.15486739			188369.2158
75985.30686	7598.30686	379426.9183	9.95E+06	95.84074834			191891.4527
77238.70558	7722.70558	386048.5284	9.75E+06	97.46989747			194935.7095
78584.02719	7853.42719	392670.1385	9.52E+06	99.153232			198306.9484
79868.3427	7985.3427	399388.7485	1.01E+07	100.8900556			201618.3233

1. INPUT Ring Properties
2. View the change in Radial Load
3.  $h = 1 - ((2 \times x) / B)^2 \times (h_1 - h_0) + h_0$
4. Fully Flooded Condition  $k \& I = 0$
5. Balance Radial Load /  $P_z$  to obtain  $h_0(h_{min})$
6. View Next Page

250

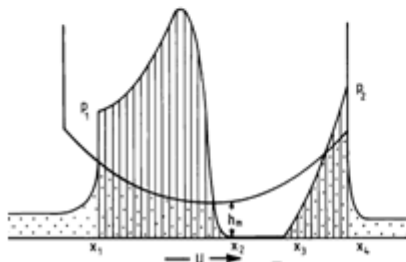
### Theory of Reynolds Equation & Radial Load

The boundary conditions, taken from the Ring's inlet and outlet, are

$p = p_1$	at $x = x_1$	Inlet
$p = 0$ (or $p_2$ )	at $x = x_2$ & $x_3$	Cavitations and Reformation
$p = p_2$	at $x = x_4$	Outlet

$$p = 12\eta u \left[ E + \frac{1}{R} \left( \frac{R\Omega}{u} \right) \frac{\partial h}{\partial \theta} \cdot F + (C_1) G + (C_2) \right]$$

$$\text{where } E = \int \frac{dx}{h^3}; \quad F = \int \frac{x}{h^3} dx \quad \text{and } G = \int \frac{dx}{h^3}$$



### Reynold's equation and radial load

$$\frac{\partial}{\partial x} \left( \frac{h^3}{12\eta} \frac{\partial p}{\partial x} \right) = 12\eta v \frac{\partial h}{\partial x} + 12\eta \frac{\partial h}{\partial t}$$

$$\frac{\partial p}{\partial x} = 12\eta v \frac{1}{h^3} + \frac{\omega}{v} \left( \frac{\partial h}{\partial \theta} \right) \frac{x}{h^3} + \frac{C_1}{h^3}$$

Where

$$V = (U_1 + U_2) / 2$$

$$h = h_0 + (1 - 2x/B)^2 (h_1 - h_0)$$

Given B.C.

$$\frac{\partial p}{\partial x} = 0 \text{ @ } x = x_2 = 0.01 = B/2 \text{ Cavitations}$$

$$h = h_0$$

Therefore,

$$C_1 = -h_0 + \frac{\omega}{v} \left( \frac{\partial h}{\partial \theta} \right) \cdot 0.01$$

$$\int \frac{\partial p}{\partial x} = \int 12\eta v \frac{1}{h^3} + \frac{\omega}{v} \left( \frac{\partial h}{\partial \theta} \right) \frac{x}{h^3} + \frac{C_1}{h^3}$$

$$P(x) = 12\eta v \left( E + \frac{\omega}{v} \left( \frac{\partial h}{\partial \theta} \right) F + C_1 G + C_2 \right)$$

$$C_2 = \frac{P(x)}{12\eta v} - E + \frac{\omega}{v} \left( \frac{\partial h}{\partial \theta} \right) F + C_1 G$$

Where

$$K = (h_1 - h_0) / h_0$$

$$E = \int \frac{1}{h^3} dx$$

$$= \int \frac{1}{(h_0 + (1 - \frac{2x}{B})^2 (h_1 - h_0))^3} dx$$

$$= \frac{b}{h_0^2} \left[ \frac{-b(b-2x)}{b^2 + k(b-2x)^2} - \frac{\tan^{-1} \left( \frac{k(b-2x)}{\sqrt{k}} \right)}{\sqrt{k}} \right]$$

$$F = \int \frac{x}{h^3} dx$$

$$G = \int \frac{1}{h^3} dx$$

Find Constants from boundary conditions

### B.C

x from 0 - 0.01

$$P(x) = P_1 \text{ @ } x = x_1 = 0$$

$$C_2 = \frac{P_1}{12\eta v} - E + \frac{\omega}{v} \left( \frac{\partial h}{\partial \theta} \right) F + C_1 G$$

Where E, F, G for x = 0 (fixed) & θ angle varies

Therefore

$$P_{x1} = 12\eta v \left( E + \frac{\omega}{v} \left( \frac{\partial h}{\partial \theta} \right) F + C_1 G + C_2 \right)$$

Where E, F, G for x range from 0- 0.01 and C<sub>2</sub> is based on P<sub>1</sub>

x from 0.011 - 0.02

$$P(x) = P_2 \text{ @ } x = x_4 = B = 0.02$$

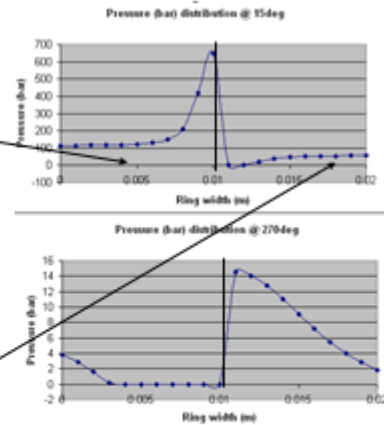
$$C_2 = \frac{P_2}{12\eta v} - E + \frac{\omega}{v} \left( \frac{\partial h}{\partial \theta} \right) F + C_1 G$$

Where E, F, G for x = 0.02 (fixed) & θ angle varies

Therefore

$$P_{x2} = 12\eta v \left( E + \frac{\omega}{v} \left( \frac{\partial h}{\partial \theta} \right) F + C_1 G + C_2 \right)$$

Where E, F, G for x range from 0.011- 0.02 and C<sub>2</sub> is based on P<sub>2</sub>



## Find pressure distribution

### Load Capacity

$$\frac{w}{L} = \int_0^B P_x dx = 12\eta v \left( \int_0^B \frac{1}{h^3} dx + \frac{\omega}{v} \left( \frac{\partial h}{\partial \theta} \right) \int_0^B \frac{x}{h^3} dx + C_1 \int_0^B \frac{1}{h^3} dx + C_2 \right) \Big|_0^B$$

Where

$$\int \frac{1}{h^3} dx = \int E dx = \frac{b(b-2x)\tan^{-1}\left(\frac{\sqrt{k}(b-2x)}{b}\right)}{8\sqrt{k}h_0^2}$$

$$\int \frac{x}{h^3} dx = \int F dx = \frac{1}{128k^2h_0^3} \left[ -\frac{4b^2\sqrt{k}x}{b^2(1+k) - 4bkx + 4kx^2} + 2(b + 3bk - 6kx)\tan^{-1}\left(\frac{\sqrt{k}(b-2x)}{b}\right) \right]$$

$$\int \frac{1}{h^3} dx = \int G dx = -\frac{1}{64Kh_0^3} \left[ \frac{2b^3}{b^2(1+k) - 4bkx + 4kx^2} + 6\sqrt{k}(-b + 2x)\tan^{-1}\left(\frac{\sqrt{k}(b-2x)}{b}\right) \right]$$

Where θ = 0° - 180° & x = 0 - 0.01

$$\frac{w_{@P_1}}{L} = \int_0^{0.5B} P_{x@C_1+P_1} dx$$

Where θ = 181° - 360° & x = 0.011 - 0.02

$$\frac{w_{@P_2}}{L} = \int_{0.5B}^B P_{x@C_2+P_2} dx$$

## Find Load capacity



### Lubricant Friction Force

$$U = \frac{-1}{2\eta} \frac{dp}{dx} (x^2 - h_0) - \frac{(U_1 - U_2)x}{h} + U_1$$

Where  $U_2 = 0$

$$h = h_0 + (h_1 - h_0) (1 - 2x/B)^2$$

$$\frac{du}{dz} = \frac{-1}{2\eta} \frac{dp}{dx} (2z - h) + \frac{U_1}{h}$$

$$\tau = \frac{du}{dz} \eta = \frac{-1}{2} \frac{dp}{dx} (2z - h) + \frac{U_1 \eta}{h}$$

Where  $z = h$  &  $U = U_1$

$$\tau = \frac{-dp}{dx} \frac{h}{2} + \frac{U_1 \eta}{h}$$

$$\frac{F}{L} = \int_0^B \tau dx = \int_0^B \left( \frac{-h}{2} \frac{dp}{dx} + \frac{U_1 \eta}{h} \right) dx$$

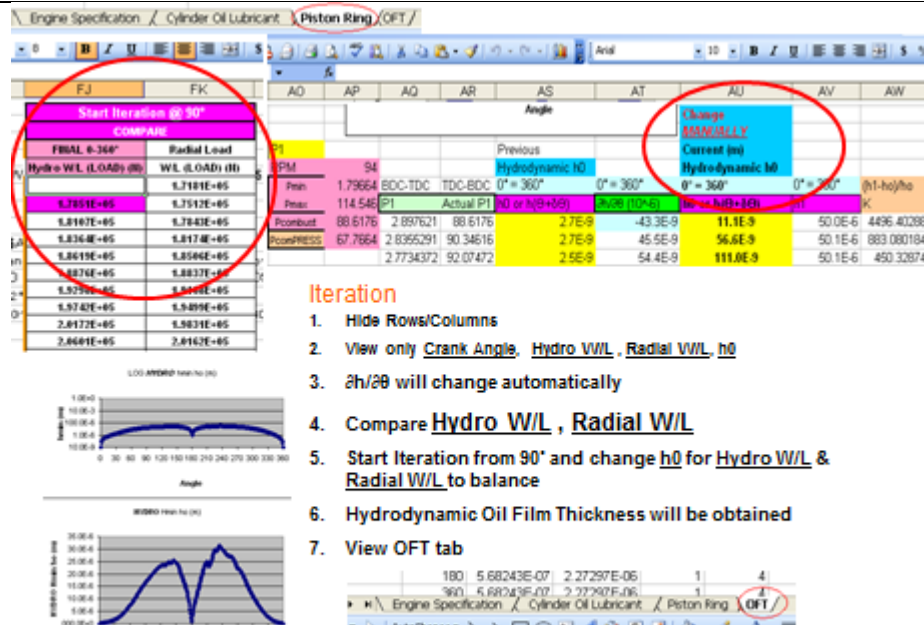
$$= - \left[ \frac{(1 - \frac{2x}{B})^2 (h_1 - h_0) + h_0}{2} P(x) - \int_0^B P(x) \left( \frac{-2}{B} + \frac{4x}{B^2} \right) (h_1 - h_0) dx \right] + \int_0^B \frac{U_1 \eta}{h} dx$$

$$= - \left[ \frac{(1 - \frac{2x}{B})^2 (h_1 - h_0) + h_0}{2} P(x) + \frac{2 P(x) \cdot x (B - x) (h_1 - h_0)}{B^2} \right]_0^B$$

$$= \frac{B \eta U_1 \tan^{-1} \left( \frac{B - 2x \sqrt{h_1 - h_0}}{B \sqrt{h_0}} \right)}{2 \sqrt{h_0} \sqrt{h_1 - h_0}} \Big|_0^B$$

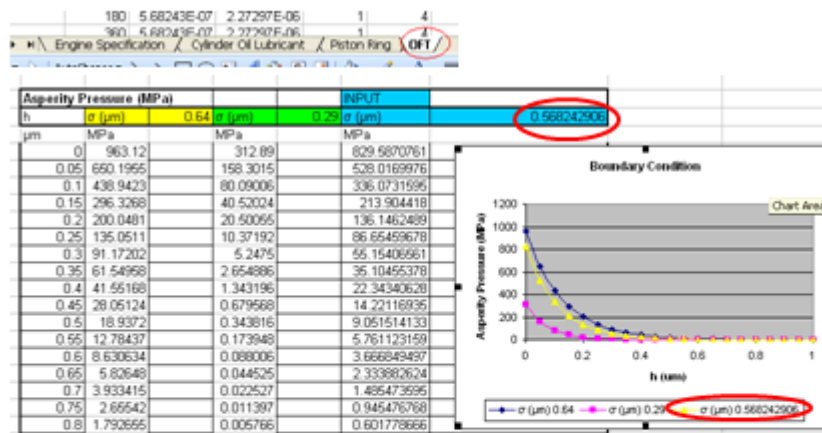
$$= - \left[ \frac{h_1}{2} P_2 - \frac{h_1}{2} P_1 \right] + \frac{B \eta U_1 \tan^{-1} \left( \frac{B - 2x \sqrt{h_1 - h_0}}{B \sqrt{h_0}} \right)}{\sqrt{h_0} \sqrt{h_1 - h_0}}$$

Find friction force



Oil film thickness changes against crank angle





1. INPUT Liner & Ring Roughness to obtain  $\sigma$  composite under *Piston Ring* tab
2. View change in *Asperity Pressure* via *h0* for Boundary Lubrication (yellow) under *OFT* tab

Engine Specification / Cylinder Oil Lubricant / Piston Ring / OFT

TOP RING			
INPUT	eLiner (roughness)	0.5	$\mu\text{m}$
INPUT	eRing (roughness)	0.27	$\mu\text{m}$
OUTPUT	$\sigma$ composite roughness	5.68243E-07	m
INPUT	h0 Boundary Lub OFT 1-1	5.68243E-07	m
INPUT	p Boundary coefficient of friction	0.1	-
INPUT	h0 Mixed Lub OFT 1-1	2.27297E-06	m
INPUT	p Mixed coefficient of friction	0.08	-
INPUT	h0 Hydrodynamic Lub OFT 1-1	2.27297E-06	m

Input ring and liner roughness and generated output gives asperity pressure for boundary lubrication

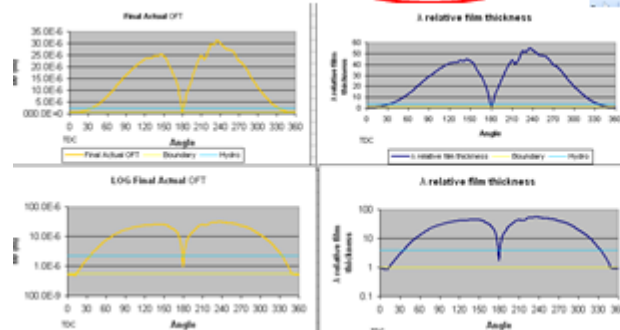
Engine Specification / Cylinder Oil Lubricant / Piston Ring / OFT

TOP RING			
INPUT	eLiner (roughness)	0.5	$\mu\text{m}$
INPUT	eRing (roughness)	0.27	$\mu\text{m}$
OUTPUT	$\sigma$ composite roughness	5.68243E-07	m
INPUT	h0 Boundary Lub OFT 1-1	5.68243E-07	m
INPUT	p Boundary coefficient of friction	0.1	-
INPUT	h0 Mixed Lub OFT 1-1	2.27297E-06	m
INPUT	p Mixed coefficient of friction	0.08	-
INPUT	h0 Hydrodynamic Lub OFT 1-1	2.27297E-06	m

Variables		Values	Units
Region			
%B		7.202216066	%
%B Original value		7.202216066	%
%M		8.310249307	%
%M Original value		8.310249307	%
%H		84.48753463	%
%H Original value		84.48753463	%

1. INPUT Liner & Ring Roughness to obtain  $\sigma$  composite under *Piston Ring* tab
2. View change in Boundary / Mixed / Hydrodynamic Lubrication



Input ring and liner roughness and output is generated for oil film thickness of boundary, mixed and hydrodynamic lubrication

## References:

01. Lacey, P.I. & Stockwell, R.T., 1999, Development of a methodology to predict cylinder liner scuffing in the 6V92TA engine lubricant test. Tribology transactions, 42, Issue 1, 192-201.
02. Galligan, J., Terrance, A. and Liraut, G., 1999, A scuffing test for piston ring/bore combinations: Part II. Formulated motor lubrication. Wear, 236 (1999b) 1-2, 210-220
03. Wilson, K., 1998. Cylinder Liner Scuffing in 2-stroke low-speed engines as experienced by "users" WG members and others. Proc. Of 22<sup>nd</sup> Intl. Congress on Combustion Engines, CIMAC, Copenhagen, Denmark, 19-21 May 1998(2), 303-310.
04. Shuster, M. M., Stong, T., Deis, M C. And Burke, D.C., 1999. Piston ring cylinder liner scuffing phenomenon: investigation, simulation and prevention. Proc. Of Conference, Detroit, USA, 1-4 March 1999, SAE Paper 1999-01-1219.
05. Allen, R.W. and Yura, S., 2000. Developments in two-stroke engine cylinder lubrication. Proc. Of 6<sup>th</sup> Intl. Symposium on Marine Engineering, ISME, Tokyo, Japan, 23-17 October 2000(2), 488-492.
06. Durga, V.; Rao, N.; Boyer, B.A.; Cikanek, H.A. and kabat, D.M., 1998. Influence of surface characteristics and oil viscosity on friction behavior of rubbing surfaces in reciprocating engines. Technical Conference ASME-ICE, 31-2, paper No. 98-ICE-131, 23-35.
07. Schenk, C., Hengeveld, J. and Aabo, K., 2000. The role of temperature and pressure in wear processes in low speed diesel engines. Proc. Of 6<sup>th</sup> Intl. Symposium on Marine Engineering, ISME, Tokyo, Japan, 23-17 Oct 2000, 2 pp. 562-569.
08. Nakano, H., 1990. Piston ring scuffing as a limit in designing future diesel engines. Proc. Of 4<sup>th</sup> Intl. Symposium on Marine Engineering, ISME, Kobe, Japan, 15-19 October 1990.
09. Ruddy, B. L. and Hillyard, M L., 1991. A Review of Tribological Aspects of Piston Assembly Design. Proc. 17<sup>th</sup> Leeds-Lyon Symposium on Tribology, Elsevier, 93-102.
10. Daros Piston rings Handbook/Manual. Elementary piston ring-Function and Mechanics. *In*. Daros Piston Rings AB; Issue 2
11. G. K. Aue, 1974. On the Mechanism of a piston Ring Seal. *In*. Sulzer Technical Review 1/1974.

12. Salzmann, F., 1940. Wärmefluss durch Kolben and Kolbenring. Diss. ETH Zurich 1932 (in German), condensed *In. 'Engineering'*, March 22, 1940, p. 297.
13. Amoser, M., 2001. Insights into piston-running behavior. *In. Marine News (2001)2, Wartsila Corporation*, 23-27.
14. Baker, A.J.S., 1972. Piston Ring Loading Factors and Method of wear Measurement. CIMAC 1972, Stockholm, paper A29.
15. Hirt, D., Steigenberger, R., 1971. Messungen und Berechnungen zur Erfassung der Kolbenringbewegungen. MTZ (1971), No. 11, p.419 (in German).
16. Maekawa, K., Akizuki, Y., Matsumoto, S., Motomura, O. and Ichimaru, K., 2001. Experimental estimation for behavior of cylinder oil on cylinder liner surface. Bulletin of the Marine Engineering Society in Japan, 2001, 29(1), 21-27.
17. Tanaka, T., Mitake, S., Taguchi, S., Goto, T. And Knudsen, S., 2000. Development of spray coated cylinder liner for diesel engine. Proc. of 6<sup>th</sup> Intl. Symposium on Marine Engineering, ISME, Tokyo, Japan, 23-27 October, 2000, 2 pp. 550-555.
18. Tanaka, M., Kitajima, Y., Endoh, Y., Watanabe, M. and Nagita, Y., 1993. Ceramic-metal composite coated piston ring and cylinder liner of marine low speed diesel engine. Bulletin of the Marine Engineering Society in Japan, 1993, 21(2), pp. 77-85.
19. Tanaka, M., 2002. Improved cylinder lubricator. Journal of the Japan Institution of Marine Engineering, 2002, 37(20, 16p.
20. Jacobsen, S., 2003. Alpha adaptive cylinder – Oil control alpha ACC. The Greek CIMAC Association – Interaction between Engine Design, Cylinder Lube Oil Design, and Cylinder Condition, Athens, Greece, 6 February 2003, 4 p.
21. Lauritsen, S., Dragsted, J. and Buchholz, B., 2001. Swirl injection lubrication – a new technology to obtain low cylinder oil consumption without sacrificing wear rates. Proc. of 23<sup>rd</sup> World Congress on Combustion Engine Technology for Ship propulsion, Power generation and Rail Traction, CIMAC, Hamburg, Germany, 7-10 May 2001, 3, pp. 921-932.
22. Stolarski, T.A., Zhou, Q., Smart, M., Green, D. and Allen, R.W., 2001. Temperature-friction characteristics of cylinder lubricants in large slow cross-

- head marine diesel engine under boundary lubrication conditions. Proc. of 3<sup>rd</sup> World Tribology Conference, Vienna, Austria, 3-7 September 2001, 4p.
23. Fog, T.L., 1998. Condition monitoring and fault diagnosis in marine diesel engines. PhD Thesis, Danish Technical University, August 1998.
  24. Jones, N.B. and Li, Y.H., 2000. A review of condition monitoring and fault diagnosis for diesel engines. Tribotest journal, 2000, 6(3), pp. 267-291.
  25. Ducu, D. O., Donahue, R.J. and Ghandhi, J.B., 2001. Design of capacitance probes for oil film thickness measurements between the piston ring and liner in internal combustion engines. Transactions of the ASME: Journal of Engineering for Gas Turbines and Power, 2001, 123(2), pp. 633-643
  26. Sherrington, I. and Smith, E.H., 1986. Experimental methods for measuring the oil-film thickness between the piston rings and cylinder wall of internal combustion engines. Tribology International, 1986, 18(6), pp.313-320.
  27. Martens, O., 1977. Experience with condition monitoring of slow speed engines. Proc. of 12<sup>th</sup> Intl. Congress of Combustion Engines, CIMAC, Tokyo, Japan, 22 May – 1 June 1977, vol B, pp. 1403-1425
  28. Shuster, M., Combs, D., Karrip, K. and Burke, D., 2000. Piston ring cylinder liner scuffing phenomenon studies using acoustic emission technique. *In*. Society of Automotive Engineers, Inc., 2000, SAE paper 2000-01-1782, 13p
  29. [http:// www.lionprecision.com/tech-library](http://www.lionprecision.com/tech-library); <http://www.eng.auburn.edu/files>
  30. Dowson, D., Economou, P.N., Ruddy, B. L., Strachan, P.J. and Baker, A.J.S., 1993. Piston Ring Lubrication. Part II. Theoretical Analysis of a Single Ring and a Complete Ring Pack. *In*. Energy Conversion through Fluid-Film Lubrication Technology, A.S.M.E. edited by C.M. Taylor, Elsevier Science Publishers B.V., 1993.
  31. Rhode, S.M.; 1980. A mixed friction model for dynamically loaded contact with application for piston ring lubrication. proc. of 7<sup>th</sup> Leeds-Lyon Symposium on Tribology, Leeds, UK, 9-12 September 1980, pp.262-278
  32. Priest, M., Dowson, D. and Taylor, C.M., 1993. Predictive wear modeling of lubricated piston rings in a diesel engine. Wear, 1999, 231(1), pp. 89-101.
  33. Ma, M. T., Sherrington, I., Smith, E.H., and Grice, N., 1997. Development of a detailed model for piston-ring lubrication in IC engines with circular and non-circular cylinder bores. Tribology International, 1997, 30(11), pp. 779-788.
  34. Gui, C.L., 1998. The effect of various factors on the scuffing of Piston Ring Cylinder Liner in Internal Combustion Engine and the Measure for Anti Scuffing Tribological Design. CNKI: ISSN: 1004-0595.0.1998-03-018

35. Greenwood J.A. and Tripp J.H., 1970. The contact of two nominally flat surfaces. proc. Inst. Mech. Eng. Part I, 1970, 185, 48, 625-633.
36. Available from <http://instserv.com/rmocoupl.htm>
37. Available from <http://www.jimpinto.com/pics/tempfig1.jpg>
38. Available from <http://digital.ni.com/public.nsf/allkb>
39. [www.micro-epsilon.com/displacement-position-sensors/eddy-current-sensor](http://www.micro-epsilon.com/displacement-position-sensors/eddy-current-sensor)
40. Tadashi Fukuyoshi, Keizo Goto, Shoichi Kanegae, Mikio koga, Takeo Takaishi. Piston ring wear diagnosis device and procedure therefor. Patent publication No. US5258930A, Nov2, 1993
41. Reuben, R. L., 1998. Role of acoustic emission in industrial condition monitoring. International journal of COMADEM, 1998, 1(4), pp. 35-46.
42. Vallen, H., 2002. AE testing, fundamentals, equipment, applications [online]. NDT.net, 2002, 7(9), available at: [http://www.ndt.net/article/az/ae\\_idx.htm](http://www.ndt.net/article/az/ae_idx.htm).
43. Steel, J.A. and Reuben, R.L., 2005. Recent developments in monitoring of engines using acoustic emission. The Journal of Strain Analysis for Engineering Design, 2005, 40(1), pp. 45-47.
44. Albarbar, A., Gennish, R., Ali, M., Harris, G., Gu, F. and Ball, A.D., 2005. Diesel engine injector condition monitoring using air-born acoustic measurement. Proc. 18<sup>th</sup> Intl. Congress on Condition Monitoring and Diagnostic Engineering Management, COMADEM, Cranfield, UK, 31 August – 2 September 2005, pp. 143-152.
45. Gu, F., Li, W., Ball, A.D. and Leung, A.Y.T., 2000. The condition monitoring of diesel engines using acoustic measurements, part 1: acoustic characteristics of the engine and representation of the acoustic signals. SAE 2000 World Congress, Noise & Vibration, Detroit, USA, 6-9 March, 2000, SAE Paper 2000-01-0730, pp. 51-57.
46. Ball, A.D., Gu, F. and Li, W., 2000. The condition monitoring of diesel engines using acoustic measurements, part 2: fault direction and diagnosis. SAE 2000 World Congress, Noise & Vibration, Detroit, USA 6-9 March 2000, SAE Paper 2000-01-0368, pp. 57-64.
47. Li, W., Gu, F., Ball, A.D., Leung, A.Y.T. and Phipps, 2001. A study of the noise from diesel engines using the independent component analysis. Mechanical Systems and Signal processing, 2001, 15(6), pp. 1165-1184.

48. Kimura, R., Nakai, N. and Kishimoto, T., 1998. Abnormal sound detection by neural network in the diesel engine. Bulletin of the Marine Engineering Society in Japan, 1998, 26(1), pp. 24-31.
49. Autar, R.K., 1996. An automated diagnostic expert system for diesel engines. Transactions of the ASME: Journal of Engineering for Gas Turbines and Power, 1996, 118(3), pp. 673-679.
50. Kawai, T., Nonomura, M., Futamurai, M. and Ito, M., 2003. Estimation of valve clearance of engine by wavelet analysis. Proc. 16<sup>th</sup> Intl. Conference on Condition Monitoring and Diagnostic Engineering management, COMADEM, Vaxjo, Sweden, 17-29 August 2003, pp. 759-766.
51. Koike, N., Kumagai, Y. and Nakamura, K., 1998. Development of detection system for abnormal wear of engine bearings. JSAE review, 1998, 19(1), pp. 27-32.
52. El-Ghamry, M., Steel, J.A., Reuben, R.L. and Fog, T.L., 2005. Indirect measurement of cylinder pressure from diesel engines using acoustic emission. Journal of Mechanical systems and signal processing 19 (2005) 751 – 765.
53. Nivesrangsan, P., Steel, J.A., Reuben, R.L., 2007. Acoustic emission mapping of diesel engines for spatially located time series – Part II : spatial reconstitution. Journal of Mechanical systems and signal processing 21 (2007) 1084 – 1102.
54. Noorul Haq, A. and Tamizharasan, T., 2007. Ring wear monitoring in IC engines: An acoustic emission approach. International journal of Advanced manufacturing and technology (2007) 31: 1148 – 1155
55. Douglas, R.M., Steel, J.A., Reuben, R.L., 2006. A study of the tribological behavior of piston ring/ cylinder liner interaction in diesel engines using acoustic emission. Tribology international 39 (2006) 1634 – 1642
56. Rogers, L. M., 2001. Structural and Engineering monitoring by acoustic emission methods – fundamentals and applications. Report: Lloyd's Register; Technical Investigation Department, 2001, 80 pages.
57. Paulson, P.O., 1998. Continuous acoustic monitoring of suspension bridges and cable stays. Structural Materials Technology III: An NDT Conference, Proc. of The Intl. Society for Optical Engineering, SPIE, San Antonio, USA, 31 March-2 April 1998, 3400 (26), pp. 205-213
58. Caneva, C., Pampallona, A. and Viskovic, S., 2004. Acoustic emission to assess the structural condition of bronze statues. Case of the “Nike” of Brescia. Proc. of 26<sup>th</sup> Conference on Acoustic Emission Testing, EWGAE, Berlin, Germany, 15-17 September 2004, pp. 567-574.

59. West, D., Venkatesan, G., Tewfik, A., Buckley, K. and Kaveh, M., 1996. Detection and modeling of acoustic emission for fault diagnostics. Proc. 8<sup>th</sup> IEEE Signal Processing Workshop on Statistical Signal and Array Processing, SSAP, Corfu, Greece, 24-26 June 1996, pp. 303-306
60. Buckley, K., Venkatesan, G., West, D. and Kaveh, M., 1996. Detection and characterization of cracks for failure monitoring and diagnostics. Proc. IEEE Intl. Conference on Acoustics, Speech and Signal Processing, ICASSP, Atlanta, USA, 7-10 May 1996, pp. 2738-2741
61. Gill, J.D., Reuben, R.L., Scaife, M., Brown, E.R. and Steel, J.A., 1998. Detection of diesel engine faults using acoustic emission. Proc. 2<sup>nd</sup> Intl. Conference: Planned Maintenance, reliability and Quality, Oxford, England, 2-3 April 1998, 1, pp. 57-61.
62. Gill, J.D., Rueben, R.L., Steel, J.A., Scaife, M.W. and Asquith, J., 2000. A study of small HSDI diesel engine fuel injection equipment faults using acoustic emission. Journal of Acoustic emission, 2000, 18, pp. 96-101.
63. El-Ghamry, M.H., Brown, E.R., Ferguson, I., Gill, J.D., Reuben, R.L., Steel, J.A., Scaife, M. and Middleton, S., 1998. Gaseous air-fuel quality identification for a spark ignition gas engine using acoustic emission analysis. Proc. 11<sup>th</sup> Intl. Conference on Condition Monitoring and Diagnostic Engineering Management. COMADEM, Launceston, Australia, 8-11 December 1998, pp. 235-244.
64. Berjger, A., 1999. An investigation of acoustic emission in fuel injection. Proc. of 3<sup>rd</sup> European Conference of Young Research and Science Workers in Transport and Telecommunications, TRANSCOM, Zilina, Slovakia, 29-30 June 1999, 7, pp. 135-138.
65. Bialkowski, M.T., Pekdemir, T., Reuben, R.L., Brautsch, M., Towers, D.P. and Elsbett, G., 2005. Preliminary approach towards a CDI system modification operating on neat rapeseed oil. 31<sup>st</sup> Intl. Scientific Conference on Internal Combustion Engines, KONES, Wroclaw, Poland, 4-7 September 2005, 12 (1-2), 14p.
66. Godinez, V., Finlayson, R.D., Miller, R.K. and Carlos, M.F., 2000. AE characterization of cavitation and detonation in combustion engines. Proc. of Acoustic Emission Working Group Meeting, AEWG-43, Seattle, USA, 18-19 July 2000.
67. Frances, A.K., Gill, J.D., Reuben, R.L. and Steel, J.A., 2004. Practical application of AE monitoring to diesel engines. Proc. 17<sup>th</sup> Intl. Conference on Condition Monitoring and Diagnostic Engineering Management, COMADEM, Cambridge, UK, 23-25 August 2004, pp. 325-333.

68. Chandroth, G.O., Sharkey, A. J. C and Sharkey, N.E., 1999. Cylinder pressures and vibration in internal combustion engine condition monitoring. Proc. 12<sup>th</sup> Intl. Congress on Condition Monitoring and Diagnostic Engineering Management, COMADEM, Sunderland, UK, 7-9 July 1999, pp. 141-151.
69. Sharkey, A.J.C., Chandroth, G.O. and Sharkey, N.E., 2000. Acoustic emission, cylinder pressure and vibration: a multisensory approach to robust fault diagnosis. Proc. IEEE-INNS-ENNS Intl. Joint Conference on Neural Networks, Como, Italy, 24-27 July 2000, 6, pp.223-228.
70. El-Gharmy, M., Steel, J.A., Reuben, R.L. and Fog, T.L., 2005. Indirect measurement of indicated power from diesel engines using acoustic emission. Mechanical Systems and Signal Processing, 2005, 19 (4), pp. 751-765.
71. Fog, T. L., Brown, E.R., Hansen, H.S., Madsen, L.B., Sorensen, P., Hansen, E.R., Steel, J.A., Reuben, R.L. and Pedersen, P.S., 1998. Exhaust valve leakage detection in large marine diesel engines. Proc. 11<sup>th</sup> Intl. Conference on Condition Monitoring and Diagnostic Engineering Management, COMADEM, Launceston, Australia, 8-11 December 1998, pp. 269-278.
72. Fog, T.L., Hansen, L.K., Larsen, J., Hansen, H.S., Madsen, L.B., Sorensen, P., Hansen, E.R. and Pedersen P.S., 1999. On condition monitoring of exhaust valves in marine diesel engines. Proc. IEEE Workshop on Neural Networks for Signal Processing IX, Piscataway, USA, 23-25 August 1999, pp. 554-563.
73. El-Gharmy, M., Reuben, R.L. and Steel, J.A., 2003. The development of automated pattern recognition and statistical feature isolation techniques for the diagnosis of reciprocating machinery faults using acoustic emission. Mechanical System and Signal Processing, 2003, 17(4), pp. 805-823.
74. Nivesrangsan, P., 2004. Multi-source, multi-sensor approaches to diesel engine monitoring using acoustic emission. PhD thesis, Heriot-Watt university, Edinburgh, UK, December 2004.
75. Nivesrangsen, P., Steel, J.A. and Reuben, R.L., 2005. AE mapping of engines for spatially located time series. Mechanical Systems and Signal Processing. 2005, 19(5), pp. 1034-1054.
76. Nivesrangsen, P., Steel, J.A. and Reuben, R.L., 2007. Acoustic emission mapping of diesel engines for spatially located time series – Part II: Spatial reconstitution. Mechanical Systems and Signal Processing. 2007, 21(2), pp. 1084-1102.
77. Nivesranrangsan, P., Steel, J.A. and Reuben, R.L., 2007. Source location of acoustic emission in diesel engines. Mechanical Systems and Signal Processing, 2007, 21(2), 1103-1114.



78. Pontoppidan, N.H. and Sigurdsson, S., 2006. Independent components in acoustic emission energy signals from large diesel engines. Accepted for publication in International Journal of COMADEM, 2006.
79. Sigurdsson, S., Pontoppidan, N.H. and Larsen, J., 2005. Supervised and unsupervised condition monitoring of non-stationary acoustic emission signals. Proc. 18<sup>th</sup> Intl. Congress on Condition Monitoring and Diagnostic Engineering Management, COMADEM, Cranefield, UK, 31 August – 2 September 2005, pp. 535-541.
80. Pontoppidan, N.H. and Douglas, R.M., 2004. Event alignment, warping between running speeds. Proc. 17<sup>th</sup> Intl. Conference on Condition Monitoring and Diagnostic engineering management, COMADEM, Cambridge, UK, 23-25 August 2004, pp. 621-628.
81. Pontoppidan, N.H. and Larsen, J., 2004. Non-stationary condition monitoring through event alignment. Proc. IEEE Workshop on Machine Learning for Signal Processing, MLSP, Sao Luis, Brazil, 29 September – 1 October 2004, pp. 499-508.
82. Pontoppidan, N.H. and Larsen, J., 2003. Unsupervised condition change detection in large diesel engines. Proc. 2003 IEEE Workshop on Neural Networks for Signal Processing, NNSP, Toulouse, France, 17-19 September 2003, pp. 565-574.
83. Pontoppidan, N.H., Larsen, J. and Fog, T.L., 2003. Independent component analysis for detection of condition changes in large diesels. Proc. 16<sup>th</sup> Intl. Conference on Condition Monitoring and Diagnostic engineering management, COMADEM, Vaxjo, Sweden, 27-29 August 2003, pp. 493-502.
84. Dornfeld, D.A. and Kannatey-Asibu, E., 1980. Acoustic emission during orthogonal metal cutting. International Journal of Mechanical Sciences, 1980, 22(5), pp. 285-296.
85. Saini, D.P. and Park, Y.J., 1996. A quantitative model of acoustic emission in orthogonal cutting operations. Journal of Materials Processing technology, 1996, 58, pp. 343-350.
86. Carolan, T.A., Kidd, S.R., Hand, D.P., Wilcox, S.J., Wilkinson, P., Barton, J.S., Jones, J.D.C. and Reuben, R.L., 1997. Acoustic emission monitoring of tool wear during face milling of steels and aluminum alloys using a fibre optic sensor. 1. Energy analysis. Proc. of the ImechE part B2: Journal of Engineering manufacture, 1997, 211(4) pp. 299-309.
87. Hwang, T.W., Whitenton, E.P., Hsu, N.N., Hsu, Blessing, G.V. and Evans, C.J., 2000. Acoustic emission monitoring of high speed grinding of silicon nitride. Ultrasonic, 2000, 38(1-8), pp. 614-619.

88. Jayakumar, T. Mukhopadhyay, C.K., Venugopal, S., Mannan, S.L. and Raj, N., 2005. A review of the application of acoustic emission techniques for monitoring forming and grinding processes. Journal of Materials Processing Technology, 2005, 159(1), pp. 48-61.
89. Belyi, V.A., Kholodilov, O.V. and Sviridyonok, A.I., 1981. Acoustic spectrometry as used for the evaluation of tribological systems. Wear, 1981, 69(3), pp. 309-319
90. McBride, S.L., Boness, R.J., Sobczyk, M. and Viner, M.R., 1989. Acoustic emission from lubricated and unlubricated rubbing surfaces. Journal of Acoustic Emission, 1989, 8(1-2), pp. 192-196.
91. Boness, R.J., McBride, S.L. and Sobczyk, M., 1990. Wear studies using acoustic emission techniques. Tribology International, 1990, 23(5), pp. 291-295.
92. Boness, R.J. and McBride, S.L., 1991. Adhesive and abrasive wear studies using acoustic emission. Wear, 1991, 149(1-2), pp. 41-53.
93. Jiaa, C.L. and Dornfeld, D.A., 1990. Experimental studies of sliding friction and wear via acoustic emission signal analysis. Wear, 1990, 139(2), pp. 403-423.
94. Hanchi, J. and Klamecki, B.E., 1991. Acoustic emission monitoring of the wear process. Wear, 1991, 145(1), pp. 1-27.
95. Klamecki, B.E. and Hanchi, J., 1990. Wear process description based on acoustic emission. Transactions of ASME: Journal of Tribology, 1990, 112(3), pp. 469-476.
96. Diei, E.N., 1985. Investigation of milling process using acoustic emission signal analysis. PhD thesis, University of California, Berkeley, USA, 1985.
97. Lingard, S. and Ng, K.K., 1989. An investigation of acoustic emission in sliding friction and wear of metals. Wear, 1989, 130(2), pp. 367-379.
98. Lingard, S., Yu, C.W. and Yau, C.F., 1993. Sliding wear studies using acoustic emission. Wear, 1993, 162-164(1), pp. 597-604.
99. Mechefske, C.K., 2001. Monitoring sliding wear using acoustic emission. Proceedings of 14<sup>th</sup> Intl. Conference on Condition Monitoring and Diagnostic Engineering Management, COMADEM, Manchester, UK, 4-6 September 2001, pp. 57-65.
100. Boness, R.J., 1993. Measurements of wear and acoustic emission from fuel-wetted surfaces. Wear, 1993, 162-164(1), pp. 703-705.

101. Price, E.D., Lees, A.W. and Friswell, M.I., 2005. Detection of severe sliding and pitting fatigue wear regimes through the use of broadband acoustic emission. Proc. Of the IMechE, Part J; Journal of Engineering Tribology, 2005, 219(2), pp. 85-98.
102. Shuster, M., Combs, D., Karrip, K. and Burke, D., 2000. Piston ring cylinder liner scuffing phenomenon studies using acoustic emission technique. Proc. Of CEC/SAE Spring Fuels & Lubricants Meeting and Exposition, Paris, France, 2000, pp. 901-913.
103. Khurshudov, A.G. and Talke, F.E., 1998. A study of sub-ambient pressure tri-pad sliders using acoustic emission. Transactions of ASME: Journal of Tribology, 1998, 120(1), pp. 54-59.
104. Ravikiran, A., Low, T.S., 2000. Estimation of lubricant thickness on a magnetic hard disk using acoustic emission. Review of Scientific Instruments, 2000, 71(4), pp. 1915-1916.
105. Liew, T.Y.F., Chai, M.C., weerasooriya, S. and Low, T.S., 1997. Head-disk interaction of proximity sliders studied by the acoustic emission probe, the dynamic height tester, and the laser Doppler vibrometer. IEEE Transactions on Magnetism, 1997, 33(5), pp. 3175-3177.
106. Zhu, Y-L., Liu, B., Li, Y-H. and Leng, Q-F., 1999. Slider-disk interaction and its effect on the flying performance of slider. IEEE Transactions on Magnetism, 1999, 35(5), pp. 2403-2405.
107. Benson, R.C., Chiang, C. and Talke, F.E., 1989. The dynamics of slider bearings during contacts between slider and disk. IBM Journal of Research and development, 1989, 33(1), pp. 2-14.
108. Ravikiran, A., Liew, T. and Low, T.S., 1999. Effect of disk acceleration on the generation of acoustic emission signal at the head-disk interface. Journal of Applied Physics, 1999, 85(8), pp. 5612-5614.
109. Liu, Y., Jiaa, C.L. and Eltoukhy, A., 1997. Acoustic emission study of lubricant effect on proximity contact recording. IEEE Transactions on Magnetism, 1997, 33(5), pp. 3160-3162.
110. Tanaka, H., Yonemura, S. and Tokisue, H., 2001. Slider dynamics during continuous contact with textured and smooth disks in ultra low flying height. IEEE Transactions on Magnetism, 2001, 37(2), pp. 906-911.
111. Sharma, V., Talke, F.E. and Ng, Q., 1996. Tribological investigations of tri-pad sliders. IEEE Transactions on Magnetism, 1996, 32(5), pp. 3651-3653.

112. Benson, R.C., Sundaram, R. and Talke, F.E., 1988. A study of the acoustic emission from slider/disk interface in a 51/4 inch hard disk drive. STLE Special Publication 25: Tribology and Mechanics of Magnetic Storage System, 1988, pp. 87-93.
113. Xu, J., Tokisue, H. and Kawakubo, Y., 2000. Study on soft-particle intrusion in a head/disk interface of load/unload drives. IEEE transactions on Magnetics, 2000, 36(5), pp. 2745-2747.
114. Briggs, J.C., Chang, M-K and Tse, M.K., 1992. High frequency slider vibrations during asperity impacts in rigid magnetic disk system. Advanced Information Storage Systems, 1992, 4, pp. 181-194.
115. Matsuoka, K., Taniguchi, K. and Nakakita, M., 2001. In-situ wear monitoring of slider and disk using acoustic emission. Transactions of ASME: Journal of Tribology, 2001, 123(1), pp. 175-180.
116. McMillan, T.C. and Talke, F.E., 1998. Identification of slider/disk contacts using the energy of the acoustic emission signal. IEEE Transactions of Magnetics, 1998, 34(4), pp. 1819-1821.
117. O'Brien, K. and Harris, D., 1996. Head/disk interface contact detection using a refined acoustic emission technique. ASME: Journal of Tribology, 1996, 118(3), pp.539-542.
118. Ganapathi, S.K., Donovan, M. and Hsia, Y.T. Contact force measurements at the head/disk interface for contact recording heads in magnetic recording. Proc. Of the SPIE- the International Society for Optical Engineering, 1996, 2604, pp. 236-243.
119. Matsuoka, K., Forrest, D. and Tse, M.K., 1993. On-line wear monitoring using acoustic emission. Wear, 1993, 162-164(1), pp. 605-610.
120. Matsuoka, K., Taniguchi, K. and Ueno, Y., 1996. Evaluation technique of head/tape contact using acoustic emission. ASME: Journal of tribology, 1996, 120(2), pp. 259-265.
121. Bhushan, B., Wu, Y. and Tambe, N.S., 2003. Sliding contact energy measurement using a calibrated acoustic emission transducer. IEEE Transactions on Magnetics, 2003, 39(2), pp. 881-887.
122. Toutountzakis, T. and Mba, D., 2003. Observation of acoustic emission activity during gear defect diagnosis. NDT and E International, 2003, 36(7), pp. 471-477.
123. Tan, C.K. and Mba, D., 2004. The source of acoustic emission during meshing of spur gears. Proc. Of 26<sup>th</sup> Conference on Acoustic Emission Testing, EWGAE, Berlin, Germany, 15-17 September 2004, pp. 469-474.

124. Tan, C.K. and Mba, D., 2005. Identification of the acoustic emission source during a comparative study on diagnosis of a spur gearbox. Tribology International, 2005, 38(5), pp. 469-480.
125. Sentoku, H., 1998. AE in tooth surface failure process of spur gears. Journal of Acoustic Emission, 1998, 16(1-4), pp. S19-S24.
126. Toutountzakis, T., Tan, C.K. and Mba, D., 2005. Application of acoustic emission to seeded gear fault detection. NDT&E International, 2005, 38(1), pp. 27-36.
127. Miettinen, J. and Siekkinen, V., 1995. Acoustic emission in monitoring sliding contact behavior. Wear, 1995, 181-183(2), pp. 897-900.
128. Ferguson, I.G., Gill, J.D., Reuben, R.L., Steel, J.A., Brown, E.R. and Roosch, E., 1998. Condition monitoring of rotating seals using acoustic emission. Proc. Of the 23<sup>rd</sup> European Conference on Acoustic Emission Testing, EWGAE, Vienna, Austria, 6-8 May 1998, pp. 281-286.
129. Douglas, R.M., Beugne, S., Jenkins, M.D., Frances, A.K., Steel, J.A., reuben, R.L. and Kew, P.A., 2004. Monitoring of gas turbine operating parameters using acoustic emission. Proc. Of 26<sup>th</sup> Conference on Acoustic Emission testing, EWGAE, Berlin, Germany, 15-17 September 2004, pp. 455-466.
130. Sato, I., 1990. Rotating machinery diagnosis with acoustic emission techniques. Electrical Engineering in Japan, 1990, 100(2), pp. 115-127.
131. Board, D.B., 2000. Stress wave analysis of turbine engine faults. Proc. IEEE Aerospace Conference, Big Sky, USA, 18-25 march 2000, 6, pp. 79-95.
132. Hall, L.D. and Mba, D., 2004. Diagnosis of continuous rotor-stator rubbing in large scale turbine units using acoustic emissions. Ultrasonics, 2004, 41(9), pp. 765-783.
133. Miettinen, J., 2001. The influence of the running parameters on the acoustic emission of grease lubricated rolling bearings, Maintenance & Asset Management, 2001, 16(2), pp. 7-11.
134. Miettinen, J. and Andersson, P., 2000. Acoustic emission of rolling bearings lubricated with contaminated grease. Tribology International, 2000, 33(11), pp. 777-787.
135. Miettinen, J., Anderson, P. and Wikstrom, V., 2001. Analysis of grease lubrication of rolling bearings using acoustic emission measurement. Proc. Of the IMechE Part J: Journal of engineering tribology. 2001, 215(6), pp. 535-544.

136. Roelands, C.J.A., 1966. Correlational Aspect of Viscosity-temperature-Pressure Relationships of Lubricating Oils. PhD thesis. Delft University of Technology, The Netherlands.
137. 130.Gohar, R., 1988. *In. Elastohydrodynamics*. Ellis Horwood Limited, 1988
138. 131.Houpert, L., New Results of Traction Force Calculation in EHD Contacts. Transactions ASME, Journal of Lubrication Technology, V
139. D. Dowson., 1985. Non-Steady state effects in EHL, New Directions in Lubrication, Materials, Wear and Surface Interactions. *In. W.R. Loomis, ed. Tribology in the 80's*, Noyes Publications, Park Ridge, New Jersey, USA, 1985
140. Jeffrey Jocsak, 2005. The Effects of Surface Finish on Piston Ring-pack Performance in Advanced Reciprocating Engine Systems. Masters Thesis, Mechanical Engineering; Massachusetts Institute of Technology; June, 2005.
141. Dowson, D., Ruddy, B.L., and Economou, P.N., 1983. The Elastohydrodynamic Lubrication of Piston Rings. proc. R. Soc. London, A386, pp 409-430.
142. Keribar, R., Dursunkaya, Z. and Flemming, M.F., 1991. An integrated model of ring pack performance. Transactions of the ASME: Journal of Engineering for Gas Turbine and Power, 1991, 113(3), pp. 382-389
143. Ma, M.T., Sherrington, I. and Smith, E.H., 1997. Analysis of lubrication and friction for a complete piston ring-pack with an improved oil availability model. Part 1: circumferentially uniform film. Proc. Of the IMechE Part J: Journal of Engineering tribology, 1997, 211(1), pp. 1-15.
144. Taylor, R. I., Kitahara, T., Saito, T. and Coy, R.C., 1995. Piston assembly friction and wear: the influence of lubricant viscometry. Proc.of the Intl.Tribology Conference, Yokohama, Japan, 29 October – 2 November 1995, 6 p.
145. Cho, S., Choi, S. and Bae, C., 2000. The frictional modes of piston rings for a SI engine [in Korean with English summary]. SAE 2000-03-0094, pp. 114-120.
146. Seki, T., Nakayama, K., Yamada, T., Yoshida, A. and Takiguchi, M., 2000. A study on variation in oil film thickness of a piston ring package: variation of oil film thickness in piston sliding direction. JSAE Review, 2000, 21(3), pp. 315-320.

147. Bolander, N.W., Steenwyk, B.D., Sadeghi, F. and Gerber, G.R., Lubrication regime transitions at the piston ring-cylinder liner interface. *In. Engineering Tribology*, IMechE\_vol.219 part J:J.
148. Available from <http://www.ndt-ed.org/EducationResources/CommunityCollege/EddyCurrents/Physics/depthcurrentdensity.htm>
149. Available from: [www.cnea.gov.ar/cac/endye/glea/mateo/guide.htm](http://www.cnea.gov.ar/cac/endye/glea/mateo/guide.htm)
150. Ruddy, B L., 1979. The Lubrication and Dynamics of Piston Rings and the Theoretical Predictions of Ring Pack Gas Flow. Ph.D. Thesis, University of Leeds, UK.
151. Ruddy, B. L., Dowson, D., Economou, P. N. and Baker, A.J.S., 1979. Piston Ring Lubrication Part III – The Influence of Ring Dynamics and Ring Twist. Energy Conversion Through Fluid Film Lubrication Technology, A.S.M.E. pp 191-215
152. Ruddy, B L., Parsons, B., Dowson, D. and Economou, P N., 1980. The Influence of Thermal Distortion and Wear of Piston Ring Grooves upon the Lubrication of Piston Rings in Diesel Engines. Proc.. 6<sup>th</sup> Leeds-Lyon Symposium on Tribology, Elsevier, pp 84-94.
153. Stachowiak, G.W., Batchelor, A.W. Department of Mechanical and Materials Engineering, University of Western Australia, 'Engineering tribology'